



HAL
open science

Towards better control over supramolecular polymerization

Georges Formon

► **To cite this version:**

Georges Formon. Towards better control over supramolecular polymerization. *Polymers*. Université de Strasbourg, 2020. English. NNT : 2020STRAF017 . tel-03616040

HAL Id: tel-03616040

<https://theses.hal.science/tel-03616040>

Submitted on 22 Mar 2022

HAL is a multi-disciplinary open access archive for the deposit and dissemination of scientific research documents, whether they are published or not. The documents may come from teaching and research institutions in France or abroad, or from public or private research centers.

L'archive ouverte pluridisciplinaire **HAL**, est destinée au dépôt et à la diffusion de documents scientifiques de niveau recherche, publiés ou non, émanant des établissements d'enseignement et de recherche français ou étrangers, des laboratoires publics ou privés.

UNIVERSITÉ DE STRASBOURG

ÉCOLE DOCTORALE 222

UMR 7140

THÈSE présentée par :

Georges Jacques Marie Formon

soutenue le : **16 Octobre 2020**

pour obtenir le grade de : **Docteur de l'université de Strasbourg**

Discipline/ Spécialité : Chimie Supramoléculaire

**Towards Better Control Over Supramolecular
Polymerization**

THÈSE dirigée par :

M Thomas Hermans

Professeur, Université de Strasbourg, UMR 7140, Strasbourg, France

RAPPORTEURS :

Mme Nathalie Katsonis

Professeur, Stratingh Institute for Chemistry – University of Groningen, Groningen, Pays-bas

M Javier Montenegro

Directeur de recherche, CiQUS – Universidade de Santiago de Compostela, Santiago de Compostela, Espagne

AUTRES MEMBRES DU JURY :

M Jean Weiss

Directeur de recherche, Université de Strasbourg, UMR 7177, Strasbourg, France

Table of contents

Table of contents	i
Acknowledgements	iv
Résumé	vi
Summary	xiv
Symbols and Abbreviations	xix
Chapter 1. General Introduction: Controlling Supramolecular Polymerization	1
1.1 General Introduction	2
1.1.1 <i>Supramolecular Chemistry</i>	2
1.1.2 <i>Supramolecular Polymers</i>	2
1.2 Supramolecular Polymerization Under Thermodynamic and Kinetic Control	6
1.2.1 <i>Stimuli-Responsive Supramolecular Polymers</i>	6
1.2.2 <i>Non-Equilibrium Control Over Supramolecular Polymerization</i>	14
1.2.3 <i>Spatial Control</i>	21
1.3 Out-of-Equilibrium Reaction Networks to Control Supramolecular Polymers	26
1.3.1 <i>Fully Synthetic Reaction Cycle</i>	27
1.3.2 <i>Enzymatic Reaction Cycles</i>	31
1.3.3 <i>pH and Redox Driven Reaction Cycles</i>	33
1.4 Magnetism as a Tool to Control Soft Matter	35
1.4.1 <i>Magnetism and Magnetic Energy</i>	35
1.4.2 <i>Magnetism to Control Soft-Matter (Trivial Observations)</i>	42
1.4.3 <i>Non-Trivial Observations of Magnetic Effects on Soft Materials</i>	49
1.5 Aim and Contents of this Thesis	56
Chapter 2. Surface-Assisted Self-Assembly of a Hydrogel by Proton Diffusion	58
2.1 Introduction	59
2.2 pH-Responsive Self-Assembly	60
2.3 Kinetics and Mechanism of Supramolecular Polymerization	61
2.4 Surface-Assisted Hydrogelation	66
2.5 Conclusions	70

2.6	Appendix	71
2.7	Acknowledgements	72
2.8	Materials and Methods.....	73
2.8.1	<i>Materials and Experimental procedures.....</i>	<i>73</i>
2.8.2	<i>Synthesis.....</i>	<i>78</i>
2.8.3	<i>Mathematical Model.....</i>	<i>85</i>
2.8.4	<i>MATLAB®code</i>	<i>90</i>
Chapter 3.	Controlling Morphology and Mechanical Properties of a Hydrogel Using a Fuel-Driven Reaction Cycle	100
3.1	Introduction.....	101
3.2	Stimuli-Responsive Hydrogel and Reaction cycle.....	102
3.3	Gelation Mechanism and Kinetics	103
3.4	Kinetics of the Full Reaction Cycle.....	106
3.5	Kinetic Control of Morphology and Mechanical Properties.....	109
3.6	Syneresis.....	111
3.7	Conclusions	113
3.8	Appendix	113
3.9	Acknowledgements	116
3.10	Materials and Methods.....	116
3.10.1	<i>Materials and Experimental procedures.....</i>	<i>116</i>
3.10.2	<i>Synthesis.....</i>	<i>119</i>
3.10.3	<i>Mathematical Model and Fitting.....</i>	<i>121</i>
3.10.4	<i>MATLAB® code.....</i>	<i>124</i>
Chapter 4.	Magnetic Control over Supramolecular Networks	136
4.1	Introduction.....	137
4.2	Characterization of Supramolecular Assemblies	138
4.3	Magnetic Control Over Supramolecular Assemblies	141
4.4	Magnetic Characterization of Assemblies	142
4.5	Energetic Considerations	144
4.6	Conclusions	146
4.7	Appendix	147

4.7.1	<i>Results of Magnetic Ground-State Calculations</i>	149
4.8	Acknowledgements	152
4.9	Materials and Methods	152
4.9.1	<i>Synthesis</i>	152
4.9.2	<i>Cryo-TEM</i>	152
4.9.3	<i>Dynamic Light Scattering</i>	153
4.9.4	<i>Fractal dimension</i>	154
4.9.5	<i>SQUID (Superconducting Quantum Interference Device)</i>	155
4.9.6	<i>Magnetic dipole calculations</i>	156
Chapter 5.	Magnetic Lanthanides to Control Supramolecular Polymers	158
5.1	Introduction	159
5.2	Synthesis and Spectroscopic Characterization	160
5.3	Thermodynamics of Supramolecular Polymerization	163
5.4	Size and Morphology of Assemblies	171
5.5	Conclusions	173
5.6	Appendix	174
5.7	Acknowledgements	179
5.8	Materials and Methods	179
5.8.1	<i>Synthesis</i>	179
5.8.2	<i>Methods</i>	184
5.8.3	<i>Thermodynamic Model</i>	186
5.8.4	<i>MATLAB® codes</i>	187
Chapter 6.	Overall conclusions and outlook	206
References	210
Keyword Index	230

Acknowledgements

First of all, I would like to thank Prof. Thomas Hermans for giving me the opportunity to pursue my thesis at the *Laboratoire des systèmes complexes hors équilibre* and mentoring me over the past three years. Your guidance sparked my interest on supramolecular polymers in and out-of-equilibrium, making me fall in love with the field. Your drive to always push the envelope in so many different areas is an inspiration to me.

Thank you Prof. Nathalie Katsonis and Dr. Javier Montenegro for taking the time to read and judge my work, and together with Dr. Jean Weiss for being part of the jury for my thesis. I am grateful for having chemists that I admire analyzing my work.

I would also like to thank Dr. Nishant Singh for our daily scientific discussions and all the knowledge you transferred to me during the two years I worked alongside you. Your work ethic is an inspiration to me. I want to acknowledge Dr. Jorge Leira-Iglesias, for guiding me during the first year of my thesis, teaching me the in-and-outs of the project, lab, and different techniques.

I would like to thank Dr. Vincent Marichez, and Dr. Akihiro Sato, for starting the work on some of the projects I developed, giving me a framework for excellent science. Prof. Pol Besenius and Dr. Daniel Spitzer, also for your crucial collaboration. Dr. Peter Dunne has been an important figure during my thesis, always helping me with his theoretical knowledge in magnetism and physics in general, I also have enjoyed the experiments we performed in Saclay. Together with Prof. Michael Coey, Peter has also been fundamental for the theoretical understanding of our magneto-responsive supramolecular polymers, for that I am grateful to them. I also would like to acknowledge Alessandra Tassoni for building/fixing/aligning the light scattering set-up and helping me in doing those experiments. Bruno Lainer and Serena De Piccoli, I am grateful for collaborating with you in more than one work.

I also need to acknowledge Prof. Isja de Feijter, Dr. Pascal Hébraud, Dr. Matthieu Bailleul Dr. M. Venkatesan and Prof. E.W. (Bert) Meijer for the collaboration in the work presented in Chapter 4.

I would like to thank Michaela Schicho, Anastasiia Sharko and Bryan Pauwels for being hard working students, that helped me while I was supervising them.

I would like to thank Chunfeng Chen, even if we have not collaborated, for our many scientific and friendly discussions. To the other members of the lab, past and present, Alvaro Lopez-Acosta, Takuji Adachi, Flor Sacarelli, Lucas Giacchetti, I would like to thank you for a good atmosphere in the lab and the nice time we had.

I would also like to thank all the support staff in ISIS and at the chemistry department of the University of Strasbourg, without you, excellent science would not be possible here. Particularly, Annia Bertrand and Soumia Hnini for your administrative and personal support.

To my family, I am very grateful for always supporting me during my education and raising me to be the person I am. Without the backing of my mother Georgina and my father Christian I would not be here today. I also want to thank my brothers Arthur and Guilherme for the moral support and friendship over the years. I also need mention my grandparents, those that are not here anymore and those who still are, for being an inspiration in my life. Obrigado a todos pelo apoio e carinho. Merci à tous pour votre soutien et affection.

A special thanks must be given to the Zaia family, my family by marriage, that has helped me profoundly for the last eight years. Obrigado Thaïs, Dimas e Sophia pelo suporte e pela ajuda.

Lastly, but most importantly, I would like to thank Laura, my wife, and the love of my life, for supporting, encouraging, and helping me when I needed the most. Those past three years have been difficult, and I thank you for standing by my side. You push me to become a better person and strive to see me succeed. My present and future achievements are only meaningful by your side. This thesis is dedicated to you. Te amo.

Résumé

La chimie supramoléculaire est la science qui maîtrise les interactions physico-chimiques entre les molécules et des liaisons non-covalentes, J.-M. Lehn l'a défini comme la chimie « au-delà de la molécule ». ^{1,2} Interactions entre charges ou dipôles, liaisons hydrogène, π - π stacking, forces de Van der Waals, et les effets de solvatation et hydrophobes sont les exemples les plus courants des liaisons non-covalentes utilisées comme outils pour la formation de complexes supramoléculaires. ³

L'avantage des matériaux supramoléculaires est leur nature dynamique, les liaisons ne sont pas fixées comme dans les matériaux covalents. ^{1,2} Ceci va leur permettre d'être sensible aux stimuli externes, et donc adaptables à l'environnement et modulables selon les nécessités. Ces caractéristiques permettent de fabriquer des matériaux fonctionnels à base de polymères supramoléculaires avec des propriétés autocicatrisantes ou électroniques ou des applications biomédicales. ⁴

En cherchant des applications des polymères supramoléculaires, de nouvelles et meilleures manières de contrôler leur polymérisation, morphologie et/ou propriétés sont toujours recherchées, à fin d'avoir une meilleure maîtrise de ces matériaux. ⁵

Dans cette thèse, trois manières de contrôler la polymérisation supramoléculaire seront explorés. La première vise à contrôler spatialement la nucléation de hydrogels sensibles au pH, à partir de la diffusion de protons. Ensuite, la polymérisation supramoléculaire d'un hydrogélateur est modulée par un cycle réactionnel hors-équilibre. Les propriétés morphologiques et mécaniques dépendent de la cinétique de formation du gel, et donc du cycle réactionnel. Finalement, l'utilisation de champs magnétiques et de l'interactions de dipôles magnétiques sont explorés pour contrôler la polymérisation supramoléculaire de molécules organiques paramagnétiques contenant des terres rares.

Dans le **Chapitre 2** la molécule **BTA-1** a été synthétisée de forme qu'elle soit sensible au pH par la présence de trois fonctions acides carboxyliques dans chaque 'bras'. Quand le pH est élevé, ces acides sont déprotonés et la charge globale de la molécule est de -9. La répulsion

électrostatique fait qu'à des $\text{pH} > 6$ la molécule est en forme monomérique dans l'eau. Cependant si le pH est diminué à une valeur au-dessous de 5, **BTA-1** s'auto-assemble par des liaisons hydrogène et π - π *stacking* en fibres unidimensionnelles de plus de 500 nm de longueur et ~ 7 nm de diamètre. En mélangeant une solution tampon à $\text{pH} 5.0$ et une solution contenant les monomères de **BTA-1** dans l'eau à $\text{pH} 6.1$, la polymérisation a été suivie par l'évolution du spectre de dichroïsme circulaire à la longueur d'onde de 250 nm. La cinétique a été évaluée premièrement en variant la concentration totale de **BTA-1** et par l'analyse des temps de demi-réaction en fonction de la concentration, on peut estimer le mécanisme de polymérisation supramoléculaire par le coefficient directeur, γ , de la droite en repère log-log.⁶ Dans notre cas, γ est égal à -0.34 , proche de -0.5 , indiquant un processus de polymérisation en trois étapes : nucléation, élongation et fragmentation.^{6,7} Ensuite, la dépendance de la cinétique avec la température a été étudiée, en fixant la concentration à $80 \mu\text{M}$, de 20 à 55 °C. L'évolution du temps de demi-réaction avec la température suit la loi d'Arrhenius. Nous avons donc utilisé un modèle mathématique de polymérisation supramoléculaire comprenant nucléation, élongation, fragmentation et dépendance avec la température pour obtenir les énergies d'activation des constantes cinétiques du processus.

L'objectif suivant était de contrôler spatialement la polymérisation supramoléculaire de **BTA-1** en explorant la sensibilité au pH de cette molécule. Premièrement, un bloc de 5 à 10 mm^3 d'un hydrogel d'agarose a été trempé dans de l'acide chloridrique concentré ($\text{HCl } 37 \text{ \%wt}$) pendant 96 h . En suite ce cube a été placé dans une cuve contenant solution de **BTA-1** à $160 \mu\text{M}$ à $\text{pH} = 7.4$. Mais au lieu de former une couche d'hydrogel, **BTA-1** précipite en solution. Ceci indique que pour avoir un assemblage structuré de **BTA-1** un matériau qui diffuse les protons plus lentement que la cinétique de nucléation est nécessaire. Donc, un cube de Poly(diméthylsiloxane) (PDMS) de mêmes dimensions a subi le même traitement : 96 h de trempage dans $\text{HCl } 37\% \text{wt}$ puis il est plongé dans une solution du monomère. Cette fois, **BTA-1** nucléée à la surface du polymère et une couche de l'hydrogel grandit à partir de celle-là en direction inverse du gradient de protons. Comme le PDMS est moins poreux que l'agarose, la diffusion des protons est suffisamment lente pour la nucléation de **BTA-1** se passe sur la

surface du polymère. Cette couche d'hydrogel a pu s'étendre à des distances dans l'ordre de dizaines de millimètres. Finalement, la notion de contrôle spatial sur la nucléation et polymérisation de **BTA-1** a été approfondie par la construction d'un dispositif microfluidique composé de deux canaux superposés perpendiculairement, séparés par une couche de 100 μm de PDMS. Un des canaux contient une solution basique de **BTA-1** à 160 μM ; une solution tampon de phthalate de potassium à pH 4 écoule dans l'autre. Après deux heures, des assemblages sphériques d'environ 2 μm de diamètre sont observés par microscopie confocale sur la membrane en PDMS seulement sur l'intersection des deux canaux. Ceci rend possible un contrôle plus précis de la polymérisation supramoléculaire du **BTA-1**.

Au **Chapitre 3**, la molécule **SachCHO**, contenant une fonction aldéhyde, est capable de former des hydrogels à des concentrations à partir de 8 mg/mL.⁸ Quand un hydrogel de **SachCHO** est traité avec de l'hydrosulfite de sodium (DT), les fonctions aldéhydes sont complètement transformées en α -hydroxy-sulfonates, en formant **SachSO₃⁻** après cinq minutes (vérifié par RMN ¹H). Ces nouvelles fonctions sont chargées négativement et la répulsion électrostatique détruit l'hydrogel, en formant une solution transparente. Cette réaction est un équilibre, donc par l'addition d'un aldéhyde plus réactif (formaldéhyde) le sulfonate va être transféré vers lui. Les molécules de **SachCHO** reviennent donc en solution, et après nucléation, l'hydrogel est formé de nouveau. La cinétique de polymérisation a été suivie par la densité optique UV/Visible à une longueur d'onde de 500 nm. L'opacité de l'échantillon est directement proportionnelle au développement de l'hydrogel dans la cuvette. En traçant la droite log-log du temps de demi-réaction en fonction de la concentration, le coefficient directeur, γ , égal à -3.6 indique un mécanisme de polymérisation comprenant nucléation, élongation et nucléation secondaire (quand une fibre polymérique déjà formée catalyse la formation d'un nouveau noyau), avec des noyaux (primaires et secondaires) de six molécules. La nucléation secondaire est mise en évidence par l'observation par microscopie confocale de nouvelles fibres se formant sur des fibres déjà existantes formant des agrégats en forme de brosse. Un modèle mathématique⁶ a été utilisé pour acquérir les constantes cinétiques de la polymérisation de **SachCHO**, qu'indiquent que la polymérisation est très coopérative car la

barrière cinétique pour former un noyau primaire est huit à neuf ordres de magnitude plus élevée que celles de l'élongation et de la nucléation secondaire.

La prochaine étape est le contrôle temporel de l'hydrogel avec une seule addition de produits chimiques. Formaldéhyde et hydrosulfite de sodium réagissent entre eux, ce qui rend impossible la transformation de **SachCHO** en **SachSO₃⁻** si ces deux réactifs sont ajoutés en même temps. Hexaméthylènetétramine (HMTA) est une molécule qui se décompose dans de l'eau libérant six équivalents de formaldéhyde et quatre d'ammoniac. L'hydrolyse de HMTA est catalysée par des conditions acides. Pour cela δ -Gluconolactone (GdL) est utilisé parce qu'il peut être hydrolysé en acide gluconique. Donc en ajoutant DT, HMTA, et GdL simultanément à un hydrogel de **SachCHO**, induit à la solubilisation complète en cinq minutes du gel, après entre 20 et 60 minutes (dépendant de la concentration de GdL) l'hydrogel se forme à nouveau. Comme la dissociation du HMTA est catalysé par des acides, le temps du cycle gel-solution-gel peut être modulé par la quantité de GdL dans le cocktail chimique. Le temps de formation de l'hydrogel varie de 70 min pour 46.8 mM de GdL à 48 minutes à 374 mM. C'est important de noter que la vitesse de formation du gel n'augmente pas linéairement avec la concentration de δ -Gluconolactone et atteint une limite quand $[GdL] > 234$ mM.

En analysant les hydrogels par microscopie confocale et les gels lyophilisés par microscopie électronique à balayage, la morphologie des fibres dépend de la méthode de formation du gel. L'hydrogel thermodynamique (formé par le chauffage jusqu'à dissolution complète d'une suspension de **SachCHO** suivie par le refroidissement) comprend des fibres longues et droites, de centaines de micromètres de longueur et 1 à 2 μ m de diamètre. Quand l'hydrogel est formé par le cycle réactionnel, la morphologie dépend de de la concentration de GdL, et donc de la cinétique globale. Avec une concentration de 234 mM, les fibres formés par **SachCHO** sont plus courtes et avec les bords irréguliers, et des structures en forme d'étoile sont observés par microscopie confocale. Avec 374 mM de δ -Gluconolactone des fibres fortement ramifiées, plus fines et longues provenant d'un site de nucléation central sont observées. La concentration de GdL n'influence pas seulement la morphologie des fibres de **SachCHO**, mais aussi des propriétés mécaniques de l'hydrogel. En général, la rigidité du gel, mesurée par le

module de conservation de cisaillement, G' , augmente avec la concentration de GdL. Finalement, **SachCHO** possède une propriété appelée synérèse, c'est-à-dire qu'il éjecte le solvant quand il subit de la pression mécanique. Cette propriété a été explorée pour purifier l'hydrogel des sous-produits du cycle réactionnel qui sont nuisible à sa répétition. Pour cela, un gel de **SachCHO** a été formé dans une syringe équipée avec du coton dans le moyeu d'aiguille. Ensuite, les carburants chimiques (DT, HMTA, GdL) sont additionnés et le cycle réactionnel se déroule normalement, avec la formation de l'hydrogel après environ 30 minutes. Le piston de la syringe est pressé, en enlevant le solvant avec les sous-produits indésirables, mais laissant **SachCHO** dans le cylindre de la syringe. De l'eau avec les carburants chimiques sont additionnés de nouveau, en recommençant le cycle à zéro. Avec cette méthodologie, le cycle réactionnel a pu être répété jusqu'à 13 fois.

Au **Chapitre 4**, Les molécules **Gd(III)** et **Y(III)-DOTA-BTA**,^{9,10} ont été explorées par les propriétés paramagnétiques du Gadolinium.¹¹ Yttrium est utilisé comme le contrôle diamagnétique. Quand ces molécules sont présentes dans une solution tampon citrate à 100 mM et concentration de 100 μ M, elle forme des polymères supramoléculaires fibrillaires d'environ 6 nm de diamètre et plusieurs centaines de nanomètres de longueur, observés par cryo-microscopie électronique. Quand ces échantillons sont étudiés par diffusion dynamique de la lumière (DLS), deux processus peuvent être identifiés, indiquant une distribution bimodale des tailles des agrégats. Le processus plus rapide, **P1**, est la diffusion des fibres en solution, **P2** est plus lent et donc plus grand. L'analyse de la diffusion statique de la lumière (SLS), nous indique la dimension fractale des agrégats (d_F). Pour **Gd(III)-DOTA-BTA**, $d_F = 1.7$ ce qui indique que le processus **P2** correspond à un réseau de fibres. On peut donc dire que **P1** sont les assemblages unidimensionnels de **Gd(III)-DOTA-BTA** et **P2** est la structure de réseau de ces agrégats. Ensuite, une cuvette contenant l'échantillon dans les mêmes conditions citées ci-dessus a été placée entre les pôles d'un électroaimant pendant une heure, puis analysée pendant une heure par diffusion dynamique et statique de la lumière (DLS et SLS) et replacée dans l'électroaimant. Ce cycle a été répété de 6 à 7 fois, pour un total de 12 à 14 heures d'essai. On peut observer que dans les conditions normales sans champ magnétique l'intensité de la

lumière diffusée ($R(q)$) par **P2** de **Gd(III)-DOTA-BTA** reste constant en fonction du temps. Cependant, si l'échantillon est placé dans champ magnétique, $R(q)$ augmente au long des 12h pour atteindre un nouveau plateau 20% (1 T) à 35% (2 T) supérieur à la valeur à temps zéro. De plus, la dimension fractale change instantanément avec la présence de champs magnétique de 1.7 à 2.2 (1 T) ou 2.6 (2 T) et reste constante pour le reste de l'essai. Ceci indique que le champ magnétique induit à une densification du réseau de fibres. Le processus plus petit, **P1**, reste in affecté par le champ magnétique, de même pour **Y(III)-DOTA-BTA** qui est diamagnétique. On peut donc conclure que la présence d'un élément paramagnétique dans la structure moléculaire et la présence d'un champ magnétique sont nécessaires pour changer les polymères supramoléculaires. En outre, ces effets ne sont observés que dans le réseau de fibres, pas dans les fibres individuellement. Des calculs mathématiques, montrent que les assemblages formés par **Gd(III)-DOTA-BTA** contiennent une quantité suffisante de centres paramagnétiques pour que l'énergie magnétique soit plus importante que l'énergie thermique, mais le mécanisme responsable pour la densification et branchement du réseau supramoléculaire sont encore inconnus.

Les métaux terres rares possèdent une anisotropie magnéto-cristalline, ou anisotropie mono-ionique, qu'est l'interaction entre l'orbitale de l'ion magnétique avec son champ cristallin. Cette propriété a été explorée, dans le **Chapitre 5**, pour contrôler la polymérisation de pérylènes diimides couplés avec lanthanides (**PDI-Ln**, où Ln = Ho, Er, Gd, Y), qui s'auto-assemblent dans des solutions aqueuses par des interactions hydrophobes et π - π *stacking*. Les métaux terres rares ont été choisis, par leur susceptibilité paramagnétique élevée et l'yttrium comme un contrôle diamagnétique. Le mécanisme de polymérisation a été examiné par spectroscopie UV/Visible et dichroïsme circulaire à température variable. Le spectre UV-Visible est typique des agrégats type H de pérylène diimides, avec trois pics à ~ 540 nm, ~ 500 nm et ~ 470 nm. Le degré d'agrégation (α) peut-être estimé par le rapport des intensités des pics I_{500}/I_{540} , un ratio de ~ 0.65 correspond à la forme monomérique en solution.¹² Le spectre évolue de telle forme qu'à des températures plus élevées, le degré d'agrégation diminue. Le même peut être observé avec le dichroïsme circulaire. A 5 °C, un effet Cotton négatif prononcé

est présent entre 400 et 600 nm, indiquant la présence d'une structure hélicoïdale. Quand la température augmente, le spectre devient de plus en plus plat, ce qui montre la perte de la structure organisée dans le polymère supramoléculaire, confirmant qu'à des température plus élevées **PDI-Ln** se trouvent moins agrégés. Les courbes de fusion sont obtenues à partir des données spectroscopiques et le modèle isodésmique (quand chaque étape de polymérisation à la même constante d'équilibre) a été utilisé pour obtenir l'enthalpie de polymérisation de **PDI-Ln**.¹³ Pour tous les métaux, l'enthalpie est d'environ -30 kJ/mol. La taille des agrégats a été évaluée par la diffusion dynamique de la lumière. **PDI-Ho** forme des particules d'environ 2.5 µm en solution, trois fois plus grandes que celles formées par **PDI-Er** (~ 700 nm) et sept fois que **PDI-Gd** et **PDI-Y** (~ 350 nm). La morphologie des agrégats a été analysée par la microscopie à force atomique, découvrant des structures presque sphériques, mais sans forme vraiment définie pour tous les **PDI-Ln**. L'incorporation de centre métalliques paramagnétiques dans polymères supramoléculaire influence principalement la taille des structures formées en solution. Holmium, étant l'ion a plus haute susceptibilité paramagnétique, induit à la formation d'agrégats les plus grands. Les autres propriétés, comme la morphologie et l'enthalpie de polymérisation, ne sont pas impactés par les interactions ion-ion entre les terres rares.

Nous avons montré quatre méthodes basées sur des principes différents pour contrôler la polymérisation supramoléculaire. Premièrement, la formation d'un hydrogel sensible au pH à partir surfaces a été accomplie par la diffusion de protons dans des matériaux peu poreux. Ensuite, la formation et les propriétés morphologiques et mécaniques d'un hydrogel contenant une fonction aldéhyde ont été contrôlées par un nouveau cycle réactionnel hors-équilibre. Finalement, des interactions magnétiques ont été utilisées pour moduler la polymérisation de molécules contenant des ions terres rares. D'une part, des champs magnétiques faibles (< 2 T) densifient réseau de fibres supramoléculaires. D'autre part, les interactions d'origine magnéto-cristalline entre des centres métalliques du bloc *f* ont été utilisées pour moduler la taille d'agrégats supramoléculaires.

Les méthodes listées ci-dessus pourront être utilisées sur d'autres systèmes supramoléculaires, car leurs modes d'action sont basés sur des fonctions moléculaires

largement rependues et d'intérêt général. Ces résultats ouvrent les portes à un contrôle structural et spatial plus précis de polymères supramoléculaires par des méthodes facilement implémentables dans des conditions de laboratoire. Finalement, on peut envisager à combiner ces différents procédés pour pousser la polymérisation supramoléculaire hors équilibre et ainsi obtenir un contrôle plus dynamique et précis de ce processus.

Summary

Supramolecular chemistry is the science that masters the physicochemical interactions between molecules and non-covalent bonds, J.-M. Lehn has defined it as the chemistry "beyond the molecule".^{1,2} Interactions between charges or dipoles, hydrogen bonds, π - π stacking, Van der Waals forces, and solvation and hydrophobic effects are the most common examples of non-covalent bonds used as tools for the formation of supramolecular complexes.³

The advantage of supramolecular materials is their dynamic nature, the bonds are not fixed as in covalent materials.^{1,2} This will allow them to be sensitive to external stimuli, and therefore adaptable to the environment and flexible as necessary. These characteristics make it possible to manufacture functional materials based on supramolecular polymers with self-healing or electronic properties or biomedical applications.⁴

When looking for applications of supramolecular polymers, new and better ways to control their polymerization, morphology and / or properties are always sought.⁵

In this thesis, three methods of controlling supramolecular polymerization will be explored. The first aims to spatially control the nucleation of pH-responsive hydrogels, exploring the diffusion of protons. Then, the supramolecular polymerization of a hydrogelator is modulated by an out-of-equilibrium reaction cycle. The morphological and mechanical properties depend on the kinetics of the reaction cycle. Finally, the use of magnetic fields and the interactions of magnetic dipoles are explored to control the supramolecular polymerization of paramagnetic organic molecules containing rare earths.

In **Chapter 2** we show a method of spatiotemporally controlling the pH-triggered formation of a hydrogel. A 1,3,5-tricarboxamide with nine free carboxylic acid moieties (**BTA-1**) is monomeric at $\text{pH} > 5$ and self-assembles into fibers below that threshold. The concentration and temperature-dependent kinetic of polymerization was studied, which permitted the fitting of a supramolecular polymerization mathematical model including nucleation, elongation, fragmentation, and Arrhenius law. Spatiotemporal control was achieved by soaking a PDMS (polydimethylsiloxane) cube in saturated hydrochloric acid (HCl)

for 96 h and dropping it into a basic solution of **BTA-1**. After 4 minutes, protons start diffusing into the solution, hence protonating/activating **BTA-1** that self-assembles into fibers and forms a hydrogel, starting from the cube and growing outward in the opposite direction of the proton gradient. It is worth noting that when the PDMS was replaced by agarose, the diffusion of protons into the **BTA-1** solution led to precipitation instead of gel formation. This means that proton diffusion needs to be slower than the kinetics of nucleation for a hydrogel to be formed. To further gain spatial control over the polymerization of **BTA-1**, we built a microfluidic device composed of two channels superimposed perpendicularly, separated by a 100 μm layer of PDMS. One of the channels contains a basic solution of **BTA-1** at 160 μM ; potassium phthalate buffer at pH 4 flows in the other. After two hours, spherical assemblies of approximately 2 μm in diameter were observed by confocal microscopy on top of the PDMS membrane, only at the intersection of the two channels. Showing that spatial control over **BTA-1** was obtained using this simple, yet general, method.

A non-equilibrium reaction cycle is explored in **Chapter 3** to achieve kinetic and structural control over a hydrogel. A previously reported saccharide-based, aldehyde-containing, hydrogelator (**SachCHO**) was reacted with sodium dithionite ($\text{Na}_2\text{S}_2\text{O}_4$) forming the respective α -hydroxy-sulfonate (**SachSO₃⁻**). Because of electrostatic repulsion, **SachSO₃⁻** does not self-assemble, so treating a **SachCHO** hydrogel with sodium dithionite will destroy it in ~ 5 minutes. **SachSO₃⁻** reacts with formaldehyde giving back the original aldehyde, and the gel is formed again. However, formaldehyde and sodium dithionite react with each other, so they cannot be added simultaneously to create an autonomous reaction cycle. Hexamine (HMTA) decomposes into six molecules of formaldehyde and four of ammonia through an acid-catalyzed hydrolysis. So, by adding HMTA, dithionite and an acid (here gluconolactone) simultaneously to a **SachCHO** hydrogel will convert it into **SachSO₃⁻** in five minutes, yielding a translucent solution. In 30 to 60 minutes, depending on gluconolactone concentration, the sulfonate will be converted back to **SachCHO** making the hydrogel again. Gluconolactone concentration influences the kinetics of the reaction cycle, with higher concentration increasing the kinetics of HMTA decomposition leading to an overall faster reaction cycle. By

analyzing hydrogels by confocal microscopy and lyophilized gels by scanning electron microscopy, the morphology of **SachCHO** fibers depends on the method of gel formation. The thermodynamic hydrogel (formed by heating a suspension of **SachCHO** until complete dissolution, followed by cooling) consists of long, straight fibers, hundreds of micrometers in length and 1 to 2 μm in diameter. When the hydrogel is formed by the reaction cycle, the morphology depends on the concentration of GdL, and therefore on the overall kinetics. With a concentration of 234 mM, the fibers formed by **SachCHO** are shorter and with irregular edges, and star-shaped structures are observed by confocal microscopy. With 374 mM δ -Gluconolactone highly branched, thinner, and longer fibers originating from a central nucleation site are observed. Furthermore, GdL concentration also affects the hydrogel mechanical properties. In general, the stiffness of the gel, measured by the shear storage modulus, G' , increases with the concentration of GdL. Finally, **SachCHO** has a property called syneresis, meaning that it repels the solvent when under mechanical pressure. This property has been explored to purify the hydrogel from reaction cycle by-products which are detrimental to its repetition. For this, a SachCHO gel was formed in a syringe equipped with cotton in the needle hub. Then the chemical fuels (DT, HMTA, GdL) are added and the reaction cycle proceeds normally, with the formation of the hydrogel after ~ 30 minutes. The syringe piston is squeezed, removing the solvent together with unwanted by-products, but leaving **SachCHO** in the syringe cylinder. Water with the chemical fuels is added, starting the cycle all over again. With this methodology, the reaction cycle could be repeated up to 13 times.

Chapter 4 shows the influence of a magnetic field on the self-assembly of a Gadolinium-containing paramagnetic 1,3,5-benzene-tricarboxamide (**Gd-DOTA-BTA**). **Gd-DOTA-BTA** self-assembles into two processes: the first one, **P1**, is the fiber formation by the 1-D molecular assembly; **P2** is the network-like behavior of the fibers that emerge from their interaction in solution. The existence of these two processes was evidenced by light scattering and cryogenic transmission electron microscopy. The next step was to study supramolecular polymerization under a magnetic field, for that an electromagnet was employed applying 1 or 2 T magnetic field. After one hour under magnetic field, the aggregates were studied for sixty minutes using

dynamic and static light scattering, this cycle was repeated fourteen times (14 hours total experimental time). Remarkably, the total scattering intensity of process **P2** increased 20% and 30%, for 1 and 2 T respectively, while for **P1** it stayed constant. If no magnetic field was applied, or the diamagnetic Yttrium replaced Gadolinium in the molecular structure, the scattering intensity of **P2** did not evolve over the 14 h experiment. The fractal dimension, that can give an idea of the morphology of **P2** assemblies, also changed, but this time there was an immediate jump from 1.7 (no field) to 2.2 (1 T) or 2.6 (2 T) as soon as the sample was exposed to magnetic field and remained constant for the rest of the experiment. This indicates that **P2** becomes increasingly dense with magnetic field and more randomly branched. A theoretical model showed that, since **P2** comprises thousands of **P1** fibers, the magnetic field only affects the network structures because it contains thousands of paramagnetic Gd ions.

Finally, in **Chapter 5** a library of perylene diimide functionalized with different rare-earth metals (**PDI-Ln**, where Ln=Ho, Er, Gd, Y) were studied to evaluate the effect that paramagnetic lanthanides have on supramolecular self-assembly. Lanthanides ions were chosen because they have the highest magnetic susceptibility on the periodic table and their charge density distribution are anisotropic and different for each element. **PDI-Ln** self-assembles through π - π stacking and hydrophobic interactions, but the magnetic interaction between the metal centers are also envisaged to play a role on the molecular self-assembly. To this end, the equilibrium supramolecular polymerization of **PDI-Ln** was studied by UV/Vis and CD spectroscopy, revealing an isodesmic mechanism of aggregation with an enthalpy of polymerization of around -30 kJ/mol for all metals, indicating that self-assembly is directed by the perylene diimide core. Dynamic light scattering, however, shows that the hydrodynamic radii of the **PDI-Ln** is metal dependent, with **PDI-Ho** having R_H in the order of $2.5 \mu\text{m}$ while for the other metals the size is in the order of hundreds of nm. Atomic force microscopy (AFM) shows that **PDI-Ln** aggregates into almost spherical structures, with undefined shape. This would indicate that, even if self-assembly is driven by π - π stacking of the perylene core, the size of the aggregates is influenced by the properties of respective lanthanide.

We have shown four methods based on different principles to control supramolecular polymerization. First, the formation of a pH-responsive hydrogel from surfaces has been accomplished by the diffusion of protons from porous materials. Then, the kinetics of formation and morphological and mechanical properties of an aldehyde-containing hydrogel were controlled by a new out-of-equilibrium reaction cycle. Finally, magnetic interactions have been used to modulate the polymerization of molecules containing rare earth ions. On one hand, weak magnetic fields (<2 T) have changed the balance between fibers and their network structures. On the other hand, interactions of magnetocrystalline origin between metal centers of the *f* block have been used to modulate the size of supramolecular aggregates.

The methods listed above can be used on other supramolecular systems, because their modes of action are based on widely used molecular functions and of general interest. These results open the doors to a more precise structural and spatial control of supramolecular polymers by methods easily implemented under laboratory conditions. Finally, it is possible to envisage combining these different processes to push the supramolecular polymerization out of equilibrium and thus obtain a more dynamic and precise control of this process.

Symbols and Abbreviations

1-D	One dimensional
2-D	Two dimensional
3-D	Three dimensional
%wt	Weight percent
α	Dimensionless degree of aggregation
γ	Scaling exponent
Γ	Decay rate
ε	Extinction coefficient
$\Delta\varepsilon$	Molar circular dichroism
θ	Angle
$[\theta]$	Molar ellipticity
κ	Transmission coefficient
μ_0	Vacuum permeability
τ	Relaxation time (DLS)
$\tau_{1/2}$	Half-time of polymerization (when $\alpha = 0.5$)
χ	Magnetic susceptibility
A	Arrhenius pre-exponential factor
AAS	Atomic Absorption Spectroscopy
ADP	Adenosine diphosphate
AFM	Atomic force microscopy
ATP	Adenosine triphosphate
B	Primary magnetic field (or magnetic flux density or magnetic B-field)
BTA	Benzene-1,3,5-tricarboxamide
CD	Circular dichroism (spectroscopy)
CDCl_3	Deuterated chloroform

CHCl ₃	Chloroform
Cryo-TEM	Cryogenic transmission electron microscopy
D ₂ O	Deuterated water
d_F	Fractal dimension
DIPEA	N,N-Diisopropylethylamine
DLS	Dynamic light scattering
DMF	Dimethylformamide
DMSO	Dimethyl sulfoxide
DNA	Deoxyribonucleic acid
DOTA	1,4,7,10-Tetraazacyclododecane-1,4,7,10-tetraacetic acid
DT	Sodium Dithionite
DTPA	Diethylenetriaminepentaacetic acid
E_a	Activation energy
E_{mag}	Magnetic energy
<i>e.g.</i>	<i>exempli gratia</i> , for example
ESI-TOF	Electrospray ionization time-of-flight mass spectrometry
<i>et al.</i>	<i>et alia</i> , and others
F_{mag}	Magnetic force
ΔG	Gibbs free energy
$g_{VV}^{(1)}(q, t)$	Polarized field autocorrelation functions
$G(\tau)$	Relaxation time distribution
G'	Shear storage modulus
G''	Shear loss modulus
GdL	Glucono- δ -lactone
GDP	Guanosine diphosphate
GTP	Guanosine triphosphate
h	Planck constant

H	Magnetic field strength (or magnetizing force or H-field)
ΔH	Enthalpy
ΔH^\ddagger	Enthalpy of activation
H ₂ O	Water
HBTU	Hexafluorophosphate Benzotriazole Tetramethyl Uronium
HCl	Hydrochloric acid
HMTA	Hexamethylenetetramine
HPLC	High-performance liquid chromatography
HRMS	High Resolution Mass Spectrometry
I_{500}/I_{540}	Ratio of the absorbance at 500 nm and the one at 540 nm
<i>i.e.</i>	<i>id est</i> , that is
ICP-MS	Inductively Coupled Plasma Mass Spectrometry
ITC	Isothermal titration calorimetry
K	Equilibrium constant
k	Kinetic rate constant
k_B	Boltzmann constant
K_S	Energetic correction due to shape anisotropy
LC-MS	Liquid chromatography–mass spectrometry
m_0	Initial monomer concentration
m	Magnetic moment
m_{eff}	Effective atomic paramagnetic moment
M	Magnetization
M_S	Saturation magnetization
n_0	Refractive index
MCH	Methylcyclohexane
MeOH	Methanol
NaHCO ₃	Sodium hydrogen carbonate

NaOH	Sodium hydroxide
NMR	Nuclear magnetic resonance
O.D.	Optical density
PDI	Perylene diimide
PDMS	Polydimethylsiloxane
q	Wavevector
R	Gas constant
$R(q)$	Rayleigh ratio (corrected scattering intensity)
R_H	Hydrodynamic radius
Ref.	Reference
ΔS	Entropy
ΔS^\ddagger	Entropy of activation
SANS	Small-angle neutron scattering
SEM	Scanning electron microscopy
SLS	Static light scattering
t	Time
T	Temperature
T_m	Melting temperature (when $\alpha = 0.5$)
T_R	Reduced temperature
TEM	Transmission electron microscopy
TFA	Trifluoroacetic acid
TGA	Thermogravimetric analysis
THF	Tetrahydrofuran
UV	Ultraviolet
UV/Vis	Ultraviolet/Visible (spectroscopy)
V	Volume
XRD	X-Ray Diffraction

Chapter 1. General Introduction: Controlling Supramolecular Polymerization

Abstract: Controlling synthetic supramolecular polymerization has been a subject of research since the establishment of the field. Many techniques have been developed to tune self-assembly in and out-of-equilibrium, always aiming to gain (spatio)temporal control over aggregation with control over the final morphology and properties. The state of the art of these methodologies will be laid-out in this chapter, with a focus in the last section on magnetism and how it has been used to control soft-materials.

Parts of this chapter have been published in:

Singh, N. †; Formon, G. J. M. †; De Piccoli, S. †; Hermans, T. M. Devising Synthetic Reaction Cycles for Dissipative Nonequilibrium Self-Assembly. *Adv. Mater.* **2020**, 32 (20), 1906834. <https://doi.org/10.1002/adma.201906834>.

Parts of this chapter are present in a manuscript in preparation:

Schicho, M.†; Formon, G. J. M.†; Hermans, T.M. Soft-Matter Control Using Weak Magnetic Fields (working title). *Manuscript in preparation*.

† Authors contributed equally

1.1 General Introduction

1.1.1 Supramolecular Chemistry

Supramolecular chemistry, as defined by Nobel Laureate Jean-Marie Lehn, is “the chemistry beyond the molecule”.^{1,2} It is the science that masters the ‘physical’ bonds between molecules, responsible for the formation of multi-component complexes of synthetic and natural origins.³

Supramolecular chemistry is widely present in biological systems, being responsible for structural and functional properties in living beings, such as: protein folding,¹⁴ formation of the virus capsid¹⁵ and natural supramolecular polymers like collagen, the most abundant protein in mammals, that assembles into a triple helical structure.¹⁶ Possibly one of the most impressive supramolecular assemblies in living systems is adenosine triphosphate (ATP) synthase, an enzyme and molecular machine that self-assembles from five subunits, capable of synthesizing ATP from ADP and inorganic phosphate while revolving using a proton gradient as driving force.^{17,18}

Taking inspiration from Nature, chemists have synthesized a plethora of supramolecular materials and architectures with impressive properties and structures. To cite a few recent examples: large and discrete polyhedral assemblies, by the self-assembly of 144 sub-components (96 ligands and 48 metal centers);¹⁹ Porous (ionic) liquids constructed with self-assembled molecular cages;^{20,21} an anti-aromatic nanocage;²² a multitude of knotted molecular structures;²³ molecular machines capable of synthesizing sequence defined functional peptides;^{24,25} the creation of complex and functional nano- and micro-structures using DNA as building block, also known as DNA Origami.²⁶⁻²⁸

1.1.2 Supramolecular Polymers

Supramolecular polymers are a special class of supramolecular materials that, like their covalent counterparts, consist of a repeating monomeric unit held together, in this case, by non-covalent interactions. They have been of special interest for their dynamic nature, combining the formation of high molecular weight supra(macro)molecules with the malleability of supramolecular materials.²⁹

In Nature, supramolecular polymers also play an important role in different physiological functionalities through the polymerization of proteins or peptides.¹⁶ A prime example of this kind of structure are microtubules (MTs), present in a multitude of organisms, both uni- and multicellular. In eukaryotes, microtubules are responsible for the spatial chromosome segregation during cell division, physically pulling them to the extremities of the cell. In prokaryotes, MTs are one of the main structural units of both the flagellum and cilium. Microtubule formation, Figure 1.1, starts with the heterodimer of two proteins, α - and β -tubulin, binding to guanosine triphosphate (GTP), allowing the polymerization into hollow tubes with 25 nm diameter. The self-assembly induces hydrolysis of the GTP bound to β -tubulin into guanosine diphosphate (GDP) and inorganic phosphate, releasing ~ 12.5 kcal/mol *in vivo*. The GDP bound heterodimers destabilize the supramolecular polymer, inducing its depolymerization. Once the microtubule is destroyed, tubulin dimers can release GDP and bind to GTP once again, restarting the cycle from zero. Interestingly, these phenomena make that both (de)polymerization of microtubules happen simultaneously, this process is called dynamic instability and it is inherently out-of-equilibrium.^{30,31}

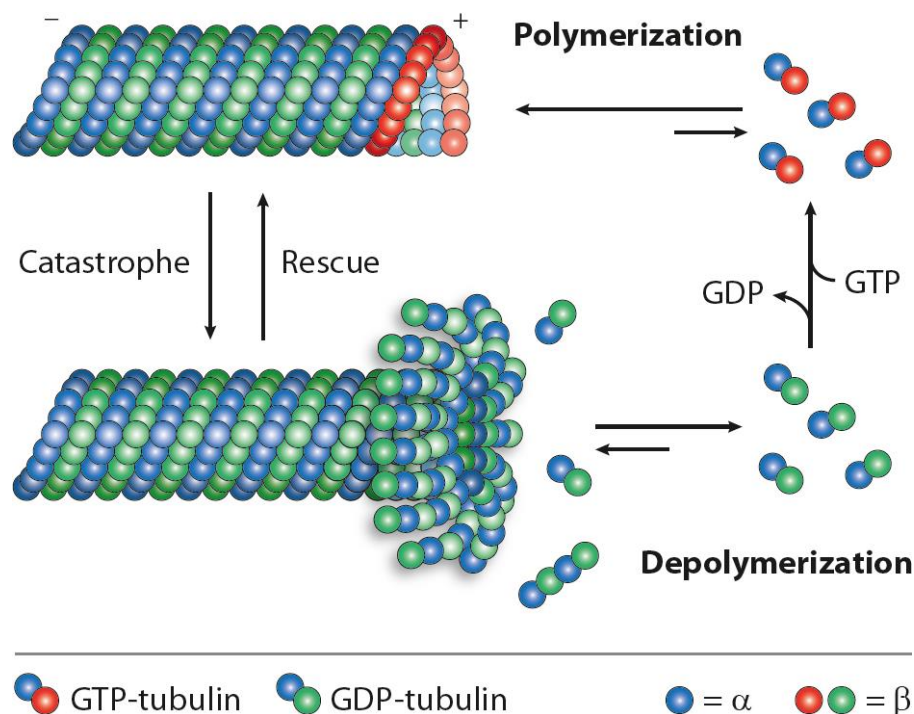


Figure 1.1 – Scheme depicting microtubules polymerization: tubulin dimer binding with GTP and polymerizing; GTP is hydrolyzed into GDP at early stages of aggregation, destabilizing the microtubules; MTs depolymerize, and the tubulin releases GDP into solution, ready to bind GTP again. Taken from <https://adipogen.com/ptms-microtubules-neurodegeneration/>.

Another natural supramolecular polymer of great significance are amyloids. Associated with the misfolding of proteins, amyloid fibrils are of interest for their direct relationship with Alzheimer's disease, type II diabetes and around 50 other illnesses. On the pathway from the synthesis to folding into functional structures, proteins can adopt many different conformations, including disordered and partially folded states, Figure 1.2. When the assembly goes off the typical pathway, sometimes guided by molecular chaperones, those proteins, or peptide fragments, can nucleate and aggregate into insoluble amyloid fibrils. Those assemblies are typically highly ordered and are formed from (partially) unfolded fragments that aggregate into β -sheets. Since the intrinsic mechanisms of formation of the native state and amyloid fibrils are different (intra versus intermolecular interactions, respectively) their relative stability is concentration dependent. Above the critical concentration, amyloid fibrils are more thermodynamically stable than the native state, and surprisingly in some cases this concentration is below the physiological concentration of the protein, making the native state metastable *in vivo*.³²

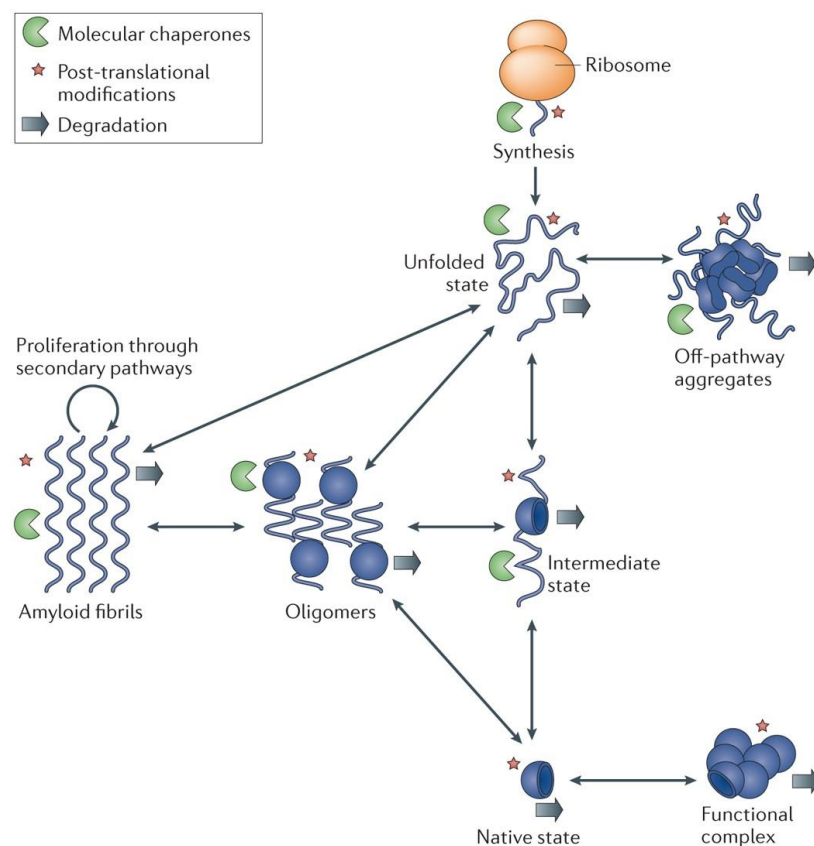


Figure 1.2 – Representation of the different pathways a protein can take from synthesis to ordered states, like amyloid fibrils, native state, and off-pathway aggregates. Taken from ref. 32.

Synthetically, supramolecular polymers are interesting for their adaptability combined with a high degree of order. With the possibility of including a multitude of functionalities into the monomers, supramolecular polymers have been used for biomedical and electronic applications.⁴ There are three main types of supramolecular polymerization mechanisms: isodesmic, cooperative and anti-cooperative.³³ Main-chain supramolecular polymers are composed of macromonomers end-functionalized with a moiety capable of strong (self)complementary non-covalent interactions. A prime example of this kind of material are polymers functionalized with self-complementary quadruple hydrogen bonding ureido-pyrimidinone (UPy).^{33,34} Isodesmic supramolecular polymerization is defined by the aggregation of small monomers where the energy release and the kinetic barrier are the same at each step, that way a single equilibrium constant drives the self-assembly. Thermodynamically and kinetically, isodesmic and main-chain polymerization have the same behavior. Cooperative polymerization, also called nucleation-elongation, is when there are two steps in polymer growth: first a nucleus of a few molecules is formed; then the supramolecular polymers go through an elongation phase, growing in size until reaching its maximum length. The nucleation step is thermodynamically less favorable and kinetically slower than the elongation step, when the reverse is true the polymerization is called anti-cooperative.^{33,35} A scheme summing up the different kinds of supramolecular polymerization can be found in Figure 1.3.

In this chapter, I will present an overview of the state the art of supramolecular polymerization control, followed by an overview on how to tune supramolecular polymers through non-equilibrium reaction cycles. Lastly, an introduction to magnetism and how it has been used to control soft matter and some non-trivial observations published in the last years.

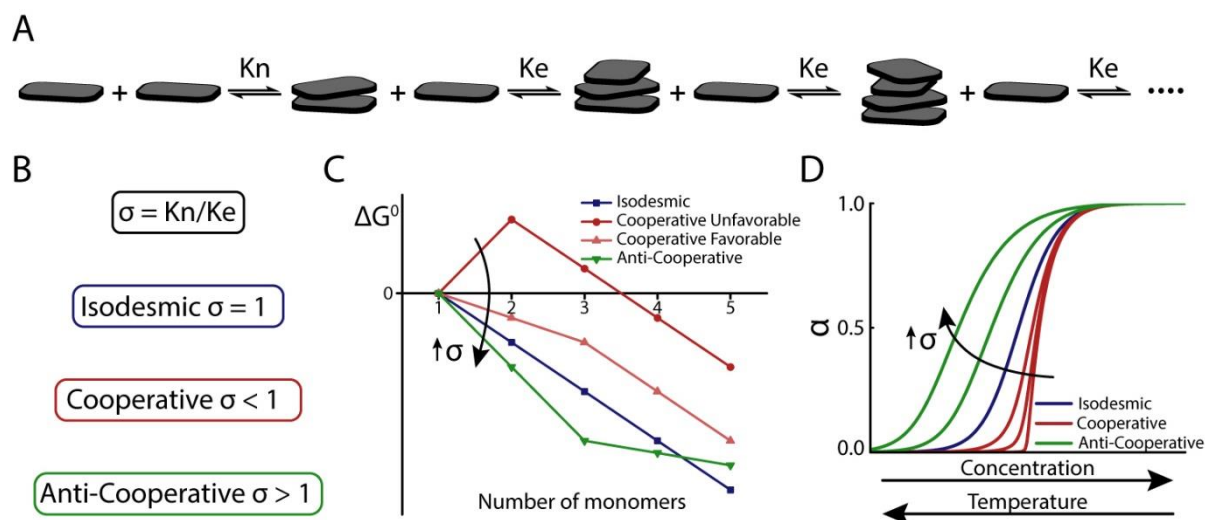


Figure 1.3 – **A** – Scheme describing the supramolecular polymerization process. The first step is nucleation, in this case the nucleus size is two monomers, with an equilibrium constant K_n . After the nucleus is formed, elongation takes place, with K_e as the equilibrium constant. **B** – Definition of the degree of cooperativity, σ . For isodesmic supramolecular polymerization the nucleation and elongation steps have the same equilibrium constant (and rate constants), so $\sigma = 1$. In the cooperative case, elongation is more thermodynamically (and kinetically) favorable than nucleation, so $\sigma < 1$. When the equilibrium constant of nucleation is bigger than the one for elongation, $\sigma > 1$, the polymerization is called anti-cooperative, in this case dimers or trimers (and other small supramolecular oligomers) are mostly observed in solution. **C** – Schematic energetic diagram of different supramolecular polymerization mechanisms, of the free energy released (ΔG^0) per monomer being incorporated into the aggregate. There are four distinct cases: Isodesmic, when every step releases the same energy; Cooperative Unfavorable, when the formation of the nucleus (here of size 2) requires energy input from the environment, making it energetically unfavorable, followed by the thermodynamically favorable elongation; Cooperative Favorable, the nucleation step (here of size 3, for clarity) has a ΔG_n^0 that is negative, but smaller in magnitude than ΔG_e^0 of elongation; lastly, Anti-Cooperative, when the nucleation step (here of size 3, for clarity) releases more energy than the elongation. **D** – The fraction of molecules in polymeric form (α) as a function of concentration or temperature for the different mechanisms listed above. Adapted from refs. 33 and 35.

1.2 Supramolecular Polymerization Under Thermodynamic and Kinetic Control

In this section, different ways of controlling supramolecular polymerization will be laid out. Starting with traditional stimuli responsive supramolecular polymers, following with supramolecular polymers under kinetic control, and the spatial control over aggregation.

1.2.1 Stimuli-Responsive Supramolecular Polymers

Supramolecular polymers are inherently stimuli responsive. Due to the nature of the polymerization process, that is driven by an equilibrium constant, temperature will have an effect on the degree of polymerization, because $K = e^{-\Delta G/RT} = e^{-\Delta H/RT + \Delta S/R}$. Typically, for an enthalpy driven system ($\Delta H < 0$) if you heat up you depolymerize. If we take for example

benzene-1,3,5-tricarboxamides (BTAs), a common building block for supramolecular polymers that self-assembles through π - π stacking and hydrogen bonding of the amides, it depolymerizes at high temperatures in organic solvents, following a cooperative melting curve, see Figure 1.3.³⁶ Perylene-diimides (PDIs), another common molecule that aggregates in organic solvents through π - π stacking due to their large planar π area, also has a higher degree of polymerization at low temperature, most frequently following an isodesmic mechanism^{12,37}, see Figure 1.3.

When supramolecular polymerization is entropy driven ($\Delta H > 0$ and $\Delta S < 0$), aggregation is favorable at higher temperatures, with a negative ΔG . This was evidenced by Würthner and co-workers in water-soluble naphthalene and perylene diimides that are aggregated at room temperature. These dyes were decorated with oligo-ethylene glycol chains to increase water solubility. Upon heating in pure water, they become increasingly assembled. By using Ultraviolet/Visible (UV/Vis) spectroscopy and isothermal titration calorimetry (ITC), the authors uncovered that the polymerization has negative entropy and positive enthalpy variations, meaning that the process is endothermic. By mixing polar organic solvent with the water, the usual enthalpy driven aggregation, typical of π - π stacking, is restored. The entropic nature of the self-assembly of these dyes is attributed by the release of water from the ethylene glycol moieties that no longer can be hydrogen bonded at high temperatures, a phenomenon that is enthalpically disfavored.^{38,39}

A few years ago, however, Takuzo Aida and collaborators reported a surprising finding unravelling a new methodology to thermally control supramolecular polymerization, Figure 1.4. A copper containing porphyrin-based monomer with eight amide groups in its side chains, self-assembles in dodecane at room temperature, and stays in polymer form when heated up to 110 °C, at 10 μ M. However, when 5.5 vol% of hexanol is added the system depolymerizes upon heating, reaching monomeric form at ~50 °C. When the temperature is further increased to 110 °C, the porphyrin is back into its polymeric form, creating what they call a 'thermally bisignate' supramolecular polymer; that goes from polymer to monomer then back to polymer upon heating. This phenomenon is explained by the fact that at low temperatures, the molecule is assembled through π - π stacking and hydrogen bonding of the amides, while hexanol

hydroxyl groups perform hydrogen bonding among themselves. When temperature is increased to $\sim 50\text{ }^{\circ}\text{C}$ the alcohol starts hydrogen bonding with the amide groups, thus inducing dissociation of the supramolecular polymer. By heating again hexanol is completely dissolved in dodecane, impairing hydrogen bonding by the hydroxyl group, and freeing the amides, allowing re-polymerization of the porphyrin. The authors attribute the high thermal stability, because of its eight amide groups, as a key factor for this thermal behavior, an analog of this molecules containing only four amides was molecularly dissolvedⁱ in dodecane when heating at $70\text{ }^{\circ}\text{C}$.⁴⁰

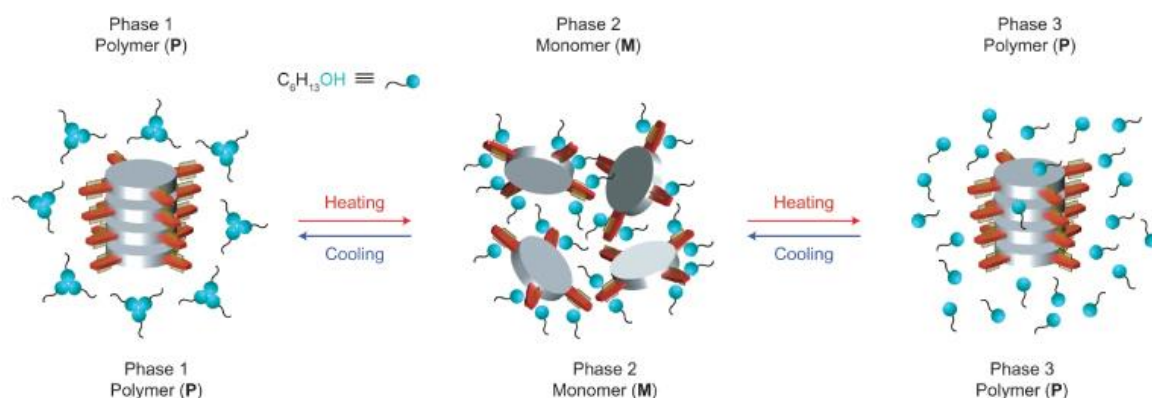


Figure 1.4 – Scheme representing the thermally bisignate behavior of the copper containing porphyrin based supramolecular polymer. Taken from ref. 40.

Concentration and temperature variations were also used to control the type of aggregate in a bay substituted core-twisted perylene diimides (PDI). In methylcyclohexane, by increasing the concentration from $0.1\text{ }\mu\text{M}$ to 2 mM three distinct supramolecular species were observed. At low concentrations, and high temperatures, the molecularly dissolved PDI is present, characterized by a high fluorescence intensity and a red shifted UV/Vis spectrum. By increasing the concentration, or cooling down the system, a fluorescence quenching and a blue shift in the spectrum indicate that an H-type dimer is the more populous species in solution. Finally, at highest concentrations in the series, and at room temperature, the fluorescence is regained and the absorption band at $\sim 600\text{ nm}$ increases in intensity, indicating that the molecule now polymerizes into J-aggregates.^{41,42}

ⁱ Molecularly dissolved means that the molecule is in monomeric form, as opposed to aggregated.

Solvent composition is also an important parameter when controlling supramolecular polymerization. It has been shown by Korevaar *et al.*, that by increasing the amount of good solvent in the solution of an assembling molecule, it induces depolymerization by changing the overall equilibrium towards the monomeric form, however it also changes the kinetics of the system, increasing the time needed to reach equilibrium.⁴³ Similarly, a recent report by Mabesoone *et al.*, where a zinc containing porphyrin self-assembles in a cooperative fashion in methylcyclohexane (MCH) but is monomeric in chloroform (CHCl₃). By changing CHCl₃/MCH ratio, a different kind of aggregate with an isodesmic assembly mechanism was observed. Chloroform, being a good solvent for the porphyrin, it induces disassembly, thus stabilizing an aggregate that is metastable at in pure MCH. This is an interesting technique to stabilize originally off-pathway aggregates and be able to easily synthesize different materials from same building blocks.⁴⁴

Light is a stimulus that also has been extensively used to control supramolecular polymers and polymerization.⁴⁵ The inclusion of light-responsive molecular switches, like azobenzene⁴⁶⁻⁴⁹ or diarylethene^{50,51}, into the molecular design of self-assembling molecules allows chemists to precisely control (dis)assembly with irradiation of a specific wavelength (depending on the switch). In a report by Stupp and co-workers, self-assembling peptide-amphiphiles produce twisted fibers in low-polarity solvents, through solvophobic interactions and β -sheet formation. By the inclusion of an azobenzene moiety into the structure, at room temperature and normal conditions the fibers present a uniform pitch of 78 nm, however when UV light is shined onto the sample, switching the trans form of azobenzene into cis, the pitch becomes irregular, varying from 40 to 70 nm, changing the conformation of the self-assembled structure by light stimulus.⁵²

In a recent report by Pavan, Kudernac and co-workers, an amphiphilic molecule containing two azobenzene moieties forms hollow tubules in water, Figure 1.5. Upon continuous light irradiation, the CD signal shows a steep decrease in the first five minutes followed by a slower decline until it reaches zero, after ~30 minutes, showing that the tubules are destroyed when the sample was exposed to UV light. A red shift, in the first five minutes, observed by UV/Vis spectroscopy show that at the initial states of irradiation the trans-to-cis

isomerization of the azobenzene leads to the change in conformation of the tubules into a J-aggregate, by the sliding of the aromatic cores in the tube walls. The spectroscopy data show that while azobenzene moieties slowly switch from trans-to-cis, in the initial times the energetic cost to dissolve the cis molecules is too high, so they become trapped into the tubules, increasing its internal strain. When the ratio of cis/trans molecules reaches a critical value, the assemblies are too unstable and are destroyed. Atomistic molecular dynamics simulations confirm that at early stages the strain build-up by the cis azobenzene is stable up to cis/trans ratio of ~15%, where the energy increases more rapidly, completely destabilizing the assemblies.⁵³

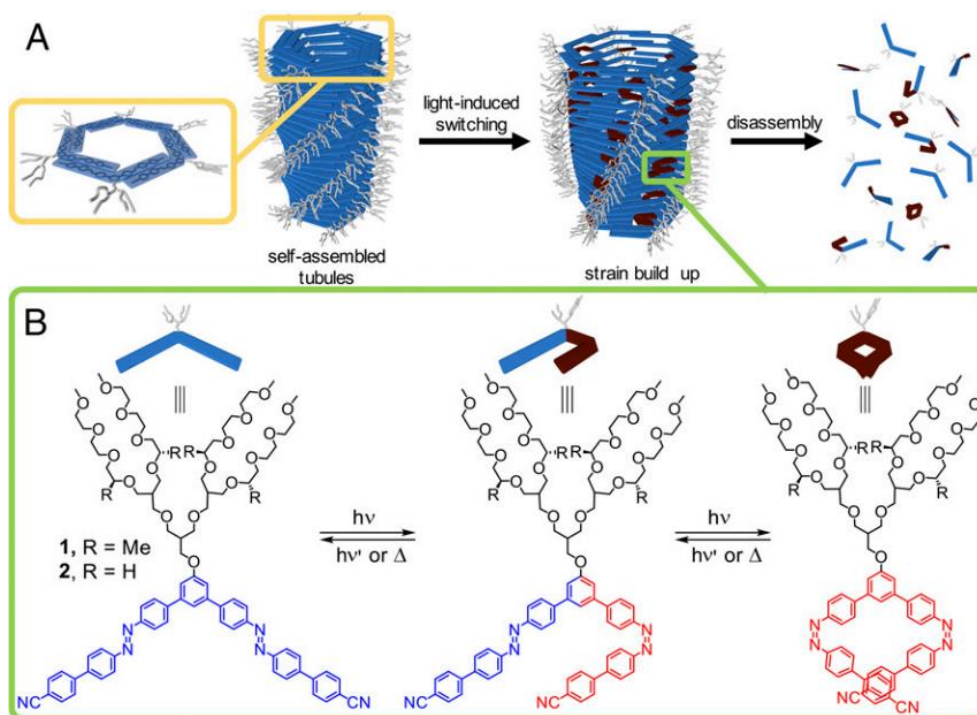


Figure 1.5 – **A** – Scheme depicting the light-induced depolymerization of the artificial microtubules. **B** – Photo-switching reactions occurring in the monomer to induce depolymerization. Taken from ref. 53.

With a similar strategy, Meijer and collaborators functionalized a benzene-1,3,5-tricarboxamide with an acyl hydrazone photoswitch (m-BTA). In its E form, m-BTA co-assembles and intercalates inside fibers of achiral BTAs (a-BTA). Upon UV irradiation, E-m-BTA is converted to the Z conformation in less than 30 minutes. Steric hinderance impedes Z-m-BTA of intercalating a-BTA fibers, turning into a “chain-capper”, thus reducing the average size of the supramolecular fibers. If a 6 %wt organogel with 10% E-m-BTA, is irradiated with UV light, gel-to-sol transition is observed. Shinning visible light, heating to 90 °C, or letting the

sample re-equilibrate at room temperature reverses the photo isomerization yielding E-m-BTA and regaining the original supramolecular polymer chain length.⁵⁴

Different chemical stimuli have also been used to control supramolecular aggregation, either by pH or ionic strength variation, redox reactions, or the addition of a reacting agent.⁵⁵

Addition of acid or base has been a widely used tool to control the (dis)assembly of supramolecular polymers. For example, Méndez-Ardoy, *et al.* showed that the aggregation of a histidine containing cyclic peptide nanotube can be triggered by increasing the pH above 6.5. The pH dependent supramolecular polymerization was studied inside microdroplets of water-in-oil emulsions, where fibrillation was observed by the addition of propanamine (base).⁵⁶ In a similar fashion, Dave J. Adams and co-workers showed multi-component hydrogels, composed of amino acid/peptide derived molecules. Although molecularly similar, those molecules present different pK_as. The addition of gluconolactone, that slowly hydrolyses into gluconic acid therefore inducing a gradual decrease in pH, induced the orthogonal assembly of the hydrogelators that would normally co-assemble by a rapid addition of acid. By the addition of stilbene (photo-switch) in the molecular structure of one of the components, its selective disassembly can be triggered by UV irradiation.^{57,58}

Boekhoven, *et al.* explored how pH-dependent catalysis rate can influence the final morphologies and mechanical properties of a hydrogel. The hydrazone based gelator is formed *in-situ* by reacting an acylhydrazine-containing hydrophobic core with a hydrophilic aldehyde, this reaction is catalyzed both by acid and nucleophilic aniline. Gelation time and maximum storage modulus were dependent on the pH, with faster kinetics and stronger gel in more acidic conditions. Those same properties were dependent of the concentration of aniline at pH 7, with gelation time decreasing with increase in catalyst concentration and maximum storage modulus first increasing, reaching a maximum and then decreasing. This can be explained by the different morphologies that were obtained: at pH 5.0 and pH 7.0 with 10 mM aniline the supramolecular fibers were more branched forming a tighter network, while the gel formed at pH 7.0 without catalyst presents thicker fibers that are less interconnected, forming a looser network that cannot trap the solvent as well.⁵⁹

Redox responsive supramolecular polymers have also been extensively used by chemists. A practical example from McNeil and collaborators, where a cysteine derived amino acid functionalized with naphthalene molecularly dimerizes in methanol with the addition of an oxidant, obtaining a gel. Due to the low critical gel concentration in methanol of the cysteine derivative, this process was used to sense the presence of TATP (triacetone triperoxide), a peroxide-based explosive.⁶⁰

Rybtchinski and co-workers, synthesized a bolaamphiphile where two perylene diimide (PDI) cores are linked by a bipyridyl spacer and functionalized with polyethylene glycol side chains for an increase in water solubility. This molecule self-assembles into a network of fibers in water/THF mixture, forming gels at concentrations above 8 mM. Upon addition of an aqueous solution of sodium dithionite, the PDI cores get reduced into the radical anion form. This transformation destroys the aggregates due to the electrostatic repulsion between the reduced species. By oxidation, with oxygen from air, the perylene recovers its neutral form and the gel is formed again, Figure 1.6. Interestingly, when the gel is heated it shrinks, expelling ~75% of the trapped solvent. The gel recovers its initial state after one day at room temperature (or one hour at 40 °C) or by its reduction with dithionite followed by air oxidation.⁶¹

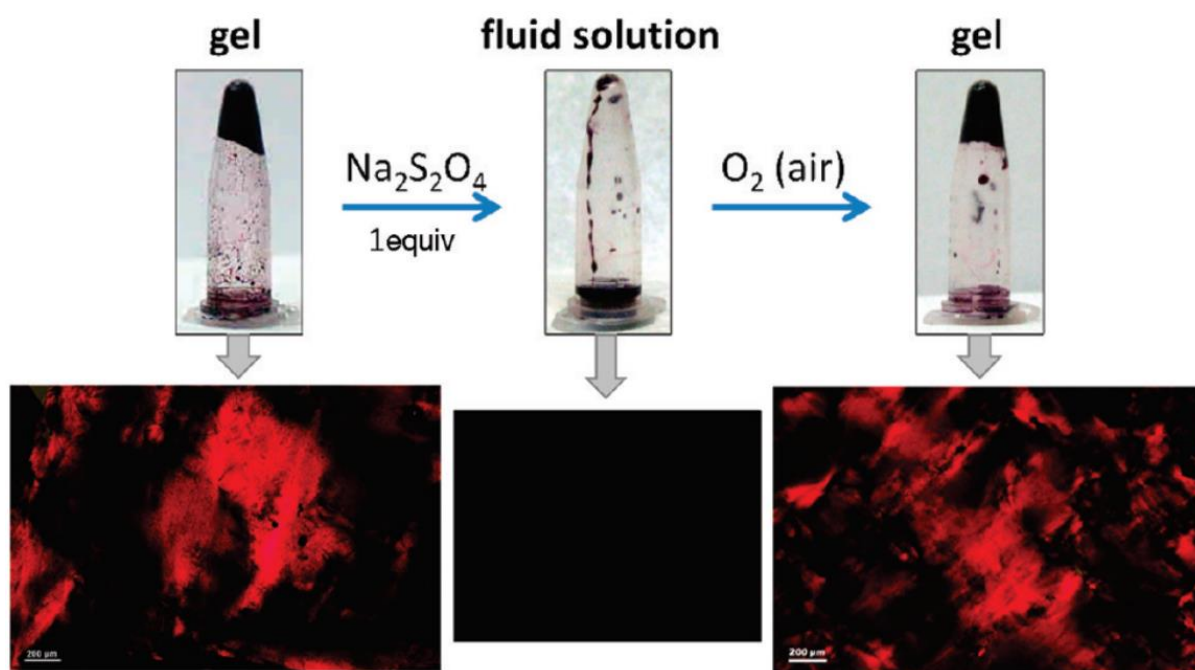


Figure 1.6 – Top: Photographs showing the destructing of the hydrogel by addition of sodium dithionite ($\text{Na}_2\text{S}_2\text{O}_4$) and its subsequent recovery by air-oxidation. Bottom: Polarized microscopy of the aggregate structures corresponding to the picture on top. Scale bar is 200 μm . Taken from ref. 61.

Salts and ions have also been used to control supramolecular polymers and materials. For example, bis-urea based low molecular-mass gelators were used to assist and control the growth of pharmaceutically relevant crystals and tune their polymorphism in a wide range of solvents. Acetate anions were used to destroy the gel, because of their ability to bind with urea groups. When the gel is totally dissolved, the crystals can be easily recovered by filtration.⁶² Salts have also been used to increase ionic strength in solution, which by itself influences the formation of supramolecular polymers. Besenius, *et al.* showed three different BTAs decorated with two distinct strong chelators, DOTA and DTPA, the latter with two different points of linkage, changing the overall charge of the molecule, giving three different self-assembling molecules. When gadolinium ion (Gd^{3+}) is chelated to these molecules, their overall charge varies from neutral with BTA-DOTA-Gd, three negative charges with BTA-DTPA-N-MA-Gd and six negative charges BTA-DTPA-Gd. The neutral molecule, forms fibers in water and aggregates by a cooperative mechanism while the charged species self-assemble into globules anti-cooperatively, due to electrostatic repulsion. However, if salt is added to the solution, increasing ionic strength, the charged BTAs start self-assembling cooperatively into fibers, Figure 1.7.⁹

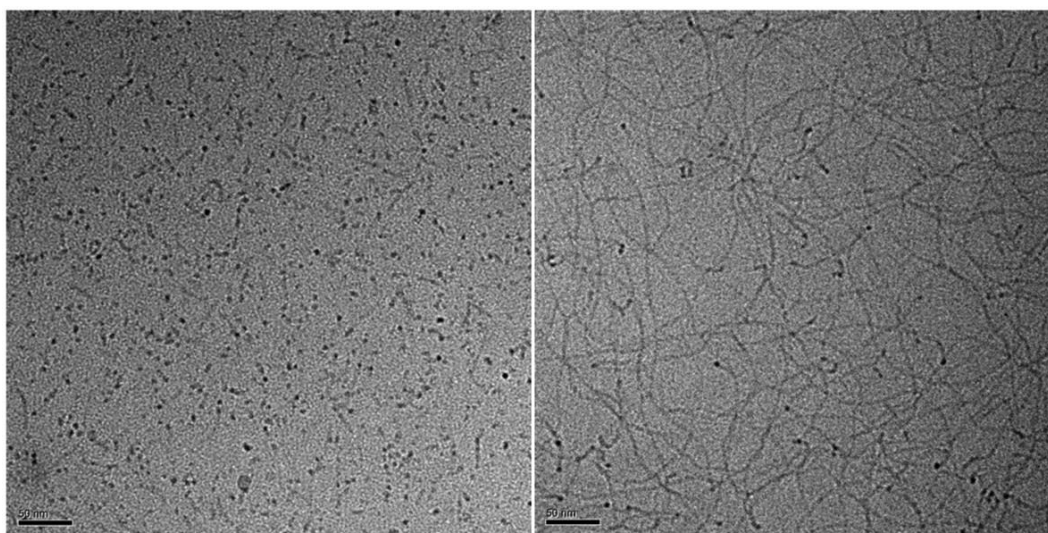


Figure 1.7 – Cryo-TEM of the BTA-DTPA-Gd, 1 mM, in citrate buffer 100 mM and pH 6. On the left, sodium chloride concentration is 3 M, so the aggregates are globular. When increasing NaCl concentration to 5 M, right, BTA-DTPA-Gd forms fibers. Taken from ref. 9.

Molecular agents that chemically react with self-assembling building-blocks have been used to control aggregation and gelation. For example, a saccharide based gelator containing and aldehyde group makes hydrogels in water. When cysteine is added to the hydrogel, it reacts

with the aldehyde forming a thiazolidine ring, increasing its hydrophilicity and destroying the hydrogel.⁸ Similarly, Miravet and Escuder have reported a peptide derived hydrogelator composed of proline, valine and a long alkyl chain. The hydrogel has been used to catalyze stereoselective aldol reactions between cyclic ketones and aromatic aldehydes, due to catalytic activity of proline. However, if an aliphatic aldehyde is added to the gel in acetonitrile, it reacts with proline forming a soluble aminal, disrupting the gel and resulting in a clear solution. The less hydrophilic is the aldehyde, the faster it reacts with the hydrogelator due to their insertion in the hydrophobic pocket of the hydrogel.^{63,64}

1.2.2 Non-Equilibrium Control Over Supramolecular Polymerization

Over the last ten years, a growing interest has been shown in to the non-equilibrium behavior of artificial supramolecular polymers.³⁵ Similar to the natural polymers discussed above (sub-section 1.1.1), synthetic supramolecular polymers also can show dissipative (like microtubules) or different pathways of polymerization with kinetically trapped/metastable states (like amyloid fibrils). The first will be discussed in more detail further down in this chapter (Section 1.3) while the latter will be the focus of this sub-section.

In a seminal publication by Korevaar, *et al.*, Figure 1.8, it was shown that a self-complementary hydrogen bonding S-chiral oligo(p-phenylenevinylene) (S-OPV) self-assembles in methyl cyclohexane (MCH) by dimerization, then nucleation followed by elongation, through π - π stacking into 1-D fibers. At equilibrium, left-handed M-type stacks are formed. If the solution is rapidly quenched at 0 °C from the molecularly dissolved state at 70 °C, a CD-spectrum with opposing handedness is observed, indicating the presence of right-handed P-type assemblies in the mixture. Those assemblies are metastable and are slowly converted to the thermodynamic product when incubated at 25 °C. The presence of this metastable state indicates that the self-assembly occurs through different pathways with an on-pathway M-type aggregate and off-pathway P-type stacks. When studying the kinetics of aggregation, at low concentrations, the polymerization follows a typical nucleation-elongation mechanism, with lag-phase followed by a rapid elongation, observed by a monotonous decrease in CD intensity. Interestingly, at concentrations above 9 μ M, at early stages of aggregation, a

positive CD signal is first observed followed by a rapid decrease to the expected values of the equilibrium aggregate. This indicates that at concentrations $> 9 \mu\text{M}$, before reaching the pathway towards the thermodynamic equilibrium, S-OPV first polymerizes into the off-pathway metastable P-type aggregate. Remarkably, the half-times of polymerization, $\tau_{1/2}$, (time at which half of the molecules are in polymeric form) decreases with increasing concentration until reaching a minimum at $10 \mu\text{M}$ then starts increasing. This further shows that at higher concentrations the S-OPV does not reach equilibrium in a straight-forward fashion, first going off-pathway then attaining the M-type aggregate. A kinetic model showed that the formation of the P-type aggregate was kinetically favored over the M-type, however it can be only formed when there is enough monomer in solution to break the nucleation barrier because the P-nucleus is thermodynamically less stable than the M.⁶⁵ This is an interesting example of how supramolecular polymerization can go through different routes to reach equilibrium, which is an important parameter when aiming to control supramolecular polymerization.

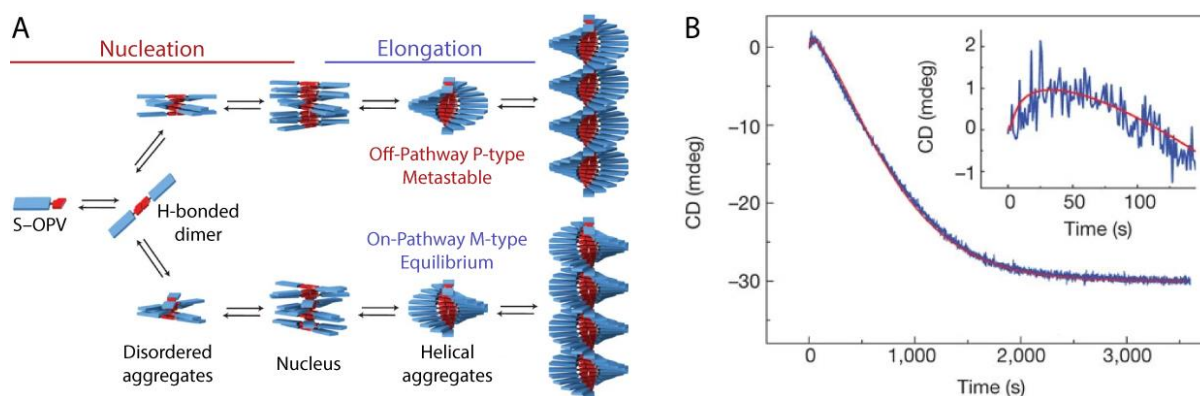


Figure 1.8 – A – Scheme of the on and off-pathways assembly of S-OPV. B – Time dependent CD signal of S-OPV aggregation: an increase in the signal in the early stages followed by a steady decrease until equilibrium is reached. Adapted from ref. 65.

In a similar fashion, Aliprandi, *et al.*, showed the multiple pathway self-assembly of a platinum complex (Pt-cpx) in aqueous mixtures, Figure 1.9, driven by metal interactions of the Pt centers, π - π stacking, and hydrogen bonding. The solvent-dependent aggregation of Pt-cpx was studied in water/dioxane mixture, being molecularly dissolved in dioxane and fully assembled in 95:5 water:dioxane. The monomeric Pt-cpx presents weak emission and low quantum yield ($\sim 1\%$), due to the presence of oxygen in the solvent, that quenches its fluorescence. At 95:5 water:dioxane, orange/red emission of the complex is observed, with the

formation of soft nanoparticles of ~ 100 nm. The aggregation-induced increase in quantum yield is typical of Pt–Pt interactions, suggesting that vesicle like aggregates are formed, with the metal centers in the hydrophobic pocket and the hydrophilic tails pointing towards the solvent, Figure 1.9–A red cartoon. However, after three weeks a new aggregate is observed in solution, with fibrous morphology, with identical spectroscopic signature as the molecularly dissolved Pt-cpx, but with much higher quantum yield. These luminescent properties indicate that no Pt–Pt or π – π interactions are present, but the increase in quantum yield is explained by the shielding of the metal centers from oxygen inside the fibers, Figure 1.9–A blue scheme. The latter assembly is the thermodynamic equilibrium in this solvent mixture while the spherical ones are kinetically trapped for long periods of time. Melting curves of the fibrous aggregates show that it self-assembles following a cooperative mechanism with a high degree of cooperativity while the kinetically trapped spheres are isodesmic, this explains why the latter is kinetically stable for three weeks. Depolymerization curves, obtained by changing the solvent ratio from 95:5 to 0:1 water:dioxane and measuring luminescence after 50 seconds, show that at $>70\%$ water the spherical aggregates are kinetically preferred while between 30 and 70% dioxane the fibers are formed and above 70% dioxane only the molecularly dissolved Pt-cpx is observed. Kinetic experiments at 79 and 83% water, Figure 1.9–B, show that at early stages the spherical aggregates are formed, but after 5 to 10 minutes a previously unaccounted aggregate is observed, green emissive fibers, typical of axial Pt–Pt interactions (Figure 1.9–A green scheme) followed by the simultaneous appearance of the equilibrium assembly and the total disappearance of the red spheres. After multiple hours, the green fibers start vanishing to give place to the thermodynamically stable blue fibers. Irradiating the blue emission fibers with a high-power laser, converts them into the green ones, hypothesized to be either a photochemical or a local thermal effect.⁶⁶

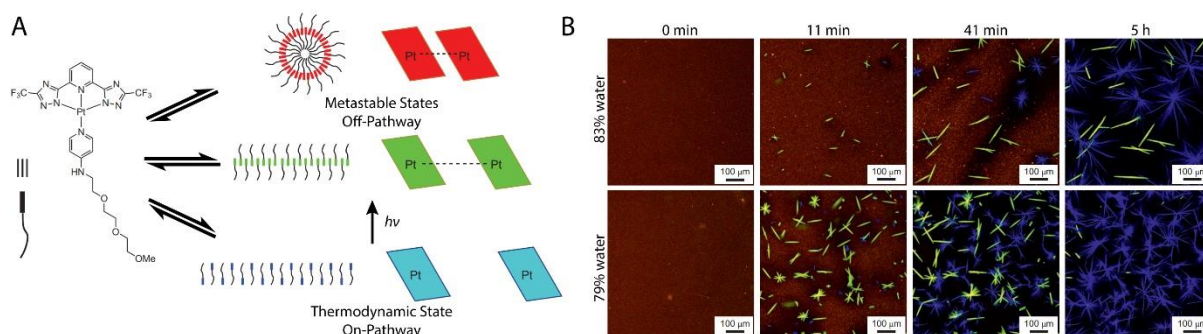


Figure 1.9 – A – Scheme of the self-assembly process of the platinum complex with two off-pathway aggregated and the thermodynamic one. B – Confocal microscopy of the kinetic evolution of the self-assembly of the platinum complex. Adapted from ref. 66.

The competition between on and off-pathway aggregates can be further explored with the advent of seeded, or living, supramolecular polymerization. Takeuchi, Sugiyasu and co-workers presented the two-pathway supramolecular polymerization of a porphyrin derivative, Figure 1.10. When heated and cooled in methylcyclohexane (MCH), the molecule forms J-aggregates nanoparticles through an isodesmic mechanism, that are stable up to days. After that, they are converted into fibrous H-aggregates, that polymerizes by a cooperative mechanism. The isodesmic J-aggregates are the kinetically trapped species while the cooperative H-aggregates are the thermodynamic equilibrium of the porphyrin assembly. The transition from J to H-aggregate can be accelerated by agitation, such as continuous stirring or sonication. Interestingly, if aged H-aggregate fibers are sonicated and added to a J-aggregate solution, it promptly induces the J-to-H transition, reaching thermodynamic equilibrium in only a few minutes, giving rise to a living supramolecular polymerization. If H-aggregate seeds are diluted with fresh J-aggregate solution, the H-type fibers grow in a linear fashion with the J/H ratio. This living supramolecular polymerization could be only achieved because the kinetic barrier for the formation of the H-aggregate thermodynamic equilibrium is very high, making the metastable J-aggregate kinetically favored and extremely stable. The complex pathway of supramolecular polymerization of this porphyrin is summed up in the scheme present in Figure 1.10–A.⁶⁷ In a follow-up study, similar porphyrins were shown to self-assemble into three distinct aggregates: metastable spherical nanoparticles, fibers and nanosheets. Those different assemblies could be unlocked by varying the size of the alkyl chain of the side chains of the porphyrin. Interestingly, with hexyl and heptyl side-chains, the self-assembly can reach the

three different states through off and on-pathway aggregation, Figure 1.10–B. After heating and cooling the molecules form J-aggregate spherical nanoparticles that slowly evolve into micrometer-sized J-type nanosheets. The decrease in the time taken for this transition with increasing concentration shows that the nanoparticle is an on-pathway metastable aggregate, while the nanosheet is the equilibrium condition. However, if the nanoparticles are ultrasonicated, H-aggregate fibers are observed in solution. Thermodynamic studies of the fibrous assembly and the nanosheet show that their equilibrium constants are in the same order of magnitude, meaning that they are thermodynamically similar, with the H-aggregate presenting slightly higher stability. The final morphology of the assemblies, either fibers or nanosheets, could be selected by injecting their respective seeds into the J-aggregate nanoparticle solutions. By further addition of freshly prepared nanoparticles, the living growth of both stable assemblies was also obtained.⁶⁸

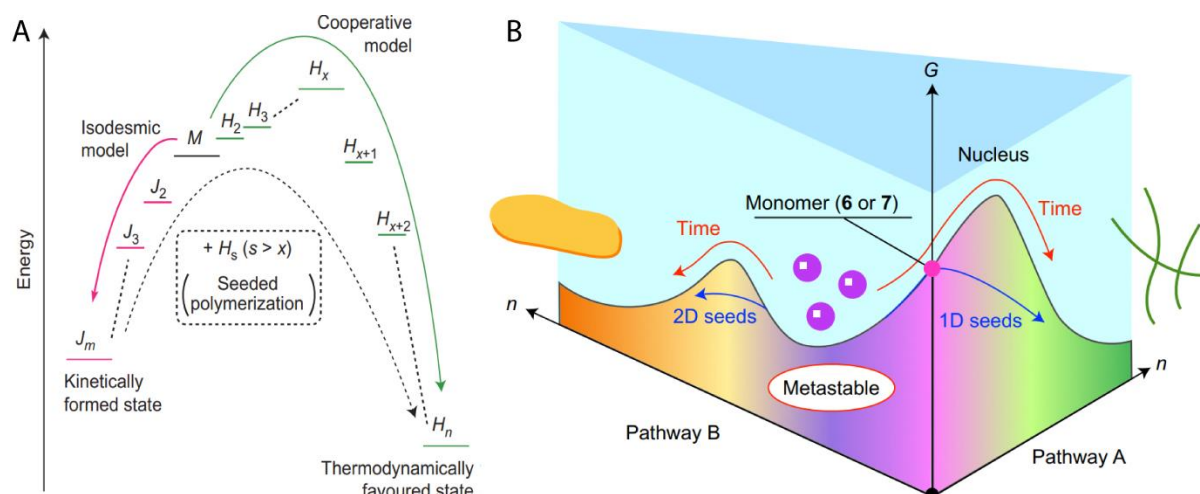


Figure 1.10 – **A** – Energy landscape of the pathway dependent self-assembly and seeded behavior of the porphyrin derivative. Taken from ref. 67. **B** – Energy landscape of the pathway dependent self-assembly and seeded behavior of the 1-D to 2-D transition of the porphyrin derivative aggregation. Taken from ref. 68.

Another impressive example of seeding-induced and living supramolecular polymerization is the design-driven example by Aida and co-workers, Figure 1.11. Bowl-shaped corannulenes with five amide-containing sidechains, perform intramolecular hydrogen-bonding, trapping them in a monomeric state. However, intramolecular hydrogen bonding is prevented by methylation of the amide, Figure 1.11–A. The free carbonyl group allows the N-methylated corannulenes to hydrogen bond with the non-methylated species, thus initiating the supramolecular polymerization process, acting as a seed. This is an example

of a true chain-growth supramolecular polymerization because aggregation can only be started by an initiator that is molecularly different, although very similar, to the monomer (like initiators in traditional molecular polymerization).⁶⁹

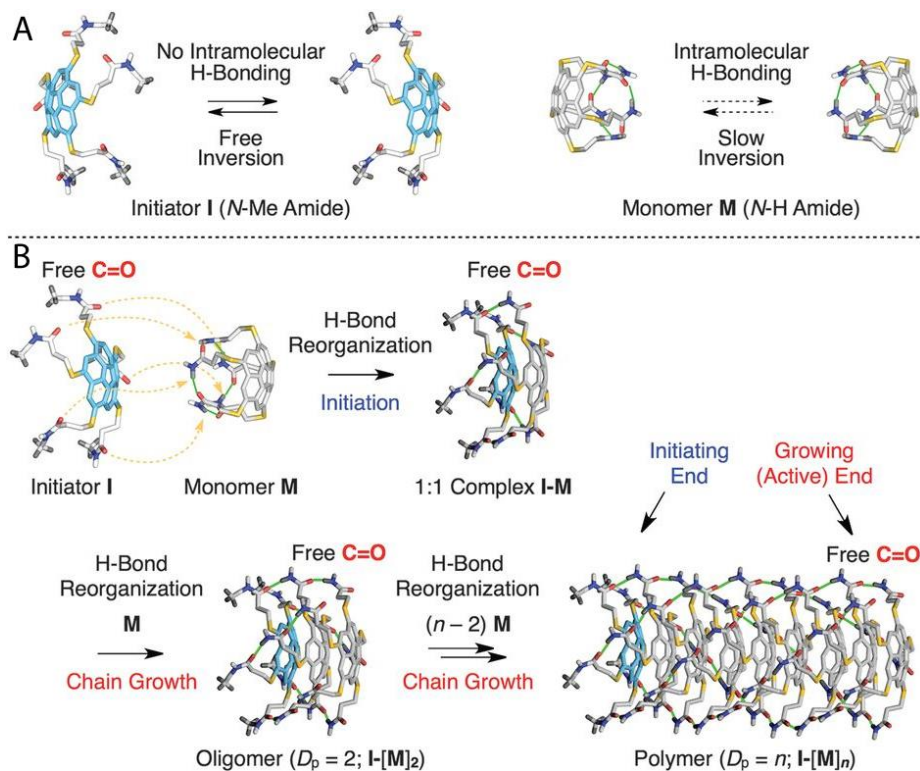


Figure 1.11 – **A** – Representation of the intramolecular hydrogen-bonding of the amide containing corannulenes and its absence when the amide is N-methylated. **B** – Scheme of the living supramolecular polymerization process: N-methylated amide corannulenes initiate supramolecular polymerization of the N-H amides. Taken from ref. 69.

Overall, the same toolset that has been used to control supramolecular polymers at equilibrium can be utilized under non-equilibrium conditions. The use of temperature has been exploited by Haedler *et al.* when studying the self-assembly of Carbonyl-Bridged Triarylamine Trisamides (CBTT) into helical one-dimensional fibers. By cooling a solution of the CBTT in ortho-dichlorobenzene from its molecular dissolved state at 80 °C to –5 °C, a gradual monomer to assembly transition was observed spectroscopically from 80 to 5 °C, however a sharp variation happens when further cooled to –5 °C. When resting at this temperature for one hour, an inversion followed by intensity increase of the CD spectrum is observed. Two states, with opposite helicity, can be identified. By slow cooling (0.2 K/min) from 30 °C, the CD signal (at 490 nm) first decreases, reaching a negative plateau between 5 and 10 °C (State A). Below 5 °C, the circular dichroism abruptly changes to positive values

(State B). Upon heating to 30 °C, after one hour at -5 °C, a decrease of the CD value is observed in the typical fashion of a cooperative aggregation mechanism with elongation temperature of 20 °C. Therefore, this molecule exhibits a strong hysteresis when cooling and heating from 30 to -5 °C and back, with the existence of the two different assemblies between 5 and 10 °C, depending if the temperature is decreasing or increasing. To synthesize State A, the solution was heated to 30 °C then directly cooled to 7 °C, parallelly to make State B, the solution was heated to 30 °C then cooled to -5 °C and heated back to 7 °C. Both states were stable for >5 hours in these final conditions. However, if State A and B are mixed in a 1:1 ratio, the mixture slowly evolves to solely State B in one hour, indicating that B is the thermodynamic equilibrium while A is kinetically trapped. This example shows how two different helical aggregates can be synthesized with the same molecule at the same conditions by controlling the heating/cooling conditions.⁷⁰

Solvent modulation has also been used to reach different kinetically stable states, but not at equilibrium, using the same molecule. This has been evidenced by Rybtchinski and collaborators with a peptide and platinum containing perylene diimide (PDI) derivative. The molecule is monomeric in chloroform, partially aggregated in tetrahydrofuran (THF) and fully aggregated in water/THF mixtures. In high water content (95:5 water:THF), a weak CD signal is observed with the formation of curved short stacks. By the addition of THF to reach 20 and 30% in the solvent composition, PDI formed wavy and straight long fibers respectively. CD signal increased with increasing THF content and the spectra significantly evolved over time (70h), especially for 7:3 water:THF. After 4 days, the fibers in 20% THF transform to aggregates identical to the ones in 30% THF, while at 95:5 water:THF the assemblies remain constant for up to two months. The high water-content kinetically traps the assemblies due to strong hydrophobic interaction between the PDIs. Adding THF to the mixture decreases the kinetic barrier, with the straight long fibers obtained at 30% THF being the thermodynamic equilibrium state. With the goal of synthesizing different aggregates at the same final conditions, the PDI was let to age for different periods of time in 20% THF then diluted with water to reach 95:5 water:THF. To make short curved stacks, the molecules is directly dissolved in 95% water; to produce the wavy fibers, PDI is dissolved in 20% THF and let to evolve for 40

min then diluted with water to reach 95:5 water:THF; finally, to synthesize the straight and long fibers the molecule is let for 40 hours in 80% water then add water to reach 95%. At the final state, those assemblies are stable for weeks.⁷¹

1.2.3 Spatial Control

So far, different techniques to control the supramolecular polymerization process and the final aggregate morphology have been laid out. A different challenge is to dictate where and how the polymers are formed spatially, with different strategies being developed, a few examples will be listed below.^{72,73}

van Esch and co-workers have developed a simple method to polymerize and align supramolecular fibers through a chemical gradient. Benzoyl protected L-cystine with free carboxylic acids, that is known to gel below pH 5, was dissolved in a pH 11 aqueous solution. The solution was put inside a flow cuvette and $\sim 3 \mu\text{L}$ of a 5 M hydrochloric acid (HCl) solution was put in one of the apertures. With the diffusion of the protons into the cystine containing solution, the gelator gets protonated and self-assembles into long fibers forming a hydrogel. Surprisingly, optical analysis of the fibers in the hydrogel showed that they are aligned with the direction of the diffusion of the acid. With this simple method, chemical diffusion, the control of the spatial distribution and the alignment of supramolecular fibers could be achieved.⁷⁴

The same group, with Eelkema, in a follow up study from an example discussed in subsection 1.2.1 above,⁵⁹ where gelation is induced by the acid catalyzed formation of an acyl hydrazone hydrogelator. In this example, a glass slide patterned with sulfonic acid groups is used to locally generate the hydrogelator in a controlled fashion. Because of its pKa (~ 1.4) the sulfonic acids are expected to be fully deprotonated in the working conditions, but the positively charged protons are likely to stay in proximity of the negatively charged sulfonates. The high local acidity catalyzes the formation of the acyl hydrazone from the hydrazine hydrophobic core and the hydrophilic aromatic aldehyde. The formation of the hydrogel was limited to where the glass slide was patterned with the sulfonic acid moieties, as it can be observed in Figure 1.12.⁷⁵

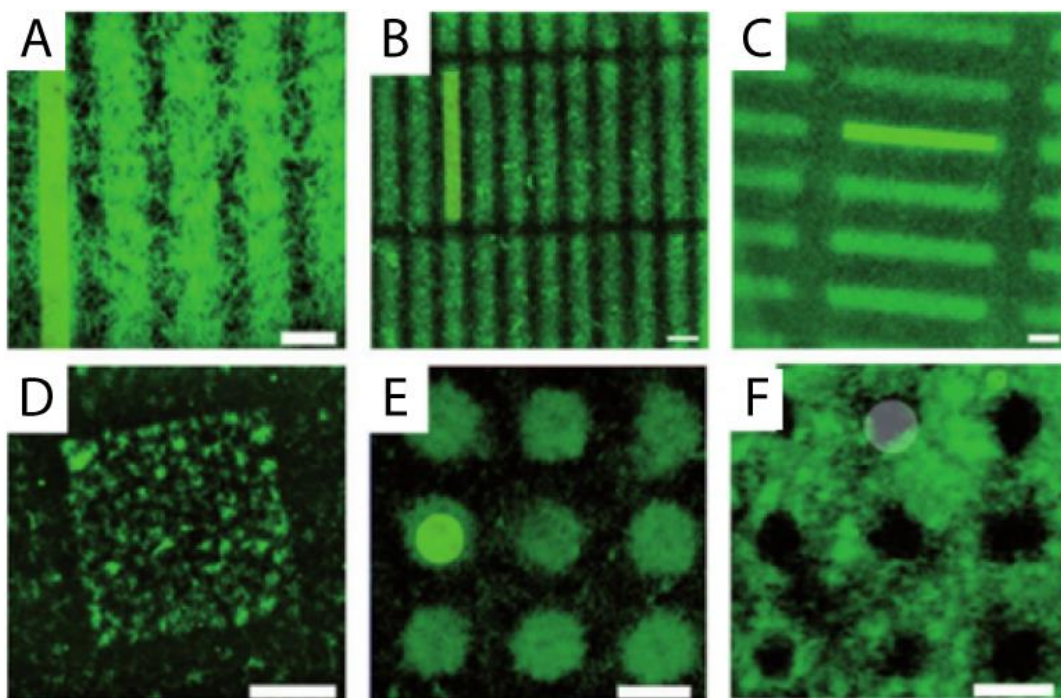


Figure 1.12 – Confocal images of spatially controlled hydrogels (A – lines; B, C – rectangles; D – squares; E, F – circles) through the patterning of a glass slide with sulfonic acid. Scale bars 20 μm . Taken from ref. 75.

Another strategy, using the same acid catalyzed *in-situ* formation of the acyl-hydrazone hydrogelator, applied by the same group, was to use a visible light activated photoacid and masks. By mixing the two components of the hydrogelator with the merocyanine photo-acid in an aqueous solution, the formation of hydrogel is promptly achieved in 100 minutes by the irradiation with visible light (400–800 nm). Hydrogel formation took 200 min without light and 350 without the presence of the photoacid. Spatial control was achieved using photomasks with designed patterns, Figure 1.13.⁷⁶

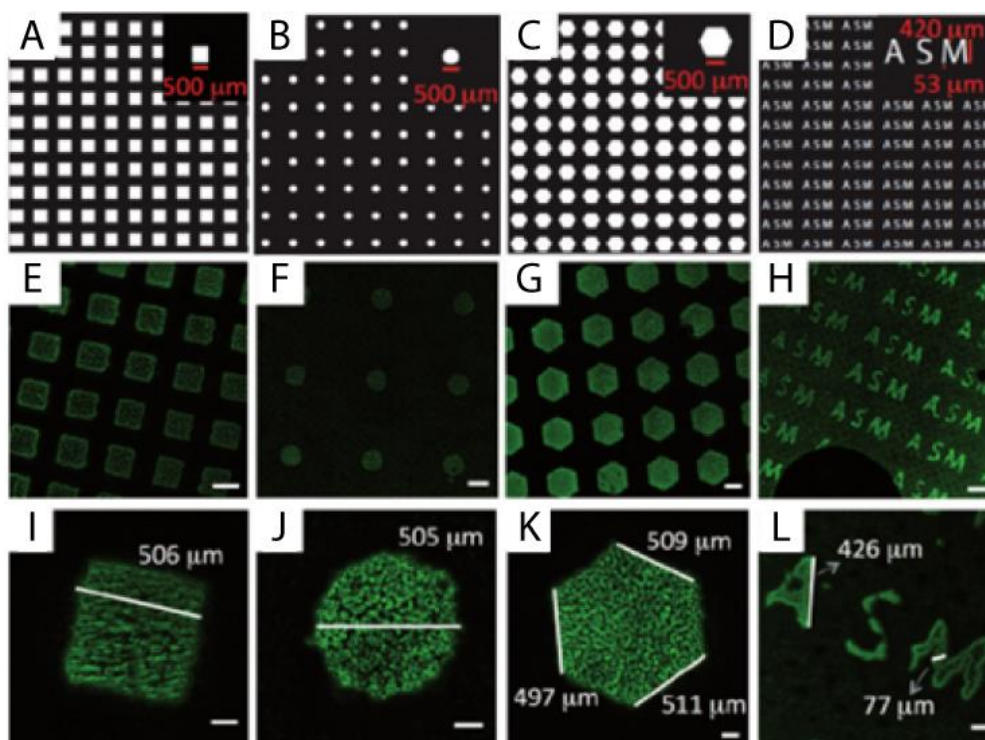


Figure 1.13 – First row – Examples of the photomasks used to achieve the photo-patterned hydrogel. Scale bars 500 μm . Second row – Examples of the photo-patterned hydrogels. Scale bar 500 μm . Third row – Close-ups of the second row. Scale bar 100 μm . Taken from ref. 76.

Cameron and Adams have developed a method for the nucleation of hydrogels from a surface. Using pH sensitive hydrogelators and the electrochemical oxidation of hydroquinone into benzoquinone, that releases two protons as by-product, gelation was achieved on the surface of electrodes, Figure 1.14–A. Carboxylate terminated N-protected peptidic hydrogelators were dissolved in a neutral aqueous solution and activated by the release of protons issued from an electrochemical reaction. The high acidity close to the electrode permitted the nucleation of supramolecular fibers on its surface, and growth towards the solution with a final gel thickness on the millimeter range. The use of patterned electrodes permitted the creation of patterned hydrogels and if two (or more) different hydrogelators were present in solution, the order in which they are formed is dictated by their respective pK_a , Figure 1.14.^{77–79}

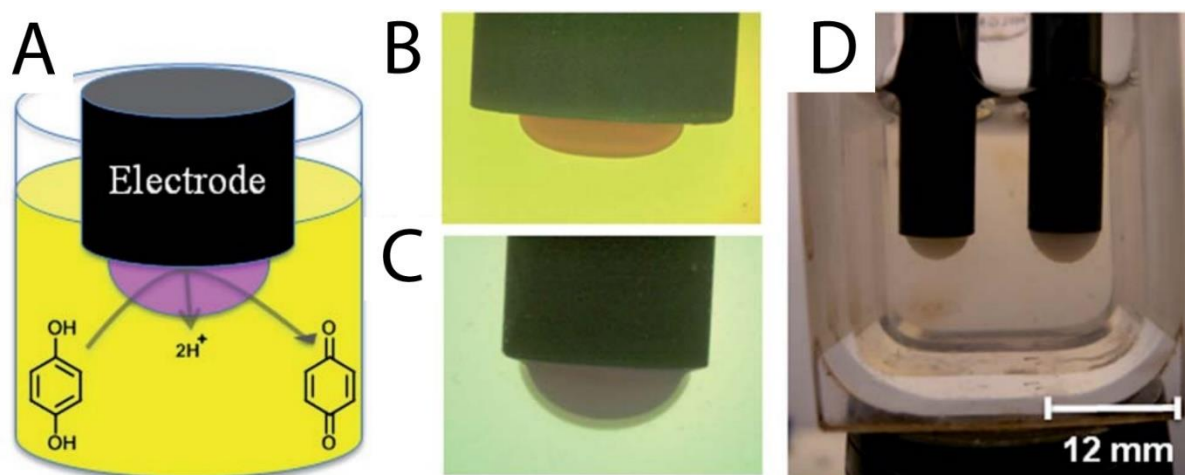


Figure 1.14 – **A** – Scheme of the electrochemical set-up and scheme of the electrochemical reaction. **B** – Photography of a hydrogel formed on the surface of an electrode. **C** – Photography of a gel formed on top of a dyed gel that was previously made on the surface of the electrode. **D** – Two gels being formed parallelly on two electrodes with different currents. Taken from ref. 79.

Ulijn and co-workers achieved spatial control with a catalytically active surface. The enzyme thermolysin, that catalyzes amide bond formation and hydrolysis, was used for the *in-situ* formation of hydrogelators from a mixture containing fmoc-leucine and leucine. Through the enzyme-catalyzed amide formation, a distribution of leucine oligomers was obtained. This mixture converged over time to the pentamer because it formed sheet-like structures that are thermodynamically stable. Thermolysin was then immobilized on a glass surface and exposed to the same solution. After five minutes, fibers can be observed by AFM and TEM, showing the nucleation process happening in proximity of the enzymes. After 24h, the self-assembled structures were only formed in the areas where thermolysin was present, without any structures being observed in regions without enzyme.⁸⁰ In a follow-up study, using the same enzyme but a simpler system with fmoc-threonine and amide terminated phenylalanine, the group showed that the irreversible immobilization of the enzyme followed by the proper washing of the surface were mutually necessary for the localized formation of the hydrogel. Otherwise, the gel is formed uniformly in the whole solution due to detaching of the enzyme from the surface.⁸¹

Recently, Montenegro and Granja have shown a method to control the morphology and spatial distribution of cyclic peptide nanotubes inside microdroplets, a follow-up study to the one discussed in sub-section 1.2.1.⁵⁶ Histidine and lysine containing cyclic peptides are protonated at $\text{pH} < 4$. Due to electrostatic repulsion, the cyclic peptide cannot self-assemble in

acidic conditions. Aggregation into nanotubes can be triggered by the addition of base (in this case sodium hydroxide, NaOH), deprotonating the charged residues, or by increasing ionic strength (here by adding calcium chloride, CaCl₂), shielding the electrostatic repulsion. The cyclic peptides also contained a pyrene moiety that imparted the molecule with strong fluorescence while in monomeric form, that was quenched when they self-assembled into nanotubes. The system was then moved to a microfluidic device where nanotube formation could be triggered inside microdroplets. First the cyclic peptide and the triggering agent (pure water, base, or salt) were mixed in a first junction, then in a second intersection the aqueous phase encountered the oil with surfactant, thus forming the water-in-oil microdroplets. The first try was to inject pure water in the second inlet, as a negative control. As expected, no aggregation was detected, and the distribution of the molecule is uniform throughout the droplet, Figure 1.15–A to D. When the trigger is a 3.5 mM NaOH solution, an increase in fluorescence was perceived at the water/oil interface of the droplet in a capsular fashion, Figure 1.15–E to H. This effect can be explained by the formation of hydrophobic nanotubes by deprotonation, that have more affinity to the hydrophobic oil, staying preferentially at the interface. When the aggregation is driven by addition of 1 M CaCl₂, small fibrils were observed at the center of the droplets, Figure 1.15–I to L. Because assembly was induced by electrostatic shielding, the cyclic peptides are still protonated and the nanotubes are hydrophilic, thus staying preferentially at the center of the droplet, far from the hydrophobic oil. This is an example of how the properties of the assemblies themselves can control the spatial distribution of supramolecular aggregates.⁸²

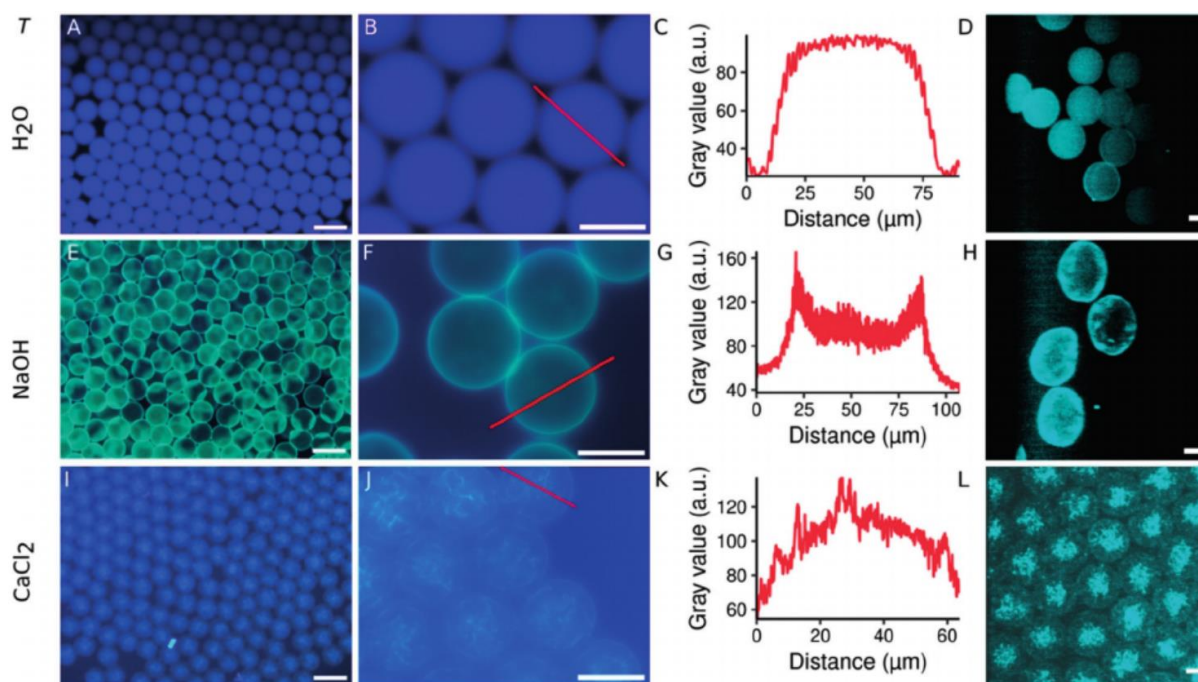


Figure 1.15 – Morphology and spatial distribution of the peptide nanotube assemblies inside microfluidic droplets. The different conditions are divided into the three rows: first row added water (A, B, C and D), second row added 3.5 mM NaOH solution (E, F, G, H) third row increase in ionic strength with 1M CaCl₂ (I, J, K, L). The first column (A, E, I) shows confocal microscopy low-magnification images of the droplets (scale bar 100 μm), the second column (B, F, J) are high-magnification pictures (scale bar 50 μm). The third column (C, G, K) are the profiles extracted from the red lines in the pictures in the second column. The last column (D, H, L) shows the confocal 3D projections of the droplets (scale bar 25 μm). Taken from ref. 82.

1.3 Out-of-Equilibrium Reaction Networks to Control Supramolecular Polymers

In the last ten years, Supramolecular Systems Chemists have been inspired by the (non)covalent dynamic processes found in nature, such as tubulin polymerization to form microtubules (as discussed previously), to create new reaction cycles to control (dis)assembly processes.⁸³ Several strategies to create (and possibly maintain) nonequilibrium conditions have been reported which include the use of enzymes, DNA, redox reactions, temporary pH-changes, or the purely synthetic formation and destruction of a covalent bond.^{84,85} These studies have shown new and surprising phenomena that cannot be observed at equilibrium (sub-section 1.2.1) or in non-dissipative non-equilibrium conditions (sub-section 1.2.2) such as supramolecular oscillations and traveling fronts,⁸⁶ reconfigurable DNA-nanotubes,^{87,88} or self-dividing coacervate droplets simulating mitosis.⁸⁹

In this section, examples of man-made systems where the control of supramolecular self-assembly is achieved through a non-equilibrium reaction cycle will be shown. First fully synthetic reaction cycles where covalent bonds are created and broken will be elucidated. Next reaction cycles involving enzyme catalyzed reactions will be presented. Finally, examples where the transient formation of self-assembling structures are accomplished by temporal pH changes or redox reaction will be laid out.

1.3.1 Fully Synthetic Reaction Cycleⁱⁱ

Here, systems where covalent bonds are made and broken synthetically in dissipative self-assembly will be listed. Generally, the studies combine chemical reactions to (de)activate building blocks so that they can (dis)assemble and later return to the original state under the same conditions. The reaction cycles can be categorized into three groups, Figure 1.16:⁹⁰

- Category (1): deactivation of the self-assembling molecules occurs spontaneously via solvent (e.g., hydrolysis in aqueous systems)
- Category (2): the same type of (un)catalyzed reaction is responsible for all (de)activation steps
- Category (3): a catalyst exclusively acts on a single reaction of the cycle

ⁱⁱ Contents of this sub-section were published on: Singh, N.; Formon, G. J. M.; De Piccoli, S.; Hermans, T. M. Devising Synthetic Reaction Cycles for Dissipative Nonequilibrium Self-Assembly. *Adv. Mater.* **2020**, 32 (20), 1906834. <https://doi.org/10.1002/adma.201906834>.

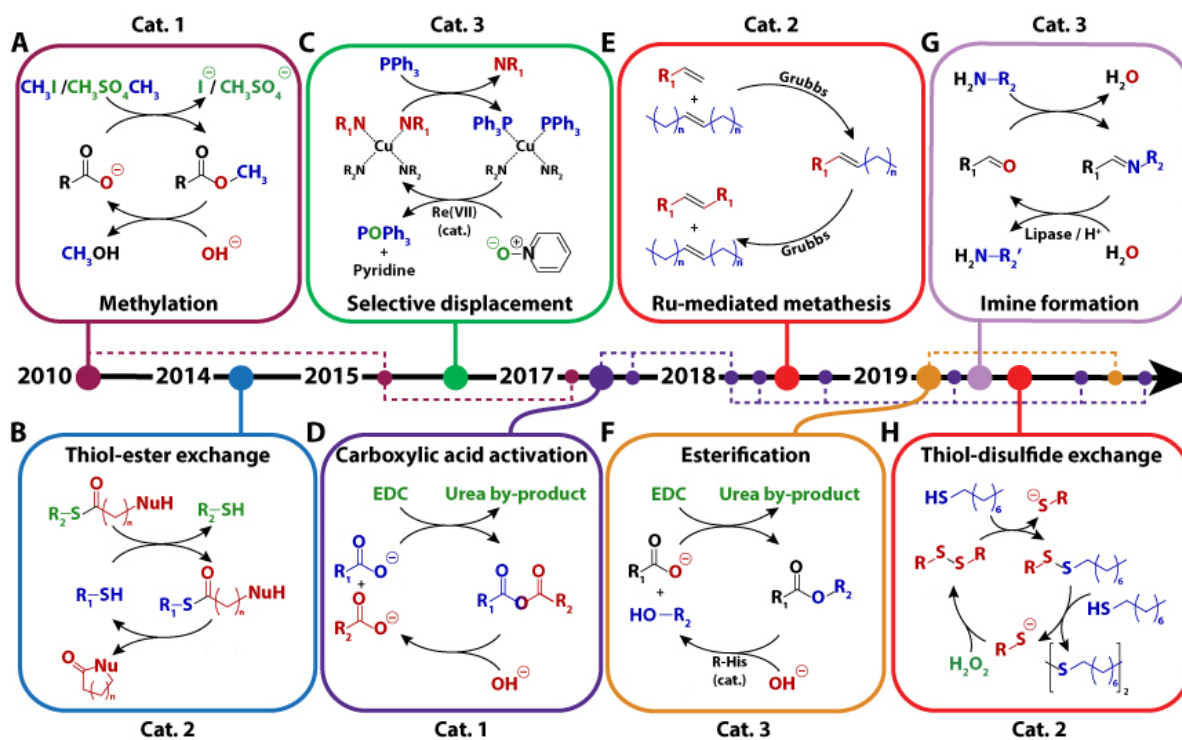


Figure 1.16 – Timeline of the different fully synthetic reaction cycles developed for dissipative self-assembly in the last ten years. Adapted from ref. 90.

Eelkema, van Esch and collaborators developed the first method for chemically fueled supramolecular polymerization using a methylation reaction to activate self-assembly (Figure 1.16–A, Category 1). Dibenzoyl-(1)-cysteine (DBC), which is soluble in water at high pH ($pK_a \approx 4.5$), was used. Methyl iodide was applied to converted at least one of the carboxylic acids of DBC to its corresponding methyl ester, increasing hydrophobicity of the molecule leading to fiber assembly. The hydrolysis of the ester triggers disassembly of the fibers by regenerating the original molecule. The cycle can be repeated by adding further aliquots of the fuel, but the performance of many cycles is hampered by accumulation of waste.⁹¹ Five years after, the methylating agent was switched to the more powerful dimethyl sulfate (DMS), improving the reaction cycle and obtaining transient gelation. Moreover, the lifetime of the gels could be regulated by the amount of fuel.⁹² The same reaction cycle was later used to control the aggregation of colloids functionalized with carboxylic acid.⁹³ This methodology, involving methylation/hydrolysis, displayed the first fuel-driven dissipative formation of an “active gel”. These works paved the way to a new class of “life-like” systems and materials that are driven out-of-equilibrium by chemical fuels.

In 2014, Dambeniaks *et al.*, showed the chemically fueled assembly of a membrane transport system. The mercaptan precursor was activated by thiol–thioester exchange (Figure 1.16–B, Category 2). Voltage-clamp activity experiments showed that the thioester product established conducting channels in bilayer membranes. The system was designed so that the precursor is restored by the intramolecular nucleophilic attack of the chain-end primary amine to the thioester, forming a lactam as waste.⁹⁴

In 2015, Nitschke and co-workers described the chemically fueled self-assembly of metal-coordinated supramolecular structures (Figure 1.16–C, Cat. 3). A copper-based pseudo-rotaxane was disassembled by the displacement of bipyridine ligand with addition of triphenylphosphine (PPh₃). Pyridine N-oxide and a Re(VIII) catalyst oxidized PPh₃ to triphenylphosphine oxide (OPPh₃), with that the initial assembly could be reobtained. With his method, the uptake and release of a fullerene guest from a macrocyclic host could be controlled. Because the oxidation reaction is catalyzed, the rate of disassembly can be easily tuned. The full cycle could be replicated six times.⁹⁵

Boekhoven and collaborators described in 2017 a reaction cycle powered by the transient anhydride formation from dicarboxylates, employing the very common coupling agent, 1-ethyl-3-(3-dimethylaminopropyl)carbodiimide (EDC) (Figure 1.16–D, Category 1). The experiments were carried out in aqueous conditions so that the metastable anhydride can be hydrolyzed back to the dicarboxylate. The transient anhydrides self-assembled into hydrogels, fibers and colloids.⁹⁶ One year later, Tena-Solsona *et al.*, demonstrated the phase separation of anhydrides derived from fatty acids using the same chemistry. The anhydride product (linking two fatty acids) forms hydrophobic droplets, therefore the hydrolysis rate decreases and becomes of zero order, because the anhydride group is protected from the water molecules.^{97,98} Grötsch *et al.* expanded the application of EDC to colloidal particles. Carboxylate decorated gold and iron-oxide nanoparticles were converted to transient N-hydroxysuccinimide (NHS) esters, triggering their aggregation. The size of the assemblies could be tuned by the amounts of fuel, but if too much EDC is added the aggregates precipitate and get kinetically trapped into these larger assemblies even after the ester is hydrolyzed.⁹⁹ Owing to the very common target functional group (carboxylate) and the widely available fuel (EDC), the system has been

replicated many times with different applications such as: the transient assembly of macrocycles that act like crown ethers;¹⁰⁰ regulating the assembly of luminescent silicon nanocrystals that were used to delay the delivery of silicon into mammalian cells;¹⁰¹ the chemically fueled cross-linking of polymers, showing a transient increase in the mechanical properties of the obtained materials;¹⁰² the formation of dynamic vesicles of controlled lifetime and can grow, change morphology, and be destroyed spontaneously by the addition of fuel;¹⁰³ the transient gel-to-gel transition from one architecture to another of an amino-acid containing gelator;¹⁰⁴ droplets that release drugs at a constant rate, dependent on the amount of fuel and the nature and concentration of the droplet;¹⁰⁵ fuel-driven coacervate formation;¹⁰⁶ and the dissipative assembly and self-sorting of macrocycles driven by EDC.¹⁰⁷

In 2018, Fletcher and collaborators developed transient self-replicating surfactants driven by alkene metathesis (Figure 1.16–E, Category 2). In a bi-phasic environment, a water-soluble alkene-containing head reacts with a hydrophobic alkene tail, catalyzed by the second-generation Grubbs catalyst. The amphiphilic reaction product forms micelles, increasing the contact area between the two immiscible phases, this enhances the reactivity between the water and oil-soluble substrates, giving a physical positive feedback (autocatalysis) to the reaction cycle. The self-assembling product will then react with itself, to form the hydrophilic thermodynamic product, with two water-soluble heads connected through metathesis. When another batch of the water-soluble alkene head is added, the transient cycle will be repeated.¹⁰⁸ This system shows positive and negative feedback, because the formation of micelles increases reactivity between the two substrates but also increases the rate of the inactivation reaction. This reaction cycle can easily be applied and replicated with other reactants and uses the common Grubbs catalyst. However, both the (de)activation reactions are of the same type (metathesis), which makes it impossible to control the kinetics of each step individually.

Das and co-workers presented a chemically fueled reaction cycle using EDC where an amphiphile (C18H), containing histidine in the hydrophilic head, reacted with 4-nitro-phenol forming an ester hydrogelator (Figure 1.16–F, Category 3). The resulting self-assembling molecule reverted to the soluble form by ester hydrolysis catalyzed by vicinal histidine. This system presents negative feedback through cooperative catalysis, provided by the assembly of

the ester molecules. The lifetime of the hydrogels is dependent on the cleavability of the ester bond, that can be tuned by the substituents of the phenol group.¹⁰⁹

Recently, George and Vemula showed the use of the dynamic imine bond to make a charge-transfer amphiphile that aggregates into fibers in water (Figure 1.16–G, Category 3). The water-soluble aldehyde-containing charge transfer complex is converted to the amphiphile by addition of an aliphatic primary amine. The deactivation reaction is performed enzymatically or by pH variation, thus changing imine stability. When a hydrolysable lactone (*e.g.*, γ -butyrolactone, β -butyrolactone, or ϵ -caprolactone) is added to the system, the pH of the solution steadily decreases over time, shifting the equilibrium of the imine toward the non-assembling aldehyde and amine. The lifetime of the assembled fibers can be controlled by the lactone concentration. The forward reaction can be partially controlled by using other stimuli, like enzymatic pH modulation or the use of lipase and its inhibitor.¹¹⁰

Fletcher and co-workers presented a chemically fueled transient bi-phasic self-replicator, similar to the first system above.¹⁰⁸ In this reaction cycle a water-soluble disulfide reacts with octanethiol (hydrophobic), by disulfide exchange, forming a transient surfactant (Figure 1.16–H, Category 2). The thiol will react with the amphiphile, giving a water-insoluble disulfide and a hydrophilic thiolate. This system shows physical autocatalysis by the increase in contact area due to the buildup of amphiphile in the system. However, adding hydrogen peroxide oxidizes the thiolates back into the water-soluble disulfide and the cycle starts again. Since all the reagents and fuel are commercially available, this system could be applicable/replicable in other conditions.¹¹¹

1.3.2 Enzymatic Reaction Cycles

Enzymes, due to their selectivity and high catalytic turnover, have also been used to drive reaction cycles out of equilibrium.

Prins and co-workers published the chemically fueled assembly of nanovesicles in a similar way to microtubules. Surfactants ($C_{16}TACN \cdot Zn^{2+}$), with a zinc-containing hydrophilic head, form small micelles in water. When adenosine triphosphate (ATP) is added, it binds to the Zn^{2+} in the amphiphile's head (each ATP binding to three surfactant molecules), inducing

the surfactant to self-assemble into vesicles. Potato apyrase is used for the enzymatic hydrolysis of ATP into AMP (adenosine monophosphate) and inorganic phosphate leading to the disassembly of the vesicles. So, when ATP is injected to a solution containing $C_{16}TACN \cdot Zn^{2+}$ and potato apyrase, vesicles of ~ 100 nm are transiently formed, with fast aggregation (< 1 min) and ATP hydrolysis induced disassembly happening in 5 to 40 minutes (depending on enzyme concentration). The cycle could be repeated, but accumulation of AMP and inorganic phosphate impeded the binding of ATP to the surfactant, further impeding vesicle formation at each cycle. The formation of a hydrophobic pocket inside the walls of the vesicles was used as medium to perform a chemical reaction that would not be possible in pure water.¹¹²

Ulijn utilized the enzyme α -chymotrypsin to catalyze amide bond formation from an ester terminated peptide functionalized with a naphthalene group (Nap) at the N-terminus. The same enzyme also catalyzes the hydrolysis of amide bonds adjacent to aromatic amino acids. Practically, a suspension of Nap-Tyrosine-OMe was converted to Nap-Tyrosine-Tyrosine-NH₂ in 1 minute by the addition of α -chymotrypsin and Tyrosine amide, forming a hydrogel. The resulting peptide hydrolyzes to Nap-Tyrosine-OH and Tyrosine amide overtime, and the hydrogel falls through when the concentration of Nap-Tyrosine-Tyrosine-NH₂ becomes lower than the critical gel concentration, this takes around 4 hours. Equilibrium is reached in around 8 hours, with the overall kinetics of the systems depending on the pH of the solution and the amount of enzyme.¹¹³ In a complementary study, starting with the dipeptide artificial sweetener aspartame (Aspartic-acid-Phenylalanine-OMe) and a mixture of Phenylalanine and Tyrosine amides, Pappas *et al.*, showed the transient formation of a hydrogel with the competitive self-selection of the nucleophile, with Tyrosine amide reacting preferentially with aspartame over Phenylalanine, because the final state was more thermodynamically stable.¹¹⁴

Hermans and co-workers developed an enzymatic reaction cycle involving (de)phosphorylation reactions, a very common chemical modification in living systems. A perylene diimide (PDI) functionalized with the Protein Kinase A (PKA) consensus sequence, LRRASL, is phosphorylated at the serine residues with the presence of the PKA and ATP. The phosphorylated PDI forms bigger assemblies than the dephosphorylated, and surprisingly the

aggregates present opposite helicity. The dephosphorylation reaction is catalyzed by λ -protein phosphatase (λ PP) yielding the original PDI and inorganic phosphate as by-product. When both PKA and λ PP are present in solution, together with PDI-LRRASL, and ATP is injected, a transient formation of the phosphorylated PDI is observed, that reverts back to the original molecule after 10 hours. The cycle cannot be repeated because the λ PP is inhibited by the presence of inorganic phosphate, that accumulates after the first cycle. To overcome this hurdle, the authors developed a membrane reactor that allows the in and outflow of reactants and waste products while keeping the enzymes and the assembling molecules inside. With this technique, non-equilibrium steady states could be achieved and maintained for multiple hours, with the ratio of phosphorylated/non-phosphorylated PDIs controlled by the concentration of ATP in the inflow.¹¹⁵

1.3.3 pH and Redox Driven Reaction Cycles

Redox reaction cycles and transient pH changes have also been extensively used in dissipative self-assembly.

Using compounds that release protons through hydrolysis (pre-acid), Walther and collaborators proceeded to control the self-assembly of different materials by delayed pH change. Different aggregators were used as examples, such as amphiphilic block-copolymers, acid decorated gold nano particles, and a peptide that forms β -sheet nanofibrils at $\text{pH} > 7$. When TRIS buffer at pH 8.8 and the hydrolysable molecule were injected simultaneously to a slightly acidic solution of the self-assembling compound, fast increase of pH is observed, followed by aggregation/assembly of the building blocks. After some time (from minutes to days depending on the nature of the pre-acid) the solution becomes acidic, provoking disassembly. The lifetime of the aggregate depends on the hydrolyzed molecule that was injected and its concentration, typically δ -Gluconolactone hydrolyzes in minutes, while methyl formate or β -butyrolactone take hours, and ϵ -caprolactone days.¹¹⁶

Following a similar strategy, of delayed pH changes in solution, the same group used a combination of two enzymes to induce the transient assembly of a pH-sensitive DNA hydrogel. Urease catalyzes the decomposition of urea into carbon dioxide and ammonia, whereas esterase

is used to hydrolyze ethyl acetate into ethanol and acetic acid. The first enzyme is at its highest activity at neutral pH, being poorly active at $\text{pH} < 5$ and > 9 . Since ammonia is released during urea degradation, pH increases as the substrate is converted, making urease autocatalytic if the starting pH is < 6 . The enzymatic reaction also presents negative feedback because the enzyme is inactive in basic conditions. Esterase, however, displays higher activity at $\text{pH} > 6$, so if both enzymes are present in the same solution, while urease activity decreases, esterase increases. The DNA hydrogel is cross-linked at $\text{pH} > 7$ but is a sol at acidic pH. Therefore, if both enzymes, urea, and ethyl acetate are added to a DNA solution, gelation is observed after ~ 5 minutes, due to the pH increase caused by urea degradation. The hydrogel reached its maximum mechanical properties at 20 minutes after the addition of the stimuli and starts decreasing. The mixture becomes a solution again after hundreds of minutes.¹¹⁷

Hermans developed a redox reaction cycle based on the reduction of perylene diimide (PDI) into its radical anion and dianion using sodium dithionite ($\text{Na}_2\text{S}_2\text{O}_4$) and its further oxidation with oxygen in air. PDI forms 10-micron sized aggregates in water that precipitate overnight due to side-to-side fusion of different aggregates. Upon reduction the aggregate size decreases to ~ 100 nm. When dianion is oxidized back to the neutral state, the self-assembly follows a cooperative mechanism. Interestingly, after oxidation the size of the assemblies is smaller than the original ones. If the redox cycle is repeated multiple times, the total scattering of the assembly decreases with each cycle and UV/Vis spectra get more intense, but only when reduction is performed before side-to-side fusion can happen. This indicates that the morphology and conformation of the assemblies change with each reaction cycle. After 7 cycles, done at 20-minute intervals, only a small portion of the aggregates precipitate after ageing, with PDI still present in the supernatant, that stays stable for months. This system shows the combination of dissipative self-assembly with pathway selectivity.¹¹⁸ When both oxygen (by vigorous mixing) and sodium dithionite are added simultaneously and continuously to a PDI solution, damped oscillations are observed. The cooperative mechanism provides positive feedback while the size-dependent kinetics of reduction affords the negative feedback, both necessary for oscillations to happen. It was also possible to perform the spatial control over the supramolecular assemblies in a two-dimensional environment. Pattern

formation occurred by letting the solution oxidize spontaneously and travelling fronts by seeding polymers into a monomeric solution.⁸⁶

Wojciechowski, *et al.*, combined redox and pH stimuli to induce the transient self-assembly of a hydrogel using TCEP (tris(2-carboxyethyl)phosphine), an acidic reducing agent. N,N'-dibenzoyl-L-cystine, disassembled in basic conditions, gets protonated and forms a hydrogel immediately upon addition of TCEP. After minutes to hours, depending on pH and TCEP concentration, the hydrogel is destroyed by the reduction of disulfide to thiol, forming the soluble benzoyl-L-cysteine. The cycle could be repeated by adding more monomeric N,N'-dibenzoyl-L-cystine, as long as active TCEP is still present in solution.¹¹⁹

1.4 Magnetism as a Tool to Control Soft Matterⁱⁱⁱ

1.4.1 Magnetism and Magnetic Energy

Magnetism has been used by humans for thousands of years, with the utilization of earth's magnetic field to direct our movement (like some animals do) by using compasses since the Antiquity, to the most sophisticated use of permanent and electromagnets in (spin) electronics nowadays.¹¹

When discussing magnetic effects on particles^{iv}, distinctions between the types of applied field have to be made.¹²⁰ First we can define an applied field by its variation in time: dynamic magnetic fields (rotating or oscillating), in which their magnitude and/or direction are time dependent; or static fields, where at any given point in space the magnetic field is constant in time. Similarly, when the significant dimension is space: we have homogenous magnetic fields, where the magnetic field is constant along a region in space; or inhomogeneous (field gradients), where the magnetic field varies along space.^{11,120} We will focus on magnetic fields that are static in time and either homogeneous or inhomogeneous in space.

The analysis of the effect of a field on a particle will depend on the magnetic field (spatially homogeneous or not) and on the magnetism of the particle. For constant fields, no linear

ⁱⁱⁱ This section will be published as a review: Schicho, M.†, Formon, G.J.M.†, Hermans, T.M. Soft-Matter Control Using Weak Magnetic Fields (working title). *Manuscript in preparation.*

^{iv} Here particles can range from a single ion to a micro or nanoparticle

movement would be expected, and the effect can be quantified by the magnetic energy, E_{mag} , acting on the particle:^{11,120,121}

$$E_{mag} = -\frac{1}{2} m B$$

Where m is the magnetic dipole moment of the particle, that quantifies how a magnetic field will act on this particle. B is the primary magnetic field also called magnetic flux density or B-field. The magnetic moment is the magnetization of the particle M multiplied by its volume V . Magnetization can also be thought as the average density of the magnetic moment.

$$m = M \cdot V$$

In ferromagnets, the magnetization is constant within a domain and is called spontaneous magnetization, M_s . In paramagnetic and diamagnetic materials (see below), the magnetization is induced linearly by the magnetic field strength H , also called magnetizing force, and their ratio is the volumetric susceptibility χ of the material.

$$M = \chi \cdot H$$

The magnetic flux density B (or B-field) and magnetic field strength H (H-field) are related by the following equation:

$$B = \mu_0 (M + H) = \mu_0 H (1 + \chi)$$

Where μ_0 is the vacuum permeability that is equal to $4\pi \times 10^{-7} \text{ H/m}$.

If the susceptibility $|\chi| \ll 1$, which is true for paramagnetic and diamagnetic materials (see below), this term can be simplified to:

$$B = \mu_0 H$$

Another important parameter that influences how a magnetic field will act on a particle is the magnetism type of the respective material. There are four classes of magnetism that are of importance to this thesis:

- Diamagnetism: the magnetic susceptibility χ is negative ($\chi < 0$) and typically small, so the material is weakly repelled by a magnetic field.
- Paramagnetism: the magnetic susceptibility χ of paramagnetic materials is positive ($\chi > 0$), meaning the material is attracted to a magnetic field.
- Ferromagnetism: the magnetization of ferromagnetic materials is non-linear. They usually exhibit the strongest response to magnetic fields.

- Superparamagnetism: small domain ferromagnets (nanoparticle size range) so the magnetization of a domain can be influenced thermally. Thermal fluctuations average the magnetization to zero, which makes them behave similarly to paramagnets on a macroscopic level.^{11,120,122}

To quantify the effect of the magnetic field on a given particle, we first need to identify if the acting magnetic field is homogeneous or not. If it is, particles can be aligned or deformed, depending on its chemical and magnetic nature. However, if the field is inhomogeneous, the gradient (∇B) gives rise to magnetic forces (F_{mag} , see below for explanation) which can induce motion of material across the space (magnetophoresis).^{120,121}

A single cubic magnet generates an inhomogeneous magnetic field, with higher intensities at its edges, following the field lines (Figure 1.17 A, B, C). Homogeneous magnetic fields in non-negligible regions of the space can easily be generated with electromagnets and specific magnetic arrays (Figure 1.17 J, K, L), with magnetic flux densities up to 1-2 T in widely available laboratory conditions.¹¹ However, different magnet arrays can be arranged to tailor the magnetic field to the experimental needs: pseudo homogeneous field, with low gradient (Figure 1.17 D, E, F); high magnetic gradient (Figure 1.17 G, H, I); constant magnetic gradient.

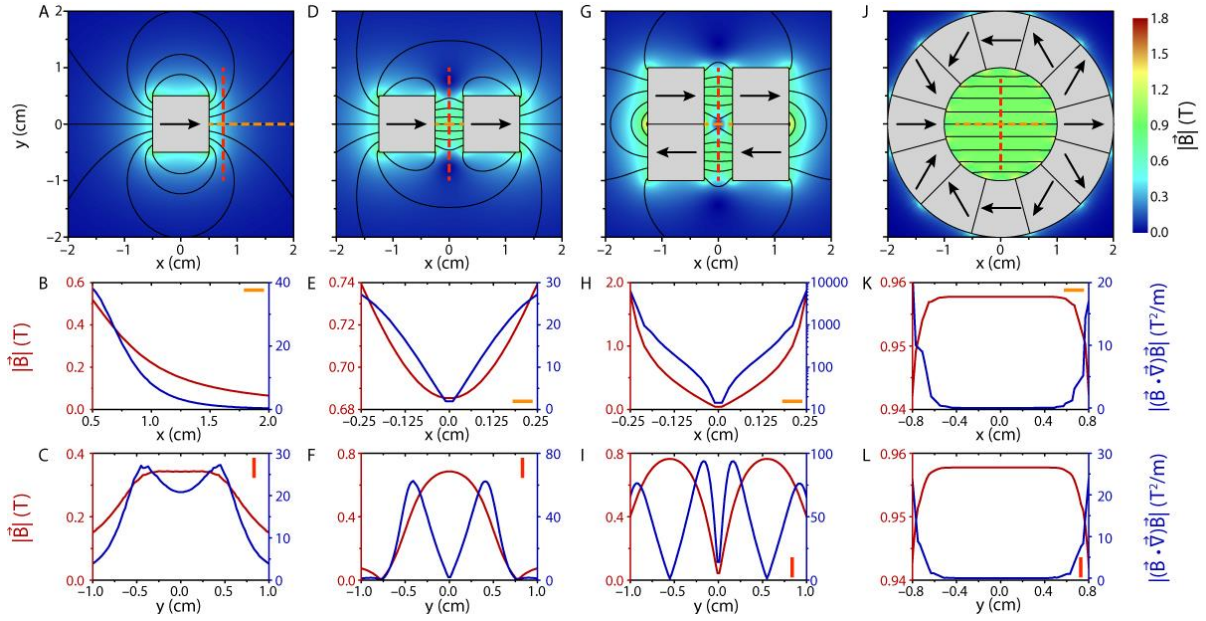


Figure 1.17 – 2D simulations of the magnetic flux density generated by different arrays of magnets. First row: heat map of the norm of the magnetic flux density; black lines represent the magnetic field lines; black arrows show the north-south orientation of the magnet; grey areas are the magnets themselves. Second and third rows: Norm of the magnetic flux density ($|\vec{B}|$, left axis of the graphs) and norm of \vec{B} multiplied by its gradient ($|(\vec{B} \cdot \nabla)\vec{B}|$, right axis of the graphs) along the horizontal (yellow) and vertical (red) dashed lines respectively. Both $|\vec{B}|$ and $|(\vec{B} \cdot \nabla)\vec{B}|$ are extracted along the same lines. – **A, B, C** – Single 1 cm x 1 cm N52 Nd₂Fe₁₄B magnet – **D, E, F** – Two 1 cm x 1 cm N52 Nd₂Fe₁₄B magnets arranged in the same direction, separated by 0.5 cm – **G, H, I** – Four 1 cm x 1 cm N52 Nd₂Fe₁₄B magnets in a quadrupole array.¹²³ This arrangement induces high magnetic field gradients. – **J, K, L** – Magnets arranged in a Halbach array with homogeneous and strong magnetic field inside and very low outside.¹¹

By combining all previous equations, the magnetic energy for paramagnetic and diamagnetic materials is as follows:

$$E_{mag} = -\frac{1}{2\mu_0} \chi V B^2$$

The magnetic energy increases quadratically with the magnetic field, making it an important parameter to manipulate particles, however magnetic fields above 2 T are difficult to obtain without resorting to expensive superconducting magnets, decreasing the ability to control particles in the nanometer range or smaller in common laboratory settings ($B \leq 2 T$).

If working in a gradient field, the field inhomogeneity gives rise to the magnetic force F_{mag} , defined as follows:

$$\vec{F}_{mag} = -\nabla E_{mag} = \frac{1}{2} \vec{m} \nabla \vec{B} = \frac{1}{2} \vec{M} V \nabla \vec{B}$$

Which is reduced, for paramagnetic and diamagnetic materials, to:

$$\vec{F}_{mag} = \frac{1}{2 \mu_0} \chi V (\vec{B} \cdot \vec{\nabla}) \vec{B}$$

As opposed to the magnetic energy in homogeneous fields, the magnetic force scales linearly with the magnetic field and the gradient of the magnetic field. High field gradients, of up to 10^3 T/m, can be achieved in common laboratory conditions which makes it easier to manipulate small particles in non-homogeneous magnetic fields than in homogeneous fields.¹²⁴

The magnetic manipulation of particles in fluid media is subjected to the competing forces and energies. The most important being the thermal fluctuation energy, E_{therm} , which for a single particle is defined by:¹²⁵

$$E_{therm} = -\frac{3}{2} k_B T$$

Where k_B is the Boltzmann constant and T the absolute temperature. At 25 °C, this energy is 6.2×10^{-21} J. This value is negligible for the macroscopic world, but it becomes increasingly significant in the (sub)micron range. This energy refers to Brownian motion, which is the random movement of small objects when surrounded by a fluid.

When there is no driving force for the directional movement of molecules or particles (e.g. concentration gradient), the movement is driven by a random thermal force, F_{therm} . The thermal force is not precisely defined; however, it is characterized as a random process moving the particle in all directions of space, meaning that the net force is zero. The characteristic value of this force for a spherical particle is:¹²⁵⁻¹²⁸

$$F_{therm} = \sqrt{2 k_B T (6 \pi \mu R)} \eta(t)$$

Where μ is the dynamic viscosity of the surrounding fluid and $\eta(t)$ is a gaussian ‘white noise’ operator (varying from -1 to 1), that imparts the randomness to the force (units of $time^{-1/2}$).

To quantify and compare the effect of a homogeneous magnetic field on an entity, we propose define a unitless figure of merit β_E that compares the magnetic energy E_{mag} with the thermal fluctuations E_{therm} :

$$\beta_E = \frac{E_{mag}}{E_{therm}} = \frac{-\frac{1}{2} m B}{-\frac{3}{2} k_B T}$$

Similarly, when applying an inhomogeneous magnetic field, the figure of merit β_F would be the ratio of the magnetic force F_{mag} over the random thermal forces F_{therm} (maxing $\eta(t) = 1 \text{ s}^{-1/2}$):

$$\beta_F = \frac{F_{mag}}{F_{therm}} = \frac{\frac{1}{2} m \nabla B}{\sqrt{2 k_B T (6 \pi \mu R)}}$$

As an example, let's take a single Ho^{3+} ion ($\chi_{mol} = 5.702 \cdot 10^{-7} \text{ m}^3/\text{mol}$; $R = 0.901 \text{ \AA}$)^{129,130} in an aqueous solution, at room temperature ($25 \text{ }^\circ\text{C} = 298 \text{ K}$), and in a 1 T homogeneous magnetic field (Figure 1.17 J, K, L). The thermal and magnetic energies are:

$$E_{therm} = -\frac{3}{2} \cdot 1.38 \cdot 10^{-23} \frac{\text{J}}{\text{K}} \cdot 298 \text{ K} = -6.16 \cdot 10^{-21} \text{ J}$$

$$E_{mag}(\text{Ho}^{3+}) = -\frac{1}{2 \mu_0} \chi V B^2 = -\frac{1}{2 \mu_0} \chi_{mol} n B^2$$

Where χ_{mol} is the molar magnetic susceptibility and n is the number of moles of the entity, in this case, for a single ion in solution: $n = \text{number of ions}/\text{Avogadro's number} = 1/(6.022 \cdot 10^{23} \text{ mol}^{-1})$.

$$\begin{aligned} E_{mag}(\text{Ho}^{3+}) &= -\frac{1}{2 \cdot 4\pi \cdot 10^{-7} \frac{\text{N}}{\text{A}^2}} 5.702 \cdot 10^{-7} \frac{\text{m}^3}{\text{mol}} \cdot \frac{1}{6.022 \cdot 10^{23} \text{ mol}^{-1}} \cdot (1 \text{ T})^2 \\ &= -3.76 \cdot 10^{-25} \text{ J} \end{aligned}$$

The ratio of the energies is:

$$\beta_E(\text{Ho}^{3+}) = \frac{-3.76 \cdot 10^{-25} \text{ J}}{-6.16 \cdot 10^{-21} \text{ J}} = 6.15 \cdot 10^{-5}$$

The thermal energy is four to five orders of magnitudes higher than the magnetic counterpart, trumping any possible effect the magnetic field would have on the ion. On the other hand, if we take a single iron oxide nanoparticle (IO-NP, $M_{sat} = 3.96 \cdot 10^5 \text{ A/m}$ and $D = 37.6 \text{ nm}$)¹²⁴ in the same 1 T field, would have an upper bound of (considering $M = M_{sat}$):

$$\begin{aligned} E_{mag}(\text{IO} - \text{NP}) &= -\frac{1}{2} M_{sat} V B = -\frac{1}{2} \cdot 3.96 \cdot 10^5 \frac{\text{A}}{\text{m}} \cdot \frac{4}{3} \pi \cdot (18.8 \cdot 10^{-9} \text{ m})^3 \cdot (1 \text{ T}) \\ &= -5.51 \cdot 10^{-18} \text{ J} \end{aligned}$$

$$\beta_E(\text{IO} - \text{NP}) = \frac{-5.51 \cdot 10^{-18} \text{ J}}{-6.16 \cdot 10^{-21} \text{ J}} = 895$$

The magnetic energy on that nanoparticle is almost three orders of magnitude higher than thermal fluctuations and 10^7 bigger than the energy of the same magnetic field on a single Ho^{3+} ion. This difference arises from the larger size of the nanoparticle, and its magnetic nature (ferromagnetic vs. paramagnetic), having a high saturation magnetization. For $\beta_E(\text{IO} - \text{NP}) \gg 1$ we would expect to observe magnetic field effects.

We can also compare the magnetic forces and thermal forces, in a inhomogeneous magnetic field, with $B = 1 \text{ T}$ and $\nabla B = 2000 \text{ T/m}$ (Figure 1.17 G, H, I) for one Ho^{3+} ion in water ($\mu = 8.91 \cdot 10^{-4} \text{ Pa} \cdot \text{s}$):¹³¹

$$\begin{aligned}
 F_{mag}(\text{Ho}^{3+}) &= \frac{1}{2 \mu_0} \chi_{mol} n (B \cdot \nabla) B \\
 &= \frac{1}{2 \cdot 4\pi \cdot 10^{-7} \frac{\text{N}}{\text{A}^2}} 5.702 \cdot 10^{-7} \frac{\text{m}^3}{\text{mol}} \cdot \frac{1}{6.022 \cdot 10^{23} \text{ mol}^{-1}} \cdot 1 \text{ T} \cdot 2000 \frac{\text{T}}{\text{m}} \\
 &= 7.53 \cdot 10^{-22} \text{ N} \\
 F_{therm}(\text{Ho}^{3+}) &= \sqrt{2 \cdot 1.38 \cdot 10^{-23} \frac{\text{J}}{\text{K}} \cdot 298 \text{ K} \cdot (6 \pi \cdot 8.91 \cdot 10^{-4} \text{ Pa} \cdot \text{s} \cdot 0.901 \cdot 10^{-10} \text{ m}) \cdot 1} \\
 &= 1.12 \cdot 10^{-16} \text{ N} \\
 \beta_E(\text{Ho}^{3+}) &= \frac{7.53 \cdot 10^{-22} \text{ N}}{1.12 \cdot 10^{-16} \text{ N}} = 6.75 \cdot 10^{-6}
 \end{aligned}$$

The magnetic force acting on the single Ho^{3+} ion is six orders of magnitude smaller than the thermal forces. Meaning that the magnetic field effects would be insignificant when compared to thermal noise, thus making any effect not observable.

If we do the same analysis on the IO-NP:

$$\begin{aligned}
 F_{mag}(\text{IO} - \text{NP}) &= \frac{1}{2} M_{sat} V \nabla B = \frac{1}{2} \cdot 3.96 \cdot 10^5 \frac{\text{A}}{\text{m}} \cdot \frac{4}{3} \pi \cdot (18.8 \cdot 10^{-9} \text{ m})^3 \cdot 2000 \frac{\text{T}}{\text{m}} \\
 &= 1.10 \cdot 10^{-14} \text{ N} \\
 F_{therm} &= \sqrt{2 \cdot 1.38 \cdot 10^{-23} \frac{\text{J}}{\text{K}} \cdot 298 \text{ K} \cdot (6 \pi \cdot 8.91 \cdot 10^{-4} \text{ Pa} \cdot \text{s} \cdot 18.8 \cdot 10^{-9} \text{ m}) \cdot 1} \\
 &= 1.61 \cdot 10^{-15} \text{ N} \\
 \beta_E(\text{Ho}^{3+}) &= \frac{1.10 \cdot 10^{-14} \text{ N}}{1.61 \cdot 10^{-15} \text{ N}} = 6.83
 \end{aligned}$$

Contrarily from the single Ho^{3+} ion in solution, the magnetic force acting on the IO-NP is ~ 7 higher than the thermal fluctuation, meaning that the nanoparticle would be attracted to the regions of higher magnetic field in the space.

This shows that magnetic field effects on small entities (nanoparticles, molecules, and ions) are dependent on the nature of the object (para, dia, or ferromagnetic) and are subjected to other competing phenomena. The smaller the particle the more important thermal fluctuation becomes, thus needing a much stronger magnetic field to observe any effect.

1.4.2 Magnetism to Control Soft-Matter (Trivial Observations)

Magnetism has been used as tool to control soft materials for decades, but as discussed above it gets increasingly difficult to control small particles. In this sub-section some examples will be laid out that use high magnetic fields (> 2 T) to control molecular assemblies, or lower magnetic field to control larger nanoparticles.

Shklyarevskiy, *et al.* showed the self-assembly of a bolaamphiphile sexithiophene, functionalized with poly-ethylene glycol side arms, into 50 to 120 nm sized spherical nano-capsules in water and alcoholic solvents below 60 °C. Because of the six thiophene moieties, the molecule possesses large anisotropic diamagnetic susceptibility, but the self-assembled nano-spheres are isotropic. When a magnetic field (up to 20 T) is applied to a sample containing the nano-capsules, it will affect differently the molecules that are perpendicular and the ones parallel to the field, thus deforming the spheres, Figure 1.18. This deformation can be observed by the magnetic dependent optical birefringence. As soon as the magnetic field is turned off, the capsules return to their spherical conformation unless a gelling agent is used to trap the nan-capsules in their deformed state.¹³²

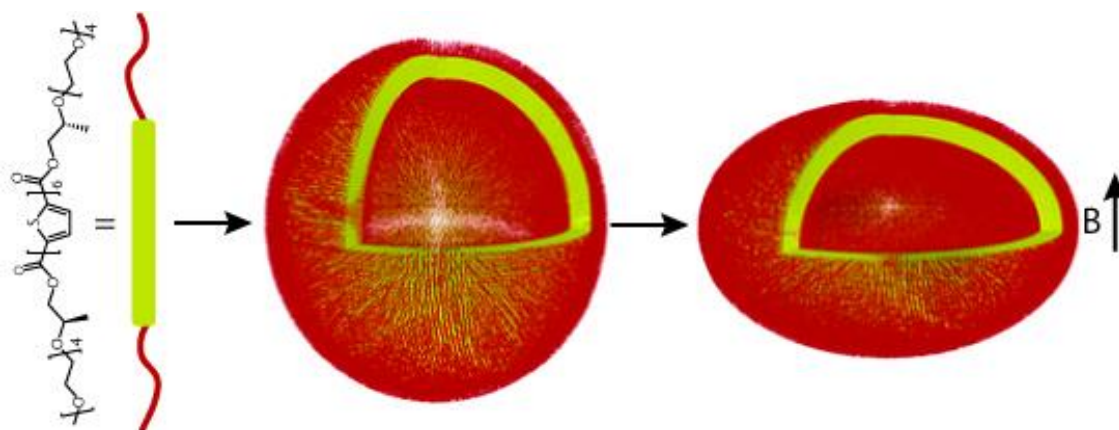


Figure 1.18 – Scheme depicting the self-assembly of the sexithiophene into nano-capsule and its subsequent deformation perpendicular to the magnetic field. Adapted from ref. 132.

Similarly, magnetic fields have been used multiple times to align diamagnetic supramolecular or polymeric assemblies in high fields ($B \geq 8$ T). Diamagnetic orientation was obtained using either polymer fibers or supramolecular assemblies, thus increasing the magnetic energy acting on those entities due to the large number of repeating units. The use of aromatic substances is also explored because, even if diamagnetic, they have more significant magnetic susceptibility than typical non-aromatic compounds, also increasing the magnetic energy (see above).^{133–137}

Vesicles of phospholipids doped with lanthanide-chelated DTPA (diethylenetriaminepentaacetic acid) could be distorted unidirectionally with magnetic fields up to 8 T. Those deformations could be observed with 2-dimensional small angle neutron scattering (2-D SANS), Figure 1.19, and Cryo-TEM. The direction of deformation depended on the lanthanide: Thulium (Tm) induced distortion parallel to the field while Dysprosium (Dy) perpendicular. This can be explained by the magnetic anisotropy ($\Delta\chi$) of the paramagnetic lanthanides. Ions like Dy^{3+} possess large but negative $\Delta\chi$, so they align preferentially perpendicular to the magnetic field. On the other hand, Tm^{3+} has positive magnetic anisotropy, so they align in a direction parallel with the field.¹³⁸ This anisotropy arises when the ion is chelated, and strongly depends on the coordination environment.¹³⁹

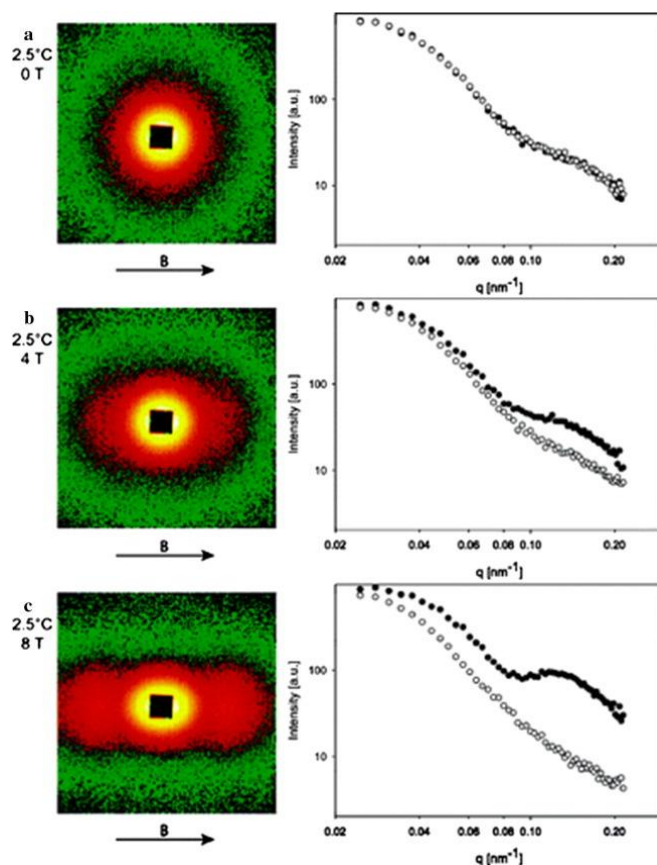


Figure 1.19 – 2D SANS patterns (left) and sectoral intensity (right) for phospholipid vesicles doped with Thulium at 2.5 °C as a function of magnetic field. The neutron scattering pattern becomes more anisotropic with higher magnetic field. Open circles represent the vertical intensity average while solid circles show the horizontal. Taken from ref. 138.

Many surfactants containing magnetic elements have been developed over the last 30 years, but they have not been utilized for their magnetic properties. However, since ~ 10 years magneto-responsive surfactants have gained increasing interest.^{140,141}

Brown, *et al.*, developed cationic surfactants with paramagnetic counter anions, using Fe(III), Ho(III) and other lanthanides. These components are surface active, lowering surface tension when dissolved in water, as expected. Interestingly, when a droplet containing 20 %wt of surfactant was placed near a magnet, it was attracted to the magnet, Figure 1.20.^{142,143} Similarly, those magnetic ionic surfactants were used to create magneto-responsive emulsions of oil (dodecane) in water that could be pulled against gravity and viscosity of the surrounding fluid with a small magnet.^{142,144}

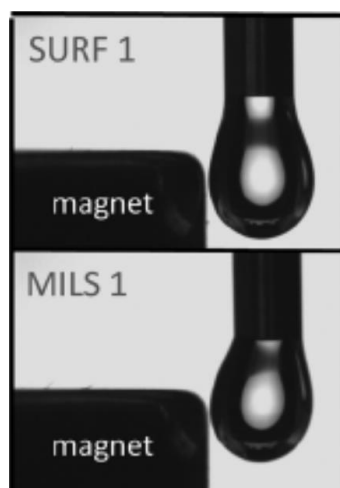


Figure 1.20 – Response of surfactant-containing droplets to a magnet. Top: cationic surfactant with Cl^- counter anion, it is not affected by magnet. Bottom: cationic surfactant with FeCl_4^- counter anion, the droplet is attracted to the magnet. Taken from ref. 142.

The ionic surfactants described above were also used for the magnetization of biological macromolecules. The surfactants adsorb to the macromolecules, and because of their magnetic properties they can be separated using a $\text{Nd}_2\text{Fe}_{14}\text{B}$ magnet (fields of 0.2-0.3 T). This technique could be extended to model proteins such as myoglobin and green fluorescent protein (GFP).¹⁴⁵

Nanoparticles are also a good scaffold for magneto-responsive materials, because they usually show superparamagnetic or ferromagnetic behavior, so they show higher induced magnetic moment than molecular assemblies, which makes the magnetic manipulation easier.

Lim, *et al.* showed the magnetophoretic effect of single iron oxide nanoparticles of ~ 35 nm of core diameter, decorated with polymers and gold nanoparticles (for plasmonic properties) resulting in 62 nm of total diameter. Magnetic field gradients of up to 3000 T/m were obtained by attaching a mu-metal (material with very high permeabilities, used for magnetic shielding¹¹) tip at the end of a solenoid. Near the mu-metal two different zones of action could be identified: one where particles migrate towards the metal, a ‘radius of capture’ of 139 μm from the tip could be recognized; another, further from the tip, where the particles were not affected. A magnetophoretic force (similar to F_{mag} discussed above) acting on the nanoparticles of as low as 1.5 fN could be detected leading to particle velocities of up to 30 $\mu\text{m}/\text{s}$. This simple technique, using high magnetic field gradient, permitted the unprecedented observation of magnetic field induced migration of nanoparticles, overcoming Brownian motion, viscous drag, and counter diffusion.¹²⁴

Klajn and co-workers showed the magnetic field induced assembly of superparamagnetic 13.4 nm-sized magnetite nanocubes into helical structures. A hexane solution of cubic iron oxide nanoparticles is placed at diethylene glycol/air interface in the presence of an external magnetic field of 0.07 T. The nanocubes partially aligned with the field forming 1D chains that further aggregate into higher order structures with slow hexane evaporation. The final shape of the structures is strongly dependent on the monolayer (surface) concentration of the nanocubes. Below 20% monolayer coverage, no superstructures were observed, while at 20%, two to three nanoparticles wide and more than 100 μm long nanobelts were formed. If the angle of the magnetic field is changed with regards to the plane of the liquid-air interface, the orientation of the nanobelts can be modulated. At higher surface concentrations, the nanocubes tend to align their [1,1,1] axes with the magnetic field (preferred magnetic orientation), thus making the nanobelts fold onto themselves forming single stranded helical structures, that fused into double and triple stranded, Figure 1.21. With increasing concentration, more helices with same chirality were observed side by side, indicating that the helicity of an assembly can be transferred to the next one. Shape anisotropy of the nanoparticles favors face-to-face van der Waals interactions, while magneto-crystalline anisotropy favors corner-to-corner. This work shows the interplay of various nanoscale forces, among them magnetic dipole-dipole interactions.¹⁴⁶

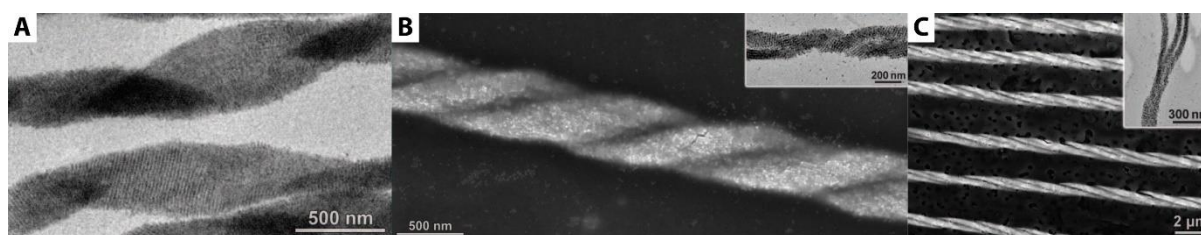


Figure 1.21 – Examples of helical structures obtained through the magnetic field induced self-assembly of magnetite nanocubes. **A** – Single stranded helix. **B** – Double stranded helix. Insert: merging of two chains forming a helix. **C** – Triple stranded helix. Insert: end of the triple helix. Adapted from ref. 146.

Mehdizadeh Taheri, *et al.*, showed the magnetic field induced assembly of sub 15 nm cube-shaped iron-oxide particles in toluene. The nanocube particles showed regular 1-D, 2-D and 3-D assemblies forming chains, ribbons, sheets, large cuboids, Figure 1.22. However, assembly could not be induced with nanocubes smaller than 7.5 nm, indicating the existence of a size limit where magnetic interactions become too small compared to thermal noise (see

sub-section 1.4.1). Spherical nanoparticles also did not produce larger assemblies, showing that the structure of the nanoparticle becomes very significant at this scale. It is estimated that the magnetic energy of the nanoparticles at 0.3 T is $E_{mag} \sim 0.9 k_B T$ being in the same order of magnitude as the van der Waals interactions, $\sim 0.5 k_B T$, and thermal noise, $\sim 1.5 k_B T$. This shows that magnetic fields < 1 T are sufficient to align the nanocubes, that ‘attach’ themselves through van der Waals interactions, forming 1-D chains. The chains will then merge with other chains forming 2-D and 3-D assemblies. Cubes have a larger surface area than spheres, thus having larger surface for van der Waals interactions, explaining why no assemblies were formed with spherical nanoparticles.¹⁴⁷

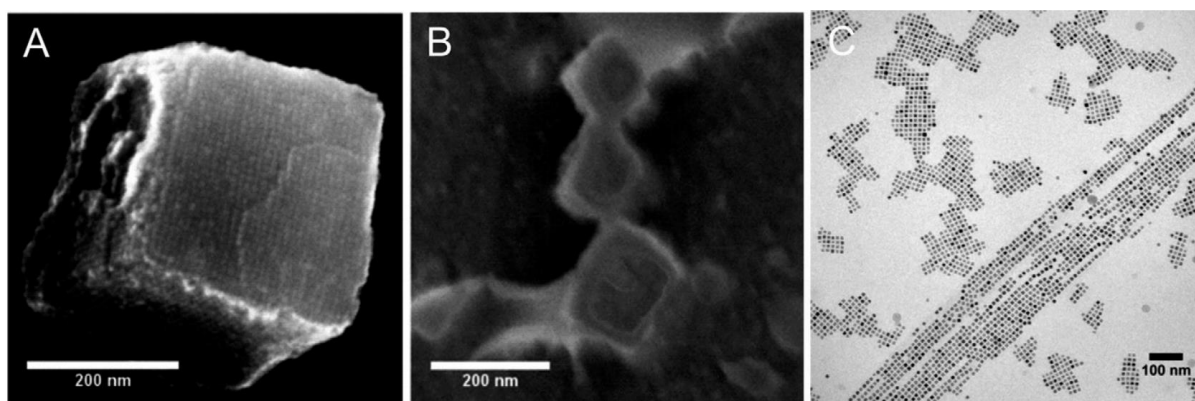


Figure 1.22 – Electron microscopy of the magnetic field induced hierarchical self-assembly of magnetite cubic nanoparticles. **A** – 3D cuboid containing ~ 10000 nanocubes. **B** – Cryogenic electron microscopy of the nanoparticle solution in toluene. **C** – Example of 1 and 2-D nanocube assembly into chains, ribbons and sheets. Adapted from ref. 147.

Metallic nanoparticles coated with polystyrene end-capped with complementary triple hydrogen bonding thymine and diaminopyridine, self-assemble into crystal-like aggregates, Figure 1.23–A. The non-covalent interactions (hydrogen bonding) between the nanoparticles make the assemblies thermally responsive, melting at high temperatures. 16 nm iron oxide NPs with 13kDa polymer coating and 15 nm Gold NPs with 14 kDa coatings, present similar melting profiles, Figure 1.23–B. However, when the polymer brush size is decreased to 8 kDa and 9 kDa, for iron oxide and gold NPs respectively, the melting temperature of the former is 10 °C higher, Figure 1.23–C. With smaller polymer chains, the iron oxide NPs are closer to one another, allowing dipole-dipole interactions between the colloids. Those interactions can be estimated by Keesom forces that scales with $1/r^6$ (r being the inter-particle distance). For 13

kDa polymer coating (38.5 nm interparticle distance) this interaction is expected to be $\sim 1.1 k_B T$ while for 8kDa (29.6nm interparticular distance) it is estimated to be $\sim 5.2 k_B T$. This example shows how magnetic interactions (here dipole-dipole) can influence supramolecular forces, in this case strengthening them.¹⁴⁸

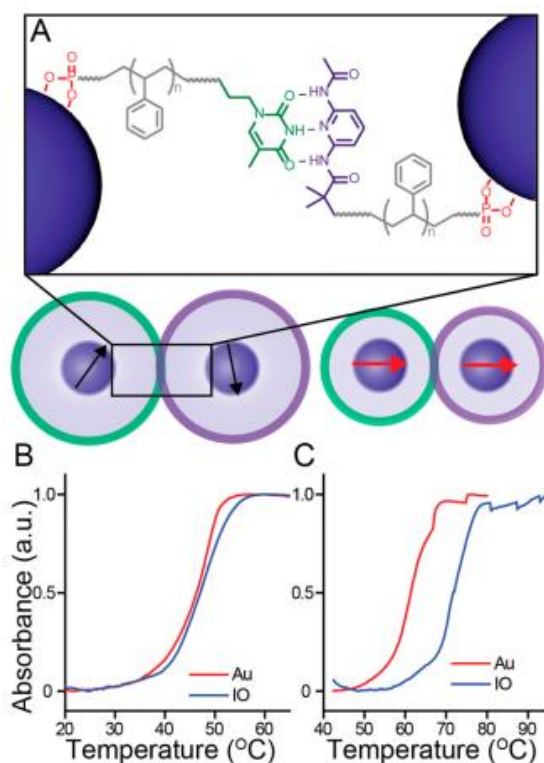


Figure 1.23 – A – Schematics of the polymer coatings of the nanoparticles and the complementary hydrogen bonding groups. B – Melting curves of the nanoparticle assembly with 13 and 14 kDa coatings for iron oxide and gold, respectively. C – Melting curves of the nanoparticle assembly with 8 and 9 kDa for iron oxide and gold, respectively. The melting curve for iron oxide is 10 °C higher than gold. Taken from ref. 148.

Magnetic interactions have also been extensively used in living systems with the final goal of manipulating biological media with magnets.

Superparamagnetic magnetite nanoparticles functionalized with signaling proteins Ran/RCC1, that regulate microtubule assembly during mitosis, were used to gain the spatiotemporal control on microtubule self-assembly. When the Ran modified nanoparticle was present in sufficient concentration, microtubule formation was triggered. So, by applying a magnetic field, next to a droplet containing the nanoparticles and tubulin, the former accumulated near the magnet locally increasing the Ran concentration. When local concentration becomes superior to the threshold, microtubule nucleation was induced locally, Figure 1.24.¹⁴⁹

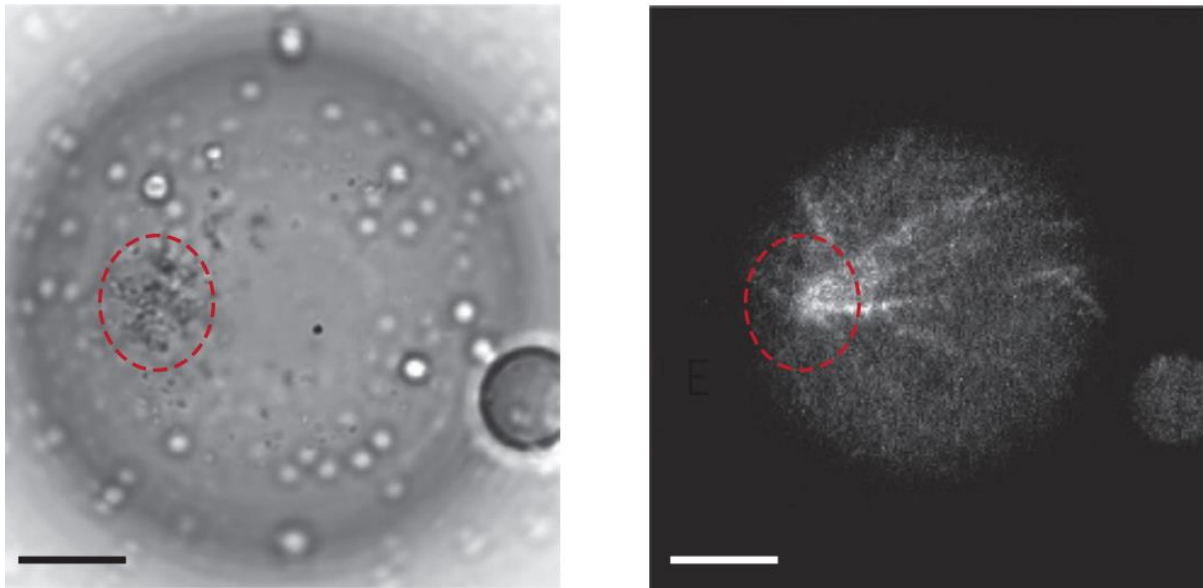


Figure 1.24 – Nanoparticle accumulation close to the magnet (left). Locally induced microtubule nucleation (right). Scale bar is 10 μm . Taken from ref. 149.

Bianxiao Cui and collaborators developed a method of engineering mammalian cells to produce ferritin containing crystals ($> 10^7$ subunits of ferritin per crystal) by co-crystallization with inka protein, needed for decent crystal growth. Crystals of $\sim 45 \mu\text{m}$ could be grown inside the cells in 72 h. Those can be controlled magnetically, with magnetic forces $> 9 \times$ higher than on single Ferritin protein because tens of thousands iron atoms are present in the crystal. This work is a step towards *in vivo* generation of magnetic entities, making possible to manipulate biological media magnetically without injecting foreign agents.¹⁵⁰

1.4.3 Non-Trivial Observations of Magnetic Effects on Soft Materials

In the last years, some unexpected and non-trivial observations involving magnetism have been reported, a few examples will be listed below. They are non-trivial in the sense that current theoretical models could not explain such behavior and/or further study is needed to comprehend these phenomena.

Starting from a homogeneous solution of paramagnetic Mn^{2+} or Dy^{3+} , Eckert and collaborators showed the magnetic field induced concentrations enrichment of those ions close to a permanent magnet. A concentration gradient was observable after ten minutes of the positioning of the magnet at the top of the recipient. Enrichments of up to 2 % and 0.6 %, for

Mn^{2+} and Dy^{3+} respectively, were obtained. Interestingly, as soon as the magnet was removed, the gradient broke down, inducing a convection flow driven by the concentration gradient.^{151,152}

Similarly, Fransaer and co-workers observed the magneto-migration of paramagnetic Gd^{3+} and Dy^{3+} ions in aqueous mixtures towards the region of the sample where the magnetic field is the strongest. Interestingly, diamagnetic Y^{3+} moves in opposite direction, with enrichment further from the magnet. The final enrichment depended on the experimental time and magnetic field intensity, with increase in concentration of 2 % for Dy^{3+} at 0.5 T for 6 h and 5 % for the same ion and time at 5 T. For Y^{3+} a decrease of 0.6 % in concentration took longer than 24 h to be observed. An important experimental difference between this example and the previous is that here the authors wanted to limit convection, so the magneto-migration experiments were performed in a gel (6 %wt gelatin) or inside porous glass disks.¹⁵³

Fujiwara, *et al.* showed the movement of paramagnetic ions inside an inhomogeneous field on a silica gel support saturated with water. Transition metal ions (Ag^+ , Cr^{3+} , Mn^{2+} , Co^{2+} , Ni^{2+} , and Cu^{2+}) were spotted on a silica gel and exposed to a magnetic field gradient of $\sim 400 \text{ T}^2/\text{m}$ ($(\mathbf{B} \cdot \nabla)\mathbf{B}$, see Sub-Section 1.4.1) and magnetic field between 4 and 8 T, supplied by a superconducting magnet. The diamagnetic silver ion does not move while the paramagnetic ones are drawn towards the region with maximum field, Figure 1.25. The distance travelled by each ion depends on: their susceptibility, ions with higher χ travelled the farther; the concentration, with higher values moving more; and the size of silica gel particles, with larger particles inducing a greater distance travelled. If a diamagnetic (Ag^+) and paramagnetic (Cu^{2+}) species are co-spotted in the silica gel only the copper ion moves towards the high-field region, allowing the magnetic separation of these two species.¹⁵⁴⁻¹⁵⁶

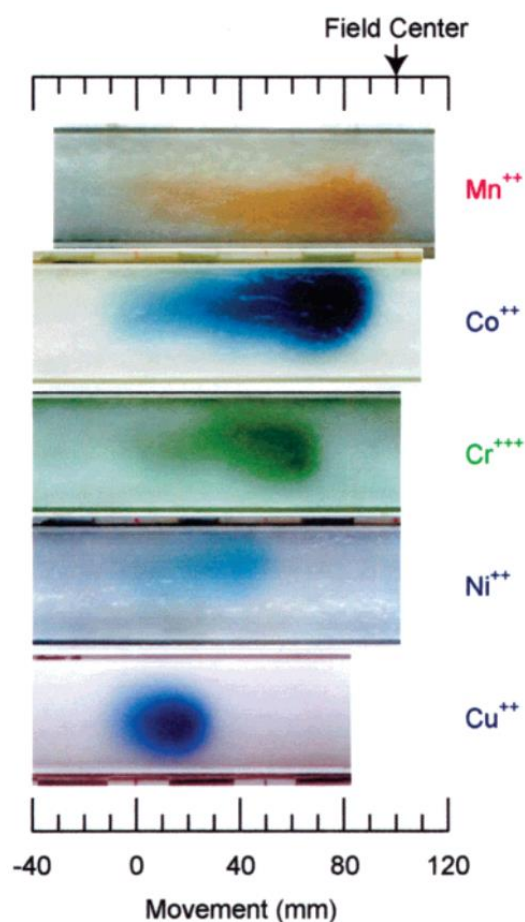


Figure 1.25 – Migration of paramagnetic ions deposited on silica gel. The distance travelled by the ion depends on its magnetic susceptibility. All solutions were spotted at the 0 mm position. Taken from 155.

A 2 mm steel sphere as submerged in a 5 % nitric acid solution and the system was placed between the poles of an electromagnet with a homogeneous magnetic field. Nitric acid oxidizes the iron in the steel into Fe^{2+} that is subsequently oxidized into Fe^{3+} , both ions are paramagnetic. $\text{Fe}(\text{II})$ can be observed by its characteristic blue color while potassium ferricyanide is present in solution to stain $\text{Fe}(\text{III})$ -rich regions in light brown. Interestingly, an anisotropic blue halo is observed around the ball after 100 s, while the rest of the solution becomes brown, Figure 1.26. The region containing high Fe^{2+} concentration delineates the inhomogeneous magnetic field created by the induced magnetization of the steel ball, which was confirmed by theoretical calculations. The size and shape of the pattern stays constant for up to 1000 s, with only the intensity of the colors increasing.¹⁵⁷

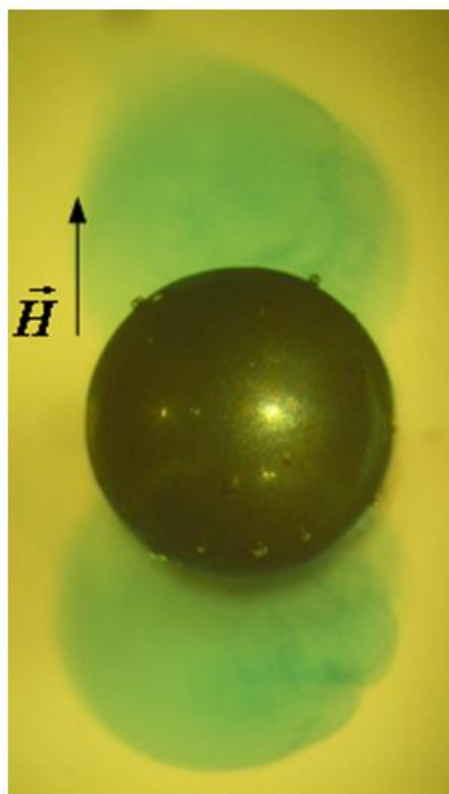


Figure 1.26 – Pattern formation during the etching of a 2 mm steel ball by 5 % HNO₃ solution in a homogeneous magnetic field (~ 0.3.T). Taken from 157.

The four examples above were very surprising, because the magnetic energy and force acting on a single paramagnetic ion is orders of magnitude smaller than the thermal noise ($k_B T$, see discussion in Sub-Section 1.4.1). These findings were not fully comprehended, which led to the speculation that these paramagnetic ions act collectively under a magnetic field, which would explain, at least energetically, these results. Gorobets even coined the term ‘magnions’ (magnetic ions) for such cluster, that would contain thousands of ions moving collectively, thus breaking the thermal barrier.^{158,159} However, no evidence has been found to corroborate this theory and no nanocluster formation was observed in either light scattering¹⁵¹ or small angle neutron scattering^v. Most likely, some ‘hidden’ triggering process are present in those experiments that would facilitate the movement of those entities, such as the pre-existence of a concentration^{160,161} or susceptibility¹⁶² gradient that would induce the magneto-migration of paramagnetic substances. For example, evaporation can locally induce a concentration increase

^v Unpublished results. Small angle neutron scattering experiments performed at CEA Saclay in homogeneous solutions of GdCl₃ and TbCl₃ with and without magnetic field. No structuring was observed.

of a given paramagnetic ion that will be exaggerated by the presence of magnetic field.¹⁶³ This knowledge has been applied recently to selectively crystallize and separate mixtures of rare earth complexes by applying a magnetic field and a temperature induced concentration gradient simultaneously.¹⁶⁴

Schefer *et al.* developed a method to synthesize iron containing iota carrageenan polysaccharides by ion exchange. The single chains of these polymers form random coil and helical structures, observed by AFM. The Fe(III)-containing saccharide form superstructures, by the association of many chains, because Fe³⁺ is trivalent and induces cluster formation with many anionic sites. When placed in a homogeneous 1.1 T magnetic field and dried, the helical portions of the Fe(II) containing polysaccharide exhibit 1.5-fold stiffening and 1.1-fold stretching of the structures. The random coils contain less iron and consequently respond much less to the magnetic field. This work shows that single polymer chains can be manipulated with an easily obtainable magnetic field in laboratory conditions, which is unexpected due to the small size of these entities and their low susceptibility.¹⁶⁵

Yue, *et al.*, synthesized a block copolymer containing polystyrene and poly quaternary ammonium ethylmethacrylate with Fe(III)-tetrabromate as counter-anion. The ratio of the two segments was chosen to facilitate cylindrical microphase separation in the polymeric ionic liquid. Films of the block co-polymer are prepared by coating substrates, that are placed on top of a commercial magnet in a closed container. Without magnet a random microphase segregation with non-orientational domains was obtained. Whereas with magnetic field, the paramagnetic segments align along the magnetic field with perpendicular or parallel nanostructures, and ~ 30 nm periodicity. Orientation can be controlled precisely by adjusting the angle between the magnet and the substrate, Figure 1.27.¹⁶⁶

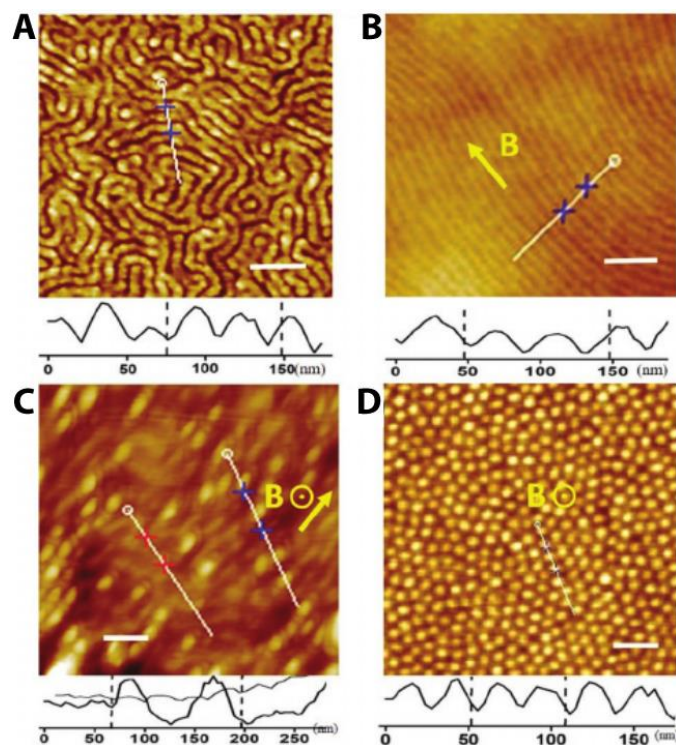


Figure 1.27 – AFM height images of the structure of the block copolymer film. **A** – Phase separation without magnetic field. **B** – Cylindrical structures aligned with magnetic field towards the northwest direction. **C** – Magnetic field 45° out of the plane. **D** – Magnetic field perpendicular to the plane. Taken from 166.

Polarz, *et al.*, showed the surprising hierarchical self-assembly of a Dysprosium-containing surfactant. By heating to 80 °C an aqueous solution containing the amphiphile then cooling down to room temperature leads to the formation of millimeter-sized dumbbell-shaped objects that are optically and structurally anisotropic, Figure 1.28. The assemblies align with magnetic fields and further aggregate into super-structures. When Dysprosium is replaced by the diamagnetic Lutetium and the same procedure was applied, no millimeter-sized objects were observed, only forming micelles. It is then presumed that the magnetic anisotropy of the paramagnetic heads combined with the formation of an anisotropic lamellar lyotropic liquid crystal phase was responsible for the formation of fibers with magnetic structural anisotropy. This would lead to the formation of these distinct hierarchical structures. However, the exact mechanism of formation is still unknown.¹⁶⁷

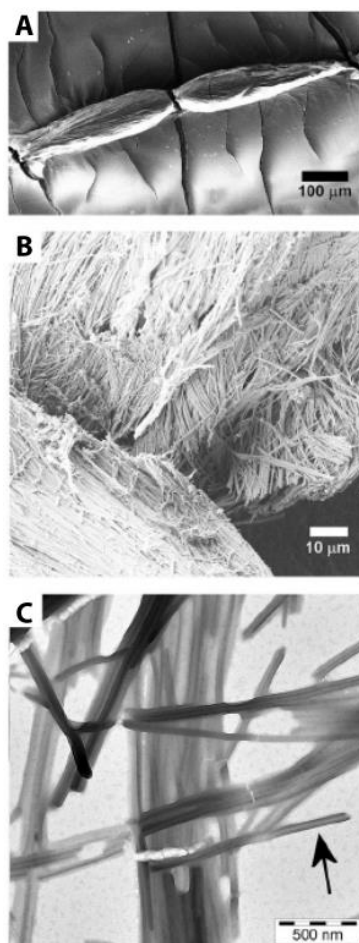


Figure 1.28 – Hierarchical self-assembly of the dumbbell-shaped structures. **A** – SEM of the mm-sized structures. **B** – Zoom-in into the structure above revealing bundles of fibers. **C** – TEM of the individual fibers, building-block of the hierarchical structure. Taken from 167.

First, third and fifth generation Poly(propylene imine) dendrimers, functionalized with Gadolinium chelating end-groups were synthesized as MRI (Magnetic Resonance Imaging) contrast agents. Longitudinal and transversal relaxation times, measured at 1.5 T and 20 °C, strongly increased for higher generation dendrimers, even when expressed per gadolinium ion. This is an effect of high molecular weight, local mobility of Gd complexes, and additional contribution of paramagnetic interactions between gadolinium moieties because of its high local concentration, showing a dendritic effect.¹⁶⁸

Yu, *et al.* recently synthesized an ionic liquid/poly(ionic liquid) system, with a repeating imidazolium moiety and FeCl_4^- as counter-anion. A bi-phenyl group is included in the molecular structure, thus inducing π - π stacking between each molecule/repeating unit. The magnetic behavior of the system without the biphenyl group was paramagnetic. However,

when π - π stacking is incorporated and the iron atoms are closer to each other ($\sim 4 \text{ \AA}$, π - π stacking distance) the system is super-paramagnetic. This is evidenced by temperature dependent magnetization curves and zero field cooled/field cooled experiments. This behavior is explained by the decreased distance between each Fe atom, 4 \AA being in the ferromagnetic interaction distance, inducing spin coupling interactions between the FeCl_4^- counter-anions.¹⁶⁹

These examples above are interesting and unexpected because of the unanticipated interaction between metal centers or energetically unfavorable phenomena. The mechanism of action of some of those findings are still unknown and further study on the magnetic structure-property relationship of (supra)molecular species is still needed.

1.5 Aim and Contents of this Thesis

The control of supramolecular polymerization is a vast subject with still plenty of room for improvement and creative methodologies. New methods for designing experimental procedures and molecules to tune self-assembly have been developed since the inception of supramolecular chemistry. By mimicking living systems, supramolecular chemists have come up with new ideas bringing supramolecular chemistry closer to processes encountered in biological media. The advent of non-equilibrium (and dissipative) supramolecular polymerization, over the last ten years, shifted the focus of chemists towards this area. However, self-assembly at equilibrium is still important for the development of functional materials and as basis for further development of the field.

With this, the aim of this thesis is to find new ways of controlling supramolecular polymers and polymerization in and out of the thermodynamic equilibrium.

In **Chapter 2** the spatiotemporal control over hydrogel formation is achieved by soaking a polymeric material in acid and placing it in a basic solution of a pH-responsive hydrogelator. Proton diffusion, which must be slower than nucleation kinetics, will initiate and direct gel formation.

A non-equilibrium reaction cycle is explored in **Chapter 3** to achieve kinetic and structural control over a hydrogel. Treating a sugar-based aldehyde-containing hydrogel with sodium dithionite, a formaldehyde releasing molecule and a hydrolysable lactone will lead to

its complete dissolution in a few minutes followed by re-formation in less than one hour. The final material properties can be controlled by the amount of catalyst added.

Chapter 4 shows the magnetic control on the self-assembly of a Gadolinium-containing paramagnetic benzene-1,3,5-tricarboxamide, which forms fibers and fiber networks in solution. By applying 1 or 2 T magnetic field, the fiber network becomes denser and more randomly branched, changing its morphology and topology.

Finally, in **Chapter 5** water soluble perylene diimide functionalized with different rare-earth metals were studied to evaluate the effect that paramagnetic lanthanides have on supramolecular self-assembly. The size of the supramolecular aggregates could be controlled by choosing the right rare earth, even if the thermodynamics of supramolecular polymerization is the same for all lanthanides.

Lastly, **Chapter 6** will provide a summary of what has been found during this thesis and outlook for further research on the control of supramolecular self-assembly.

Chapter 2. Surface-Assisted Self-Assembly of a Hydrogel by Proton Diffusion

Abstract: Inspired by the precise spatiotemporal control existing in biological systems, triggering supramolecular growth at solid surfaces has been a challenging goal over the past 10 years. Here we show the pH-dependent self-assembly of a benzene-1,3,5-tricarboxamide peptide conjugate. Stopped-flow CD spectroscopy and mathematical modeling provide a quantitative understanding of the aggregation mechanism. Assembly at a solid-liquid interface was achieved by proton diffusion from a polymeric material. Diffusion needs to be slower than the kinetics of nucleation and elongation so that a structured robust hydrogel layer can grow outward from a solid surface. This method could be easily applied to other pH-responsive gelators and can be used to create precisely structured supramolecular materials.

This chapter has been published in:

Spitzer, D.†; Marichez, V.†; Formon, G. J. M.; Besenius, P.; Hermans, T. M. Surface-Assisted Self-Assembly of a Hydrogel by Proton Diffusion. *Angew. Chemie - Int. Ed.* **2018**, 57 (35), 11349–11353. <https://doi.org/10.1002/anie.201806668>.

† Authors contributed equally

2.1 Introduction

In biological systems, spatiotemporal recognition and organization are of utmost importance for proper function. Multi-cellular organisms are divided into different kinds of cells and tissues that are precisely located to perform a multitude of specific functions. Even cells themselves are sub-divided into different organelles, present in specific positions within the cell. These properties are achieved through signaling, compartmentalization and colocalization, all mediated by chemical reaction networks with the goal of using the available resources as efficiently as possible and to perform the prescribed function in at the specific location.¹⁷⁰⁻¹⁷² During mitosis, for example, centrosomes have to be precisely located in opposite poles in the cell. Microtubules nucleate from centrosomes to pull apart the chromosomes and bring each half to the edges of the cell, thus precisely dividing it into two parts.¹⁷³

With the goal of creating materials that self-assemble at a specific position in time and space, like in biological systems, precise spatiotemporal control over supramolecular polymerization has been an ongoing objective of chemists, as written in Chapter 1. Vigier-Carrière et al. recently reviewed the different strategies to obtain hydrogels from a surface.⁷³ Two general approaches can be identified: First, the (in)direct modification of a surface to modulate its electrochemical composition¹⁷⁴ or hydrophilicity¹⁷⁵, or by direct grafting of monomers,¹⁷⁶ this approach leads to accumulation of monomers in the vicinity of a surface, inducing nucleation; the second strategy consists in the surface catalyzed, or confined, *in-situ* production of monomers, provoking localized gelation. Examples of the latter were discussed in Chapter 1, Sub-Section 1.2.3, such as the modification of a surface with sulfonic acid groups by Van Esch and Eelkema, to catalyze the local formation of an acyl-hydrazone hydrogelator,⁷⁵ or the work by Ulijn, where an enzyme was attached to a surface to locally transform a mixture of amino acids into a gelling agent.⁸⁰

In line with the second method, in this chapter the pH-dependent self-assembly of a benzene-1,3,5-tricarboxamide peptide conjugate will be described. Diffusion of protons from a polymeric material was employed to gain spatiotemporal control over hydrogelation. This

strategy is applicable to other pH-responsive systems and does not require the expensive modification of surfaces with external agents such as catalysts.

2.2 pH-Responsive Self-Assembly

The C_3 -symmetrical benzene-1,3,5-tricarboxamide peptide conjugate (**BTA-1**, Figure 2.1) was synthesized following a modified literature procedure:^{177,178} the peptide sequence was synthesized by solid-phase peptide synthesis and coupled to the benzene core by nucleophilic substitution (see Sub-Section 2.8.2 for details). **BTA-1** has three carboxylic acid moieties per arm, giving a total of nine negative charges when the molecule is deprotonated. In this condition **BTA-1** is molecularly dissolved in water due to electrostatic repulsion, Figure 2.1–B. However, when pH is low enough to protonate the carboxylates, **BTA-1** self-assembles into 1-D fibers of ~ 7 nm average diameter and more than 500 nm length, as evidenced by Cryo-TEM (Figure 2.1–C, and Figure 2.9 in the Appendix). **BTA-1** polymerizes through the π - π stacking of the benzene core and phenylalanine residues, hydrogen bonding of the amide moieties, and solvophobic interactions between hydrophobic amino acids, forming high aspect ratio fibers in water.

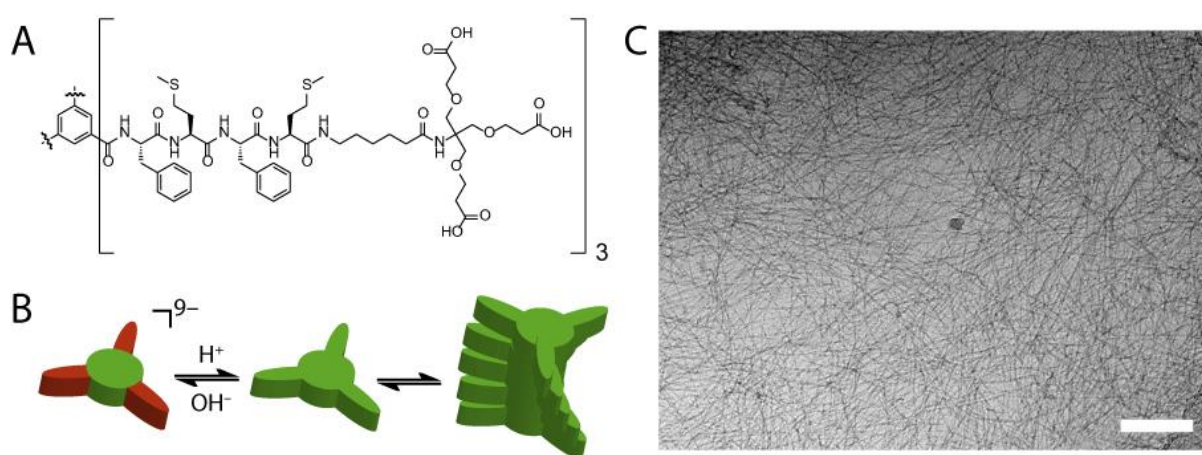


Figure 2.1 – A – pH-responsive C_3 -symmetrical **BTA-1**. B – Representation of the pH-triggered self-assembly of **BTA-1**. C – Cryo-TEM picture of the self-assembled fibers of **BTA-1** at pH 5 in 10 mM TRIS buffer. Scale bar: 200 nm.

To study the influence of pH in the self-assembly of **BTA-1**, CD spectroscopy at different pH was performed, Figure 2.2–A. At pH < 5.5, a strong cotton effect is observed with peaks at

205, 222 and 255 nm, indicating the presence of supramolecular structuring. Upon increasing the pH, the intensity of the peaks decreases, reaching a flat spectrum with no sign of assembly for $\text{pH} > 5.8$, indicating that **BTA-1** is molecularly dissolved. Usually carboxylic acids have a pK_a around 4,¹⁷⁹ which seems to be ~ 5.6 for **BTA-1**, point at which there is a strong shift in CD intensity (Figure 2.2-B). This difference probably arises from the additional driving force provided by the supramolecular self-assembly of protonated **BTA-1**, thus shifting the apparent pK_a . Hence, by correlating CD intensity with the degree of aggregation (α , fraction of molecules in polymeric form), Figure 2.2-B, **BTA-1** is fully deprotonated at $\text{pH} > 6.0$ and completely assembled at $\text{pH} < 5.0$. This is further confirmed by cryo-TEM at different pH, with long fibers at $\text{pH} = 5.0$ and no assembly at $\text{pH} = 7.4$ (Figure 2.9 in the Appendix).

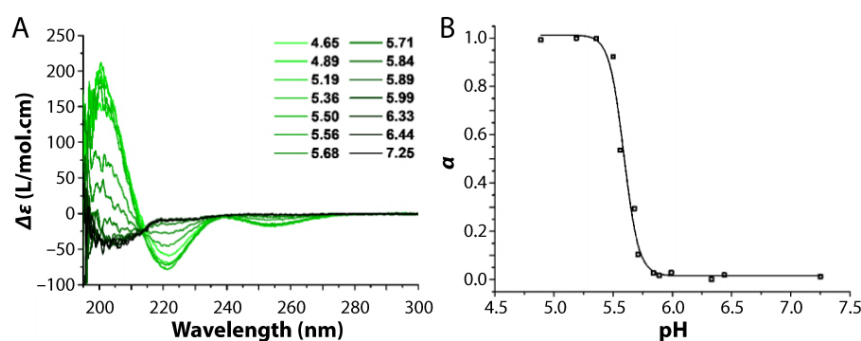


Figure 2.2 – A – CD spectra of **BTA-1** at different pH from 4.65 to 7.25 (Concentration of $60 \mu\text{M}$ in 10 mM phosphate buffer). B – Normalized pH-dependent CD data at $\lambda = 222 \text{ nm}$, data taken from graphs in A. Dimensionless degree of aggregation (α) is set to 1 for the fully polymerized state and to 0 for the monomeric state.

We can conclude that **BTA-1** self-assembles into high aspect ratio fibers at $\text{pH} \leq 5.0$. Due to the presence of nine carboxylic acid moieties per molecule, the functional groups render strong electrostatic repulsion when deprotonated, which leads to disassembly. Assembly can thus be triggered by pH jump, abruptly lowering the pH. Finally, supramolecular polymerization of **BTA-1** can easily be followed by CD spectroscopy.

2.3 Kinetics and Mechanism of Supramolecular Polymerization

To further investigate the mechanism of polymerization of **BTA-1**, the kinetics of self-assembly was measured employing stopped-flow CD-spectroscopy (Figure 2.12 and Subsection 2.8.1.4). Practically, CD intensity at 222 nm was followed after the rapid mixing of a pH

7.4 solution of **BTA-1** with a pH 5.0 sodium acetate buffer. The abrupt increase in acidity leads to the protonation of the carboxylic acids of **BTA-1**, which will lead to aggregation. The CD intensity has a sigmoidal growth that happens after a lag-phase, which is typical of cooperative supramolecular polymerization, Figure 2.3–A&B (see Sub-Section 1.1). To gain a better, and more quantitative, understanding on the mechanism of self-assembly, the half-times of polymerization ($\tau_{1/2}$, time when $\alpha = 0.5$) were plotted against the initial monomer concentration, Figure 2.3–C. An exponential function, of the type $\tau_{1/2} = a m_0^\gamma$ (where m_0 is **BTA-1** initial concentration), could be fitted to the data, the exponent γ (called scaling exponent) was found to be -0.34 . The numerical value of the scaling exponent indicates the phenomena involved in the mechanism of self-assembly. In this case, $\gamma = -0.34$, the scaling exponent suggested a nucleation–elongation mechanism that also includes fragmentation of the fibers (usually if $\gamma = -0.5$).⁶ Practically speaking, this mechanism means that in the first stages of aggregation, **BTA-1** assembles into small-size nuclei that are kinetically disfavored. Once a nucleus is formed, elongation can proceed consuming most of the monomers. Fibers grow until a certain critical length and fragmentate (presumably because of size-related instability) into two distinct assemblies. To confirm this theory, a simple cooperative supramolecular polymerization model, originally developed by Knowles and co-workers to study amyloid aggregation, was used to fit the kinetic parameters to our data (see Sub-Section 2.8.3 for details and derivation).^{180–183} Unfortunately, concentration-dependent kinetic data at 40°C was not perfect and global fitting of the kinetic parameters was not possible. So, we proceeded to perform fitting of the individual datasets and the nucleation–elongation–fragmentation mechanism indeed yielded the best fits, Figure 2.3–A&B.

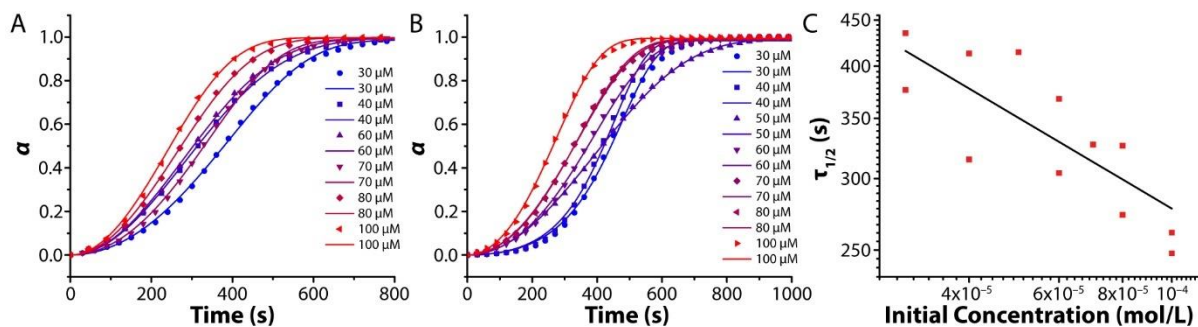


Figure 2.3 – **A & B** – Concentration dependent kinetics of supramolecular polymerization, the dimensionless degree of polymerization α (normalized from CD intensity at 222 nm) is shown versus time. Circles are the experimental data points and lines are the fitting of the nucleation–elongation–fragmentation mathematical model to the individual datasets. Data acquired at 40 °C. Adjusted- $R^2 > 0.998$. **C** – Log-log plot of half-times of polymerization in function of initial monomer concentration (m_0). The black line is an exponential fit: $\tau_{1/2} = a m_0^\gamma$, see text above. The scaling exponent is found to be $\gamma = -0.34 \pm 0.18$ with Adjusted- $R^2 = 0.5923$.

Unfortunately, because only unseeded experiments were performed, the model can only give us the combined rate constants of the multiple processes: $k_p k_n$, $k_p k_f$, and $k_f k_d$. Here, k_p is the elongation, k_d depolymerization, k_n nucleation, and k_f fragmentation rate constants. After individual fitting, the combined rate constant $k_f k_d$ was found to be more than 6 orders of magnitude smaller than the two others ($k_p k_n$, $k_p k_f$). When $k_d \ll k_p m_0$ (where m_0 is the initial monomer concentration) the depolymerization rate can be considered negligible.⁶ The ratio $k_d/k_p m_0$ was determined to be $\sim 10^{-2}$, so for subsequent global fitting, k_d was considered to be zero to reduce the number of free parameters and avoid over-fitting. Since there is no way of knowing the exact nucleus size from our data and to simplify our method, the nucleus size n_c was set to the minimum possible for cooperative mechanism, that is $n_c = 2$.

We then proceeded to perform variable temperature kinetic experiments at a constant concentration of 80 μM , and to our surprise this dataset was of much better quality. To initially probe how the kinetics of **BTA-1** evolve with temperature, $\tau_{1/2}$ was plotted against the inverse of temperature (T). The semi-log plot yielded an almost perfect linear relationship, Figure 2.4–A, and an Arrhenius-type equation could be fitted to this data with adjusted- $R^2 = 0.9916$. This means that the (combined) kinetic rate constants follow an Arrhenius law variation with temperature.

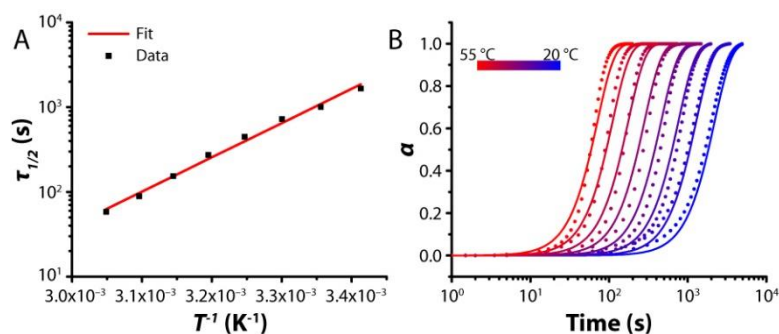


Figure 2.4 – **A** – Semi-log plot of the half-times of polymerization as a function of the inverse of temperature (adjusted- $R^2 = 0.9916$). The black squares are the data points and the red line is the fit to an Arrhenius-type equation **B** – Variable-temperature kinetics of **BTA-1** aggregation, where the degree of aggregation (α) is plotted against time. The circles are the data points while the solid lines are the global-fit of the nucleation–elongation–fragmentation model with Arrhenius equation. Adjusted- R^2 of 0.9848.

Recently, Cohen et al,¹⁸⁴ included temperature-dependence into the amyloid aggregation mathematical models discussed above. A modification of the latter, employing Arrhenius law, was used herein to include temperature variance in the kinetic model of **BTA-1** polymerization, that already includes nucleation–elongation–fragmentation. The derivation of the model, as well other details can be found in Sub-Section 2.8.3.1. Since this data is of much better quality, the global-fitting of the entire multi-temperature dataset to a single model and set of variables (solely the activation energy and pre-exponential factor for the two combined rate constants are free variables) could be performed, Figure 2.4–B. The global fit yielded an adjusted- R^2 of 0.9848 meaning that our model and the kinetic parameters are in good accordance with the experimental data. The results are summed up in Table 2.1.

Table 2.1 – Results of the global fitting of the mathematical model considering nucleation–elongation–fragmentation and Arrhenius law to predict the rate constants.

Variable	Value
$\ln (A_p A_n)$	67.78 ± 0.13
$\ln (A_p A_f)$	81.42 ± 0.05
$E_{a,p} + E_{a,n}$	$156.7 \pm 0.3 \text{ kJ.mol}^{-1}$
$E_{a,p} + E_{a,f}$	$264.3 \pm 0.2 \text{ kJ.mol}^{-1}$

To gain insight on other physically meaningful parameters, the enthalpy and entropy of activation can be extracted from the Eyring plot or global fitting using the Eyring equation

(Figure 2.5 and Sub-Section 2.8.3.4 for details). Eyring equation is similar to Arrhenius law, but has a physical significance rooted in the physical/energetical origin of rate constants,¹³¹ and is defined by:

$$k = \frac{\kappa k_B T}{h} e^{-\frac{\Delta G^\ddagger}{RT}}$$

Where k is any rate constant, R is the universal gas constant, T is temperature, ΔG^\ddagger is the free energy of activation, κ is the transmission coefficient, k_B is the Boltzmann constant, and h is the Planck constant. For simplicity reasons κ is considered as equal to 1. The linearization, Figure 2.5–A&B, is performed by plotting the natural logarithm of the combined rate constants (obtained from previous global-fitting) multiplied by the Planck constant and divided by the Boltzmann constant and temperature ($\ln\left(\frac{k_1 k_2 h}{k_B T}\right)$) as a function of inverse of temperature. For the global fitting, Eyring equation was directly used instead of Arrhenius law, obtaining $\Delta H_{n,e}^\ddagger$ is $154.1 \pm 0.3 \text{ kJ} \cdot \text{mol}^{-1}$ and $\Delta S_{n,e}^\ddagger$ is $310.0 \pm 1.1 \text{ J} \cdot \text{mol}^{-1} \cdot \text{K}^{-1}$ ($T\Delta S_{n,e}^\ddagger = 92.38 \pm 0.32 \text{ kJ} \cdot \text{mol}^{-1}$ at 298 K). All the results are shown in Table 2.2. Since not many variable-temperature kinetic studies of supramolecular polymerization exist, especially in water, and because our results are given in terms of combined rate constants, the comparison of our results with existing literature results is difficult. However, the enthalpies of activation are in the same magnitude as in other studies.^{184,185}

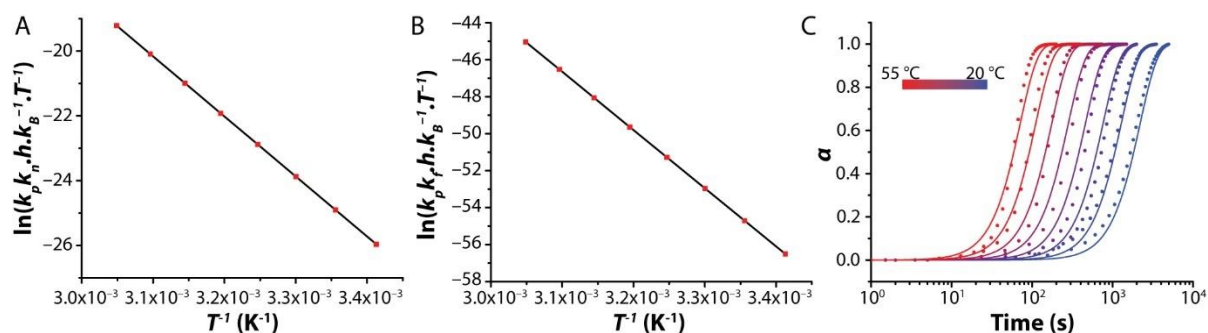


Figure 2.5 – A&B – Linearization of the rate constants obtained from previous global-fitting (using Arrhenius equation) as a function of the inverse temperature. The slope of the linear fit is the enthalpy of activation (ΔH^\ddagger) and the intercept is entropy of activation (ΔS^\ddagger). **C** – Variable temperature self-assembly of **BTA-1**. The circles are the kinetic data, and the solid lines are the result of the global fitting using the nucleation–elongation–fragmentation model and Eyring equation. Adjusted- R^2 of 0.9848.

Table 2.2 – Results of the linearization and global fitting of the mathematical model considering nucleation–elongation–fragmentation and Eyring equation to predict the rate constants.

Variable	Value Linearization	Value Global Fitting
$\Delta H_{n,e}^\ddagger$	154.08±0.04 kJ.mol ⁻¹	154.1±0.3 kJ.mol ⁻¹
$\Delta S_{n,e}^\ddagger$	310.0 ±0.1 J.mol ⁻¹ K ⁻¹	310.0 ± 1.1 J.mol ⁻¹ K ⁻¹
$\Delta G_{n,e}^\ddagger$ at 298 K	61.70±0.05 kJ.mol ⁻¹	61.72±0.44 kJ.mol ⁻¹
$\Delta H_{e,f}^\ddagger$	261.68±0.04 kJ.mol ⁻¹	229.5 ± 0.6 kJ.mol ⁻¹
$\Delta S_{e,f}^\ddagger$	423.3 ±0.13 J.mol ⁻¹ K ⁻¹	326.2 ± 0.9 J.mol ⁻¹ K ⁻¹
$\Delta G_{e,f}^\ddagger$ at 298 K	135.54±0.06 kJ.mol ⁻¹	132.29±0.66 kJ.mol ⁻¹

Our data could be fitted with kinetic models including nucleation–elongation–fragmentation and temperature variability, by either Eyring or Arrhenius law. This result is surprising because supramolecular polymerization in aqueous media is often affected by the hydrophobic effects, that are entropic in origin.¹⁸⁶ Therefore we can conclude that **BTA-1** polymerization is predominantly enthalpic in nature, driven by the hydrogen bonding of the peptide sequence and π – π stacking, while solvophobic interactions play a secondary role.

2.4 Surface-Assisted Hydrogelation

The next step was to gain spatiotemporal control over **BTA-1** hydrogelation. The logical strategy was to take advantage of the pH-dependent aggregation behavior of **BTA-1** with little to no surface modification needed. To achieve this goal, a (semi)porous material was used to absorb an acidic agent and subsequently release the protons into a basic solution of (monomeric) **BTA-1**.

Firstly, a cube of 5 to 10 mm³ of agarose gel was placed in saturated HCl for 96h and then placed in a 160 μ M solution of **BTA-1** at pH 7.4. Since agarose is a hydrogel, it is too porous and proton diffusion into the monomer-containing solution was too fast. The nucleation kinetics are not fast enough to keep up with proton diffusion from agarose and **BTA-1** precipitates in the whole solution, Figure 2.6. No ordered structure nor hydrogel were

observed, and no spatial control over aggregation was achieved. To achieve our goal, proton diffusion needed to be slowed down.

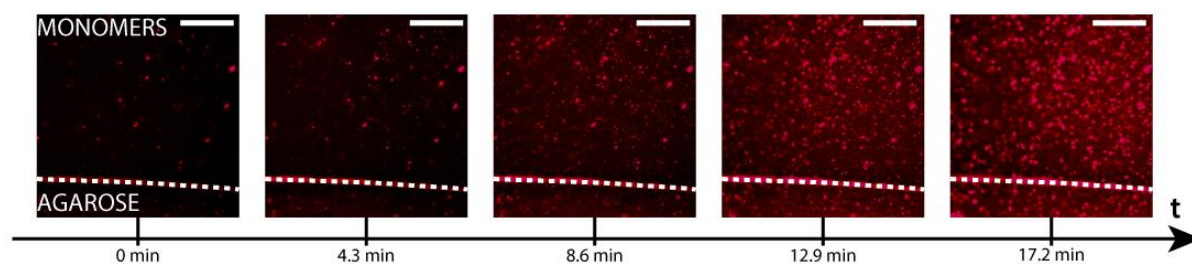


Figure 2.6 – Attempt to induce surface-assisted self-assembly from an agarose cube. Confocal microscopy of a 5 mm³ cube made of agarose gel, soaked in saturated HCl solution for 96 hours and subsequently dropped in a 160 μM **BTA-1** solution at pH 7.4 (monomers). Only precipitates and disordered aggregates are observed, no hydrogel is formed. Nile Red at 5 μM is used as a dye. The scale bar is 50 μm.

From the kinetic studies, we know that nucleation at room temperature takes between 10 to 100 s, so diffusion needs to be slower than that for hydrogelation to take over precipitation. Therefore, a less porous material is needed. We chose poly(dimethyl siloxane), PDMS, a polymeric material with low porosity (compared to agarose hydrogel), but still able to absorb protons and release them back into solution. So, the same procedure was repeated, but with PDMS instead of agarose: a 5–10 mm³ polymeric cube was soaked in concentrated HCl for 96 h and dropped into a pH 7.4 solution of 160 μM **BTA-1**. Differently from the try with agarose, no precipitation was observed whatsoever. Instead, after four minutes a thin hydrogel layer is formed from the solid surface, and continuously grows outward at a velocity of $\sim 3 \mu\text{m}\cdot\text{s}^{-1}$, Figure 2.7. Proton diffusion from the PDMS seems to be the rate limiting step in the hydrogelation process, which is needed for proper supramolecular polymerization, i.e. diffusion slower than nucleation and elongation. Interestingly, hydrogels of up to 3 mm thickness could be generated (Figure 2.10 in Appendix) showing the robustness of the self-assembled material and that this methodology can be scale-up to larger dimensions. After around 9 minutes, the gel, that was previously uniform, starts showing signs of coarsening, probably due to the diffusion of deprotonated **BTA-1** from the bulk solution. This leads to new supramolecular architectures, Figure 2.11 in Appendix, that were not achieved previously when aggregation was induced in solution, Figure 2.1–C.

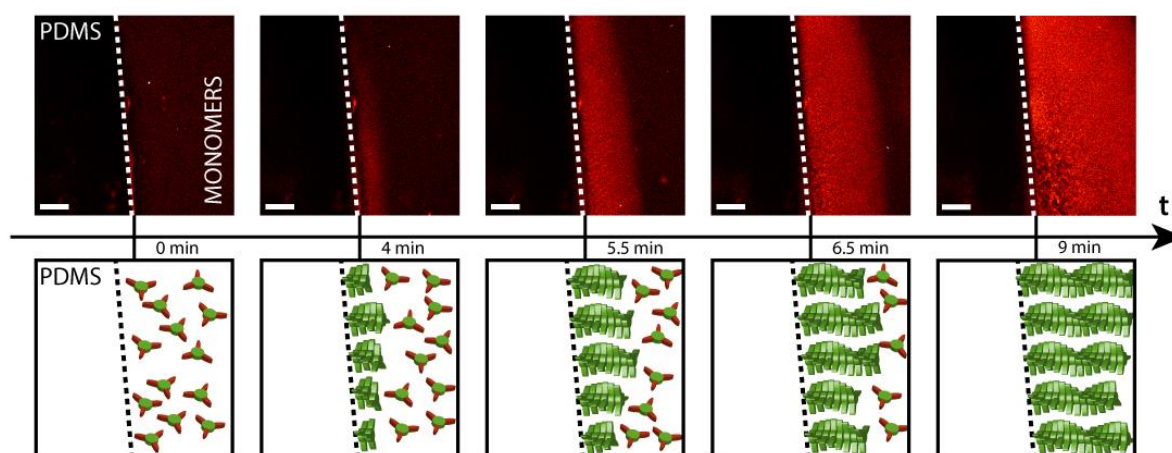


Figure 2.7 – Surface-assisted self-assembly from a PDMS cube. Confocal microscopy of a 5 mm³ PDMS cube, soaked in saturated HCl solution for 96 hours and subsequently dropped in a 160 μM **BTA-1** solution at pH 7.4 (monomers). After 4 min, one can see a thin hydrogel layer emerging from the PDMS block, followed by a propagating front of polymerization. Nile Red at 5 μM is used as a dye. The scale bar is 200 μm.

Next, a 3-D printed microfluidic device was constructed to investigate the first stages of the surface-assisted self-assembly. The device was designed to have two perpendicular channels on top of each other, separated by a 100 μm PDMS film. On the top channel, a stagnant 160 μM **BTA-1** solution at pH 7.4, on the bottom a pH 4 KHP (potassium hydrogen phthalate) buffer was continuously flowed, Figure 2.8–A (see Figure 2.13 and Sub-Section 2.8.1.6). Aggregation occurs close to the intersection of the two channels, Figure 2.8–B, showing that proton diffusion from the buffer through the PDMS membrane is responsible for the local **BTA-1** assembly. The experiment was run for two hours and the device was taken apart so the film can be imaged by confocal microscopy (since the whole set-up is too big for the confocal stage).

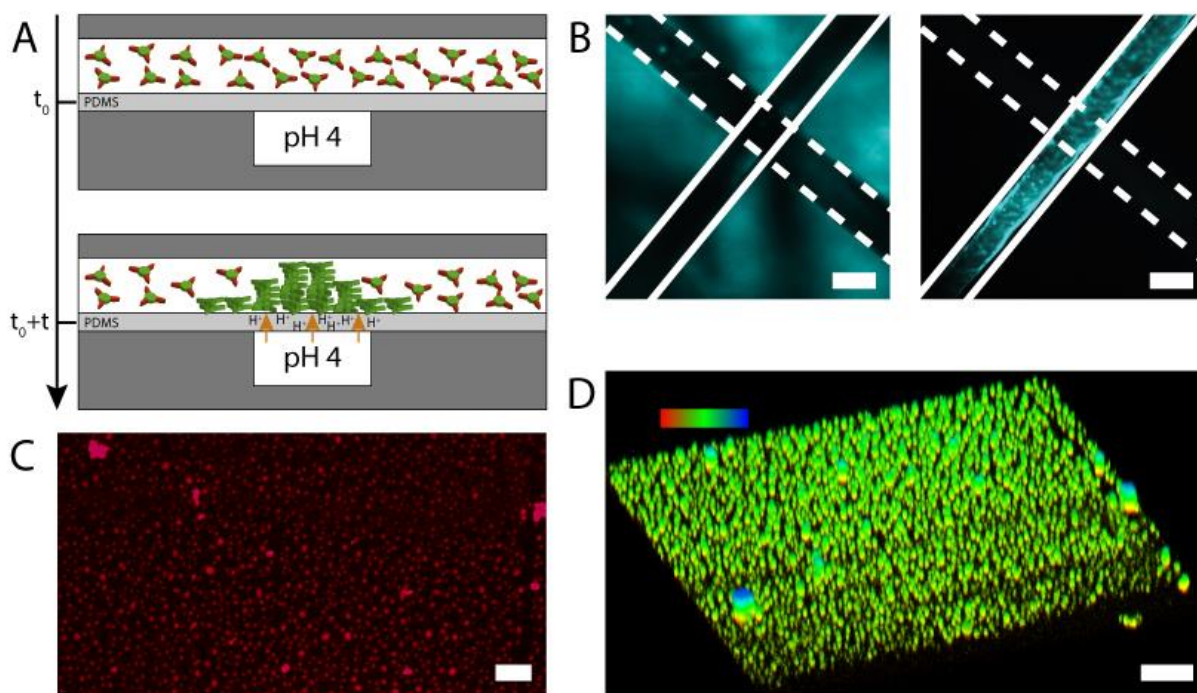


Figure 2.8 – **A** – Representation of the side-view of the microfluidic device with two perpendicular channels separated by a 100 μm PDMS membrane. Top channel contains a stagnant solution of BTA-1 at pH 7.4. A pH 4 KHP buffer continuously flows in the bottom channel. **B** – Transmitted light (left) and fluorescence image (right) of the intersection between the two microfluidic channels taken after the experiment. Fluorescence is only observed at the intersection between the two channels, showing that proton diffusion locally induces BTA-1 self-assembly. Scale bar is 500 μm . **C** – Image from z-slice confocal experiment at 3.85 μm height from the PDMS membrane at the intersection of the two channels, after the 2-hour experiment. Scale bar is 10 μm . **D** – 3D-reconstructed image (from a z-slice confocal experiment in **C**) of the PDMS membrane at the intersection of the two channels. Scale bar is 10 μm . The top left colour gradient indicates the height in the z-axis, where red is 0 and blue is 10 μm . Note that the image is elongated in the z-direction (up) due to the point spread function. Nile Red at 5 μM is used as a dye for all these experiments.

Surprisingly, spherical assemblies of $\sim 2 \mu\text{m}$ were formed on top of the PDMS membrane (Figure 2.8–C&D). Since the pH 4 KHP buffer is a much ‘softer’ acid than concentrated HCl, polymerization is expected to occur much slower in the microfluidic device than in the cube experiments. This would mean that, probably, these spherical assemblies are the early stages of aggregation, that would evolve to the hydrogel formed in the previous experiments. Interestingly, this phenomenon has already been described in surface-assisted hydrogelation, where spherical aggregates appear before fibers and hydrogels.⁸⁰

We can therefore conclude that the kinetic studies of BTA-1 polymerization were important to properly design the surface-assisted hydrogelation. A careful choice of the solid support is needed so that proton diffusion is slower than the kinetics of nucleation and elongation, so that a robust hydrogel is synthesized. Otherwise just precipitation occurs. Also,

the self-assembled materials made from proton diffusion were morphologically different from the ones obtained in solution and depending on the ‘strength’ of the acid, different stages of aggregation can be isolated

2.5 Conclusions

We showed the pH-dependent self-assembly of the C_3 -symmetrical discotic **BTA-1**, that is monomeric at $\text{pH} > 6$ and self-assembles into high aspect ratio fibers at $\text{pH} < 5$. Using a porous material capable of releasing protons, surface-assisted self-assembly was achieved by soaking a PDMS cube in concentrated HCl and dropping it in a basic solution of **BTA-1**. The hydrogel is nucleated in the vicinity of the surface and gradually grows outwards, reaching many millimeters in length. Our approach leads to robust hydrogels, and different stages of self-assembly can be unlocked depending on the experimental conditions. The same methodology can be applied to many pH-responsive low molecular-weight hydrogelators to synthesize functionalized and patterned surfaces. For instance, using multiple gelators with different pKa to sequentially obtain 3-D-structured functional gels.⁷³

2.6 Appendix

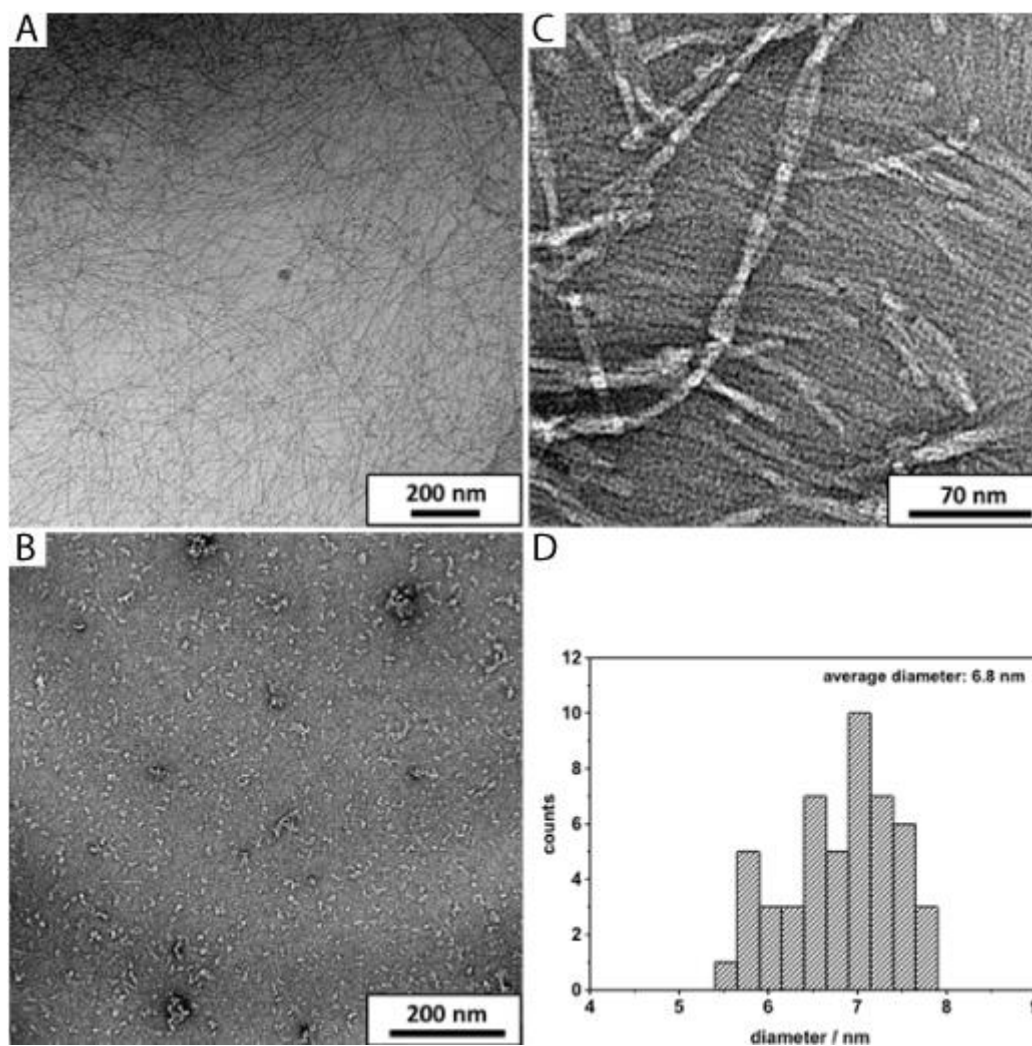


Figure 2.9 – A – cryo-TEM image of **BTA-1** (2.5 mg/ml), in 10 mM TRIS-buffer adjusted to pH = 5.0. **B & C** – TEM images of the peptide amphiphile **BTA-1** (20 μ M) stained with a solution of uranyl acetate (2.0% w/w) in 20 mM TRIS-buffer. **B** – At pH = 7.4 no discernible supramolecular structure, **BTA-1** is disassembled in this condition. **C** – Ordered fibers can be observed, at pH 5.0 **BTA-1** is protonated thus assembled. **D** – Histogram of diameters of **BTA-1** fibers based on the evaluation of negatively stained TEM images at pH = 5.0. This analysis gives an average diameter of 6.8 nm, or \sim 7 nm.

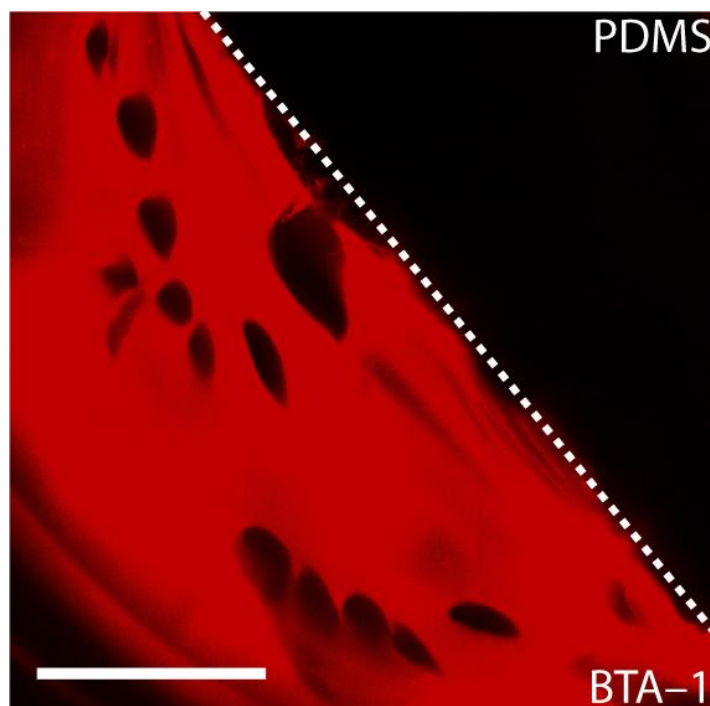


Figure 2.10 – Confocal microscopy of a hydrogel formed by proton diffusion from PDMS, ~ 80 minutes after the cube was placed in the monomeric solution of BTA-1. Nile Red 5 μM was used as a dye. Scale bar is 1 mm.

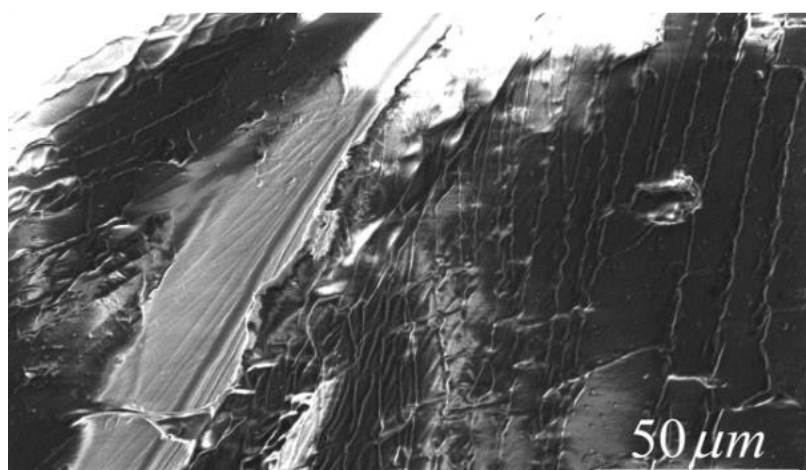


Figure 2.11 – SEM picture of the surface of the PDMS cube. Bundles of fibers can be seen laying on the surface.

2.7 Acknowledgements

Dr. Daniel Spitzer synthesized **BTA-1**, performed the CD spectroscopy experiments and part of the diffusion experiments. Dr. Vincent Marichez performed the diffusion experiments, designed the microfluidic set-up and performed the experiments related to it. Georges Formon performed the kinetic and mechanistic analysis and wrote the model-fitting codes. Prof. Thomas Hermans and Prof. Pol Besenius supervised the project.

This chapter was written by Georges Formon based on the publication: Spitzer, Daniel†, Marichez, Vincent†, Formon, Georges J.M., Besenius, Pol, and Hermans, Thomas M. “Surface-Assisted Self-Assembly of a Hydrogel by Proton Diffusion.” *Angew. Chemie - Int. Ed.* 57, no. 35 (2018): 11349–53. <https://doi.org/10.1002/anie.201806668>. † Authors contributed equally

2.8 Materials and Methods

2.8.1 Materials and Experimental procedures

2.8.1.1 General Considerations

Air and moisture sensitive reactions were carried out under an argon atmosphere with common *Schlenk* techniques and dry solvents. For this purpose, all glassware was previously oven-dried or dried *via* heat gun *in vacuo* at least three times. In addition, all necessary solvents and liquid starting materials were added *via* septum and with disposable syringes, which were previously flushed with argon. Solids were added under continuous counterflow of argon. Water was deionized using an *Elga PURELAB® flex* water purification system. Whenever necessary, the pH was measured with either a *Mettler Toledo S220 SevenCompact™* device equipped with an *InLab®Routine Pro-ISM* pH-electrode or a *MI-410* (Microelectrodes, Inc.) pH-electrode. Both were calibrated against certified buffer solutions prior to use.

All reagents and chemicals were obtained from commercial sources at the highest purity available and used without further purification, if not otherwise stated and purchased from the following distributors:

ABCR (ABCR GmbH & Co. KG, Karlsruhe, Germany), *Acros Organics* (Fisher Scientific GmbH, Schwerte, Germany), *Aldrich* (Sigma Aldrich Chemie GmbH, Taufkirchen, Germany), *Alfa Aesar* (Thermo Fisher (Kandel) GmbH, Karlsruhe, Germany), *Carbolution Chemicals* (Carbolution Chemicals GmbH, St. Ingbert, Germany), *Iris Biotech* (Iris Biotech GmbH, Marktredwitz, Germany), *Merck* (Merck KGaA, Darmstadt, Germany) and *Tokyo Chemical Industry* (TCI Deutschland GmbH, Eschborn, Germany).

2.8.1.2 NMR Spectroscopy

¹H-NMR measurements were performed on a *Bruker DPX300* (¹H-NMR: 300 MHz) and *Bruker Avance 300* (¹H-NMR: 300 MHz) in the Department of Organic Chemistry at the Westfaelische Wilhelms-University Muenster. Furthermore, ¹H-NMR and ¹³C-NMR spectra were measured on a *Bruker Avance II 400* (¹H-NMR: 400 MHz, ¹³C{¹H}-NMR: 101 MHz) and *Bruker Avance III HD 300* (¹H-NMR: 300 MHz) at the Institute of Organic Chemistry of the Johannes Gutenberg-University Mainz.

The chemical shifts (δ) are given in parts per million (ppm) according to the solvent peak of DMSO-*d*₆ with 2.50 ppm for ¹H-NMRs. For ¹³C{¹H}-NMR spectra, the signals were referenced to the deuterium coupled ¹³C solvent signal of DMSO-*d*₆ with 39.52 ppm. The signal splittings are listed as s (singlet), d (doublet), t (triplet), m (multiplet), br (broad singlet) and in suitable combinations. The coupling constant (*J*) is stated in hertz (Hz). For complex molecular structures, signal assignment was supported by 2D-NMR techniques: COSY, HSQC and HMBC. All spectra were analyzed using *MestReNova 10.0.2-15465* (*Mestrelab Research S. L.*).

2.8.1.3 Mass Spectrometry

Mass spectra were recorded in the Department of Organic Chemistry at the Westfaelische Wilhelms-University Muenster. As electrospray ionization (ESI) devices a *Bruker Daltonics MicroTof* and a *Thermo Scientific Orbitrap LTQ XL* were used. In addition, for molecules with a higher molecular mass, matrix-assisted laser desorption/ionization (MALDI) mass spectra were performed on a *Bruker Daltonics Autoflex speed* in the linear and reflector mode, respectively.

Furthermore, mass spectra were received at the Johannes Gutenberg-University Mainz. ESI measurements were executed on a *Waters/Micromass QToF Ultima 3* device. MALDI samples were measured on a *Shimadzu Axima CFR ToF*. The corresponding matrices used are stated in the synthetic procedures.

2.8.1.4 Circular Dichroism Spectroscopy

CD measurements were carried out on a *JASCO J-815* spectrometer run with *Spectra Manager 2.12.00*. Unless not otherwise stated, all sample measurements were buffer-corrected in advance and measured at 20 °C controlled by a *Jasco PTC-423S/15* Peltier-element. Moreover, each measurement was repeated at least three times and averaged to minimize errors. The concentrations were adjusted to keep the photomultiplier's high voltage (HV) below 600 V in the wavelength area of interest to prevent noise increasement. In the UV-Vis spectra no evidence for scattering was observed in any of the solutions. The pH values were adjusted by addition of diluted aqueous HCl and NaOH and afterwards measured with a *MI-410* (Microelectrodes, Inc.) pH-electrode. The data was analyzed using *OriginPro 9.1*.

Kinetic investigations were conducted by attachment of a temperature-controlled *BioLogic SFM 3000* stopped-flow device equipped with a *Berger* Ball mixer, an electro-valve hard-stop and a micro-cuvette of 1.5 mm optical path length. To control the temperature of the cuvette and syringes, the *SFM 3000* was connected to a *Polystat 36* (Fisher Scientific GmbH, Schwerte, Germany) thermostat.

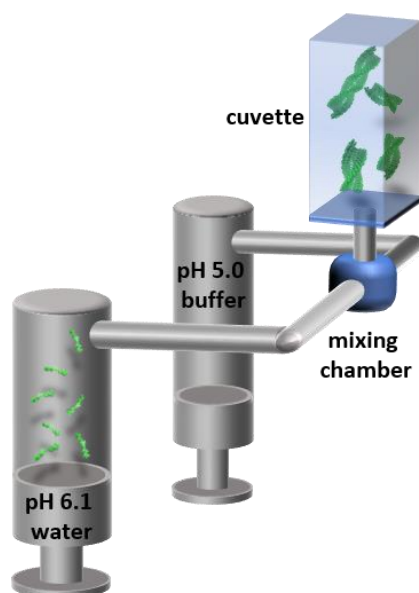


Figure 2.12 – Schematic representation of the stopped-flow set-up attached to the CD spectrometer: the front syringe is filled with an aqueous solution of BTA-1 at pH = 6.1 with a concentration of 200 μ M; the back syringe is filled with a pH = 5.0 sodium acetate buffered solution. A fast mixing process in the mixing chamber triggers the supramolecular polymerization of BTA-1 and subsequent transfer into the measurement cuvette provides fast signal recording in the range of milliseconds.

2.8.1.5 Transmission Electron Microscopy

TEM images were accomplished on a FEI Tecnai™ T12 transmission electron microscope equipped with a BioTWIN lens and a LaB₆ cathode operated at 120 kV. Samples were prepared on freshly glow-discharged copper grids (CF300-Cu, 300 mesh, *Electron Microscopy Sciences*) coated with a 3-4 nm carbon layer. Thereeto, 5 μ L samples were allowed to deposit on the grid for 1 min and excess solvent was afterwards carefully removed with *Whatman*® No. 4 filter papers. Subsequently, the samples were negatively stained by incubation with a 5 μ L drop of 2% v/v solution of uranyl acetate and allowed to dry prior to the measurement.

Cryo-TEM samples were prepared using a *GATAN Cryoplunge 3 System* together with freshly glow-discharged C-Flat™ holey carbon grids (*Protochips CF-1/1-3C-T-50*, hole size: 1.0 μ m, spacing: 1.0 μ m, 300 mesh). The blotting process was performed at 95% humidity and the blotting time is given in the synthetic procedures. Images were acquired not until the sample and temperature were equilibrated to give accurate results.

Digital electron micrographs were recorded with a *TVIPS 4k x 4k CMOS* camera and a *MEGASYS 1k x 1k CCD* camera (only TEM).

2.8.1.6 PDMS cube experiment

A 10:1 mixture of base and curing agent Sylgard® 184 Silicone Elastomer (DOW CORNING, PDMS) was mixed vigorously and degassed. Small 10 x 10 mm cubes were cut and soaked in concentrated HCl_{aq} for 96 hours. Before the experiment, the cube had to be rinsed in water for 1 min to prevent small convections to drag the protons in the bulk too rapidly. Proceeding like this allowed us to remove the outer layer of acid from the PDMS cube and provided more time before the first protons diffuse out of the PDMS. The cube was then suspended (with a steal needle) in a 160 μ M solution of the monomers at pH 7.4. The supramolecular growth from the surface was imaged with confocal microscopy using a Zeiss LSM 710 system with a 10x magnification objective, or a 63x objective for higher resolution images. The samples were excited by continuous wave laser at $\lambda_{exc} = 543$ nm. The emission of

the assemblies was collected in the range from 415 to 735 nm (using a spectral detector). The assemblies were fluorescent due to the intercalation of Nile Red dye (5 μM).

After the surface-assisted self-assembly of the **BTA-1** monomers, the PDMS cube was lifted out of the solution and allowed to dry under vacuum for three hours. The cube was then imaged by SEM using a FEI Quantum FEG 225 at 5 KV.

2.8.1.7 Microfluidic supramolecular growth

The microfluidic chip was designed and 3D-printed on a Form 1+ 3D-printer with the clear resin FLGPCL03 purchased from FORMLABS, Figure 2.13 and Figure 2.14. The membrane was made from a known amount of a 10:1 mixture of base and curing agent Sylgard[®] 184 Silicone Elastomer (DOW CORNING, PDMS) which was prepared, degassed and cured overnight at 50 °C. The monomers were dissolved into a 160 μM solution at pH 7.4 with a final concentration of 5 μM Nile Red. A pH 5 buffer was flowed in one channel and the other channel was filled with the monomer solution. To image the growth of the supramolecular fibers on the PDMS membrane, we used a Nikon eclipse Ti inverted fluorescence microscope with a Nikon Intensilight C-HGFI lamp, CoolSNAP HQ2 CCD and a 1 x objective (Plan UW). The microscope was equipped with a TxRed filter cube with a 540 – 580 nm band-pass excitation filter, a 600 – 660 nm band pass emission filter and a 595 nm dichroic mirror.

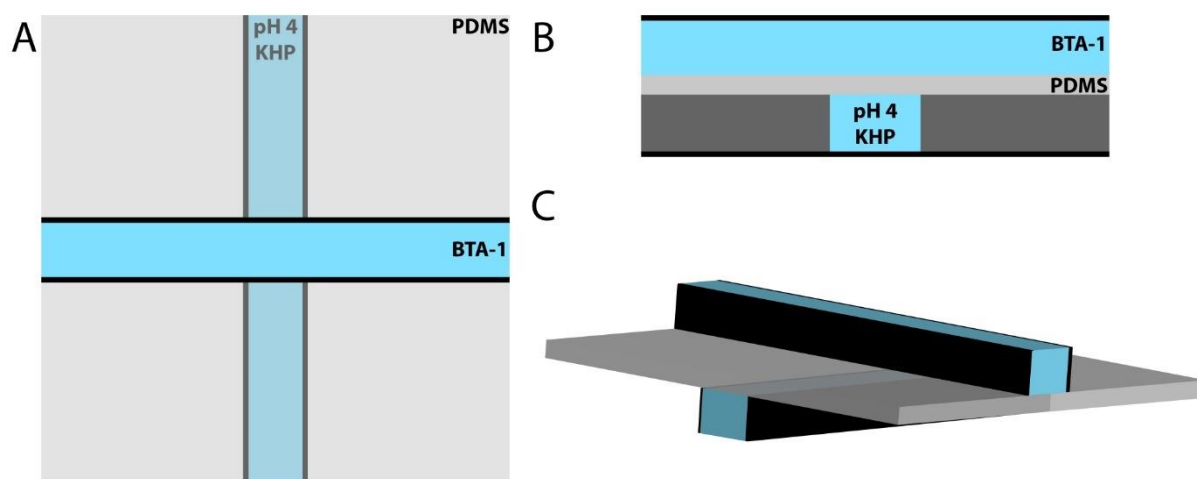


Figure 2.13 – Schemes representing the microfluidic device: two perpendicular channels are separated by a 100 μm PDMS membrane; the top channel contains a basic solution of **BTA-1**; pH 4 KHP buffer flows in the bottom channel . **A** – Top view. **B** – Sideview. **C** – 3-D Rendering of the schemes. These drawing are not to scale.

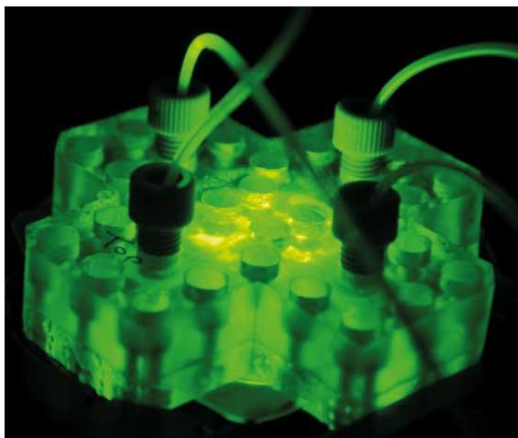
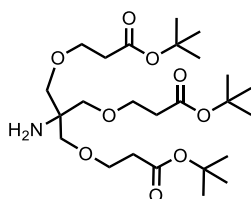


Figure 2.14 – Picture of the 3D-printed microfluidic device 75 by 75 by 13 mm on the fluorescence microscope stage.

2.8.2 Synthesis

2.8.2.1 Compound 1



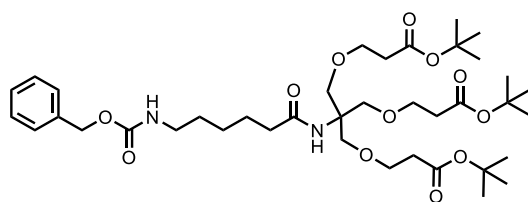
Tris(hydroxymethyl)aminomethane (6.06 g, 50.00 mmol, 1.0 eq.) was dissolved in DMSO (10 mL) and treated with NaOH (1 mL, 5 M). Afterwards tert-butylacrylate (22.43 g, 25.4 mL, 175.00 mol, 3.5 eq.) was added. The opaque solution was stirred at rt for 24 h. The reaction mixture was concentrated under reduced pressure and purified by FC (EtOAc:CH₂Cl₂ → 2:1 to + 0.05% v/v NH₄OH, R_f = 0.14). A colorless oil was obtained.

Yield: 10.58 g, 20.93 mmol, 42%.

¹H-NMR (400 MHz, 296 K, DMSO-*d*₆): δ / ppm = 3.55 (t, *J* = 6.0 Hz, 6H, OCH₂CH₂), 3.17 (s, 6H, CH₂O), 2.39 (t, *J* = 6.0 Hz, 6H, OCH₂CH₂), 1.40 (s, 27H, CH₃).

ESI-HRMS (MeOH) (*m/z*): calculated for [C₂₅H₄₇NO₉H]⁺: 506.3324, found: 506.3332; calculated for [C₂₅H₄₇NO₉Na]⁺: 528.3143, found: 528.3147.

2.8.2.2 Compound 2



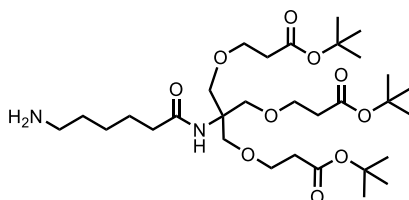
Compound 1 (3.034 g, 6.00 mmol, 1.0 eq.) was dissolved in dry DCM (10 mL). Afterwards PyBOP (3.746 g, 7.20 mmol, 1.2 eq.) and DIPEA (3.112 g, 4.180 mL, 24 mmol, 4.0 eq.) were added to the solution followed by the addition of Cbz-6-aminohexanoic acid (1.910 g, 7.2 mmol, 1.2 eq.). The solution was stirred for 18 h at rt and the solvent was removed *in vacuo*. The resulting oil was purified via FC (EtOAc:DCM → 4:5, $R_f = 0.52$). The product was obtained as a colorless oil.

Yield: 4.489 g, 5.96 mmol, 99%.

$^1\text{H-NMR}$ (400 MHz, 296 K, DMSO- d_6): δ / ppm = 7.41-7.26 (m, 5H, CH^{Ph}), 7.21 (t, $J = 5.7$ Hz, 1H, NHCH_2), 6.90 (s, 1H, NHC_q), 4.99 (s, 2H, PhCH_2), 3.59-3.44 (m, 12H, $\text{C}_q\text{CH}_2\text{OCH}_2$), 3.00-2.91 (m, 2H, NHCH_2), 2.38 (t, $J = 6.1$ Hz, 6H, OCH_2CH_2), 2.03 (t, $J = 7.4$ Hz, 2H, $\text{CH}_2\text{CO}^{\text{Ahx}}$), 1.47-1.32 (m, 4H, CH_2^{Ahx}), 1.39 (s, 27H, CH_3), 1.26-1.18 (m, 2H, CH_2^{Ahx}).

ESI-HRMS (MeOH) (m/z): calculated for $[\text{C}_{39}\text{H}_{64}\text{N}_2\text{O}_{12}\text{H}]^+$: 753.4532, found: 753.4520; calculated for $[\text{C}_{39}\text{H}_{64}\text{N}_2\text{O}_{12}\text{Na}]^+$: 775.4351, found: 775.4342.

2.8.2.3 Compound 3



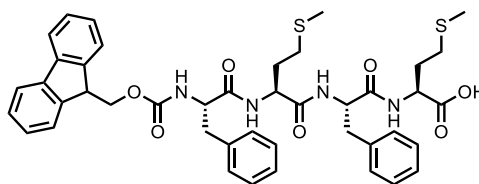
Compound 2 (1.15 g, 1.52 mmol, 1.0 eq.) was dissolved in MeOH (30 mL) under an argon atmosphere. Pd/C (115 mg, 10% *w/w*) was carefully poured into the solution. The flask was evacuated and a H_2 -balloon was connected to the flask *via* syringe. After stirring for 24 h, the crude product was filtered over celite and washed with MeOH (3 x 70 mL). The solvent was removed under reduced pressure leading to a colorless oil.

Yield: 0.943 g, 1.52 mmol, quantitative.

¹H-NMR (300 MHz, 293 K, DMSO-*d*₆): δ / ppm = 6.91 (s, 1H, NH), 3.61-3.47 (m, 12H, C_qCH₂OCH₂), 2.38 (t, *J* = 6.1 Hz, 6H, OCH₂CH₂), 2.03 (t, *J* = 7.4 Hz, 2H, CH₂CO^{Ahx}), 1.49-1.35 (m, 31H, CH₂^{Ahx}/CH₃), 1.34-1.16 (m, 4H, CH₂^{Ahx}).

ESI-HRMS (MeOH) (*m/z*): calculated for [C₃₁H₅₈N₂O₁₀H]⁺: 619.4164, found: 619.4163; calculated for [C₃₁H₅₈N₂O₁₀Na]⁺: 641.3984, found: 641.3980.

2.8.2.4 Compound 4



Fmoc-protected methionine (3.566 g, 9.6 mmol, 2.0 eq.) to be coupled to the 2-chlorotrityl chloride resin (3 g, 1.0-1.6 mmol capacity, 1.0 eq.) was dissolved in dry DCM (30 mL, 10 mL/g resin). The dissolved amino acid was added to the reaction vessel containing the resin under an argon atmosphere followed by the addition of DIPEA (1.241 g, 1.673 mL, 9.6 mmol, 2.0 eq.). The reaction mixture was shaken for 5 min. Afterwards, DIPEA (1.861 g, 2.508 mL, 14.4 mmol, 3 eq.) was added and the reaction mixture was shaken for 1 h, treated with MeOH (1 mL/g resin) and subsequently shaken for another 15 min. The vessel was drained and the resin was washed three times consecutively with 20 mL of DCM, DMF, DCM and MeOH. The resin was dried *in vacuo* overnight. The resin loading was calculated (4.62 mmol loading, 1.54 mmol/g resin) and the beads were transferred to the reaction vessel of the peptide synthesizer.

The dried beads were swollen in DCM p.a. and DMF for 10 min while shaking the reaction vessel. After sucking off the solution, piperidine (20% in DMF) was added and the vessel was shaken for 10 min. After draining of the vessel, the beads were washed two times with DMF and the deprotection was repeated two times prior to the next coupling step. After the third deprotection, the resin was consecutively washed two times with DMF, DCM and DMF. Next, the resin was treated with a solution of the corresponding protected amino acid (0.4 mM, 4.0 eq.), HBTU (0.4 mM, 4.0 eq.), HOBT (0.4 mM, 4.0 eq.) and DIPEA (0.6 mM,

6.0 eq.) in DMF. After shaking for 1 h, the solution was removed, and the resin was washed five times with DMF. This procedure was repeated with the corresponding amino acid for every coupling process, starting with the Fmoc deprotection on the resin. The resin was consecutively washed with DMF and DCM after the last coupling step.

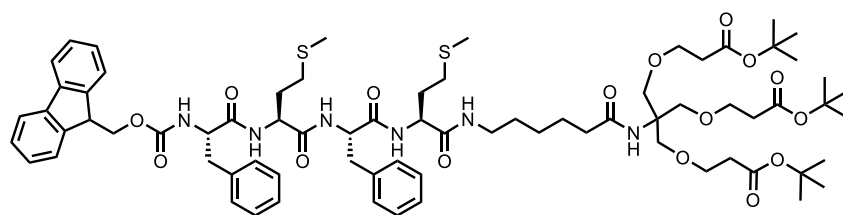
In a final step, the peptide was cleaved from the resin by addition of a mixture of TFA and DCM (1:1, 15 mL). The reaction mixture was shaken for 1 h. The solution was sucked off, collected and the beads were washed two times with DCM (20 mL). The solution was concentrated under reduced pressure and slowly dropped into a solution of cold Et₂O (50 mL). The obtained precipitate was centrifuged at 4350 rpm for 10 min. The supernatant was removed, and the precipitate was washed with Et₂O (30 mL) two times. The precipitate was dried *in vacuo* overnight to yield a colorless solid. The cleavage procedure was repeated two more times.

Yield: 3.658 g, 4.59 mmol, 99% (referenced to 4.62 mmol/3g resin loading)

¹H-NMR (400 MHz, 296 K, DMSO-*d*₆): δ /ppm = 12.73 (br, 1H, COOH), 8.30 (d, $J = 7.9$ Hz, 2H, NH), 8.11 (d, $J = 8.0$ Hz, 2H, NH), 8.05 (d, $J = 8.1$ Hz, 2H, NH), 7.87 (d, $J = 7.6$ Hz, 2H, CH^{Fmoc}), 7.66-7.56 (m, 2H, CH^{Fmoc}), 7.44-7.36 (m, 2H, CH^{Fmoc}), 7.34-7.03 (m, 13H, CH^{Fmoc}/NH/CH^{Phe}), 4.61-4.50 (m, 1H, α -CH), 4.39-4.04 (m, 6H, CHCH₂^{Fmoc}/ α -CH), 3.05 (dd, $J = 14.0, 4.4$ Hz, 1H, CH₂^{Phe}), 2.93 (dd, $J = 13.9, 3.7$ Hz, 1H, CH₂^{Phe}), 2.81 (dd, $J = 14.1, 9.4$ Hz, 1H, CH₂^{Phe}), 2.74 (dd, $J = 13.9, 10.9$ Hz, 1H, CH₂^{Phe}), 2.48-2.29 (m, 4H, CH₂S), 2.03 (s, 3H, CH₃^{Met}), 1.99 (s, 3H, CH₃^{Met}), 2.05-1.69 (m, 4H, CH₂CH₂S).

ESI-HRMS (MeOH) (*m/z*): calculated for [C₄₃H₄₈N₄O₇S₂Na]⁺: 819.2857, found: 819.2834; calculated for [C₄₃H₄₇N₄O₇S₂Na₂]⁺: 841.2676, found: 841.2646; calculated for [(C₄₃H₄₈N₄O₇S₂)₂Na]⁺: 1615.5821, found: 1615.5527.

2.8.2.5 Compound 5



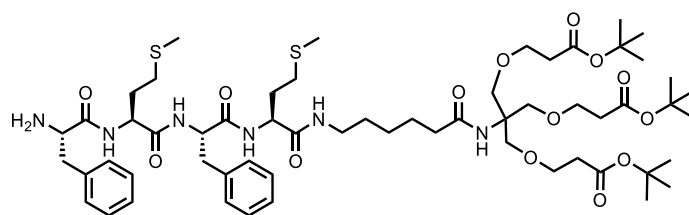
Compound 4 (1.219 g, 1.53 mmol, 1.0 eq.), **Compound 3** (947 mg, 1.53 mmol, 1.0 eq.), DIPEA (198 mg, 267 μ L, 1.53 mmol, 1.0 eq.), PyBOP (796 mg, 1.53 mmol, 1.0 eq.) and HOAt (208 mg, 1.53 mmol, 1.0 eq.) were dissolved in a mixture of THF (20 mL) and DMF (5 mL) and stirred for 24 h at rt. The solvent was removed under reduced pressure. The residue was redissolved in DMF (10 mL), precipitated in H₂O centrifuged and washed twice with H₂O. The crude mixture was purified by FC (EtOAc:DCM:MeOH:DMF \rightarrow 10:10:0.8:0.04, R_f = 0.41) yielding a colorless solid.

Yield: 1.245 g, 0.89 mmol, 58%.

¹H-NMR (400 MHz, 296 K, DMSO-*d*₆): δ / ppm = 8.13 (d, J = 8.0 Hz, 1H, NH), 8.09 (d, J = 8.2 Hz, 1H, NH), 8.07 (d, J = 7.6 Hz, 1H, NH), 7.87 (d, J = 7.6 Hz, 3H, CH^{Fmoc}), 7.69 (t, J = 5.6 Hz, 1H, NH^{Ahx}), 7.65-7.57 (m, 3H, CH^{Fmoc}/NH), 7.44-7.36 (m, 2H, CH^{Fmoc}), 7.35-7.10 (m, 12H, CH^{Fmoc}/CH^{Phe}), 6.90 (s, 1H, NHC_q), 4.58-4.48 (m, 1H, α -CH), 4.40-4.06 (m, 6H, CHCH₂^{Fmoc}/ α -CH), 3.60-3.48 (m, 12H, C_qCH₂OCH₂), 3.08-2.64 (m, 6H, NHCH₂^{Ahx}/ CH₂^{Phe}), 2.46-2.30 (m, 4H, CH₂S), 2.38 (t, J = 6.1 Hz, 6H, OCH₂CH₂), 2.06-1.98 (m, 2H, CH₂CO^{Ahx}), (2.01 (s, 3H, CH₃^{Met}), 1.99 (s, 3H, CH₃^{Met}), 1.93-1.70 (m, 4H, CH₂CH₂S), 1.47-1.31 (m, 4H, CH₂^{Ahx}), 1.39 (s, 27H, CH₃^{tBu}), 1.25-1.14 (m, 2H, CH₂^{Ahx}).

ESI-HRMS (MeOH) (m/z): calculated for [(C₇₄H₁₀₄N₆O₁₄S₂)₂Na]⁺: 721.3367, found: 721.3362; calculated for [C₇₄H₁₀₄N₆O₁₄S₂Na]⁺: 1419.6842, found: 1419.6808; calculated for [C₇₄H₁₀₄N₆O₁₄S₂K]⁺: 1435.6582, found: 1435.6765.

2.8.2.6 Compound 6



Compound 5 (409 mg, 293 μmol , 1.0 eq.) was stirred in a mixture of ACN:DMF:piperidine (5:2:1, 31 mL) for 2 h at rt. The solvent was removed under reduced pressure and the residue was purified by SEC in MeOH ($R_f = 0.63$ in CHCl_3 :MeOH \rightarrow 9:1). The product was obtained as a colorless, sticky solid.

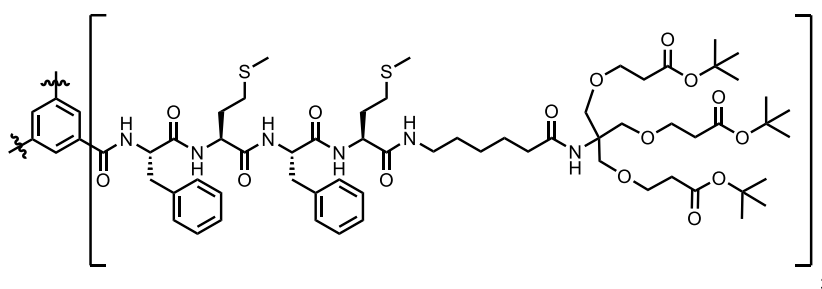
Yield: 317 mg, 270 μmol , 92%.

¹H-NMR (400 MHz, 296 K, DMSO-*d*₆): δ / ppm = 8.17 (d, $J = 7.8$ Hz, 1H, NH), 8.12-8.00 (m, 2H, NH), 7.69 (t, $J = 5.7$ Hz, 1H, NH^{Ahx}), 7.31-7.12 (m, 10H, CH^{Phe}), 6.90 (s, 1H, NHC_q), 4.58-4.45 (m, 1H, α -CH), 4.38-4.18 (m, 2H, α -CH), 3.58-3.49 (m, 12H, CH₂OCH₂), 3.47-3.43 (m, 1H, H₂N α -CH), 3.10-2.87 (m, 4H, NHCH₂^{Ahx}/CH₂^{Phe}), 2.80 (dd, $J = 13.9, 9.4$ Hz 1H, CH₂^{Phe}), 2.62 (dd, $J = 13.5, 8.4$ Hz 1H, CH₂^{Phe}), 2.38 (t, $J = 6.1$ Hz, 6H, OCH₂CH₂), 2.45-2.32 (m, 2H, CH₂S), 2.27 (t, $J = 7.9$ Hz, 2H, CH₂S), 2.02 (s, 3H, CH₃^{Met}), 2.00 (s, 3H, CH₃^{Met}), 2.11-1.97 (m, 2H, CH₂CO^{Ahx}), 1.95-1.65 (m, 4H, CH₂CH₂S), 1.39 (s, 27H, CH₃^{tBu}), 1.48-1.15 (m, 6H, CH₂^{Ahx}).

MALDI-MS (CHCA) (*m/z*): calculated for [C₅₉H₉₄N₆O₁₄S₂H]⁺: 1175.63, found: 1175.63; calculated for [C₅₉H₉₄N₆O₁₄S₂Na]⁺: 1197.62, found: 1197.64; calculated for [C₅₉H₉₄N₆O₁₅S₂H]⁺: 1213.61, found: 1213.63.

ESI-HRMS (MeOH) (*m/z*): calculated for [C₅₉H₉₄N₆O₁₄S₂H]⁺: 1175.6342, found: 1175.6342.

2.8.2.7 Compound 7



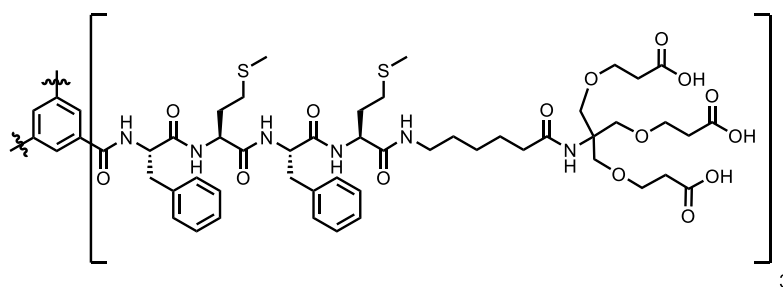
Compound 6 (313 mg, 266 μmol , 3.6 eq.) was dissolved in DMF (6 mL). DIPEA (96 mg, 129 μL , 740 μmol , 10.0 eq.) and 1,3,5-benzenetricarbonyl chloride (19.6 mg, 74 μmol , 1.0 eq.) dissolved in DMF (1 mL) were added to the solution. The solution was stirred for 48 h at rt. PyBOP (127 mg, 244 μmol , 3.3 eq.) was added and the solution was stirred for 24 h. The reaction mixture was precipitated in H_2O (50 mL) and centrifuged at 4300 rpm for 6 min. The precipitate was consecutively washed twice with H_2O and MeOH followed by centrifugation. The desired product was obtained as a colorless solid.

Yield: 194 mg, 53 μmol , 72%.

$^1\text{H-NMR}$ (400 MHz, 296 K, $\text{DMSO-}d_6$): δ / ppm = 8.73 (d, $J = 8.2$ Hz, 3H, $\text{CONH}^{\text{Phe(BTA)}}$), 8.29 (d, $J = 7.7$ Hz, 3H, NH^{Met}), 8.22 (s, 3H, CH^{BTA}), 8.11 (d, $J = 8.1$ Hz, 3H, NH^{Met}), 8.05 (d, $J = 7.6$ Hz, 3H, NH^{Phe}), 7.69 (t, $J = 5.7$ Hz, 3H, CONH^{Ahx}), 7.39-7.05 (m, 30H, CH^{Phe}), 6.90 (s, 3H, NHC_q), 4.80-4.71 (m, 3H, $\alpha\text{-CH}^{\text{Phe(BTA)}}$), 4.59-4.50 (m, 3H, $\alpha\text{-CH}^{\text{Phe}}$), 4.39-4.32 (m, 3H, $\alpha\text{-CH}^{\text{Met}}$), 4.31-4.24 (m, 3H, $\alpha\text{-CH}^{\text{Met}}$), 3.65-3.44 (m, 36H, CH_2OCH_2), 3.08-2.78 (m, 18H, $\text{NHCH}_2^{\text{Ahx}}/\text{CH}_2^{\text{Phe}}$), 2.38 (t, $J = 6.1$ Hz, 18H, OCH_2CH_2), 2.44-2.30 (m, 12H, CH_2S), 2.01 (s, 9H, CH_3^{Met}), 1.99 (s, 9H, CH_3^{Met}), 2.07-1.69 (m, 18H, $\text{CH}_2\text{CO}^{\text{Ahx}}/\text{CH}_2\text{CH}_2\text{S}$), 1.50-1.15 (m, 99H, $\text{CH}_2^{\text{Ahx}}/\text{CH}_3^{\text{tBu}}$).

MALDI-MS (CHCA) (m/z): calculated for $[\text{C}_{186}\text{H}_{282}\text{N}_{18}\text{O}_{45}\text{S}_6\text{Na}]^+$: 3704.86 found: 3705.52; calculated for $[\text{C}_{186}\text{H}_{282}\text{N}_{18}\text{O}_{46}\text{S}_6\text{Na}]^+$: 3720.86 found: 3721.44; calculated for $[\text{C}_{186}\text{H}_{282}\text{N}_{18}\text{O}_{47}\text{S}_6\text{Na}]^+$: 3736.85 found: 3737.02.

2.8.2.8 Compound 8 (BTA-1)



7 (185 mg, 50 μ mol, 1.0 eq.) was dissolved in a mixture of DCM:TFA (1:1, 14 mL). The solution was stirred for 1 h. The deprotection was repeated once. The solvent was removed under reduced pressure and after lyophilization a colorless solid remained.

Yield: 156 mg, 49 μ mol, 98%.

$^1\text{H-NMR}$ (400 MHz, 296 K, DMSO- d_6): δ / ppm = 12.17 (br, 9H, COOH), 8.73 (d, J = 8.0 Hz, 3H, $\text{NH}^{\text{Phe(BTA)}}$), 8.29 (d, J = 7.7 Hz, 3H, NH^{Met}), 8.22 (s, 3H, CH^{BTA}), 8.12 (d, J = 8.1 Hz, 3H, NH^{Met}), 8.05 (d, J = 7.6 Hz, 3H, NH^{Phe}), 7.70 (t, J = 5.7 Hz, 3H, CONH^{Ahx}), 7.38-7.08 (m, 30H, CH^{Phe}), 6.93 (s, 3H, NHC_q), 4.81-4.72 (m, 3H, $\alpha\text{-CH}^{\text{Phe(BTA)}}$), 4.60-4.52 (m, 3H, $\alpha\text{-CH}^{\text{Phe}}$), 4.41-4.33 (m, 3H, $\alpha\text{-CH}^{\text{Met}}$), 4.32-4.25 (m, 3H, $\alpha\text{-CH}^{\text{Met}}$), 3.65-3.45 (m, 36H, CH_2OCH_2), 3.12-2.72 (m, 18H, $\text{NHCH}_2^{\text{Ahx}}/\text{CH}_2^{\text{Phe}}$), 2.41 (t, J = 6.3 Hz, 18H, OCH_2CH_2), 2.49-2.28 (m, 12H, CH_2S), 2.01 (s, 9H, CH_3^{Met}), 1.99 (s, 9H, CH_3^{Met}), 2.16-1.65 (m, 18H, $\text{CH}_2\text{CO}^{\text{Ahx}}/\text{CH}_2\text{CH}_2\text{S}$), 1.50-1.12 (m, 18H, CH_2^{Ahx}).

MALDI-MS (CHCA) (m/z): calculated for $[\text{C}_{150}\text{H}_{210}\text{N}_{18}\text{O}_{45}\text{S}_6\text{Na}]^+$: 3198.29 found: 3198.24; calculated for $[\text{C}_{150}\text{H}_{210}\text{N}_{18}\text{O}_{45}\text{S}_6\text{K}]^+$: 3214.27 found: 3214.22.

2.8.3 Mathematical Model

2.8.3.1 Description of the model

The cooperative model of supramolecular polymerization usually considers the balance of the monomers and of polymers of every chain length considering a nucleation step, followed by the elongation. The same idea was developed since the 60's to describe the kinetics of filamentous aggregates, but also including fragmentation of the filaments. The equations governing the aggregation mechanism are as follows:¹⁸¹

$$\begin{aligned}
\frac{\partial f(t, j)}{\partial t} = & 2m(t)k_p f(t, j - 1) - 2m(t)k_p f(t, j) \\
& + 2k_d f(t, j + 1) - 2k_d f(t, j + 1) \\
& - k_f(j - 1)f(t, j) + 2k_f \sum_{i=j+1}^{\infty} f(t, i) \\
& + k_n m(t)^n
\end{aligned} \tag{S1}$$

$$\frac{dm(t)}{dt} = -\frac{d}{dt} \left[\sum_{j=n}^{\infty} j \times f(t, j) \right] \tag{S2}$$

Where: $f(t, j)$ is the polymers concentration of length j at time t ; $m(t)$ is the concentration of free monomers at time t ; k_p is the elongation rate constant; k_d is the depolymerization rate constant; k_n is the nucleation rate constant; k_f is the fragmentation rate constant; and n is the nucleus size.

The two first moments, $F(t)$ and $P(t)$, being the total number and molar concentration of polymers respectively, are given by:

$$F(t) = \sum_{j=n}^{\infty} f(t, j) \tag{S3}$$

$$P(t) = \sum_{j=n}^{\infty} j \times f(t, j) \tag{S4}$$

$$m(t) = m_0 - P(t) \tag{S5}$$

The time derivation of the moments results in:⁶

$$\frac{dF}{dt} = k_n m(t)^n + k_f P(t) \tag{S6}$$

$$\frac{dP}{dt} = 2(m(t)k_p - k_d)F(t) \tag{S7}$$

The linearized analytical solution of this differential equation was derived by Knowles and co-workers in 2009,¹⁸⁰ and is given by:⁶

$$P(t) = P_{\infty} + \exp \left[-\frac{k_p(4c\kappa \cosh(\kappa t) + F_0 \kappa^2 \sinh(\kappa t))}{\kappa^3} \right] \times \tag{S8}$$

$$\left[(P_0 - P_\infty) \exp\left(\frac{2k_p c}{\kappa^2}\right) \right]$$

$$c = k_n m_0^{n_c} + k_f P_0 \quad (\text{S9})$$

$$\kappa = \sqrt{2(k_p m_0 - k_d)k_f} \quad (\text{S10})$$

$$P_\infty = m_{tot} - k_d/k_p \quad (\text{S11})$$

Where F_0 and P_0 are the initial polymer number and molar concentrations, m_0 is the total initial monomer concentration and m_{tot} is the total monomer concentration (monomers in monomeric or polymeric form). For unseeded experiments these F_0 and P_0 are zero and $m_{tot} = m_0$, so equations S8 to S11 can be simplified to:

$$P(t) = P_\infty \left\{ 1 - \exp\left[\frac{2k_p c}{\kappa^2} (1 - \cosh(\kappa t))\right] \right\} \quad (\text{S12})$$

$$c = k_n m_0^{n_c} \quad (\text{S13})$$

$$\kappa = \sqrt{2(k_p m_0 - k_d)k_f} \quad (\text{S14})$$

$$P_\infty = m_0 - k_d/k_p \quad (\text{S15})$$

In the case of unseeded experiments these equations depend only on the combined rate constants – $k_p k_n$, $k_p k_f$, and $k_f k_d$ – and the individual constants cannot be extracted.

For the case where k_d is negligible the equations are reduced to:

$$P(t) = m_0 \left\{ 1 - \exp\left[\frac{2k_p c}{\kappa^2} (1 - \cosh(\kappa t))\right] \right\} \quad (\text{S16})$$

$$c = k_n m_0^{n_c} \quad (\text{S17})$$

$$\kappa = \sqrt{2k_p k_f m_0} \quad (\text{S18})$$

For the data fitting, mainly equations S12 to S15 were used.

For the temperature dependency, the Arrhenius equation was used to get the rate constants as follows:

$$k = A e^{-\frac{E_a}{RT}} \quad (\text{S19})$$

Where k is any rate constant, E_a is the activation energy, R is the universal gas constant, T is temperature, and A is a pre-exponential factor. For the combined rate constants this equation transforms to:

$$k_p k_n = A_p A_n e^{-\frac{E_{a,p} + E_{a,n}}{RT}} \quad (\text{S20})$$

$$k_p k_f = A_p A_f e^{-\frac{E_{a,p} + E_{a,f}}{RT}} \quad (\text{S21})$$

where: $E_{a,p}$ and A_p are respectively the activation energy and pre-exponential factor of elongation; $E_{a,n}$ and A_n are respectively the activation energy and pre-exponential factor of nucleation; and $E_{a,f}$ and A_f are respectively the activation energy and pre-exponential factor of fragmentation.

To simplify the fitting and to overcome the built-in function limitations to very large numbers (i.e. the pre-exponential factor) equations S20 and S21 were linearized as follows:

$$\ln(k_p k_n) = \ln(A_p A_n) - \frac{E_{a,p} + E_{a,n}}{RT} \quad (\text{S22})$$

$$\ln(k_p k_f) = \ln(A_p A_f) - \frac{E_{a,p} + E_{a,f}}{RT} \quad (\text{S23})$$

2.8.3.2 Individual fitting

The fitting of the model to the data was done in MATLAB using the built-in function *fit* (Code is available in Section 2.8.4). For simplicity, the nucleus size n_c was always considered as the minimum possible for cooperative self-assembly, that is $n_c = 2$.

Firstly, the individual fitting to each dataset was performed, to initially estimate the global rate constants. Using equations S12 to S15 and fitting the combined rate constants $k_p k_n$, $k_p k_f$, and $k_f k_d$, the difference between the model and the data was minimized using the *fit* function.

After individual fitting, the combined rate constant $k_f k_d$ was found to be more than 6 orders of magnitude smaller as compared to the two others ($k_p k_n$, $k_p k_f$). For the case where $k_d \ll k_p m_0$ (where m_0 is the initial monomer concentration) the depolymerization rate can be considered negligible.⁶ The ratio $k_d/k_p m_0$ was determined to be $\sim 10^{-2}$, so for subsequent global fitting, k_d was considered to be zero.

2.8.3.3 Global Fitting

The global fit of the temperature dependent model to the data was performed applying equations S16 to S18 combined with equations S22 and S23. As discussed in the main text, the

depolymerization rate was neglected, because it is not significant to the process and the results of the individual fittings were used as initial guesses for the global procedure.

2.8.3.4 Eyring treatment

The Eyring equation was developed from transition state theory, and is an Arrhenius type equation, with physical significance,¹⁸⁷ and it can be written as follows:

$$k = \frac{\kappa k_B T}{h} e^{-\frac{\Delta G^\ddagger}{RT}} \quad (\text{S24})$$

Where k is any rate constant, R is the universal gas constant, T is temperature, ΔG^\ddagger is the free energy of activation, κ is the transmission coefficient, k_B is Boltzmann's constant, and h is Planck's constant. For simplicity reasons κ is considered as equal to 1.¹⁸⁵ The free energy of activation is temperature dependent and can be written as $\Delta G^\ddagger = \Delta H^\ddagger - T\Delta S^\ddagger$. Where ΔH^\ddagger and ΔS^\ddagger are the enthalpy and entropy of activation, respectively. So, equation S24 transforms to equations S25 and S26 for the combined rate constants.

$$k_p k_n = \frac{k_B T}{h} e^{-\frac{\Delta H_{n,p}^\ddagger}{RT} + \frac{\Delta S_{n,p}^\ddagger}{R}} \quad (\text{S25})$$

$$k_p k_f = \frac{k_B T}{h} e^{-\frac{\Delta H_{p,f}^\ddagger}{RT} + \frac{\Delta S_{p,f}^\ddagger}{R}} \quad (\text{S26})$$

Where: $\Delta H_{n,p}^\ddagger = \Delta H_n^\ddagger + \Delta H_p^\ddagger$; $\Delta H_{p,f}^\ddagger = \Delta H_p^\ddagger + \Delta H_f^\ddagger$; $\Delta S_{n,p}^\ddagger = \Delta S_n^\ddagger + \Delta S_p^\ddagger$; $\Delta S_{p,f}^\ddagger = \Delta S_p^\ddagger + \Delta S_f^\ddagger$; ΔH_n^\ddagger , ΔH_p^\ddagger , ΔH_f^\ddagger are the activation enthalpies of nucleation, elongation and fragmentation respectively; ΔS_n^\ddagger , ΔS_p^\ddagger , ΔS_f^\ddagger are the activation entropies of nucleation, elongation and fragmentation respectively. By linearizing equations S25 and S26 we get the equations for the Eyring plot:

$$\ln \left(\frac{k_p k_n \cdot h}{k_B T} \right) = -\frac{\Delta H_{n,p}^\ddagger}{RT} + \frac{\Delta S_{n,p}^\ddagger}{R} \quad (\text{S27})$$

$$\ln \left(\frac{k_p k_f \cdot h}{k_B T} \right) = -\frac{\Delta H_{p,f}^\ddagger}{RT} + \frac{\Delta S_{p,f}^\ddagger}{R} \quad (\text{S28})$$

The enthalpy and entropy of activation were extracted from the Eyring plot using the rate constants collected from the variable temperature global fitting.

The next step was to perform the global fit of the model to our data using Eyring's equation instead of Arrhenius. The same procedure as detailed in the previous section was implemented, but instead of equations S22 and S23 the equations S25 and S26 were used.

2.8.4 MATLAB® code

Note that for simplicity a numerical stability, all E_a , ΔH^\ddagger and ΔS^\ddagger are expressed as E_a/R , $\Delta H^\ddagger/R$ and $\Delta S^\ddagger/R$.

2.8.4.1 Model with Arrhenius

```
function [Alpha] = polymfit_knowles2_multifit_T(t,opt,a1,e1,a2,e2,a3,e3,x,T)
%Multi fitting variable temperature
%THIS MODEL DESCRIBES COOPERATIVE SUPRAMOLECULAR POLYMERIZATION (nuc. size
% x) - using the linearized moments equations unseeded taking into account
% fragmentation and arrhenius law
% cf T. P. J. Knowles, et al., Nat. Protoc. 2016, 11, 252-272.
% Georges Formon 28 FEB 2018 - HERMANS@UNISTRA.FR
% #####
% #####

nT=size(T);
Tu = unique(T);
nTu=size(Tu);
x_=1;
y=nT(1)/(nTu(1));

if nT(1)==nTu(1)
    Alpha(1:nT,1)=1; % Trick to bypass the software
else
    for i=1:nTu(1)
        Ti=Tu(i);
        CON = 0; %Polymer initial concentration
        COM=opt; %monomer initial concentration

        Y0 = zeros(2,1); % define initial conc. vector (first x vals, then y vals)
        Y0(1)=0; % initial condition M(t)
        Y0(2)=0; % initial conc P(t)
        t_range = t(x_:y,1); % better sampling since most event happen early on

        kfefn=exp(a1)*exp(-e1/Ti); % Arrhenius equation to predict the combined elongation-nucleation rate
        constant
        kfefrag=exp(a2)*exp(-e2/Ti); % Arrhenius equation to predict the combined elongation-fragmentation
        rate constant
        kfragre=exp(a3)*exp(-e3/Ti); % Arrhenius equation to predict the combined depolymerization-
        fragmentation rate constant

        kappa=sqrt(2*(kfefrag*COM-kfragre));
        kpc=kfefn*COM.^x; %kfe*c
        Minf=COM-kfragre/kfefrag;

        Alpha(x_:y,i)=(Minf*(1-exp((2*kpc/kappa.^2)*(1-cosh(kappa*t_range)))))/COM; % calculation of alpha
        x_=x_+1000;
        y=x_+1000-1;
    end
end
```

```
end
end
```

2.8.4.2 Model with Eyring

```
function [Alpha] = polymfit_knowles2_multifit_T_Eyring(t,opt,H1,S1,H2,S2,H3,S3,x,T)
%Multi fitting variable temperature
%THIS MODEL DESCRIBES COOPERATIVE SUPRAMOLECULAR POLYMERIZATION (nuc. size
% x) - using the linearized moments equations unseeded taking into account fragmentation and % Eyring
equation
% cf T. P. J. Knowles, et al., Nat. Protoc. 2016, 11, 252-272.
% Georges Formon 28 FEB 2018 - HERMANS@UNISTRA.FR
% #####
% #####

nT=size(T);
Tu = unique(T);
nTu=size(Tu);
x_=1;
y=nT(1)/(nTu(1));

if nT(1)==nTu(1)
Alpha(1:nT,1)=1;% Trick to bypass the software
else
for i=1:nTu(1)
Ti=Tu(i);
CON = 0; %Polymer initial concentration
COM=opt;%monomer initial concentration

Y0 = zeros(2,1); % define initial conc. vector (first x vals, then y vals)
Y0(1)=0; % initial condition M(t)
Y0(2)=0; % initial conc P(t)
t_range = t(x_:y,1);

kb=1.38064852e-23; % Boltzmann constant
h=6.62607004e-34; % Planck constant

kfefn=(kb*Ti/h)*exp(-H1/Ti+S1); %Eyring equation to predict the combined elongation-nucleation rate
constant
kfefrag=(kb*Ti/h)*exp(-H2/Ti+S2); % Eyring equation to predict the combined elongation-fragmentation
rate constant
kfragre=(kb*Ti/h)*exp(-H3/Ti+S3); % Eyring equation to predict the combined depolymerization-
fragmentation rate constant

kappa=sqrt(2*(kfefrag*COM-kfragre));
kpc=kfefn*COM.^x; %kfe*c
Minf=COM-kfragre/kfefrag;

Alpha(x_:y,1)=(Minf*(1-exp((2*kpc/kappa.^2)*(1-cosh(kappa*t_range)))))/COM;% Calculation of alpha

x_=x_+1000;
y=x_+1000-1;
end
end
```

2.8.4.3 Fitting Routine with Arrhenius

```
function Besenius_Fitroutine_T_var_frag_unseeded_multifit
```

```

%%Besenius
%%Fitting routine for analyze experimental data using a cooperative supramolecular
polymerization model
%Nucleation elongation fragmentation unseeded - analytical
% Georges Formon - 16 February 2018 (Hermans@unistra.fr)
clc
close all
clear all

tic % start timer

```

Load Data

```

S=load('Temp_var_80uM'); %conc 80 uM
% time in seconds.
t(:,1) = S.B_80uM_20C(:,1);
t(:,2) = S.B_80uM_25C(:,1);
t(:,3) = S.B_80uM_30C(:,1);
t(:,4) = S.B_80uM_35C(:,1);
t(:,5) = S.B_80uM_40C(:,1);
t(:,6) = S.B_80uM_45C(:,1);
t(:,7) = S.B_80uM_50C(:,1);
t(:,8) = S.B_80uM_55C(:,1);
% alpha
a(:,1) = S.B_80uM_20C(:,2);
a(:,2) = S.B_80uM_25C(:,2);
a(:,3) = S.B_80uM_30C(:,2);
a(:,4) = S.B_80uM_35C(:,2);
a(:,5) = S.B_80uM_40C(:,2);
a(:,6) = S.B_80uM_45C(:,2);
a(:,7) = S.B_80uM_50C(:,2);
a(:,8) = S.B_80uM_55C(:,2);

T=[20; 25; 30; 35; 40; 45; 50; 55];
Tk=T+273;
Tkinv=1./Tk;
nT=size(Tk);
nt=size(t);
x_=1;
y=nt(1,1);

```

Putting all data into one vector

```

for j=1:nT(1,1)
    a_(x_:y,1)=a(:,j);
    t_(x_:y,1)=t(:,j);
    T_(x_:y,1)=Tk(j);
    x_=x_+1000;
    y=x_+1000-1;
end

```

Setting Parameters

```

opt=80e-6;
R=8.314;
kfragkre1=0;
x=2;
a3=-inf;
e3=0;

```

Fitting

```

fomm = fitoptions('Method', 'NonLinearLeastSquares', 'StartPoint', [75,1.7e4,80,2.5e4], ...
    'Lower', [10,1e3,10,1e3], 'Upper', [1e3,1e6,1e3,1e6], ...
    'TolFun', 1e-14, 'TolX', 1e-14, 'MaxIter', 5000, 'MaxFunEval', 2500, 'Display', 'iter');

ftmm = fittype('polymfit_knowles2_multifit_T(t,opt,a1,e1,a2,e2,a3,e3,x,T)', ...
    'coefficients', {'a1','e1','a2','e2'}, ...
    'independent', {'t','T'}, ...
    'problem', {'opt','x','a3','e3'}, ...
    'options', fomm);

[f,gof] = fit ([t_,T_], a_, ftmm, 'problem', {opt,x,a3,e3})

```

Success, but fitting stopped because change in coefficients less than tolerance (TolX).

General model:

$f(t,T) = \text{polymfit_knowles2_multifit_T}(t,\text{opt},a1,e1,a2,e2,a3,e3,x,T)$

Coefficients (with 95% confidence bounds):

```

a1 = 67.78 (67.66, 67.91)
e1 = 1.884e+04 (1.88e+04, 1.888e+04)
a2 = 81.42 (81.36, 81.48)
e2 = 3.176e+04 (3.173e+04, 3.178e+04)

```

Problem parameters:

```

opt = 8e-05
x = 2
a3 = -Inf
e3 = 0

```

gof =

```

sse: 15.4259
rsquare: 0.9848
dfe: 7996
adjrsquare: 0.9848
rmse: 0.0439

```

Acquiring Results

```

A1=f.a1; %%logA
E1=f.e1*R; %%E
A2=f.a2; %%logA
E2=f.e2*R; %%E
A3=f.a3; %%logA
E3=f.e3*R; %%E

ConfidenceInterval=confint(f);

confintA1=ConfidenceInterval(:,1);

```

```

confintE1=ConfidenceInterval(:,2).*R;
confintA2=ConfidenceInterval(:,3);
confintE2=ConfidenceInterval(:,4).*R;

R1=gof.sse;
R2=gof.rsquare;
R3=gof.dfe;
R4=gof.adjrsquare;
R5=gof.rmse;
% message=output.message;

kfekfn=exp(A1)*exp(-E1./(R*Tk));
kfekfrag=exp(A2)*exp(-E2./(R*Tk));
kfragkre=exp(A3)*exp(-E3./(R*Tk));

```

```

A3 =
    -Inf

```

```

E3 =
     0

```

Plotting

```

nT=size(Tk);
cor_i = [0 0 1];
cor_f = [1 0 0];
var = (cor_f - cor_i)/(nT(1)-1);
cor = cor_i;
for ii=2:(nT(1))
    cor=[cor; cor(end,:) + var];
end

F=polymfit_knowles2_multifit_T(t_,opt,A1,E1/R,A2,E2/R,A3,E3/R,x,T_);

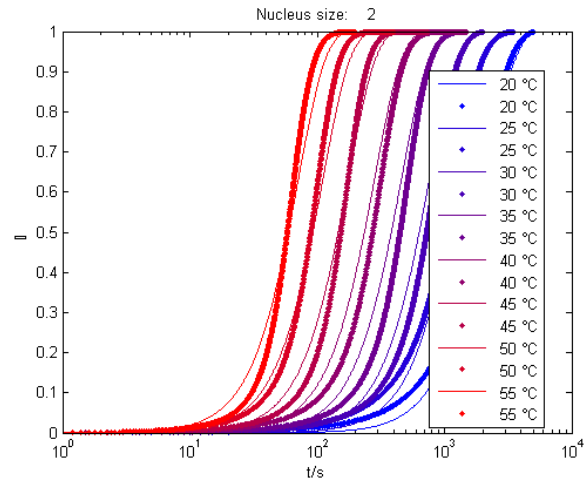
x_=1;
y=nt(1,1);
fig=figure;
for i=1:nT(1)
    Results(:,3*i-2)=t_(x_:y,1);
    Results(:,3*i-1)=a(:,i);
    Results(:,3*i)=F(x_:y,1);
    plot(t_(x_:y,1),F(x_:y,1),'color',cor(i,:))
    hold on
    plot(t(:,i),a(:,i),'.','MarkerEdgeColor',cor(i,:));
    hold on
    lgdttl{2*i-1}=sprintf('%4.0f %c',T(i),176);
    lgdttl{2*i}=sprintf('%4.0f %c',T(i),176);
    hold on;
    x_=x_+1000;
    y=x_+1000-1;
end
legend(lgdttl,'Location','best');
ttl=sprintf('Nucleus size: %4.0f',x);
title(ttl);
axis([1 10000 0 1])

```

```

y1b1=sprintf('%c',945);
ylabel(y1b1);
xlabel('t/s');
set(gca,'xscale','log')
hold off

```



```
end
```

2.8.4.4 Fitting Routine with Eyring

```
function Besenius_Fitroutine_T_var_frag_unseeded_multifit_Eyring
```

```

%%Besenius
%%Fitting routine for analyze experimental data using a cooperative supramolecular
polymerization model
%Nucleation elongation fragmentation unseeded - analytical
% Georges Formon - 16 February 2018 (Hermans@unistra.fr)
clc
close all
clear all

tic % start timer

```

Load data

```

S=load('Temp_var_80uM'); %conc 80 uM
% time in seconds.
t(:,1) = S.B_80uM_20C(:,1);
t(:,2) = S.B_80uM_25C(:,1);
t(:,3) = S.B_80uM_30C(:,1);
t(:,4) = S.B_80uM_35C(:,1);
t(:,5) = S.B_80uM_40C(:,1);
t(:,6) = S.B_80uM_45C(:,1);
t(:,7) = S.B_80uM_50C(:,1);
t(:,8) = S.B_80uM_55C(:,1);
% alpha
a(:,1) = S.B_80uM_20C(:,2);
a(:,2) = S.B_80uM_25C(:,2);

```

```

a(:,3) = S.B_80uM_30C(:,2);
a(:,4) = S.B_80uM_35C(:,2);
a(:,5) = S.B_80uM_40C(:,2);
a(:,6) = S.B_80uM_45C(:,2);
a(:,7) = S.B_80uM_50C(:,2);
a(:,8) = S.B_80uM_55C(:,2);

T=[20; 25; 30; 35; 40; 45; 50; 55];
Tk=T+273;
Tkinv=1./Tk;
nT=size(Tk);
nt=size(t);
x_=1;
y=nt(1,1);

for j=1:nT(1,1)
    a_(x_:y,1)=a(:,j);
    t_(x_:y,1)=t(:,j);
    T_(x_:y,1)=Tk(j);
    x_=x_+1000;
    y=x_+1000-1;
end

```

Setting Parameters

```

opt=80e-6;
R=8.314;
kfragkre1=0;
x=2;
H3=inf;
S3=0;

```

Fitting

```

fomm = fitoptions('Method', 'NonLinearLeastSquares', 'StartPoint', [1.7e4,37,2.5e4,40], ...
    'Lower', [1000,1e1,1000,1e1], 'Upper', [1e6,1e2,1e6,1e2], ...
    'TolFun',1e-14,'TolX',1e-14,'MaxIter',5000,'MaxFunEval',2500,'Display','iter')

ftmm = fittype('polymfit_knowles2_multifit_T_Eyring(t,opt,H1,S1,H2,S2,H3,S3,x,T)',...
    'coefficients',{ 'H1', 'S1', 'H2', 'S2'},...
    'independent', { 't', 'T'},...
    'problem',{ 'opt', 'x', 'H3', 'S3'},...
    'options',fomm)

[f,gof,output] = fit ([t_,T_], a_, ftmm,'problem',{opt,x,H3,S3})

```

```

fomm =
    Normalize: 'off'
    Exclude: []
    weights: []
    Method: 'NonlinearLeastSquares'
    Robust: 'off'
    StartPoint: [17000 37 25000 40]
    Lower: [1000 10 1000 10]

```

```

    Upper: [1000000 100 1000000 100]
    Algorithm: 'Trust-Region'
    DiffMinChange: 1.0000e-08
    DiffMaxChange: 0.1000
    Display: 'Iter'
    MaxFunEvals: 2500
    MaxIter: 5000
    TolFun: 1.0000e-14
    TolX: 1.0000e-14

ftmm =
    General model:
    ftmm(H1,S1,H2,S2,opt,x,H3,S3,t,T) = polymfit_knowles2_multifit_T_Eyring(t,
        opt,H1,S1,H2,S2,H3,S3,x,T)

Success, but fitting stopped because change in coefficients less than tolerance (TolX).
    General model:
    f(t,T) = polymfit_knowles2_multifit_T_Eyring(t,opt,H1,S1,H2,S2,H3,S3,x,T)
    Coefficients (with 95% confidence bounds):
    H1 = 1.853e+04 (1.849e+04, 1.857e+04)
    S1 = 37.29 (37.16, 37.42)
    H2 = 2.745e+04 (2.733e+04, 2.757e+04)
    S2 = 39.24 (39.07, 39.41)
    Problem parameters:
    opt = 8e-05
    x = 2
    H3 = Inf
    S3 = 0

gof =
    sse: 15.3660
    rsquare: 0.9849
    dfe: 7996
    adjrsquare: 0.9848
    rmse: 0.0438

output =
    numobs: 8000
    numparam: 4
    residuals: [8000x1 double]
    Jacobian: [8000x4 double]
    exitflag: 2
    firstorderopt: 1.4888
    iterations: 36
    funcCount: 185
    cgiterations: 0
    algorithm: 'trust-region-reflective'
    message: [1x87 char]

```

Acquiring Results

```

H_fefn=f.H1*R;%%logA
S_fefn=f.S1*R;%%E
H_fefrag=f.H2*R;%%logA
S_fefrag=f.S2*R;%%E
H_fragre=f.H3*R;%%logA
S_fragre=f.S3*R;%%E

```



```

TS_fefn=Tk.*S_fefn;
TS_fefrag=Tk.*S_fefrag;
G_fefn=H_fefn-Tk.*S_fefn;
G_fefrag=H_fefrag-Tk.*S_fefrag;

ConfidenceInterval=confint(f);

confintH_fefn=ConfidenceInterval(:,1).*R;
confintS_fefn=ConfidenceInterval(:,2).*R;
confintH_fefrag=ConfidenceInterval(:,3).*R;
confintS_fefrag=ConfidenceInterval(:,4).*R;

R1=gof.sse;
R2=gof.rsquare;
R3=gof.dfe;
R4=gof.adjrsquare;
R5=gof.rmse;
message=output.message;

kb=1.38064852e-23;
h=6.62607004e-34;

kfekfn=(kb.*Tk./h).*exp(-H_fefn./(Tk.*R)+S_fefn./R);
kfekfrag=(kb.*Tk./h).*exp(-H_fefrag./(Tk.*R)+S_fefrag/R);
kfragkre=(kb.*Tk./h).*exp(-H_fefrag./(Tk.*R)+S_fefrag/R);

```

Plotting

```

nT=size(Tk);
cor_i = [0 0 1];
cor_f = [1 0 0];
var = (cor_f - cor_i)/(nT(1)-1);
cor = cor_i;
for ii=2:(nT(1))
    cor=[cor; cor(end,:) + var];
end

F=polymfit_knowles2_multifit_T_Eyring(t_,opt,H_fefn/R,S_fefn/R,H_fefrag/R,S_fefrag/R,H_fefragre,S_fefragre,x,T_);

x_=1;
y=nt(1,1);
fig=figure;
for i=1:nT(1)
    Results(:,3*i-2)=t_(x_:y,1);
    Results(:,3*i-1)=a(:,i);
    Results(:,3*i)=F(x_:y,1);
    plot(t_(x_:y,1),F(x_:y,1),'color',cor(i,:))
    hold on
    plot(t(:,i),a(:,i),'.','MarkerEdgeColor',cor(i,:));
    hold on
    lgdt1{2*i-1}=sprintf('%4.0f %c',T(i),176);
    lgdt1{2*i}=sprintf('%4.0f %c',T(i),176);

```

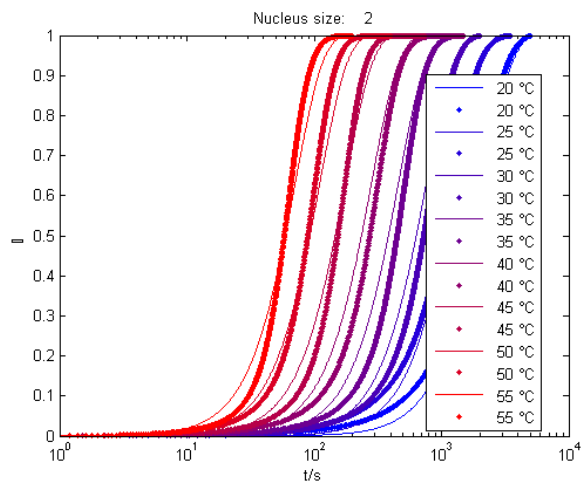
```

hold on;
x_=x_+1000;
y=x_+1000-1;
end
legend(lgdtt1,'Location','best');
ttl=sprintf('Nucleus size: %4.0f',x);
title(ttl);
axis([1 10000 0 1])
y1b1=sprintf('%c',945);
ylabel(y1b1);
xlabel('t/s');
set(gca,'xscale','log')
% saveas(fig,'C:\Users\Owner\Google Drive\Doctorat\1st year\Besenius\Moments
model\Besenius_Fitroutine_T_var_unseeded_multifit_Eyring\Model_data_overlay.png')
% saveas(fig,'C:\Users\Owner\Google Drive\Doctorat\1st year\Besenius\Moments
model\Besenius_Fitroutine_T_var_unseeded_multifit_Eyring\Model_data_overlay.eps')
hold off

save('T_var_kopt_nuc_elong_frag_Nuclide_fix_multifit_Eyring')
toc % stop timer

```

Elapsed time is 3.027391 seconds.



```
end
```

Chapter 3. Controlling Morphology and Mechanical Properties of a Hydrogel Using a Fuel-Driven Reaction Cycle

Abstract: In this Chapter, we will show how an aldehyde-targeting reaction cycle can be used to control hydrogel formation. By adding dithionite, hexamine and glucono- δ -lactone to an aldehyde containing sugar-based hydrogelator we see its complete dissolution after 5 to 10 minutes due to the conversion of aldehyde into an α -hydroxy-sulfonate. Hexamine hydrolyses into formaldehyde, mediated by acid catalysis, which will react with the sulfonate, bringing back the original hydrogel. The amount of gluconolactone, *i.e.* catalysis rate, will influence the reaction cycle kinetics, which by itself controls the morphological and mechanical properties of the final material. Lastly, the syneresis property of the hydrogel is explored to develop a methodology for waste removal, that allows us to repeat the cycle up to thirteen times.

This chapter has been published in:

Singh, N.; Lainer, B.; Formon, G. J. M.; De Piccoli, S.; Hermans, T. M. Re-Programming Hydrogel Properties Using a Fuel-Driven Reaction Cycle. *J. Am. Chem. Soc.* **2020**, *142* (9), 4083–4087. <https://doi.org/10.1021/jacs.9b11503>.

3.1 Introduction

Biological systems use chemical reaction cycles to precisely control multiple mechanisms, such as microtubule polymerization during mitosis, as has been discussed in Section 1.1. These reaction cycles are responsible for the circadian rhythm, for example, which synchronizes the metabolism and cell replication with the 24 hours in a day. These cycles rely on the accumulation and subsequent decrease in concentration of metabolites that control or signal different functions. The subsequent repetition of these cycles leads to oscillations that are responsible for the periodicity in living systems.⁸⁵

Chemists have been capable of replicating these oscillations, but in a limited fashion because there are specific minimal requirements for autonomous chemical oscillations that are not easily achievable in man-made chemical systems.¹⁸⁸ Examples of (supra)molecular oscillators using enzymatic networks,¹⁸⁹ autocatalysis in small organic molecules,¹⁹⁰ and redox reactions coupled to cooperative polymerization,⁸⁶ have been demonstrated recently but these observations are still elusive. Some success has been found in developing DNA string displacement reaction networks that are capable of oscillations,¹⁹¹⁻¹⁹³ signaling,^{194,195} spatial pattern formation,¹⁹⁶ and reconfigurable nanotubes.^{87,88} However, DNA is a very powerful toolbox, with a much higher degree of control than fully synthetic systems.

With the advent of dissipative supramolecular polymerization, chemists have been able to perform at least one ‘oscillatory’ cycle of disassembly–assembly–disassembly driven by a chemical reaction cycle, some examples have been listed in Section 1.3.⁸⁴ These single cycles seem very simple when compared to chemical oscillations, however they have to be carefully designed and are an important stepping stone for more complex phenomena like non-equilibrium steady-states¹¹⁵ and supramolecular oscillations and patterns.⁸⁶

Since the field of fully synthetic fuel-driven reaction cycles is still new, the variety of chemistries being used is very small when compared to the plethora of reactions that exist in the toolset of synthetic chemists. The opportunity of growth within this field is immense and the design of new reaction cycles is of utmost importance for the development of man-made dissipative self-assembly.⁹⁰ With the goal to expand towards this route, a new dissipative

reaction cycle targeting an aldehyde-containing hydrogelator will be discussed. Catalytic hexamine hydrolysis is used to drive this cycle out-of-equilibrium, with the rate of catalysis being directly correlated with the final morphology and mechanical properties of the hydrogel. Finally, syneresis (where a gel can expel the solvent from its matrix) of the hydrogel is explored to repeat the cycle by waste-removal.

3.2 Stimuli-Responsive Hydrogel and Reaction cycle

The previously reported,⁸ sugar-based aldehyde-containing hydrogelator, **SachCHO**, forms micron-sized fibers in water that are visible by the naked eye, Figure 3.1. Sodium dithionite (DT) reacts with aldehydes forming α -hydroxy-sulfonates,¹⁹⁷ so by treating a **SachCHO** hydrogel with a DT solution, the aldehyde is converted to **SachSO₃⁻** (this reaction is an equilibrium). Since the sulfonate is completely soluble in water, the hydrogel becomes a clear solution 5–10 minutes after it is treated with dithionite, Figure 3.1. To revert back to the hydrogel, a more reactive aldehyde has to be added to snatch the sulfonate group from **SachSO₃⁻**. Formaldehyde, being one of the most reactive aldehydes, was used to convert **SachSO₃⁻** to **SachCHO** in a few minutes. However, DT and formaldehyde react with each other and if the goal is to achieve an autonomous reaction cycle, they cannot be added simultaneously to the reaction mixture. To that end, hexamine (HMTA), a compound that is hydrolyzed into formaldehyde and ammonia, was used to delay the back reaction. The HMTA decomposition reaction is acid-catalyzed, so glucono- δ -lactone (GdL) is utilized for its slow hydrolysis into gluconic acid. If DT, HMTA and GdL are added simultaneously to a **SachCHO** hydrogel, **SachSO₃⁻** is obtained in 5–10 minutes, yielding a clear solution. After 20 to 60 minutes (depending on GdL concentration) the hydrogel is obtained once again by the reaction of formaldehyde with the sulfonate, driven by the acid-catalyzed hydrolysis of HMTA, Figure 3.1. Experimental details in Sub-Section 3.10.1.3.

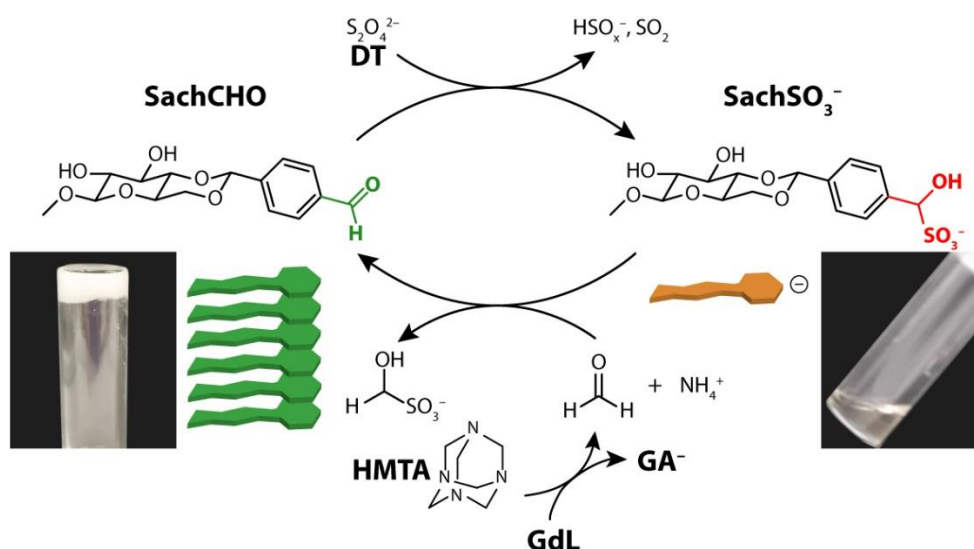


Figure 3.1 – Reaction cycle targeting the aldehyde-containing hydrogelator **SachCHO**.

3.3 Gelation Mechanism and Kinetics

To obtain an insight into the polymerization of **SachCHO**, before studying the full reaction cycle, the kinetics and thermodynamics of self-assembly (hydrogelation) were studied. To attempt to obtain the thermodynamic parameters of **SachCHO** assembly, the temperature-dependent behavior was measured by UV/Vis spectroscopy, following the optical density at 500 nm (translated into turbidity of the sample) as a function of temperature. We assume that the turbidity is linear to the degree of polymerization of **SachCHO** since the final hydrogel is completely opaque. Impressively, the self-assembly showed a 70 °C hysteresis at a heating/cooling rate of 10 K/min that decreased to 50 °C at 1 K/min and 20 °C when there was a 5 minute equilibration at each temperature point, Figure 3.2. This large hysteresis means that the self-assembly is very cooperative,³³ and is not under thermodynamic control, meaning that no quantitative thermodynamic parameters can be obtained.¹⁹⁸

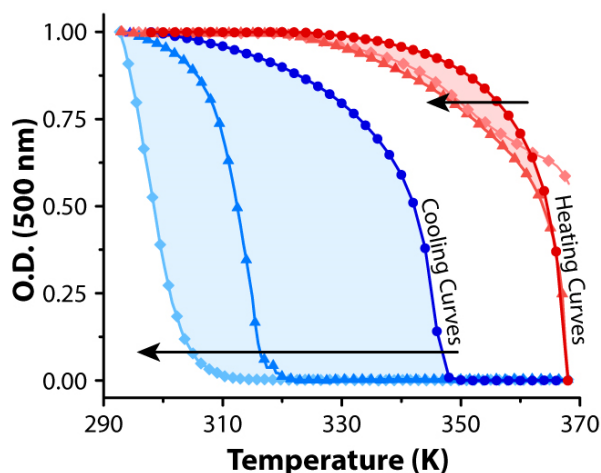


Figure 3.2 – Heating/Cooling curves of **SachCHO** using UV/Vis turbidity measurements. Heat/Cool rates: 10 K/min (\blacklozenge), 1 K/min (\blacktriangle), and 5 min hold at each temperature (\bullet). Arrows indicate increasing rate of heating/cooling.

To further gain insight into the **SachCHO** assembly mechanism, the kinetics of the chemically triggered hydrogelation was studied. For that, a solution containing **SachSO₃⁻** was treated with 50 to 100 equivalents of formaldehyde, to quickly convert the sulfonate into aldehyde and induce hydrogelation, which was followed by measuring the turbidity of the sample by UV/Vis spectroscopy, Figure 3.3–A (experimental details in Sub-Section 3.10.1.7). The kinetics of assembly, which also included seeded experiments, showed the typical behavior of nucleation–elongation aggregation. A lag-time followed by a fast increase in turbidity, indicated that the kinetic barrier of nucleation was strong, but elongation was fast. This was further confirmed by seeding experiments, that yielded fast aggregation, overcoming the nucleation obstacle, Figure 3.3–A. The same way as performed in Chapter 2, the half-times of polymerization ($\tau_{1/2}$) were plotted against the initial monomer concentration, Figure 3.3–B. The slope of the log-log plot (γ) was found to be -3.6 (~ -3.5) which would indicate towards either a simple nucleation–elongation mechanism with nucleus size of 7, or a case where secondary nucleation (where the existing fibers catalyze the creation of new nuclei) with secondary nucleus size of 6 plays an important role in **SachCHO** aggregation.⁶

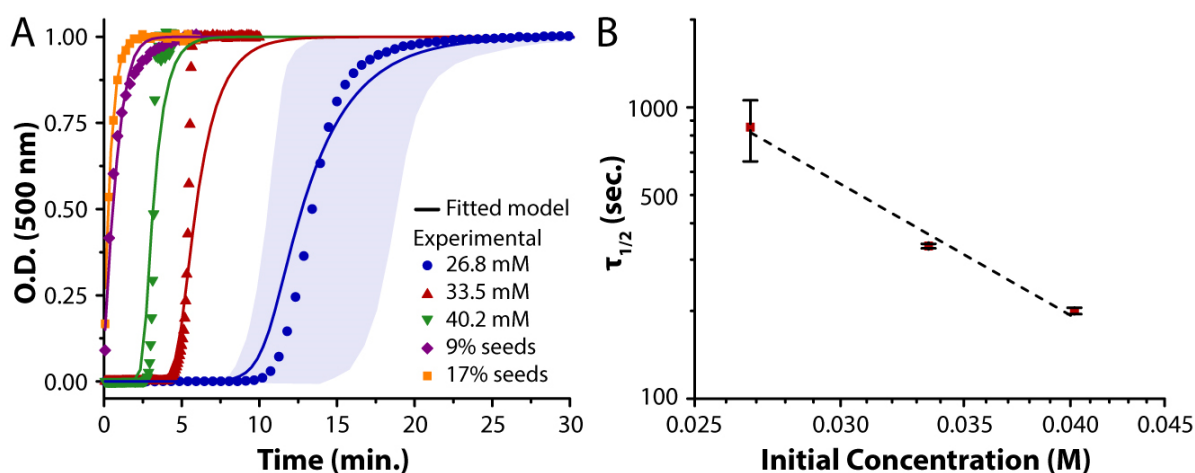


Figure 3.3 – **A** – Kinetics of the chemically triggered gelation of **SachCHO**. Symbols are the representative experimental data, and the lines are the global-fit of the supramolecular polymerization model considering nucleation–elongation–secondary nucleation. The faded blue region delineates the upper/lower boundaries of triplicate experiments. **B** – Log-log plot of the half-times of polymerization as a function of initial monomer concentration. The squares are the experimental points and the error bars are the standard deviation over three replicates. The dashed line is the exponential fit of the type: $\tau_{1/2} = a m_0^\gamma$. The scaling exponent is found to be $\gamma = -3.61$.

The global fitting of the kinetic data in Figure 3.3–A which included secondary nucleation (setting primary and secondary nucleus size as 6) yielded better fits than the mechanism with solely nucleation–elongation. Further evidence of secondary nucleation is that when dithionite is added in an insufficient quantity to destroy all the existing **SachCHO** fibers, and GdL and HMTA are also added, new fibers are formed on top of the pre-existing ones, forming brush-like structures, Figure 3.9 in the Appendix. Similarly to Chapter 2 a cooperative polymerization model, initially developed by Knowles and co-workers to study amyloid fibril polymerization, was used, but this time with secondary nucleation.^{6,182,199} To fit the data, a home-built code in MATLAB® was employed (Sub-Sections 3.10.3 and 2.8.4, for model derivation and code respectively), and the results were compared with fitting acquired using the *amylofit* online toolbox.^{vi} The kinetic rate constant obtained by both methods were similar, but slightly different probably due to differences in the fitting algorithm. The results are listed in Table 3.1.

^{vi} <https://www.amylofit.ch.cam.ac.uk/fit>

Table 3.1 – List of the kinetic parameters obtained by the global fitting of the kinetic data. The errors to the fit presented in the table are directly obtained from the fitting algorithms.

Parameter	Home-built code	<i>amylofit</i>
n_1 and n_2	6	6
k_{n1}	$2.84 \pm 0.64 \cdot 10^{-10} L^5 mol^{-5} s^{-1}$	$4.79 \begin{pmatrix} +0.59 \\ -1.99 \end{pmatrix} \cdot 10^{-5} L^5 mol^{-5} s^{-1}$
k_{n2}	$4.81 \pm 0.11 \cdot 10^4 L^6 mol^{-6} s^{-1}$	$1.75 \begin{pmatrix} +0.19 \\ -0.15 \end{pmatrix} \cdot 10^4 L^6 mol^{-6} s^{-1}$
k_e	$1.69 \pm 0.02 \cdot 10^3 L mol^{-1} s^{-1}$	$1.67 \begin{pmatrix} +0.12 \\ -0.16 \end{pmatrix} \cdot 10^3 L mol^{-1} s^{-1}$

Where n_1 and n_2 are the primary and secondary nucleus size, k_{n1} is the rate constant of primary nucleation, k_{n2} the secondary nucleation rate constant and k_e the elongation rate constant. The depolymerization rate constant, k_{off} , was set to a global constant of $10^{-9} s^{-1}$ (discussion in Sub-Section 3.10.3). The secondary nucleation and elongation rate constants are of the same order of magnitude, for both fitting methods, with the biggest difference being the primary nucleation rate. This difference arises from the different fitting algorithms used by both methods. However, *amylofit* is a black box software, and we do not know how it works, so it is difficult to probe the differences that would cause different fitting results. From the numerical parameters, it can be said that the degree of cooperativity of **SachCHO** assembly is very high, with the rate of primary nucleation being many orders of magnitude lower than the rate of elongation and secondary nucleation. This means that the formation of a primary nucleus is highly kinetically unfavorable, giving a long lag-time before elongation, 8–15 minutes for 26.8 mM (Figure 3.3). However, this lag-time decreases quickly when increasing concentration because nucleus size is relatively big (6). Once nucleation occurs, elongation and secondary nucleation take over and the conversion of monomers into polymers happens very quickly.

3.4 Kinetics of the Full Reaction Cycle

Now that the mechanism and kinetics of **SachCHO** polymerization are known, the kinetics of the full reaction cycle will be studied. Practically speaking, a **SachCHO** hydrogel was prepared by heating a suspension of the hydrogelator in water adjusted to pH 8, until dissolution, followed by slow cooling, so uniform long fibers are present. Next, a mixture of

dithionite (3.6 equivalents), HMTA (3.5 equivalents, and glucono- δ -lactone (0.9 to 7 equivalents) was added on top of the hydrogel (experimental details in sub-section 3.10.1.3 and 3.10.1.5). Each hexamine molecule releases six formaldehyde equivalents into solution, so the effective formaldehyde released is ~ 20 equivalents in relation to **SachCHO**, this large amount is needed for two reasons: first, formaldehyde needs to react with the remaining dithionite present in solution; second, since the reaction between aldehyde and sulfonate is an equilibrium, a large amount of formaldehyde would ensure the completion of the reaction, shifting the equilibrium towards **SachCHO**. In maximum 20 minutes, **SachCHO** is fully converted in **SachSO₃⁻**, Figure 3.4, rendering a clear solution. The kinetics of the next phase of the reaction cycle, i.e. HMTA degradation and conversion of sulfonate into aldehyde, is fully dependent on the amount of GdL added, with higher concentration giving a faster rate of hydrolysis, thus faster **SachSO₃⁻** to **SachCHO** conversion, Figure 3.4. A minimum threshold of GdL (or acid) is needed to fully hydrolyze HMTA, as we can see that adding 46.8 mM (0.85 equivalents) is not enough to fully convert **SachSO₃⁻** to **SachCHO**, even after 48 hours.^{vii} [GdL]=93.6 mM (1.7 equivalents) leads to full conversion in ~ 100 minutes, reaching 90% at ~ 75 minutes. The times for full conversion steadily decrease with increasing GdL, reaching a plateau at 312 and 374 mM, with full conversion happening at ~ 60 minutes. This happens because the pH drop caused by GdL is around the same from 312 mM and up (Figure 3.10 in Appendix). The influence of GdL concentration on the kinetics of **SachSO₃⁻** to **SachCHO** conversion is further confirmed by the first order rate constants obtained by the semi-log plot of mole fraction of **SachSO₃⁻** in function of time, Figure 3.11 and Table 3.2 in Appendix. The apparent rates increase with increasing amount of glucono- δ -lactone, reaching a plateau at 312 mM.

^{vii} Data not shown.

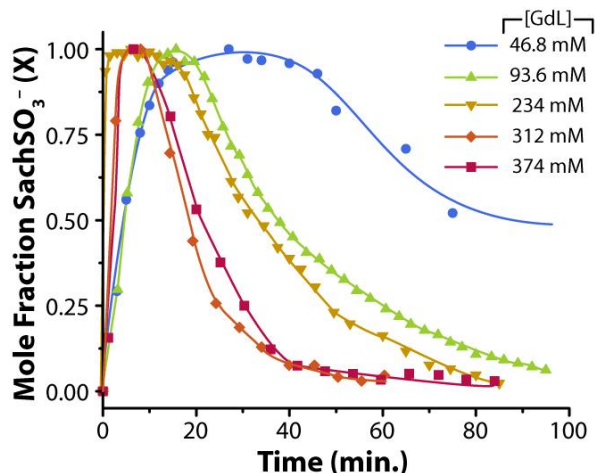


Figure 3.4 – Mole fraction of SachSO_3^- in function of time, for different [GdL]. Kinetics of the full reaction cycle, i.e. DT (190 mM), GdL (variable, see figure legend) and HMTA (190 mM) are added simultaneously to a SachCHO (53.6 mM) hydrogel. Data obtained by quantitative NMR experiments.

Next, the kinetics of gelation for the full-reaction cycle, was studied by UV/Vis optical density measurements, relating turbidity to hydrogel conversion. So, the same procedure as above was followed: a mixture of dithionite (3.6 equivalents), HMTA (3.5 equivalents), and glucono- δ -lactone (0.9 to 7 equivalents) was added on top of a heat/cool hydrogel (experimental methods in sub-section 3.10.1.7). The turbidity of the sample was then followed for different [GdL], Figure 3.5–A. In this case, gelation takes 30 to 90 minutes, depending on the amount of GdL, compared to 5 to 20 minutes with just formaldehyde, Figure 3.3. Three characteristic times of gelation can be identified, where optical density reaches 10%, 50% and 90% of the maximum: $\tau_{0.1}$ indicates the onset of gelation, or nucleation, $\tau_{0.5}$ indicates the half-time of gelation where the elongation is the dominant phenomenon, $\tau_{0.9}$ indicates the time where the gel is almost fully formed and ripening/depletion of SachCHO is dominant (see Figure 3.5–B). The same trend as observed for SachSO_3^- conversion can be identified, higher [GdL] leads to faster onset of gelation with all characteristic times decreasing, until a plateau is reached for [GdL] > 312 mM. Interestingly, the difference between these characteristic times also decrease with increasing [GdL], meaning that not only the nucleation process is influenced by glucono- δ -lactone but also the gelation process itself is faster with higher amount of acid.

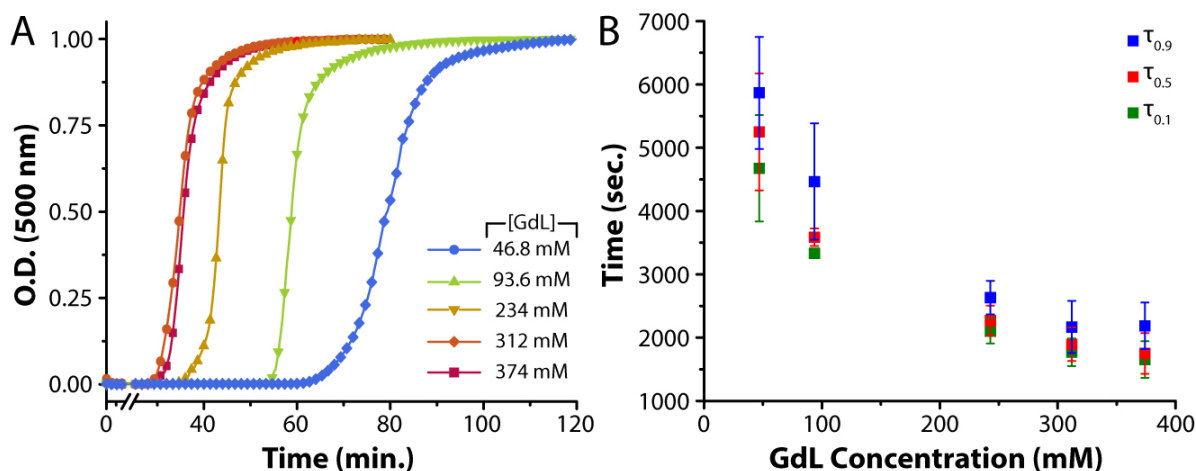


Figure 3.5 – Kinetics of gelation for the full reaction cycle, i.e. DT, GdL and HMTA are added simultaneously to a SachCHO hydrogel. **A** – Normalized optical density in function of time for different GdL concentrations. **B** – Different characteristic times in function of GdL concentration. $\tau_{0.1}$, $\tau_{0.5}$ and $\tau_{0.9}$ represent the times at which optical density reaches 10%, 50% and 90% of the maximum, respectively. Error bars are the standard deviation over three replicates.

This reaction cycle allows us to gain temporal control over gel formation, with a direct correlation between GdL mediated catalysis of HMTA hydrolysis and the kinetics of the reaction cycle and gelation.

3.5 Kinetic Control of Morphology and Mechanical Properties

Since [GdL] is directly responsible for an increase in gelation onset and kinetics, we investigated the morphology of SachCHO fibers, obtained by heat/cool and the reaction cycle, imaged by electron and confocal microscopy, Figure 3.6 (experimental details in sub-sections 3.10.1.9 and 3.10.1.11). The thermogel (prepared by heating/cooling, sub-section 3.10.1.2) presented long thin fibers with $\sim 2 \mu\text{m}$ diameter and hundreds of microns long, Figure 3.6–A&B. However, when the gel is prepared by the reaction cycle, with a low [GdL] amount, the fibers become shorter and raggedy and grow from central nuclei forming flower-like assemblies, Figure 3.6–C&D. When a higher amount of glucono- δ -lactone is used, 374 mM, the structures become much more branched, producing fractal aggregates, Figure 3.6–E&F. This happens probably because the heat/cool gel is the thermodynamic conformation of SachCHO, with slow nucleation and growth. With the reaction cycle, the release of formaldehyde is relatively fast, and the concentration of the hydrogelator grows very rapidly. Since the rate of nucleation is much slower than elongation and secondary nucleation, fewer

nuclei are formed and multiple fibers grow from a single nucleus. For higher amount of GdL, the SachSO_3^- conversion is so fast that secondary nucleation takes over, with elongation from a central nucleus and new fibers branching from pre-existing ones.

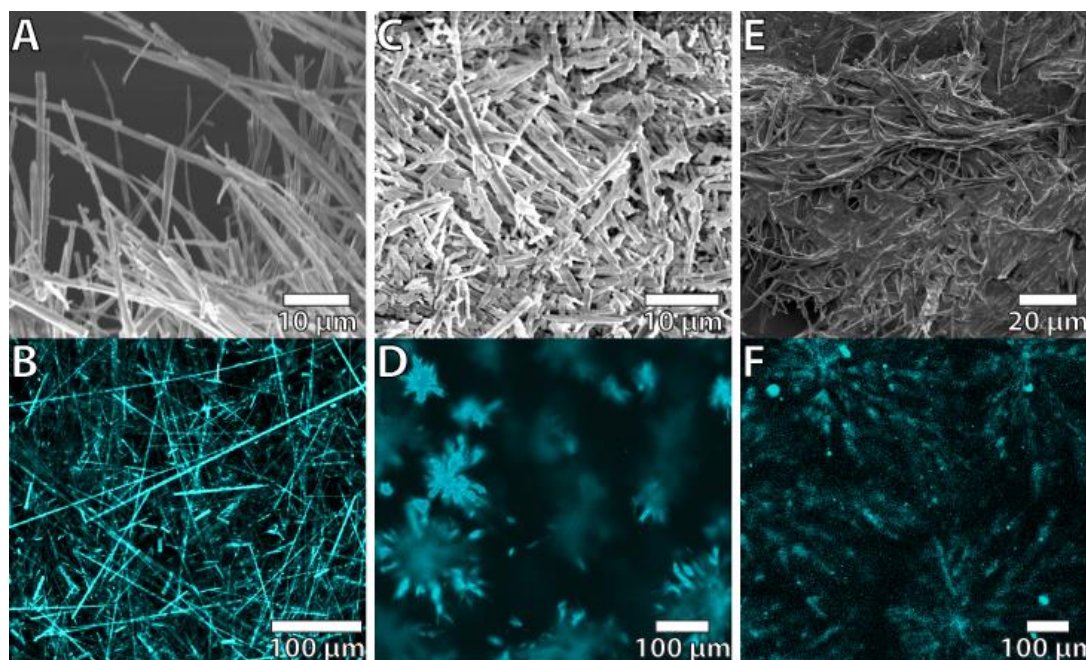


Figure 3.6 –SEM photographs (top) and confocal microscopy photographs (bottom) of: **A&B** – The thermogel, prepared by heat/cool; **C&D** – Hydrogel formed by the full reaction cycle using $[\text{GdL}] = 234 \text{ mM}$; **E&F** – Hydrogel formed by the full reaction cycle using $[\text{GdL}] = 374 \text{ mM}$.

The different morphologies arising from the different preparation conditions were further confirmed by powder X-Ray Diffraction (XRD) of the xerogels, Figure 3.12 and Table 3.3 (Sub-Section 3.10.1.10 for experimental details). The thermally annealed hydrogel shows peaks at 1.15 nm and 0.648 nm, likely related to inter-columnar distances, and at 0.38 nm, arising from the intermolecular stacking distance within the columns. The XRD patterns of the gels made with 93.6 mM and 234 mM $[\text{GdL}]$ do not differ substantially from the thermogel. However, in the hydrogel prepared with 374 mM glucono- δ -lactone two new peaks appear at 0.325 and 0.305 nm indicating smaller intermolecular packing distances. These results show that GdL concentration, and thus the rate of catalysis, have a direct influence on hydrogel morphologies, a phenomenon already demonstrated in the past.^{59,200}

Interestingly, the amount of GdL not only influences the reaction cycle kinetics and the resulting fiber morphologies, it also influences the mechanical properties of the hydrogel. Rheology shows that the gelation time decreases with increasing $[\text{GdL}]$, which was already

known, Figure 3.7. Additionally, the maximum shear storage modulus increases with increasing amount of glucono- δ -lactone, Figure 3.7, going from ~ 110 Pa for $[\text{GdL}] = 46.8$ mM to ~ 2100 Pa for $[\text{GdL}] = 374$ mM (thermally annealed hydrogel has $G' \sim 800$ Pa). This means that the faster kinetics, with increasing $[\text{GdL}]$, lead to morphological changes within the hydrogel which are directly responsible for the gel mechanical properties. The branchier structures obtained with 374 mM $[\text{GdL}]$ lead to a tighter gel resulting in a stronger material.

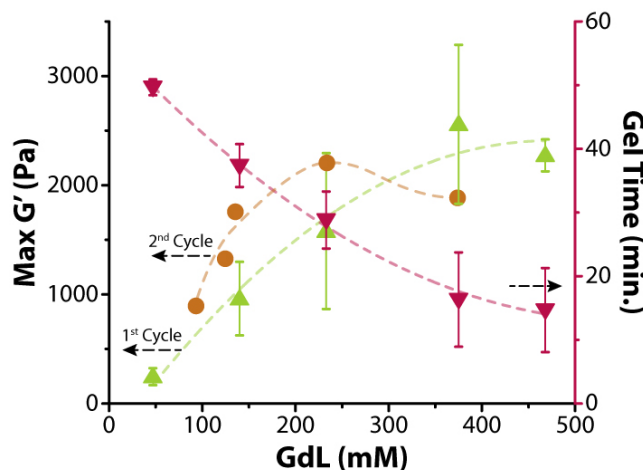


Figure 3.7 – Maximum shear storage modulus of first and second cycle (left) and gelation time measured by rheology (right) in function of GdL concentration. Error bars are the standard deviation over triplicate experiments.

Interestingly, if the cycle is performed with a low GdL amount, 140 mM ($G' \sim 1100$ Pa), the system can be re-fueled with DT, HMTA and varying amounts of GdL to reset the material and obtain a hydrogel with new mechanical properties. The storage moduli of the second cycle are dependent on the $[\text{GdL}]$ in the re-fueling, Figure 3.7 (2nd cycle). The cycle could not be further repeated because of waste accumulation that hinders re-fueling and re-formation of the hydrogel.

The properties of the **SachCHO** hydrogel obtained by the chemically fueled reaction cycle are dependent on the catalysis rate, driven by GdL, yielding different gel morphologies that are responsible for increasing storage modulus when $[\text{GdL}]$ increases.

3.6 Syneresis

Lastly, **SachCHO** presents an interesting property called syneresis,²⁰¹ which permits the solvent to be expelled from the hydrogel matrix by mechanical pressure. Since all the waste

products and fuels are water soluble, this property was explored to remove waste from the system, allowing to repeat the reaction cycle multiple times, Figure 3.8–A. Essentially, a chemically fueled hydrogel was formed inside a syringe, equipped with a cotton swab at the tip, [SachCHO] = 53.6 mM. After the completion of the reaction cycle, 60–70 minutes, the piston of the syringe was pressed, expelling all the solvent (with waste products) retaining SachCHO fibers inside. Then a solution containing DT (121 mM), HMTA (190 mM) and GdL (312 mM) was added to the syringe to re-fuel hydrogel formation (methodology in Sub-Section 3.10.1.8).^{viii} After 60 to 70 minutes the gel is re-formed, with the same structural integrity as the original one.

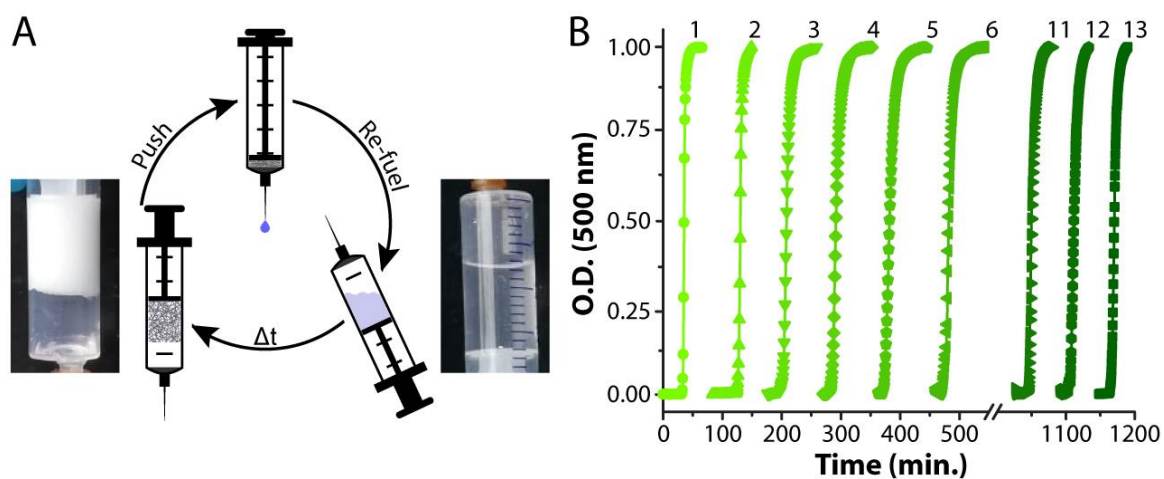


Figure 3.8 – A – Scheme of the syneresis-driven waste removal. In clockwise direction, chemically fueled SachCHO gel made inside a syringe (bottom left), solvent with the soluble waste products are pushed out of the system while the hydrogel fibers stay trapped (top), dissolution of fibers after refueling ([DT] = 121 mM, [HMTA] = 190 mM, [GdL] = 312 mM, bottom right), and re-formation of gel after a defined time. **B** – UV/Vis turbidity measurements of the syneresis cycles. Up to 13 cycles can be repeated by refueling and subsequent waste removal.

This cycle could be repeated up to thirteen times, and the kinetics of every cycle was very similar, Figure 3.8–B, with $\tau_{0.9}$ and the rate of elongation staying constant after the first sequence, Figure 3.13 in Appendix. Showing that this method maintains the integrity of gelation at each repetition. This method of waste removal surmounts the common hurdle that is waste accumulation in fuel-driven systems,⁹⁰ that usually impedes the reaction cycle to be repeated multiple times and requires creative problem-solving to be overcome.¹¹⁵

^{viii} To overcome the partial solubility of SachCHO in water, 5.3 mM of building block had to be added together with the fuels.

3.7 Conclusions

We have shown a new fuel-driven reaction cycle that powers the gel-sol-gel transition in an aldehyde containing hydrogel. The fuel ‘cocktail’ contains sodium dithionite to solubilize the gel and hexamine and glucono- δ -lactone to re-form the material. Since GdL catalyzes HMTA hydrolysis, its concentration influences the kinetics of the system, the final hydrogel morphologies, and the mechanical properties of the resulting material. This is an interesting tool to control hydrogel properties and kinetics by simply varying a single parameter. These properties can be reset and re-programmed by either performing a second cycle, or by purifying the material through syneresis and repeating the cycle up to thirteen times.

Overall, this approach gives new parameters to control dissipative self-assembly as well as adding a new chemistry to the library of fully synthetic reaction cycles (Sub-Section 1.3.1).⁹⁰ The methodology that was developed can open the door to new smart materials that have their mechanical properties tuned according to the environmental needs.

3.8 Appendix

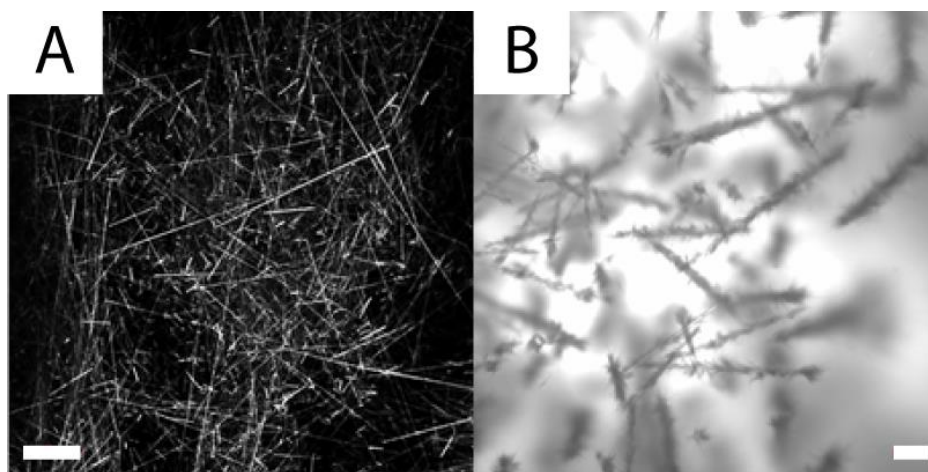


Figure 3.9 – Confocal image proving the secondary nucleation phenomenon by formation of new fibers on top of already existing fibers giving brush-like morphology. **A** – Straight needle like fibers present in the thermally annealed gel. **B** – Brush-like assemblies formed after a reaction cycle chemically fueled with an insufficient amount of dithionate to dissolve all the primary fibers of the thermally annealed gel, HMTA and GdL. The remaining fiber act as nuclei for the formation of new fibers once the SachSO_3^- is converted back to SachCHO giving brush like morphologies. Scale bar: 100 μm

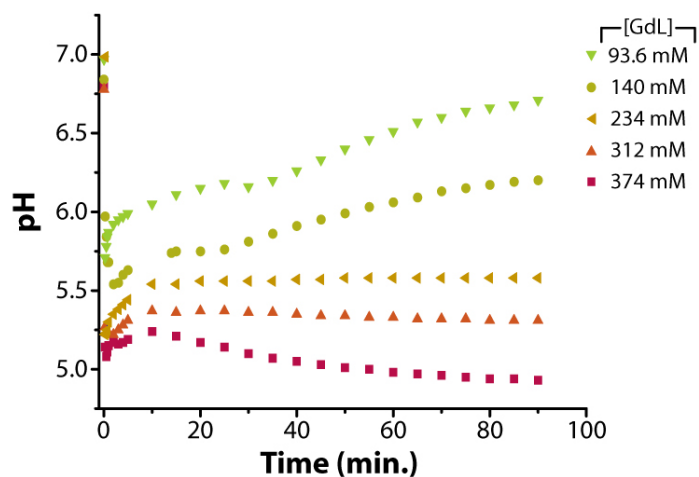


Figure 3.10 – pH in function of time for different GdL concentrations. Note: the pH increases overtime because HMTA hydrolysis releases ammonia.

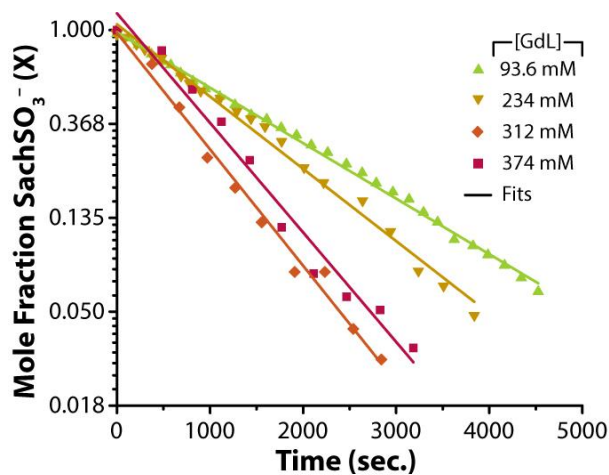


Figure 3.11 – Semi-log plot of the mole fraction of SachSO_3^- (from quantitative NMR experiments) as a function of time. Apparent first order rates could be extracted. Symbols represent the experimental data; solid lines are the linear fits from the semi-ln plot. Results of the apparent first-order rate constants found in Table 3.2.

Table 3.2 – Apparent first-order rate constants of SachSO_3^- to SachCHO conversion for different [GdL]. Obtained from fit in Figure 3.11.

[GdL] (mM)	$k_{app} (s^{-1})$
93.6	$5.91 \pm 0.05 \cdot 10^{-4}$
234	$7.70 \pm 0.17 \cdot 10^{-4}$
312	$1.24 \pm 0.04 \cdot 10^{-3}$
374	$1.17 \pm 0.06 \cdot 10^{-3}$

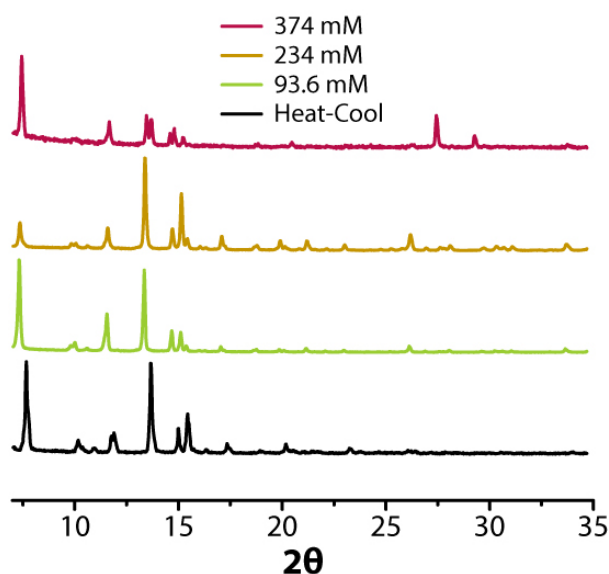


Figure 3.12 – Powder X-Ray Diffraction (XRD) patterns of the different xerogels (lyophilized) obtained from different conditions. The peak list is in Table 3.3.

Table 3.3 – List of the XRD peaks for the xerogels obtained from different conditions.

Peak #	Heat-Cool		93.6 mM		234 mM		374 mM	
	2θ	d (nm)	2θ	d (nm)	2θ	d (nm)	2θ	d (nm)
1	7.671	1.153	7.322	1.208	7.377	1.199	7.433	1.190
2	11.758	0.753	11.534	0.768	11.608	0.763	11.664	0.759
3	11.907	0.744	13.346	0.664	13.421	0.660	13.477	0.657
4	13.640	0.650	14.698	0.603	14.712	0.603	13.696	0.647
5	14.991	0.591	15.122	0.586	15.178	0.584	14.605	0.607
6	15.434	0.574	15.359	0.577	15.397	0.576	14.805	0.599
7	17.340	0.512	17.060	0.520	17.079	0.519	15.234	0.582
8	20.201	0.440	26.156	0.341	26.170	0.341	27.465	0.325
9							29.278	0.305

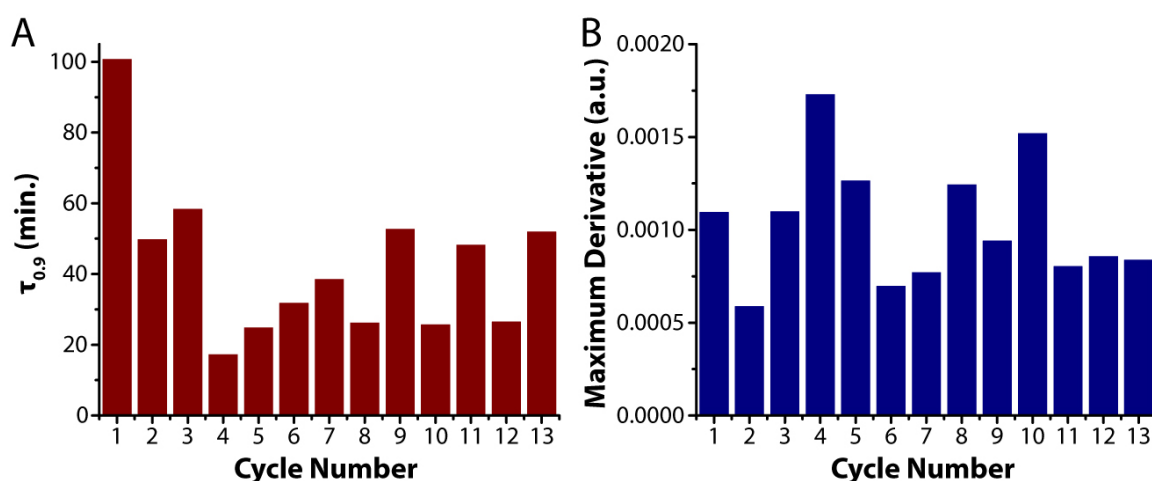


Figure 3.13 – A – Times of gelation for each syneresis recycling cycle, $\tau_{0.9}$ indicates the time where 90% of maximum Optical Density at 500 nm is reached. The gelation times remain similar for every cycle after the first.

B – Maximum derivative (or slope) of the gelation curves for each syneresis cycle. The gelation rate remains similar for every cycle.

3.9 Acknowledgements

Dr. Nishant Singh developed the reaction cycle and concept. Dr. Nishant Singh and Bruno Lainer synthesized **SachCHO** and **SachSO₃⁻**, optimized the parameters and performed kinetic and rheological experiments. Georges Formon performed kinetic experiments and the numerical analysis. Serena De Piccoli performed the syneresis experiments. Prof. Thomas Hermans and Dr. Nishant Singh supervised the research.

This chapter was written by Georges Formon based on the publication: Singh, Nishant, Lainer, Bruno, Formon, Georges J. M., De Piccoli, Serena, and Hermans, Thomas M. “Re-Programming Hydrogel Properties Using a Fuel-Driven Reaction Cycle.” *J. Am. Chem. Soc.* 142, no. 9 (2020): 4083–87. <https://doi.org/10.1021/jacs.9b11503>

3.10 Materials and Methods

3.10.1 Materials and Experimental procedures

3.10.1.1 Materials

The reagents and deuterated solvents were purchased from TCI chemicals, Fischer Scientific or Sigma Aldrich and used without further purification. Terephthalaldehyde, Methyl α -D-Glucopyranoside, Hexamethylenetetramine, p-Toluidine were bought from TCI Belgium, Formaldehyde solution from Fischer Scientific and Glucono delta-lactone, Sodium Dithionite technical grade 85%, D₂O from Sigma-Aldrich.

3.10.1.2 Thermally annealed gel

A suspension of **SachCHO** (54mM unless mentioned otherwise) in pH 8 water was heated to around 80-90°C until a clear solution was formed. This solution was allowed to cool down at room temperature yielding a white gel able to support its weight when inverted.

3.10.1.3 Transient Cycles

To a thermally annealed gel of **SachCHO** (30 mg in 1.5 mL pH 8 water), the fuels: HMTA-48 mg unless mentioned otherwise, appropriate amount of GdL (see main text), Sodium

dithionite (DT-60 mg unless mentioned otherwise), dissolved in 300 μ L of pH 8 water were added. The thermally annealed gel dissolves and reforms into a gel after a certain time dependent on [GdL]. This method of creating transient cycles was used for NMR kinetic experiments, UV-Vis experiments, Rheology experiments (except for 2 cycle experiments).

3.10.1.4 pH experiments

A VWR Model 110 pH meter was used to record the pH measurements.

The pH was recorded at different time intervals for different systems involving GdL, GdL+HMTA, DT+GdL+HMTA, DT+GdL+HMTA+SachCHO (full transient cycle, and for two consecutive cycles with 2 times fuels addition).

3.10.1.5 NMR experiments

(^1H and ^{13}C , and kinetic measurements using a coaxial tube with an external reference.) NMR spectra were recorded on a **Bruker UltraShield Plus Avance III** NMR instrument at 25°C.

Thermally annealed gels (10 mg in 500 μ L D₂O pH 8) were made in a NMR tube. To this tube was introduced a co-axial tube containing p-toluidine as an external reference (0.97 mg in 200 μ L). The fuels dissolved in 100 μ L (HMTA-16 mg, GdL appropriate amounts, DT-20 mg) D₂O pH 8 were added to the NMR tube and spectra were recorded for specified time intervals. The peaks of the aldehyde-proton (9.99 ppm) and the sulfonate-proton (5.77 ppm) were used to follow the reaction kinetics.

3.10.1.6 Rheology experiments

Rheology experiments were performed on a Thermofischer Scientific MARS 40 rheometer using parallel plate geometry with plate distance of 1.8 mm, $\gamma = 0.08\%$, $\nu = 1\text{Hz}$ at 25°C.

Fuels (dissolved in 300 μ L) were added to thermally annealed gels (1.5 mL) and upon dissolution the solution was transferred to the bottom plate of the rheometer and measurements were recorded until the values plateaued. Time points reflecting $\sim 50\%$ of G' max

values were considered as gelation time. G' and G'' crossover was seen early during the measurements in the experiments.

DT degrades rapidly in acidic environment. This is bound to happen when DT, HMTA and GdL are all mixed together in a solution before addition to the thermal gel. Thus, to attain complete transient cycles while using lesser amount of fuels and thus generating lesser wastes we add all the fuels directly in powder form to 1.8 mL thermally annealed gel. This method was used for rheology experiments involving two consecutive cycles. The fuels used for the 1st cycle were **SachCHO** (30 mg in 1.8 ml pH 8 water), DT (40 mg), HMTA (24 mg), GdL (30 mg) and for the 2nd cycle DT (40 mg), HMTA (48 mg), GdL (different concentrations). The pH was not readjusted after each cycle. Only the first solution is adjusted to pH 8 by addition of a solution of NaOH (aq.; 0.1 M)

3.10.1.7 UV-Vis experiments

UV experiments were performed on Agilent CARY 8454-UV spectrometer in 1 mm cuvettes. Results found in **Figure 1c** are UV-Vis normalized absorbance at 500 nm of seeded and unseeded chemical gel formation with the addition of the same large amount of Formaldehyde solution (50 to 100 equivalents) to a SachSO_3^- solution, to ensure rapid conversion of the α -hydroxy sulfonate to aldehyde.

In a typical reaction cycle experiment, **Figure 1d**, the fuels were added to the gel in a vial. Once the gel turned to solution, the solution was transferred to the cuvette. The measurement started with a delay of 6 minutes from fuel addition.

The fibers formed by **SachCHO** are big enough to be visible by naked eye and they are opaque, so gelation can be easily followed by the increase in 'absorbance' followed by UV-Vis. We assume that the increase in opacity is proportional to the gelation process.

3.10.1.8 Syneresis experiments

For utilizing syneresis to extrude the dissolved waste products we made a simple set up comprising of a syringe and a needle. The needle was stuffed with cotton to avoid seeping out of any fibers which are several micrometers in length and width. A thermally annealed gel was transferred to the syringe using a spatula to which the fuels were added in powder form. After

each transient cycle, the plunger was pushed slowly so as to compress the gel and allow solvent + waste to be expelled via the outlet of the needle. For the next cycle, the solvent (1.8 mL) and fuels were added. Importantly, for each cycle an extra 3 mg of **SachCHO** was added along with the fuels to compensate the amount of soluble **SachCHO** coming out during syneresis. This amount of replenished **SachCHO** was calculated based on the concentration of soluble **SachCHO** (10% of the total amount) evident by NMR in the hydrogel using the ERECTIC NMR method as described before. After syneresis we could confirm the amount of **SachCHO** coming out with the waste products, which was 2.96 ± 0.68 mg (10% of the total amount).

3.10.1.9 Confocal Microscopy

Images were acquired using a ZEISS LSM 710 confocal microscope. No fluorescent markers were used.

3.10.1.10 Powder X-Ray diffraction

Powder X-ray diffraction measurements were performed on a Bruker D2 Phaser diffractometer (Source: Standard ceramic sealed tube CuK α 1.54184 Å. Detector: Bruker 1D-LYNXEYE). The lyophilized hydrogels were washed repeatedly with water to remove the salts and wastes, and then mounted on a silicon wafer for measurements. The measurements were done at 25 °C.

3.10.1.11 Scanning Electron Microscopy

SEM images were taken using a FEI Quanta FEG 450 microscope. Using a 5.0 kV High Voltage and dwell time of 50 μ s. The lyophilized hydrogels were washed repeatedly with water to remove the salts and wastes, mounted on a silicon wafer and sputtered with 10 to 15 nm of gold.

3.10.2 Synthesis

3.10.2.1 SachCHO

SachCHO was synthesized following a previously reported method.⁸ UV/Vis $\lambda_{\max} = 250$ nm (Figure 3.14).

3.10.2.2 SachSO₃⁻

SachSO₃⁻ was prepared by adding the required amount of Dithionite (typically 3.6 equivalents, 85% pure) to SachCHO. NMR spectra were recorded in D₂O (Figure 3.15).

¹H NMR 400MHz (D₂O, ppm): δ 3.46 (3H, s) 3.67-3.74 (2H, m) 3.90-3.91 (3H, m) 4.35 (1H, q, J= 10.7 Hz) 4.90 (1H, d, J= 3.25 Hz) 5.57 (1H, s) 5.77 (1H, s) 7.60 (4H, q, J = 7.94 Hz)

¹³C NMR 100MHz (D₂O, ppm): δ 55.3, 62.3, 68.1, 70.1, 71.7, 80.4, 85.2, 100.1, 101.4, 126.2, 127.9, 136.8, 137.0

UV/Vis λ_{max} = 218 nm (Figure 3.14).

Calculated mass (m/z): 391.0704, Mass found (m/z): 391.0703.

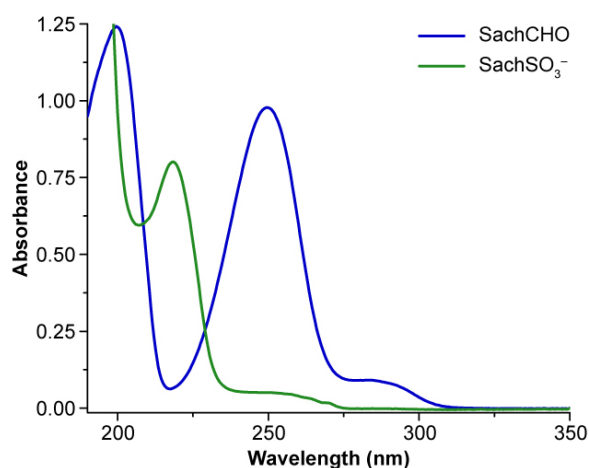


Figure 3.14 – UV-Vis spectra of SachCHO and SachSO₃⁻. The blue line is the spectra of SachCHO at 500 μM. The green line is the same solution with 3.6 equivalents of dithionite, the same proportion used in the reaction cycles.

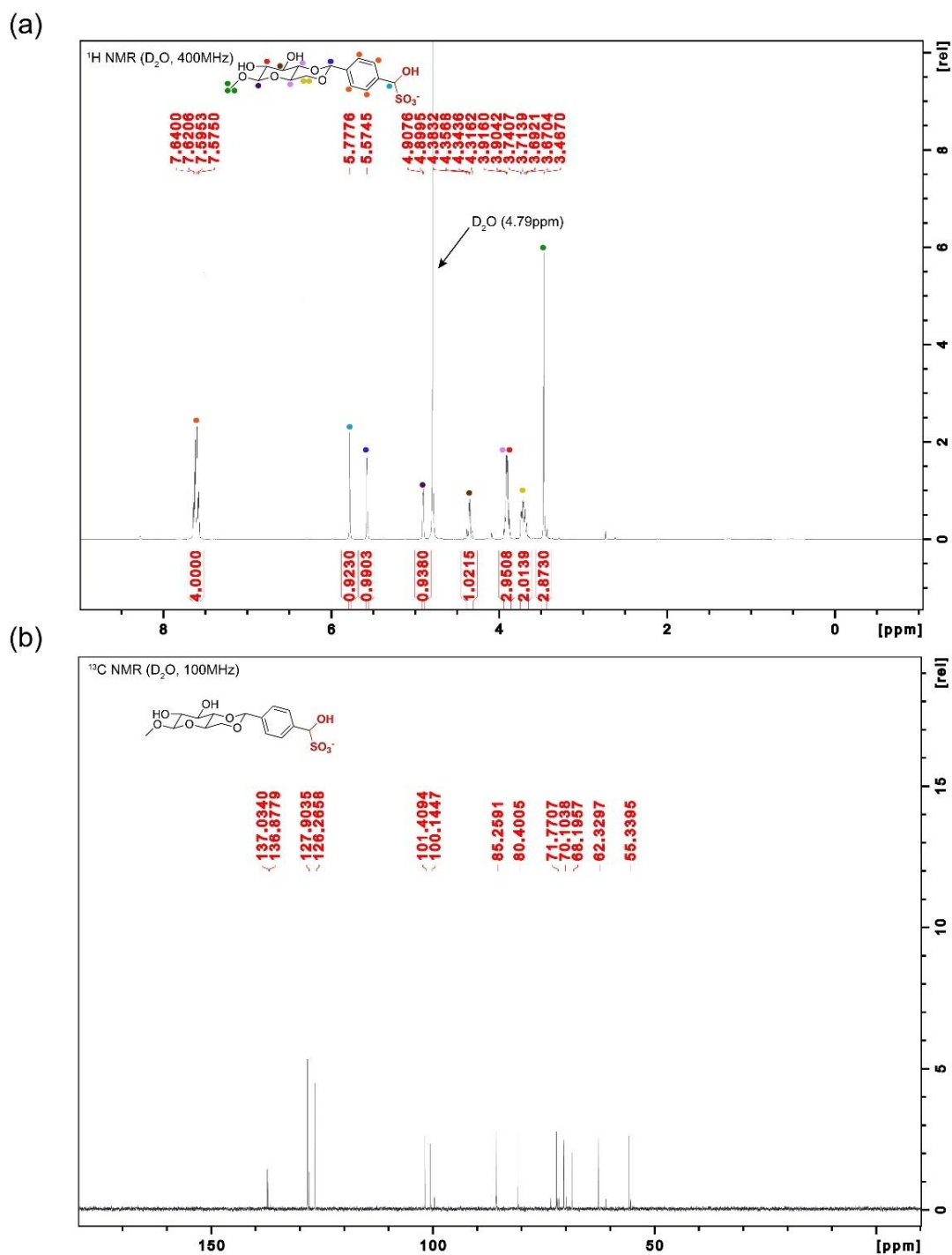


Figure 3.15 – NMR (a) ¹H (D₂O, 400MHz), (b) ¹³C (D₂O, 100MHz) NMR spectra of SachSO₃⁻.

3.10.3 Mathematical Model and Fitting

The model chosen to be fitted to the experimental supramolecular polymerization kinetic data was the analytical solution of the nucleation-elongation moments model derived by T. Knowles et al.,¹⁸⁰ including secondary nucleation.^{182,199} This particular mechanism (nucleation,

elongation and secondary nucleation) was chosen after the analysis of the half-times of nucleation as a function of monomer initial concentration, discussion in Sub-Section 3.3 and Figure 3.3, and because of microscopy data evidencing the phenomenon of secondary nucleation (Figure 3.9 in Appendix).

The original differential equations for the moments model are as follows:

$$\frac{dP(t)}{dt} = k_{n1}m(t)^{n1} + k_{n2}m(t)^{n2}M(t) \quad (1)$$

$$\frac{dM(t)}{dt} = 2(m(t)k_e - k_{off})P(t) + n1k_{n1}m(t)^{n1} + n2k_{n2}M(t)m(t)^{n2} \quad (2)$$

Where $P(t)$ is the supramolecular polymer concentration at a given time (number of fibers in solution), $M(t)$ is the concentration of molecules in the polymeric form (number of molecules in fibers), $m(t)$ is the free monomer molar concentration, k_{n1} is the primary nucleation rate constant, k_{n2} is the secondary nucleation rate constant, k_e is the elongation rate constant, k_{off} is the depolymerization rate constant, $n1$ is the primary nucleus size and $n2$ is the secondary nucleus size.

The analytical solution of coupled differential equations for the calculation of $M(t)$ is:¹⁸²

$$\frac{M(t)}{M(\infty)} = 1 - \left(1 - \frac{M(0)}{M(\infty)}\right) \times \left(\frac{B_+ + C_+}{B_+ + C_+ e^{\kappa t}} \frac{B_- + C_+ e^{\kappa t}}{B_- + C_+}\right)^{\frac{k_{\infty}^2}{\kappa k_{\infty}}} e^{-k_{\infty} t} \quad (3)$$

Where $M(0)$ is the initial concentration of molecules in the polymeric form, $M(\infty)$ is the final concentration of molecules in the polymeric form, and the other parameters are:

$$\kappa = \sqrt{2k_{n2}m(0)^{n2}(m(0)k_e - k_{off})} \quad (4)$$

$$\lambda = \sqrt{2k_e k_{n1}m(0)^{n1}} \quad (5)$$

$$C_{\pm} = \frac{k_e P(0)}{\kappa} \pm \frac{k_e M(0)}{[2(m(0)k_e - k_{off})]} \pm \frac{\lambda^2}{2\kappa^2} \quad (6)$$

$$k_{\infty} = \kappa \sqrt{\frac{2}{n_2(n_2+1)} + \frac{2\lambda^2}{n_1\kappa^2} + \frac{2M(0)}{n_2m(0)} + \left(\frac{2k_e P(0)}{\kappa}\right)^2} \quad (7)$$

$$\tilde{k}_{\infty} = \sqrt{k_{\infty}^2 - 4C_+C_-\kappa^2} \quad (8)$$

$$B_{\pm} = \frac{k_{\infty} \pm \tilde{k}_{\infty}}{2\kappa} \quad (9)$$

Where $P(0)$ is the initial supramolecular polymer concentration and $m(0)$ is the initial free monomer molar concentration.

Practically, the equations (3) to (9) were used to perform the fitting. The fitting is done by comparing the results of Equation (3) to the experimental data set and using the kinetic rate constants as free parameters.

The supramolecular polymerization model, described above, was fitted to match the normalized Optical Density experimental data present in Figure 3.3–A. It is assumed that Optical Density is linearly related to $M(t)$, because the opacity of the sample is directly proportional to gelation. This is not to be confused with actual light scattering experiments where intensity is changed by the number of scatterers (linearly) and by the size of the aggregates (nonlinearly).

To perform the fitting the values n_1 and n_2 (primary and secondary nucleus size) were set as global constants with a value of 6, Figure 3.3–B. For the model to be applicable, k_{off} (depolymerization rate constant) must be negligible when compared to the elongation rate constant, so in this case it is set as a global constant with a value of 10^{-9} s^{-1} . For seeded experiments, the value of $P(0)$ is a needed parameter, but it is a very difficult value to measure or estimate since it is almost impossible to count the number of fibers injected in solution.⁶ The results of the fits are listed in Table 3.1.

3.10.4 MATLAB® code

3.10.4.1 Model

```
function [Alpha] =  
polymfit_knowles2seeded_secondarynucleation_multifit(t,kfe,kfn,kfn2,koff,x1,x2,c1,s1,c2,s2,c3  
,s3,c4,s4,c5,s5,n1,n2,n3,n4,n5,P1,P2)  
  
% THIS MODEL DESCRIBES COOPERATIVE SUPRAMOLECULAR POLYMERIZATION (nuc. size  
% x) - using the linearized moments equations taking into account  
% secondary nucleation  
% cf T. P. J. Knowles, et al., Nat. Protoc. 2016, 11, 252-272.  
% Georges Formon 28 Aug 2019 - HERMANS@UNISTRA.FR  
% kfn: primary nucleation;  
% kfn2: secondary nucleation;  
% kfe: Elongation;  
% koff: Depolymerization (negligeable and set to a small global constant koff=1e-9)  
% #####  
% #####
```

Trick to bypass the fitting algorithm

```
nt=size(t);  
tu = unique(t);  
ntu=size(tu);  
  
if nt(1)==ntu(1)  
    Alpha(1:nt,1)=1;  
else  
  
kfn=kfn/1000;
```

26.8 mM unseeded

```
M0 = s1; %Polymer initial molar concentration  
P0 = 0; %Initial Polymer number concentration  
m0=c1; %monomer initial molar concentration  
  
K = sqrt((2.*m0.^x2).*(m0.*kfe-koff).*kfn2);  
  
L = sqrt(2.*kfe.*kfn.*m0.^x1);  
  
C_p = kfe.*P0./K + kfe.*M0./(2.*(m0.*kfe-koff)) + (L.^2)./(2.*K.^2);  
  
C_m = kfe.*P0./K - kfe.*M0./(2.*(m0.*kfe-koff)) - (L.^2)./(2.*K.^2);  
  
k_inf =  
K*sqrt((2./(x2.*(x2+1)))+(2.*L.^2)./(x1.*K.^2)+(2.*M0)./(x2.*m0))+((2*kfe*P0)/(K))^2);  
  
k_inf_ = sqrt(k_inf.^2 - 2.*C_p.*C_m.*K.^2);  
  
B_p = (k_inf+k_inf_)./(2.*K);  
  
B_m = (k_inf-k_inf_)./(2.*K);
```

```

Alpha(1:n1,1)=(1-(1-M0./(M0+m0)).*exp(-
k_inf.*t(1:n1,1)).*(((B_m+C_p.*exp(K.*t(1:n1,1)))./(B_p+C_p.*exp(K.*t(1:n1,1))).*((B_p+C_p)).
/(B_m+C_p))).^(k_inf.^2)./(K.*k_inf_)))*100; %%%output

```

33.5 mM unseeded

```

M0 = s2; %Polymer initial molar concentration
P0 = 0; %Initial Polymer number concentration
m0=c2; %Monomer initial molar concentration

K = sqrt((2.*m0.^x2).*(m0.*kfe-koff).*kfn2);

L = sqrt(2.*kfe.*kfn.*m0.^x1);

C_p = kfe.*P0./K + kfe.*M0./(2.*(m0.*kfe-koff)) + (L.^2)./(2.*K.^2);

C_m = kfe.*P0./K - kfe.*M0./(2.*(m0.*kfe-koff)) - (L.^2)./(2.*K.^2);

k_inf =
K*sqrt((2./(x2.*(x2+1)))+(2.*L.^2)./(x1.*K.^2))+((2.*M0)./(x2.*m0))+((2*kfe*P0)/(K))^2);

k_inf_ = sqrt(k_inf.^2 - 2.*C_p.*C_m.*K.^2);

B_p = (k_inf+k_inf_)./(2.*K);

B_m = (k_inf-k_inf_)./(2.*K);

Alpha(n1+1:n1+n2,1)=(1-(1-M0./(M0+m0)).*exp(-
k_inf.*t(n1+1:n1+n2,1)).*(((B_m+C_p.*exp(K.*t(n1+1:n1+n2,1)))./(B_p+C_p.*exp(K.*t(n1+1:n1+n2,
1))).*((B_p+C_p))./(B_m+C_p))).^(k_inf.^2)./(K.*k_inf_)))*100; %%%output

```

40.2 mM unseeded

```

M0 = s3; %Polymer initial molar concentration
P0 = 0; %Initial Polymer number concentration
m0 = c3; %Monomer initial molar concentration

K = sqrt((2.*m0.^x2).*(m0.*kfe-koff).*kfn2);

L = sqrt(2.*kfe.*kfn.*m0.^x1);

C_p = kfe.*P0./K + kfe.*M0./(2.*(m0.*kfe-koff)) + (L.^2)./(2.*K.^2);

C_m = kfe.*P0./K - kfe.*M0./(2.*(m0.*kfe-koff)) - (L.^2)./(2.*K.^2);

k_inf =
K*sqrt((2./(x2.*(x2+1)))+(2.*L.^2)./(x1.*K.^2))+((2.*M0)./(x2.*m0))+((2*kfe*P0)/(K))^2);

k_inf_ = sqrt(k_inf.^2 - 2.*C_p.*C_m.*K.^2);

B_p = (k_inf+k_inf_)./(2.*K);

B_m = (k_inf-k_inf_)./(2.*K);

Alpha(n1+n2+1:n1+n2+n3,1)=(1-(1-M0./(M0+m0)).*exp(-

```

```
k_inf.*t(n1+n2+1:n1+n2+n3,1)).*((B_m+C_p.*exp(K.*t(n1+n2+1:n1+n2+n3,1)))/(B_p+C_p.*exp(K.*t(n1+n2+1:n1+n2+n3,1))).*((B_p+C_p))/(B_m+C_p)).^((k_inf.^2)/(K.*k_inf_))*100; %%output
```

10% seeds

```
M0 = s4; %Polymer initial molar concentration
P0 = P1; %Initial Polymer number concentration
m0 = c4; %Monomer initial molar concentration

K = sqrt((2.*m0.^x2).*(m0.*kfe-koff).*kfn2);

L = sqrt(2.*kfe.*kfn.*m0.^x1);

C_p = kfe.*P0./K + kfe.*M0./(2.*(m0.*kfe-koff)) + (L.^2)/(2.*K.^2);

C_m = kfe.*P0./K - kfe.*M0./(2.*(m0.*kfe-koff)) - (L.^2)/(2.*K.^2);

k_inf =
K*sqrt((2./(x2.*(x2+1)))+(2.*L^2)/(x1.*K^2)+(2.*M0)/(x2.*m0)+(2*kfe*P0)/(K)^2);

k_inf_ = sqrt(k_inf.^2 - 2.*C_p.*C_m.*K.^2);

B_p = (k_inf+k_inf_)/(2.*K);

B_m = (k_inf-k_inf_)/(2.*K);

Alpha(n1+n2+n3+1:n1+n2+n3+n4,1)=(1-(1-M0/(M0+m0)).*exp(-
k_inf.*t(n1+n2+n3+1:n1+n2+n3+n4,1)).*((B_m+C_p.*exp(K.*t(n1+n2+n3+1:n1+n2+n3+n4,1)))/(B_p+C_p.*exp(K.*t(n1+n2+n3+1:n1+n2+n3+n4,1))).*((B_p+C_p))/(B_m+C_p)).^((k_inf.^2)/(K.*k_inf_))
)*100; %%output
```

20% seeds

```
M0 = s5; %Polymer initial molar concentration
P0 = P2; %Initial Polymer number concentration
m0 = c5; %Monomer initial molar concentration

K = sqrt((2.*m0.^x2).*(m0.*kfe-koff).*kfn2);

L = sqrt(2.*kfe.*kfn.*m0.^x1);

C_p = kfe.*P0./K + kfe.*M0./(2.*(m0.*kfe-koff)) + (L.^2)/(2.*K.^2);

C_m = kfe.*P0./K - kfe.*M0./(2.*(m0.*kfe-koff)) - (L.^2)/(2.*K.^2);

k_inf =
K*sqrt((2./(x2.*(x2+1)))+(2.*L^2)/(x1.*K^2)+(2.*M0)/(x2.*m0)+(2*kfe*P0)/(K)^2);

k_inf_ = sqrt(k_inf.^2 - 2.*C_p.*C_m.*K.^2);

B_p = (k_inf+k_inf_)/(2.*K);

B_m = (k_inf-k_inf_)/(2.*K);

Alpha(n1+n2+n3+n4+1:n1+n2+n3+n4+n5,1)=(1-(1-M0/(M0+m0)).*exp(-
```

```
k_inf.*t(n1+n2+n3+n4+1:n1+n2+n3+n4+n5,1)).*((B_m+C_p.*exp(K.*t(n1+n2+n3+n4+1:n1+n2+n3+n4+n5,1)))./(B_p+C_p.*exp(K.*t(n1+n2+n3+n4+1:n1+n2+n3+n4+n5,1))).*((B_p+C_p))./(B_m+C_p))).^(k_inf.^2)./(K.*k_inf_)))*100; %%output
```

```
end
```

```
end
```

3.10.4.2 Fitting Routine

```
function SacCHO_Fitroutine_multifit_seeded
```

```
%%Fitting routine for analyze experimental data using a cooperative supramolecular polymerization model
```

```
% Georges Formon - 05 August 2019 (Hermans@unistra.fr)
```

```
close all
```

```
% clear all
```

```
load('All_kinetics_revisions.mat');
```

26.8 mM

```
N=1;
```

```
[n1,m1]=size(kin_1mgc);
```

```
t(1:n1,1)=kin_1mgc(:,1);
```

```
Y(1:n1,1)=kin_1mgc(:,2)*100;
```

```
c1=0.0268;
```

```
s1=0;
```

33.5 mM

```
N=2;
```

```
[n2,m2]=size(kin_1_25mgc);
```

```
t(n1+1:n1+n2,1)=kin_1_25mgc(:,1);
```

```
Y(n1+1:n1+n2,1)=kin_1_25mgc(:,2)*100;
```

```
c2=0.0335;
```

```
s2=0;
```

40.2 mM

```
N=3;
```

```
[n3,m3]=size(kin_1_5mgc);
```

```
t(n1+n2+1:n1+n2+n3,1)=kin_1_5mgc(:,1);
```

```
Y(n1+n2+1:n1+n2+n3,1)=kin_1_5mgc(:,2)*100;
```

```
c3=0.0402;
```

```
s3=0;
```

9% seeds

```
N=4;
[n4,m4]=size(kin_10percentseeds);

t(n1+n2+n3+1:n1+n2+n3+n4,1)=kin_10percentseeds(:,1);

Y(n1+n2+n3+1:n1+n2+n3+n4,1)=kin_10percentseeds(:,2)*100;

c4=0.02948;
s4=2.68e-3;
```

17% seeds

```
N=5;
[n5,m5]=size(kin_20percentseeds);

t(n1+n2+n3+n4+1:n1+n2+n3+n4+n5,1)=kin_20percentseeds(:,1);

Y(n1+n2+n3+n4+1:n1+n2+n3+n4+n5,1)=kin_20percentseeds(:,2)*100;

c5=0.03216;
s5=5.36e-3;
```

Fitting

```
tic % start timer
koff=1e-9;
x1=6;
x2=6;
P1=1e-5;
P2=2e-5;

fomm = fitoptions('Method', 'NonLinearLeastSquares', 'StartPoint', [2000 4.79e-5 50000],
...
'Lower', [1e-5 1e-12 1e-5], 'Upper', [1e6 1e-3 1e6],...
'TolFun',1e-16,'TolX',1e-8,'MaxIter',40000,'MaxFunEval',48000,...
'DiffMaxChange',1e6,'Algorithm','Trust-Region','Robust','LAR','Normalize','off')
ftmm =
fitype('polymfit_knowles2seeded_secondary_nucleation_multifit(t,kfe,kfn,kfn2,koff,x1,x2,c1,s1,
c2,s2,c3,s3,c4,s4,c5,s5,n1,n2,n3,n4,n5,P1,P2)',...
'coefficients',{'kfe','kfn','kfn2'},...
'independent','t',...

'problem',{'koff','x1','x2','c1','s1','c2','s2','c3','s3','c4','s4','c5','s5','n1','n2','n3',
'n4','n5','P1','P2'},...
'options',fomm)
[f,gof,output] = fit (t,Y, ftmm,'problem',{'koff,x1,x2,c1-s1,s1,c2-s2,s2,c3-s3,s3,c4-
s4,s4,c5-s5,s5,n1,n2,n3,n4,n5,P1,P2})

Y_val=polymfit_knowles2seeded_secondary_nucleation_multifit(t,f.kfe,f.kfn,f.kfn2,f.koff,f.x1,f
.x2,c1-s1,s1,c2-s2,s2,c3-s3,s3,c4-s4,s4,c5-s5,s5,n1,n2,n3,n4,n5,f.P1,f.P2)/100;
```

fomm =

```

Normalize: 'off'
Exclude: []
Weights: []
Method: 'NonlinearLeastSquares'
Robust: 'LAR'
StartPoint: [2000 4.7900e-05 50000]
Lower: [1.0000e-05 1.0000e-12 1.0000e-05]
Upper: [1000000 1.0000e-03 1000000]
Algorithm: 'Trust-Region'
DiffMinChange: 1.0000e-08
DiffMaxChange: 1000000
Display: 'Notify'
MaxFunEvals: 48000
MaxIter: 40000
TolFun: 1.0000e-16
TolX: 1.0000e-08

```

ftmm =

```

General model:
ftmm(kfe,kfn,kfn2,koff,x1,x2,c1,s1,c2,s2,c3,s3,c4,s4,c5,s5,n1,n2,n3,n4,n5,
P1,P2,t) = polymfit_knowles2seeded_secondary_nucleation_multifit(t,
kfe,kfn,kfn2,koff,x1,x2,c1,s1,c2,s2,c3,s3,c4,s4,c5,
s5,n1,n2,n3,n4,n5,P1,P2)

```

f =

```

General model:
f(t) = polymfit_knowles2seeded_secondary_nucleation_multifit(t,kfe,kfn,kfn2,
koff,x1,x2,c1,s1,c2,s2,c3,s3,c4,s4,c5,s5,n1,n2,n3,n4,
n5,P1,P2)

```

Coefficients (with 95% confidence bounds):

```

kfe = 1687 (1666, 1708)
kfn = 2.438e-07 (1.887e-07, 2.99e-07)
kfn2 = 4.855e+04 (4.748e+04, 4.962e+04)

```

Problem parameters:

```

koff = 1e-09
x1 = 6
x2 = 6
c1 = 0.0268
s1 = 0
c2 = 0.0335
s2 = 0
c3 = 0.0402
s3 = 0
c4 = 0.0268
s4 = 0.00268
c5 = 0.0268
s5 = 0.00536
n1 = 350
n2 = 150
n3 = 122
n4 = 63
n5 = 86
P1 = 1e-05
P2 = 2e-05

```


gof =

```
sse: 666.7769
rsquare: 0.9996
dfe: 768
adjrsquare: 0.9996
rmse: 0.9318
```

output =

```
numobs: 771
numparam: 3
residuals: [771x1 double]
Jacobian: [771x3 double]
exitflag: 2
firstorderopt: 4.0901e+04
iterations: 599
funcCount: 2604
cgiterations: 0
algorithm: 'trust-region-reflective'
message: [1x87 char]
```

Plotting

```
mod1=Y_val(1:n1,1);

mod2=Y_val(n1+1:n1+n2,1);

mod3=Y_val(n1+n2+1:n1+n2+n3,1);

mod4=Y_val(n1+n2+n3+1:n1+n2+n3+n4,1);

mod5=Y_val(n1+n2+n3+n4+1:n1+n2+n3+n4+n5,1);

h=figure;
plot(kin_1mgc(:,1),kin_1mgc(:,2),'s','MarkerEdgeColor',[0 0 204/255],'MarkerFaceColor',[0 0 204/255],'MarkerSize',8)
hold on
plot(kin_1_25mgc(:,1),kin_1_25mgc(:,2),'s','MarkerEdgeColor',[102/255 0 204/255],'MarkerFaceColor',[102/255 0 204/255],'MarkerSize',8)
hold on
plot(kin_1_5mgc(:,1),kin_1_5mgc(:,2),'s','MarkerEdgeColor',[204/255 0 204/255],'MarkerFaceColor',[204/255 0 204/255],'MarkerSize',8)
hold on
plot(kin_10percentseeds(:,1),kin_10percentseeds(:,2),'s','MarkerEdgeColor',[204/255 0 102/255],'MarkerFaceColor',[204/255 0 102/255],'MarkerSize',8)
hold on
plot(kin_20percentseeds(:,1),kin_20percentseeds(:,2),'s','MarkerEdgeColor',[204/255 0 0],'MarkerFaceColor',[204/255 0 102/255],'MarkerSize',8)
hold on
plot(kin_1mgc(:,1),mod1,'-','Linewidth',3,'color',[0 0 204/255])
hold on
plot(kin_1_25mgc(:,1),mod2,'-','Linewidth',3,'color',[102/255 0 204/255])
hold on
```

```

plot(kin_1_5mgc(:,1),mod3,'-','Linewidth',3,'Color',[204/255 0 204/255])
hold on
plot(kin_10percentseeds(:,1),mod4,'-','Linewidth',3,'Color',[204/255 0 102/255])
hold on
plot(kin_20percentseeds(:,1),mod5,'-','Linewidth',3,'Color',[204/255 0 0])
hold off
set(gca,'FontName','arial','FontSize',24,'Linewidth',2.5,'box','off')
xlabel('Time (sec.)','FontName','arial','FontSize',24,'FontWeight','bold')
ylabel('Normalised Absorbance @500nm','FontName','arial','FontSize',24,'FontWeight','bold');
legend({'26.8 mM','33.5 mM','40.2 mM','9% seeds','17% seeds','26.8 mM - Fit','33.5 mM - Fit',
'40.2 mM - Fit','9% seeds - Fit','17% seeds - Fit'},'FontName','arial','FontSize',17,'FontWeight','bold','Location','SouthEast');
legend('boxoff')
set(gcf,'color','w','Position',[470,200,1000,750]);
ylim([-0.00 1.00])
% title('G\deltaL 233 mM','FontName','arial','FontSize',24,'FontWeight','bold')

```

```

h=figure;
plot(kin_1mgc(:,1),kin_1mgc(:,2),'o')
hold on
plot(kin_1mgc(:,1),mod1,'-')
hold off
title('26.8 mM')

```

```

h=figure;
plot(kin_1_25mgc(:,1),kin_1_25mgc(:,2),'o')
hold on
plot(kin_1_25mgc(:,1),mod2,'-')
hold off
title('40 mM')

```

```

h=figure;
plot(kin_1_5mgc(:,1),kin_1_5mgc(:,2),'o')
hold on
plot(kin_1_5mgc(:,1),mod3,'-')
hold off
title('53.6 mM')

```

```

h=figure;
plot(kin_10percentseeds(:,1),kin_10percentseeds(:,2),'o')
hold on
plot(kin_10percentseeds(:,1),mod4,'-')
hold off
title('10% seeds')

```

```

h=figure;
plot(kin_20percentseeds(:,1),kin_20percentseeds(:,2),'o')
hold on
plot(kin_20percentseeds(:,1),mod5,'-')
hold off
title('30% seeds')

```

```

Y_val=polymfit_knowles2seeded_secondary_nucleation_multifit(t,1666.3,4.79e-

```

```

5*1000,17517.0,koff,x1,x2,c1,s1,c2,s2,c3,s3,c4,s4,c5,s5,n1,n2,n3,n4,n5,P1,P2)/100;

mod1=Y_val(1:n1,1);

mod2=Y_val(n1+1:n1+n2,1);

mod3=Y_val(n1+n2+1:n1+n2+n3,1);

mod4=Y_val(n1+n2+n3+1:n1+n2+n3+n4,1);

mod5=Y_val(n1+n2+n3+n4+1:n1+n2+n3+n4+n5,1);

h=figure;
plot(kin_1mgc(:,1),kin_1mgc(:,2),'s','MarkerEdgeColor',[0 0 204/255],'MarkerFaceColor',[0 0
204/255],'MarkerSize',8)
hold on
plot(kin_1_25mgc(:,1),kin_1_25mgc(:,2),'s','MarkerEdgeColor',[102/255 0
204/255],'MarkerFaceColor',[102/255 0 204/255],'MarkerSize',8)
hold on
plot(kin_1_5mgc(:,1),kin_1_5mgc(:,2),'s','MarkerEdgeColor',[204/255 0
204/255],'MarkerFaceColor',[204/255 0 204/255],'MarkerSize',8)
hold on
plot(kin_10percentseeds(:,1),kin_10percentseeds(:,2),'s','MarkerEdgeColor',[204/255 0
102/255],'MarkerFaceColor',[204/255 0 102/255],'MarkerSize',8)
hold on
plot(kin_20percentseeds(:,1),kin_20percentseeds(:,2),'s','MarkerEdgeColor',[204/255 0
0],'MarkerFaceColor',[204/255 0 102/255],'MarkerSize',8)
hold on
plot(kin_1mgc(:,1),mod1,'-','Linewidth',3,'Color',[0 0 204/255])
hold on
plot(kin_1_25mgc(:,1),mod2,'-','Linewidth',3,'Color',[102/255 0 204/255])
hold on
plot(kin_1_5mgc(:,1),mod3,'-','Linewidth',3,'Color',[204/255 0 204/255])
hold on
plot(kin_10percentseeds(:,1),mod4,'-','Linewidth',3,'Color',[204/255 0 102/255])
hold on
plot(kin_20percentseeds(:,1),mod5,'-','Linewidth',3,'Color',[204/255 0 0])
hold off
set(gca,'FontName','arial','FontSize',24,'Linewidth',2.5,'box','off')
xlabel('Time (sec)','FontName','arial','FontSize',24,'FontWeight','bold')
ylabel('Normalised Absorbance @500nm','FontName','arial','FontSize',24,'FontWeight','bold');
Legend({'26.8 mM','33.5 mM','40.2 mM','9% seeds','17% seeds','26.8 mM - Fit','33.5 mM - Fit',
'40.2 mM - Fit','9% seeds - Fit','17% seeds -
Fit'],'FontName','arial','FontSize',17,'FontWeight','bold','Location','SouthEast');
Legend('boxoff')
set(gcf,'color','w','Position',[470,200,1000,750]);
ylim([-0.00 1.00])
% title('G\deltaL 233 mM','FontName','arial','FontSize',24,'FontWeight','bold')

h=figure;
plot(kin_1mgc(:,1),kin_1mgc(:,2),'o')
hold on
plot(kin_1mgc(:,1),mod1,'-')
hold off
title('26.8 mM')

```

```

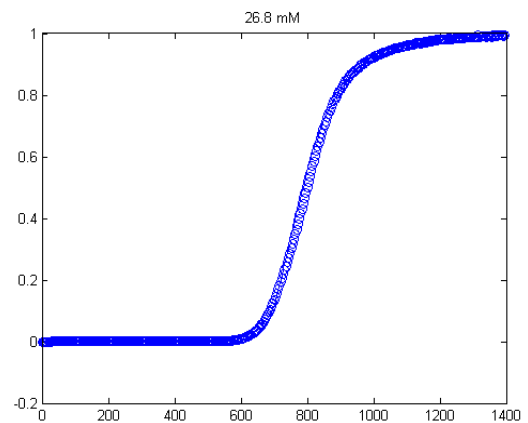
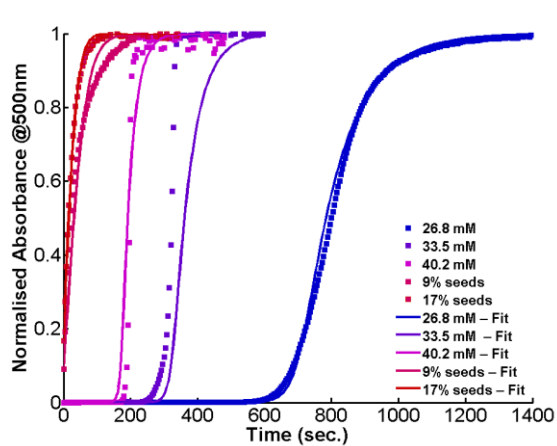
h=figure;
plot(kin_1_25mgc(:,1),kin_1_25mgc(:,2),'o')
hold on
plot(kin_1_25mgc(:,1),mod2,'-')
hold off
title('33.5 mM')

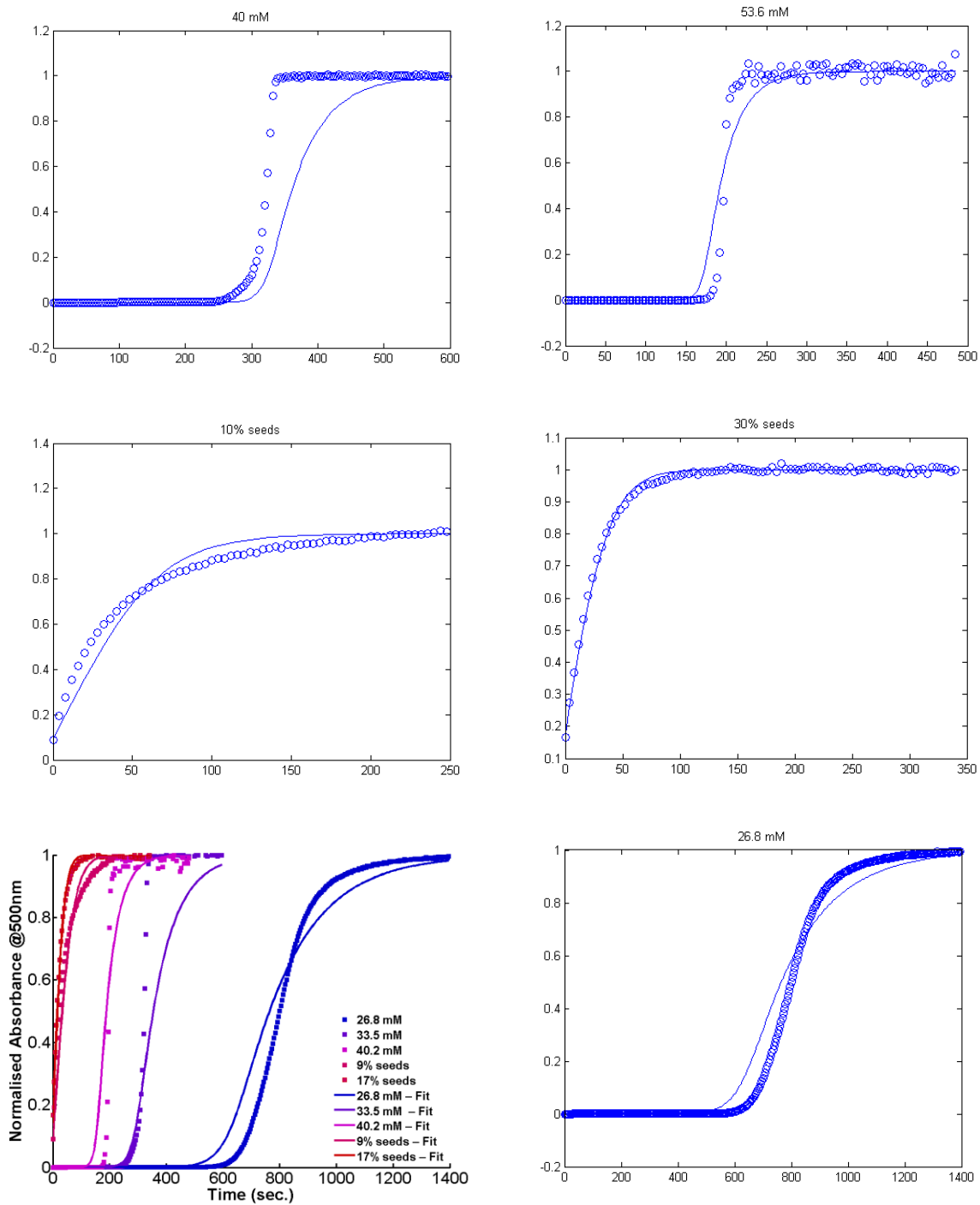
h=figure;
plot(kin_1_5mgc(:,1),kin_1_5mgc(:,2),'o')
hold on
plot(kin_1_5mgc(:,1),mod3,'-')
hold off
title('40.2 mM')

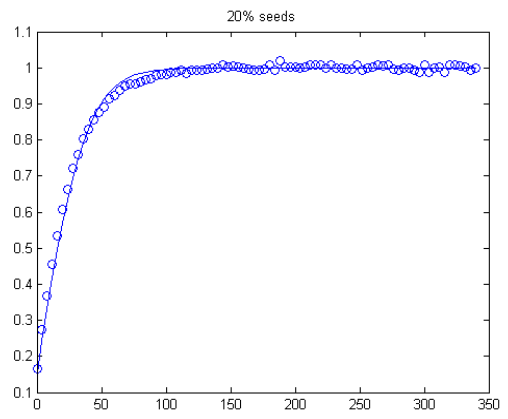
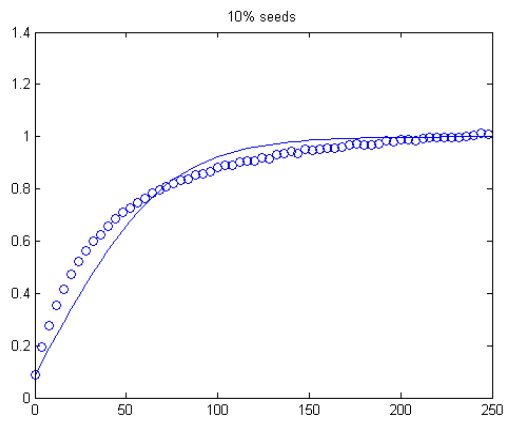
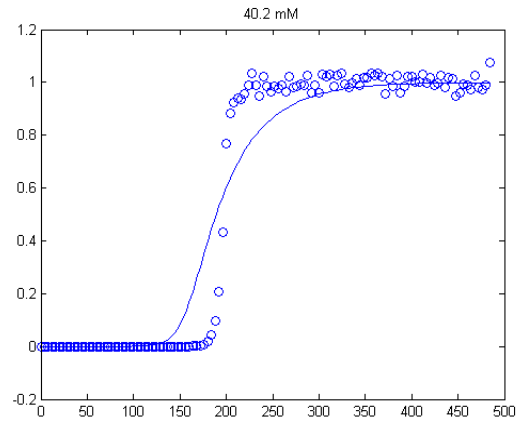
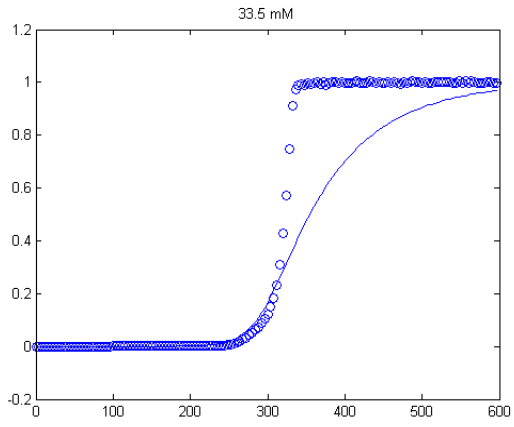
h=figure;
plot(kin_10percentseeds(:,1),kin_10percentseeds(:,2),'o')
hold on
plot(kin_10percentseeds(:,1),mod4,'-')
hold off
title('10% seeds')

h=figure;
plot(kin_20percentseeds(:,1),kin_20percentseeds(:,2),'o')
hold on
plot(kin_20percentseeds(:,1),mod5,'-')
hold off
title('20% seeds')

```







end

Chapter 4. Magnetic Control over Supramolecular Networks

Abstract: Rare-earth-containing C_3 -symmetrical paramagnetic discotic molecules self-assemble into rods in water, that interact with each other forming a network. We show in this Chapter, that applying a relatively weak magnetic field will densify and change the topology of these networks. This change in structure also influences the magnetic properties of the sample. Magnetic calculations show that, even if the magnetic energy acting on a single magnetic ion is negligible when compared to thermal noise, these aggregates are large enough to overcome this barrier.

This chapter has been published in:

Marichez, Vincent; Sato, Akihiro; Dunne, Peter A.; Leira-Iglesias, Jorge; Formon, Georges J.M.; Schicho, Michaela K.; de Feijter, Isja; Hébraud, Pascal; Bailleul, Matthieu; Besenius, Pol; Venkatesan, M.; Coey, J.M.D.; Meijer, E.W.; Hermans, Thomas, M. "Magnetic Control over the Topology of Supramolecular Rod Networks." *ChemRxiv*. Preprint. (2020) <https://doi.org/10.26434/chemrxiv.12762269.v1>

4.1 Introduction

The precise control of biological assemblies is a requirement for the good functioning of living systems. The balance between the chemical structure of protein and nucleic acids (and other biologically relevant (macro)molecules) with the environmental conditions is the driving factor for proper structure–function relationship.²⁰²

The precise control over synthetic self-assembled structures is needed if we want to impart advanced functions and applications to supramolecular polymers. For that, new and practical systems must be developed to gain multiple levels of control over aggregate structural properties. As it has been discussed in Chapter 1, different techniques and stimuli have been used to achieve thermodynamic control over supramolecular assemblies, such as: pH,⁵⁶ ionic strength,⁹ light,⁵³ temperature,⁴⁰ and chemical species.⁸ Other methods like the use of strong flow^{203,204} and electric^{205–207} fields have also been employed but are not as practical because they require the use of specific and specialized equipment. Using magnetic fields to control molecular assemblies (Section 1.4) usually require strong fields, > 8 T, because the magnetic energy must overcome thermal noise for the magnetic effect to be observable.^{132,208} Take for instance a single paramagnetic Gd^{3+} ion in water, its magnetic energy is $E_{mag} = -\frac{1}{2\mu_0} \chi V B^2 = -3 \cdot 10^{-25}$ J, for 1 T and 25 °C.¹¹ The thermal energy would be $E_{therm} = k_B T = 4 \cdot 10^{-21}$ J, which is four orders of magnitude higher than E_{mag} . But for assemblies containing thousands of ions at 8 T the magnetic energy would be around $k_B T$, since energy grows quadratically with magnetic field for paramagnets.¹²⁰ However, recent reports show the control of supra or macromolecular assemblies using magnetic fields < 2 T (as discussed in Sub-Section 1.4.3), like the self-assembly of a Dy^{3+} -containing surfactant into millimeter-sized dumbbell-shaped structures that could be aligned with a simple neodymium magnet,²⁰⁹ or the alignment of the cylindrical phases of Fe-containing block-co-polymers with $B \sim 0.35$ T.¹⁶⁶

Inspired by these last reports, in this chapter we show the control over paramagnetic supramolecular of rods containing rare-earth elements with 1 to 2 T homogeneous magnetic fields, which can be easily achieved in common laboratory facilities. The use of relatively weak magnetic fields, when compared to previous studies that apply > 8 T, to control supramolecular

assemblies opens the door to new uses of magnets in supramolecular chemistry. Moreover, calculations using physical models unveil possible new design paradigms for magnetically controlled self-assembly.

4.2 Characterization of Supramolecular Assemblies

The previously well studied C_3 -symmetrical **Y(III)-DOTA-BTA** and **Gd(III)-DOTA-BTA**, Figure 4.1–B, is comprised of a benzene-1,3,5-tricarboxamide (BTA) core, with one 1,4,7,10-tetraazacyclododecane- N,N',N'',N''' -tetraacetic acid (DOTA) group per arm, which chelates the rare earth elements Yttrium or Gadolinium. Both **Y(III)-DOTA-BTA** and **Gd(III)-DOTA-BTA** are known to self-assemble into long fibers (rods) by a cooperative polymerization, K_f^{ix} in Figure 4.1–A.^{9,210} At a concentration of 100 μM , the aggregates show a bimodal distribution observed by dynamic light scattering (DLS), Figure 4.1–C. There are two diffusive relaxation processes in solution: **P1**, that presents fast diffusion; and **P2**, a slow process. Both processes are diffusive in nature, with q^2 dependence, meaning that both hydrodynamic radii can be calculated using the Stokes-Einstein equation (see Sub-Section 4.9.3.1).

^{ix} Even if for cooperative supramolecular polymerization there are two equilibria governing self-assembly (one for nucleation and one for elongation), in this case we chose to represent this equilibrium by a single constant since a detailed analysis of this process is not in the scope of this work. Furthermore, in the studied concentration, the elongation equilibrium would be the dominant phenomenon.

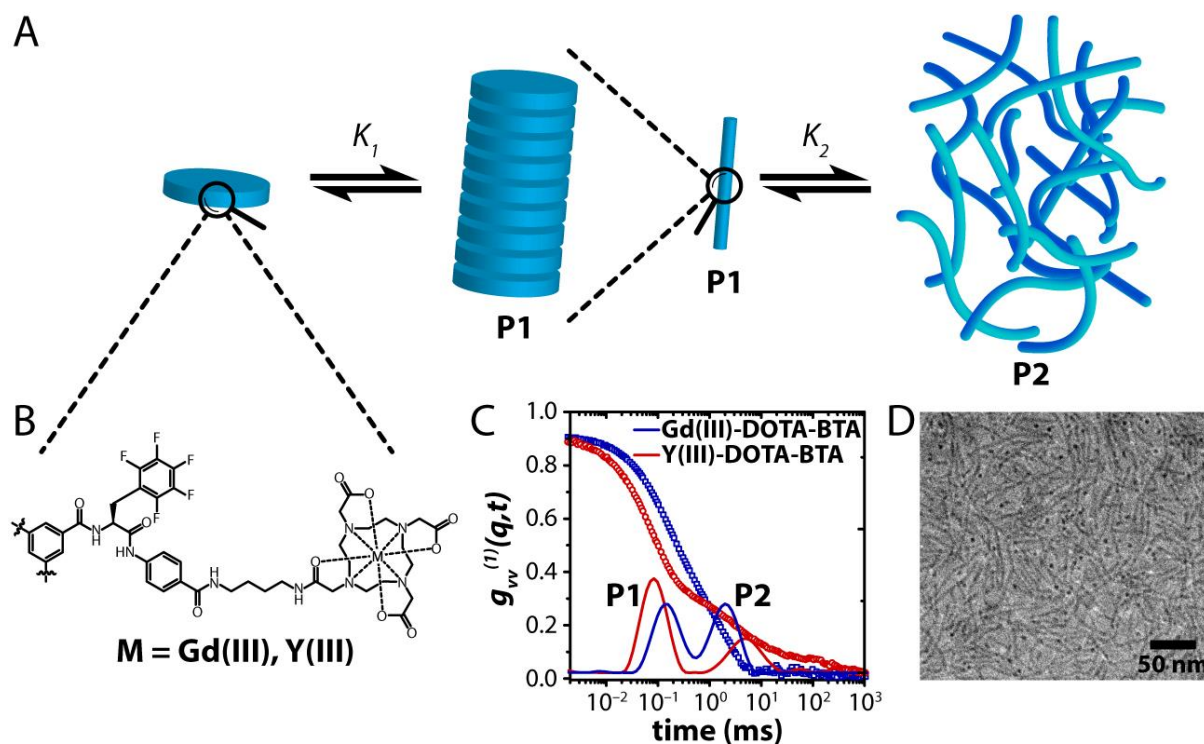


Figure 4.1 – A – Depiction of the different equilibria driving the assembly of **M(III)-DOTA-BTA** into rods (**P1**) and a network of rods (**P2**). **B** – Chemical structure of the C_3 -symmetrical **M(III)-DOTA-BTA** where **M(III)** is either **Y(III)** or **Gd(III)**. Only one arm out of 3 is shown for clarity. **C** – Polarized field correlation function $g_{VV}^{(1)}(q, t)$ of **Gd(III)** and **Y(III)-DOTA-BTA** at 100 μM concentration in 100 mM pH 6 citrate buffer, measured at $q = 0.0288 \text{ nm}^{-1}$, shown by the hollow symbols. The solid lines show the corresponding distribution of relaxation times $G(\tau)$ obtained by the Contin analysis at this wavevector, showing **P1** and **P2**. The hydrodynamic radii obtained by DLS are summed up in Table 4.1. **D** – Cryo-TEM of **Gd(III)-DOTA-BTA** at 100 μM concentration in 100 mM pH 6 citrate buffer.

Cryo-TEM shows that **Gd(III)-DOTA-BTA** self-assembles into 6 nm diameter rods, Figure 4.1–D. A model by Tirado, permits the calculation of the average lengths of rods by inputting the hydrodynamic radius and the rod diameter.²¹¹ If we use the hydrodynamic radii of **P1** (Table 4.1) with a diameter of 6 nm, the model gives calculated rod lengths of $\sim 245 \text{ nm}$ for **Gd(III)-DOTA-BTA** and $\sim 120 \text{ nm}$ for **Y(III)-DOTA-BTA**, which are in agreement in Cryo-TEM and previously reported data.^{9,210} This means that the fast process **P1** corresponds to the rod assemblies formed by the molecular aggregation of **Y(III)-DOTA-BTA** and **Gd(III)-DOTA-BTA**. The hydrodynamic radii of both processes, as well as the calculated rod lengths of **P1** are listed in Table 4.1.

Table 4.1 – Hydrodynamic radii obtained by DLS of **P1** and **P2** and calculated rod length of **P1** for **Y(III)-DOTA-BTA** and **Gd(III)-DOTA-BTA**.

Species	R_H (P1) (nm)	Rod length (from P1) (nm)	R_H (P2) (nm)
Gd(III)-DOTA-BTA	30.5 ± 4.5	245 (calc.)	348.2 ± 69
Y(III)-DOTA-BTA	17.9 ± 1.5	120 (calc.)	503.7 ± 169.6

From DLS, we know that **P2** is ~10 times larger than **P1** for **Gd(III)-DOTA-BTA** and ~30 times larger for **Y(III)-DOTA-BTA**. To gain further insight into the **P2** process, its fractal dimension was calculated using two different methods: static light scattering (SLS) and box-counting of TEM pictures²¹² (Sub-Section 4.9.4 for details). The slope in the log-log plot of the normalized scattering intensity (Rayleigh ratio, $R(q)$) as a function of the wavevector q , gives the fractal dimension, which is used to characterize the topology of aggregates (where the lower limit of $d_F = 1$ describes a line, and the upper limit $d_F = 3$ a sphere).²¹³ In our case, $d_F = 1.7 \pm 0.2$ for the SLS analysis (Figure 4.2–A below and Figure 4.4 and Table 4.3 in Appendix) and $d_F = 1.77$ –1.85 for box-counting (Figure 4.5 and Table 4.4 in Appendix). The values found by the two different methods, being on agreement, show that process **P2** would correspond to a rod network.^{214,215}

From electron microscopy and light scattering, the assembly of **Y(III)-DOTA-BTA** and **Gd(III)-DOTA-BTA** (at 100 μ M in pH 6 100 mM citrate buffer and without magnetic field) could be better understood. First, the molecule self-assembles through π - π stacking and hydrogen bonding into 6 nm diameter rods, with 245 nm and 120 nm length for **Y(III)-DOTA-BTA** and **Gd(III)-DOTA-BTA** respectively, this process is called **P1**. The rods interact with each other, forming a network, **P2**, comprised of thousands of rods. Overall, there are two equilibria driving the assembly of **M(III)-DOTA-BTA**: K_1 , which is the equilibrium between the molecules and the one-dimensional **P1**; and K_2 , that governs the aggregation of **P1** into larger network-like structures, **P2** (Figure 4.1–A). No ordering (i.e. mesophases or gelation) in both assemblies was observed. Furthermore, depolarized dynamic light scattering (DDLS)²¹⁶ did not yield any correlation.

4.3 Magnetic Control Over Supramolecular Assemblies

Since Gd(III)-DOTA-BTA is paramagnetic, and Gd³⁺ ions present one of the highest ionic magnetic moments,¹¹ the magnetic behavior of those assemblies was investigated. For that, a 100 μ M solution of either Y(III)-DOTA-BTA and Gd(III)-DOTA-BTA in 100 mM pH 6 citrate buffer was placed between the poles of an electromagnet and the magnetic field was set to either 1 or 2 T. After one hour inside the magnet, the sample was removed and analyzed in a light scattering set-up for one hour as well. This cycle was repeated until the measurements reached a plateau after 12 to 14 h. Interestingly, the scattering intensity (Rayleigh ratio, $R(q)$) steadily increases over time for the process P2 of Gd(III)-DOTA-BTA, stabilizing at a 20% to 35% increase, for 1 and 2 T respectively, Figure 4.2–B. The fractal dimension, d_F , of the same process increases from 1.7 ± 0.2 at 0 T to 2.2 ± 0.2 at 1 T, and 2.6 ± 0.2 at 2 T, Figure 4.2–A. However, the hydrodynamic radius of P2, measured by DLS, does not change during the experiment. This means that the magnetic field causes P2 to become an increasingly dense rod network at 1 T, reaching randomly branched clusters at 2 T, without a change in size.^{217–219} P1 is unaffected by the magnetic field,^x neither for Gd(III)-DOTA-BTA nor for the diamagnetic Y(III)-DOTA-BTA, because P1 does not contain an amount of paramagnetic entities in its structure for the magnetic energy to surpass the thermal noise. Y(III)-DOTA-BTA, P1 and P2, is completely unaffected by the magnetic field, since Y(III) is diamagnetic, and the magnetic energy acting on diamagnetic entities is very small. As a control, Gd(III)-DOTA-BTA was placed between the poles of the magnet, without any magnetic field, and both the scattering intensity and the fractal dimension stayed constant for the duration of the experiment.

This process is reversible, so when Gd(III)-DOTA-BTA is removed from the magnet, the scattering intensity of the assemblies and the fractal dimension revert back to the original values, a process that takes ~two days.

^x Note that $R(q) \sim r^6$ (r being the radius of the particle). As P2 is one order of magnitude larger than P1, the scattering intensity of the former would be $\sim 10^6$ bigger than for the latter. So, if there is any change in P1 scattering, it is not observable.

Overall, it can be then concluded that both magnetic field and paramagnetic assemblies are necessary for the reversible densification of the rod-network and changes in the network topology, both phenomena observed by static light scattering.

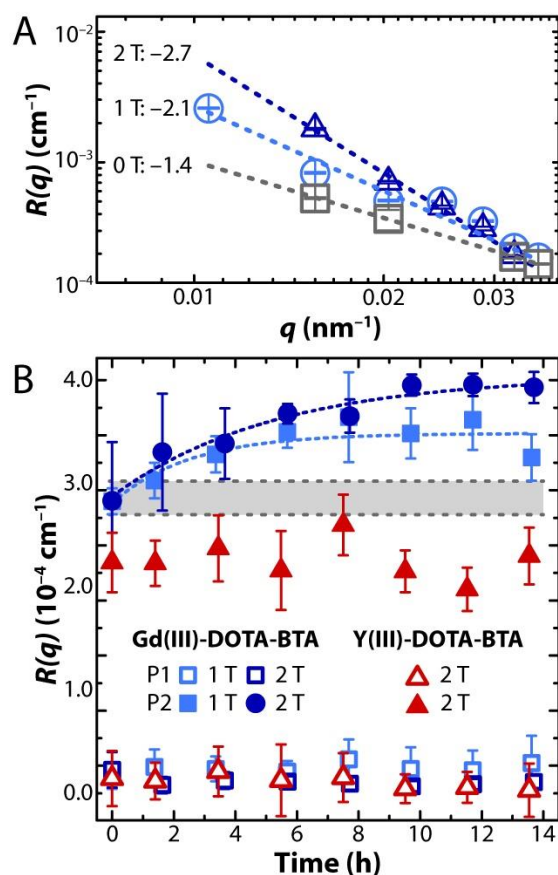


Figure 4.2 – A – Log-log plot of the Rayleigh ratio ($R(q)$), *i.e.* corrected scattered intensity) of P2, as a function of wavevector q , for different magnetic fields. The slope of this plot is the fractal dimension of P2, which the value is shown for each plot. B – Rayleigh ratio, $R(q)$, versus time of Y(III)-DOTA-BTA and Gd(III)-DOTA-BTA at 100 μM concentration in 100 mM pH 6 citrate buffer under 1 or 2 T (only 2 T for Y(III)), for P1 and P2. The gray area represents Gd(III)-DOTA-BTA under no magnetic field (mean and standard deviation). Error bars are the standard deviations of 50 measurements.

4.4 Magnetic Characterization of Assemblies

To understand how the magnetic field affects the assemblies, the magnetic properties of Y(III)-DOTA-BTA and Gd(III)-DOTA-BTA were measured in a superconducting quantum interference device (SQUID) magnetometer, following the magnetization of the molecule in powder form as a function of temperature, Figure 4.3–A. For the yttrium containing molecule, typical diamagnetism was measured. Gd(III)-DOTA-BTA shows a Curie-Weiss behavior with a small negative paramagnetic Curie temperature of -0.7 K, meaning that at low temperatures, close to 0 K, it displays antiferromagnetism but at room temperature this effect is negligible

and Gd(III)-DOTA-BTA behaves like a paramagnet. The crystal field interaction between the Gd³⁺, is also insignificant at room temperature, meaning that Gd(III)-DOTA-BTA does not display any special magnetic property beyond the trivial that would explain the observed magnetic field effects.

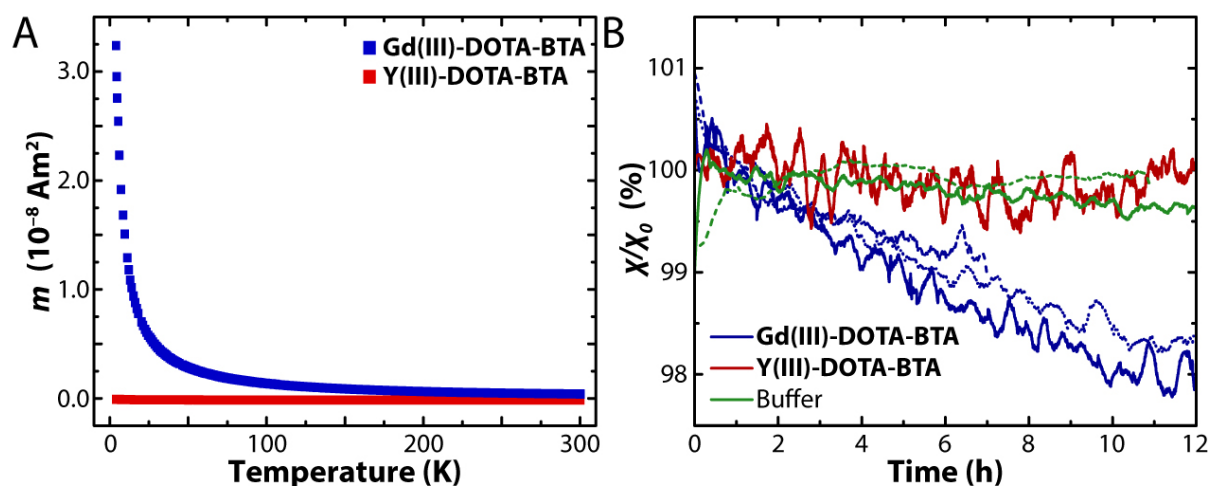


Figure 4.3 – A – Temperature-dependent magnetization, m , curve of Gd(III)-DOTA-BTA and Y(III)-DOTA-BTA in powder form. Gd(III)-DOTA-BTA shows weak antiferromagnetism of -0.7 K while the Y(III)-DOTA-BTA is diamagnetic. B – Magnetization of Gd(III)-DOTA-BTA and Y(III)-DOTA-BTA in solution as a function of time. Buffer is used as an additional control. The samples were placed in a SQUID under 5 T magnetic field and their magnetization was followed for 12 h. The solid and dotted lines represent different runs.

100 μ M solutions of Y(III)-DOTA-BTA and Gd(III)-DOTA-BTA (in 100 mM pH 6 citrate buffer) were placed inside a SQUID magnetometer at 5 T and the susceptibility of the sample was followed for 12 h, Figure 4.3–B. This experiment was performed to probe the effect that the change in network topology, caused by applying a magnetic field, would have in the magnetic properties of Gd(III)-DOTA-BTA in solution. Curiously, the magnetic susceptibility of Gd(III)-DOTA-BTA solution decreases $\sim 2\%$ over 12 hours under 5 T,^{xi} this result indicates in a loss in anisotropy in the structures when they become more randomly branched. When the same experiment is performed with Y(III)-DOTA-BTA (or only buffer) no changes in susceptibility are observed over the course of the experiment.

It has been shown that Gd(III)-DOTA-BTA does not possess non-trivial magnetic properties, capable of explaining its behavior under a magnetic field. Additionally, the

^{xi} A strong magnetic field is needed for this experiment because the effect on the magnetic susceptibility is very small and could not reliably be detected at 1 or 2 T.

magnetic field not only influences the topology of **Gd(III)-DOTA-BTA P2** assemblies it also changes the magnetic properties of the material.

4.5 Energetic Considerations

As it has been briefly discussed in the

Introduction of this chapter and more in detail in Sub-Section 1.4.1, at 1 or 2 T the magnetic energy acting on a single paramagnetic Gd^{3+} ion at 25 °C is insignificant, being four orders of magnitude smaller than the thermal energy. For **Gd(III)-DOTA-BTA** the magnetic energy of a single monomer can be defined as:¹¹

$$E_{mag,1} = -\frac{1}{2} m B = 3 \frac{1}{2 \mu_0} \chi V B^2 = \frac{3}{2} \frac{m_{eff}^2 B^2}{3 k_B T} = \frac{m_{eff}^2 B^2}{2 k_B T}$$

Where m is the magnetic moment induced by the field B at temperature T , χ is the volumetric magnetic susceptibility of the monomer, V is the volume of the monomer, m_{eff} is the effective atomic paramagnetic moment in Am^2 (given in units of Bohr magneton μ_B). The factor 3 arises from having three paramagnetic ions per monomer. We can therefore define a critical length L_c of the supramolecular rod, with N_c the critical number of monomers per rod, where the magnetic energy of the object is in the same order as the thermal energy ($|E_{mag}| \geq k_B T$). The critical energy for a rod would be:

$$E_{m,rod} = N_c E_{m,1} = \frac{L_c}{d_{\pi-\pi}} E_{m,1}$$

Where $d_{\pi-\pi}$ is the π - π stacking distance between each **Gd(III)-DOTA-BTA**.³ Equating this equation to the thermal noise ($k_B T$), we get for the critical rod length:

$$L_c = \frac{d k_B T}{E_{m,1}} = 2 d \left(\frac{k_B T}{m_{eff} B} \right)^2$$

The critical length and supramolecular magnetic energy was calculated for different paramagnetic ions (Table 4.2 and Table 4.5 in Appendix). In addition, a more detailed model considering the exact positioning of Gd^{3+} ions within the supramolecular rods, and dipole-dipole interactions, was in quantitative agreement (see Sub-Section 4.9.6 and Sub-Section 4.7.1 in the Appendix).

Table 4.2 – Magnetic energies of assemblies (**M(III)-DOTA-BTA**, where M(III) is a trivalent paramagnetic ion) and critical length for different paramagnetic ions at $B = 2$ T and $T = 298$ K. Gd^{3+} is used in the current work. Effective magnetic moment data taken from Coey, J. M. D. *Magnetism and Magnetic Materials*.

Ion	m_{eff}	$E_{m,1}$	L_c
M(III)	(μ_B)	($J \cdot mol^{-1} monomer^{-1}$)	(nm)
Nd^{3+}	3.4	-0.29	2980
Gd^{3+}	8.9	-1.99	435
Tb^{3+}	9.8	-2.42	359
Dy^{3+}	10.6	-2.83	307
Ho^{3+}	10.4	-2.73	318

Since the lengths of the **P1** rod is 245 nm (see Table 4.1), which corresponds to $\sim 56\%$ of the critical length, the magnetic energy acting on the rod assemblies is smaller than $k_B T$. However, **P2** aggregates consist of a large number of entangled rods, meaning that the magnetic energy acting on the rod network would surpass the thermal energy. A problem with this reasoning, however, is that for the magnetic energy it does not matter how the Gd^{3+} ions are distributed across space. The magnetic energy is the same for monomers floating freely in solution or for monomers contained within self-assembled rods. There is, however, another aspect that we can consider, which can qualitatively explain our observations. Namely, there is a small energetic correction due to shape anisotropy (K_s):¹¹

$$K_s = \frac{1}{4} \mu_0 M_s^2 (1 - 3N)$$

Where N is the shape-dependent demagnetizing factor ($N = 0$ for an axially magnetized long rod), M_s is the saturation magnetization that depends on the distribution of the magnetized material and μ_0 is the vacuum permeability. For the rods, the saturation magnetization is $M_s = 600 \text{ Am}^{-1}$, leading to a maximum anisotropy energy of $K_s = 0.11 \text{ Jm}^{-3}$. A minimal critical volume of the assembly of $V_c = k_B T / K_s = 36 \cdot 10^{-21} \text{ m}^3$ is therefore needed to overcome thermal energy. Since a single **Gd(III)-DOTA-BTA P1** rod is $\sim 4 \cdot 10^{-24} \text{ m}^3$, thousands of rods are necessary for the anisotropy energy to overcome $k_B T$.

P2, being the network behavior of **P1**, probably comprises thousands of rods,^{xii} giving enough size to the assembly to reach the critical volume.

These energetic calculations show that, even if **Gd(III)-DOTA-BTA** does not present special magnetic properties, the supramolecular assembly into rods and rod-networks accumulate enough paramagnetic entities to overcome the thermal energy ($k_B T$). These calculations also present a rule of thumb for the design of future magneto-responsive supramolecular materials (see Table 4.2 and Table 4.5 in Appendix).

4.6 Conclusions

We have shown the magneto-responsive supramolecular assembly of paramagnetic **Gd(III)-DOTA-BTA**, that self-assembles into rods in solution, that further aggregate into rod networks comprising thousands of entities. When submitted to a magnetic field the densification and branching of the rod network topology is observed. Which is not a trivial observation, since (as discussed above) the magnetic energy acting on a single Gd^{3+} ion or a single supramolecular rod is not significant to overcome the thermal noise, needing a network of rods to break this barrier. Furthermore, the experimental magnetic response is not expected, since previous examples show alignment of assemblies parallel or perpendicularly to the magnetic field.¹³² Magnetic measurements show that this does not happen and the densification of the rod network is an unexpected observation. Energetic calculations show that the supramolecular rod network is large enough and contains sufficient paramagnetic ions for the magnetic energy to overcome the thermal energy of $k_B T$, but these calculations still cannot explain what is happening inside the aggregates.

These results open the door for a new class of supramolecular magnetic materials that are responsive to easily achievable magnetic fields (< 2 T). The energetic calculations also show that this approach can be easily expanded to other paramagnetic ions, opening the door to multi-functional materials.

^{xii} Exact number is difficult to estimate

4.7 Appendix

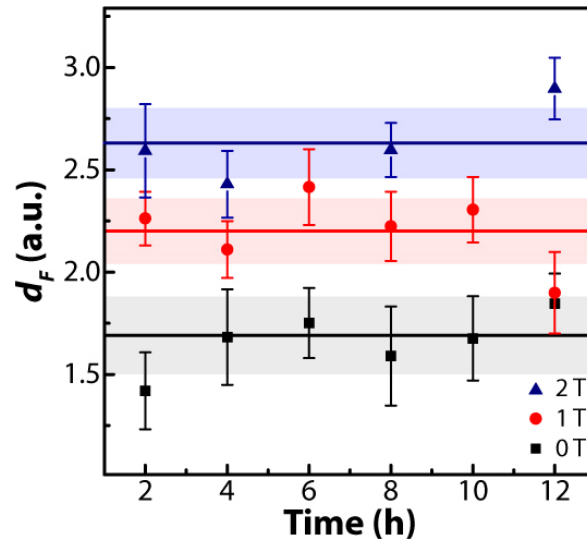


Figure 4.4 – Fractal dimension d_F and the corresponding standard deviations obtained from linear regression for 0 T, 1 T and 2 T fields (method in Sub-Section 4.9.4.1). The horizontal line represents the average values over the experiment and the shaded area the standard deviation. The error bars for the data points are the standard deviation over triplicate experiments. 2 h of measurement include 1 h of exposure to the magnetic field and 1 h of light scattering measurements in the absence of an external magnetic field. The mean values and standard deviations are summed up in Table 4.3.

Table 4.3 – Mean values of d_f and the corresponding standard deviations obtained from linear regression for 0T, 1T and 2T fields. Data taken from Figure 4.4.

B (T)	$\overline{d_f}$
0	1.7 ± 0.19
1	2.2 ± 0.18
2	2.6 ± 0.17

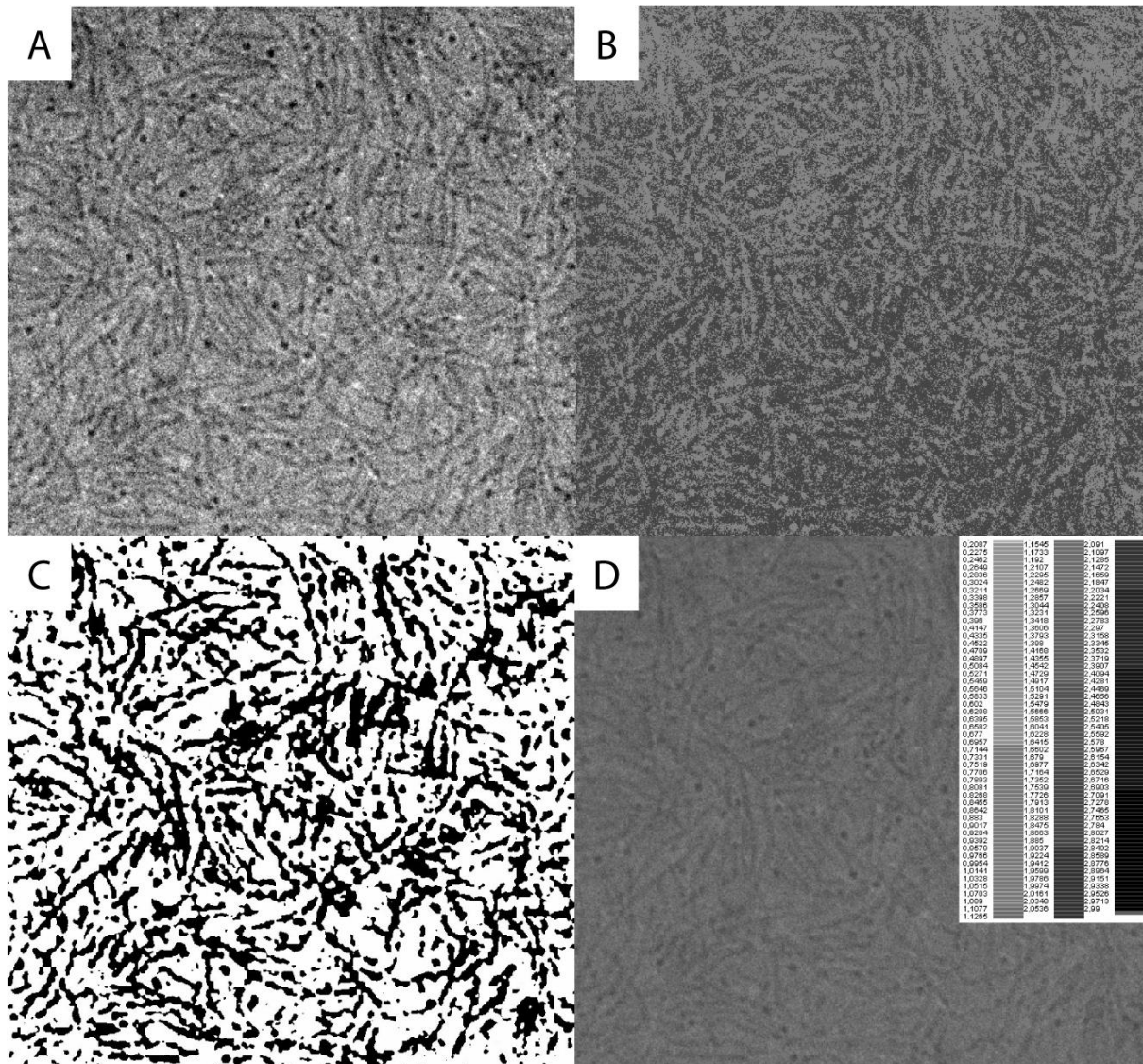


Figure 4.5 – A – Original Cryo-TEM image. B – Image obtained by automatic processing (method A). C – Image obtained from manual generation of a binary image (method B). D – Image obtained from the differential grayscale method (method C) and the respective intensity-coded legend. Methodologies in Sub-Section 4.9.4.2.

Table 4.4 – Mean values of $\overline{d_B}$, $\overline{d_M}$, and $\overline{d_X}$ and their corresponding standard errors obtained from the FracLac application. Method A refers to the automatic generation of a binary image provided by the application. Method B refers to a manual generation of a binary image using standard ImageJ commands. Method C is the differential gray scaling method provided by FracLac. Data treatment show in Figure 4.5 and methodology in Sub-Section 4.9.4.2.

method	$\overline{d_B}$	$\overline{d_M}$	$\overline{d_X}$
A (Automatic binary)	1.85 ± 0.113	1.85 ± 0.113	1.85 ± 0.069
B (Manual binary)	1.79 ± 0.084	1.79 ± 0.084	1.79 ± 0.059
C (Grey differential)	1.77 ± 0.097	0.08 ± 0.065	1.76 ± 0.052

4.7.1 Results of Magnetic Ground-State Calculations

First, as a reference value, we calculate the ideal magnetization of an assembly. The cylindrical volume for a rod containing 100 monomers is:

$$V_{rod} = \pi r^2 d_{\pi-\pi} = 557 \text{ nm}^3$$

Since there are three Gd per monomer, in this rod there are 300 Gd atoms, which means around 0.54 Gd per nm^3 . For fully aligned moments, with $B = 2 \text{ T}$ and $T = 298 \text{ K}$, the effective magnetic moment is $m_{eff} \approx 0.12 \mu_B$ per Gd atom (μ_B is the Bohr magneton which is equal to $9.27 \cdot 10^{-24} \text{ J} \cdot \text{T}^{-1}$). Then, the saturation magnetization is:

$$M_s = 0.12 \mu_B \cdot 0.54 \cdot 10^{27} \text{ m}^{-3} = 600 \text{ A} \cdot \text{m}^{-1}$$

The induced M_s is 0.04% the external field B .

We find that for any external field, B , the local magnetic moments are collinear with B in the ground state (Figure 4.6–A&B). For a sum over an assembly of 1000 monomers, with B parallel to the fiber, (2 T) the magnetization is $M = 595.1 \text{ A} \cdot \text{m}^{-1}$. With B perpendicular to the fiber (2 T) $M = 594.8 \text{ A} \cdot \text{m}^{-1}$. Both values are marginally smaller than the ideal of $600 \text{ A} \cdot \text{m}^{-1}$, the difference arises from the demagnetizing field due to the local dipolar fields. Unlike the atomic moments, the local dipolar fields form complex helical patterns (Figure 4.6–C&D). However, we find that their magnitude is $\approx 2 \text{ mT}$, three orders of magnitude smaller than the 2 T external field (Figure 4.7), and lead to the calculated magnetization being marginally smaller than the ideal case as expected for a very weak demagnetizing field. So, for the sake of simplicity, the maximum value of $M_s = 600 \text{ A} \cdot \text{m}^{-1}$ is considered. These calculations were performed using SciPy²²⁰ following the methodology in Sub-Section 4.9.6.

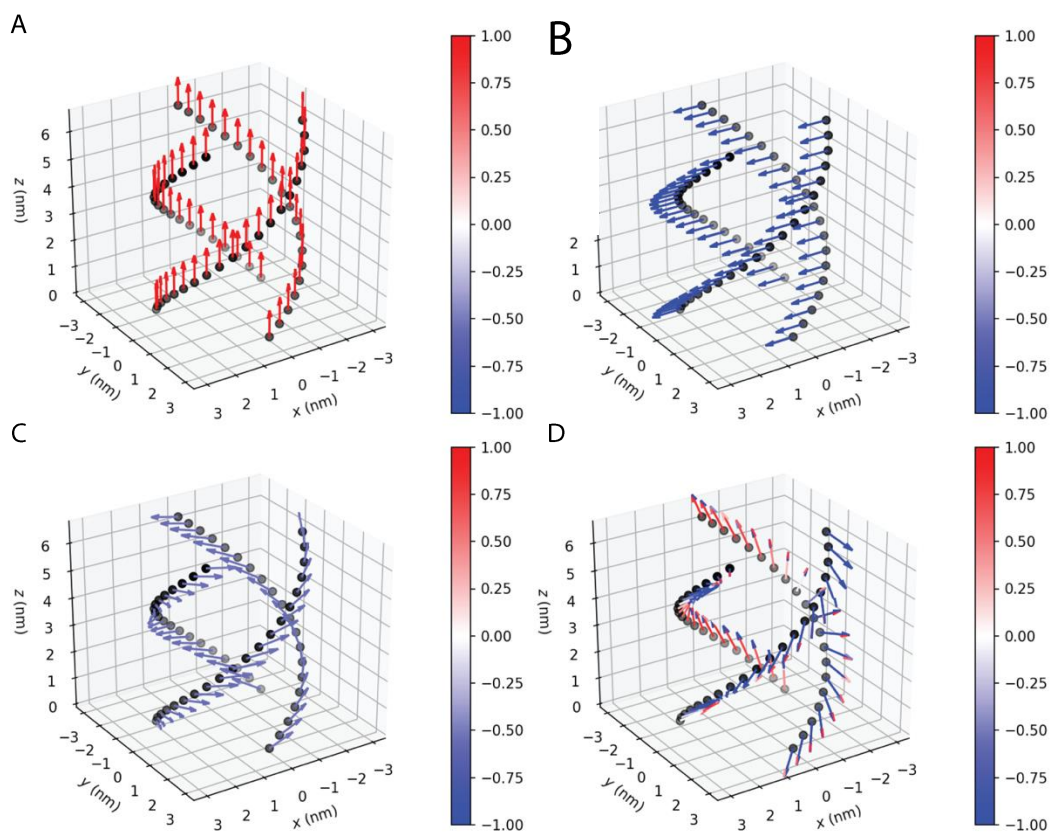


Figure 4.6 – Normalized quiver plot of the induced atomic moments under an external 2 T field – **A** – along z, – **B** – along x, with the corresponding local dipolar fields in **C** and **D** for $B // z$ and $B // x$, respectively. $B // y$ is not shown but is identical to $B // x$.

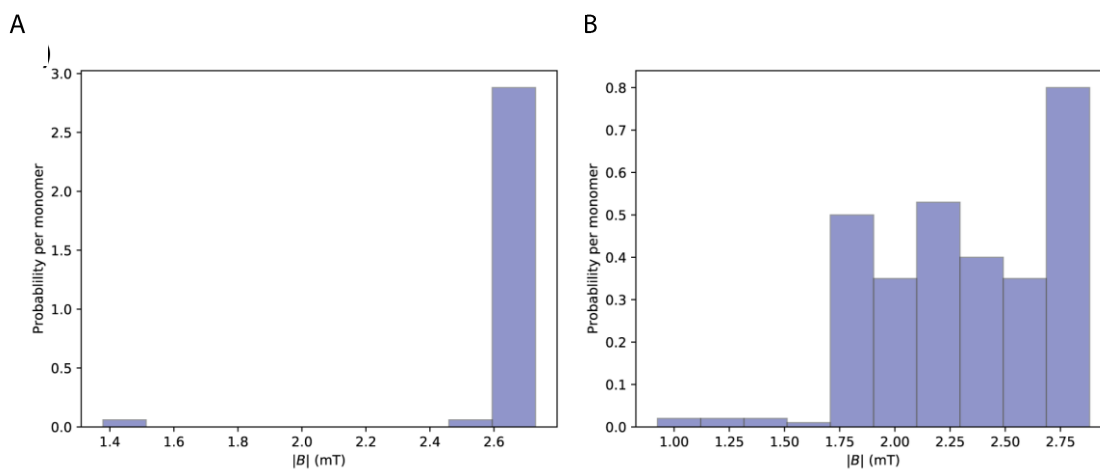


Figure 4.7 – Distribution of the magnitude of the dipolar magnetic fields for 100 monomers for – **A** – $B // z$, and – **B** – $B // x$. $B // y$ is not shown but is identical to $B // x$.

Table 4.5 – The experimental magnetic moment m , magnetic energy per monomer $E_{m,1}$, and magnetic Gibbs free energy per monomer $\Delta G_{m,1}$, critical length L_c and critical monomer number N_c , for various transition metal and rare earth ions in a **M-DOTA-BTA** assembly (M being the metal), with $B = 2$ T and $T = 298$ K. Beware that these are calculated values and that we assume that the assemblies are all rod-like as those shown in the main text.

Ion	m^{11} (μ_B)	$E_{m,1}$ (J mol ⁻¹ mono ⁻¹)	$\Delta G_{m,1}$ (J mol ⁻¹ mono ⁻¹)	L_c (nm)	N_c (monomers)
Ti ³⁺ , V ⁴⁺	1.7	-0.07	-0.04	11918	34052
Ti ²⁺ , V ³⁺	2.8	-0.20	-0.10	4393	12553
V ²⁺ , Cr ³⁺	3.8	-0.36	-0.18	2385	6816
Cr ²⁺ , Mn ³⁺	4.9	-0.60	-0.30	1435	4099
Mn ²⁺ , Fe ³⁺	5.9	-0.88	-0.44	989	2828
Fe ²⁺ , Co ³⁺	5.4	-0.73	-0.37	1181	3375
Co ²⁺ , Ni ³⁺	4.8	-0.58	-0.29	1495	4272
Ni ²⁺	3.2	-0.26	-0.13	3364	9611
Cu ²⁺	1.9	-0.09	-0.05	9541	27261
Ce ³⁺	2.5	-0.16	-0.08	5511	15746
Pr ³⁺	3.5	-0.31	-0.15	2812	8034
Nd ³⁺	3.4	-0.29	-0.15	2980	8513
Sm ³⁺	1.7	-0.07	-0.04	11918	34052
Eu ³⁺	3.4	-0.29	-0.15	2980	8513
Gd ³⁺	8.9	-1.99	-1.00	435	1243
Tb ³⁺	9.8	-2.42	-1.21	359	1025
Dy ³⁺	10.6	-2.83	-1.41	307	876
Ho ³⁺	10.4	-2.72	-1.36	318	910
Er ³⁺	9.5	-2.27	-1.14	382	1091
Tm ³⁺	7.6	-1.45	-0.73	596	1704

4.8 Acknowledgements

Prof. Pol Besenius, Dr. Isja de Feijter and D. Jorge Leira-Iglesias synthesized the molecules. Dr. Vincent Marichez, Dr. Akihiro Sato with the help of Dr. Matthieu Bailleul and Dr. Pascal Hébraud performed the light scattering experiments. Dr. Peter Dunne with the help of Dr. M. Venkatesan performed the SQUID experiments. Dr. Peter Dunne and Prof. J.M.D. Coey performed the magnetic ground-state calculations. Michaela K. Schicho calculated the fractal dimensions. Georges Formon (together with the other authors) compiled and interpreted the data. Prof. Thomas Hermans conceived and supervised the research.

This chapter was written by Georges Formon based on the publication: Marichez, Vincent; Sato, Akihiro; Dunne, Peter A.; Leira-Iglesias, Jorge; Formon, Georges J.M.; Schicho, Michaela K.; de Feijter, Isja; Hébraud, Pascal; Bailleul, Matthieu; Besenius, Pol; Venkatesan, M.; Coey, J.M.D.; Meijer, E.W.; Hermans, Thomas, M. (2020): Magnetic Control over the Topology of Supramolecular Rod Networks. ChemRxiv. Preprint. <https://doi.org/10.26434/chemrxiv.12762269.v1>

4.9 Materials and Methods

4.9.1 Synthesis

Gd(III)-DOTA-BTA and Y(III)-DOTA-BTA were synthesized following a previously described methodology.⁹

4.9.2 Cryo-TEM

The cryoTEM experiments were performed on the TU/e CryoTitan (FEI), using a Gatan cryo-holder operating at ~ -170 °C (www.cryotem.nl). The TU/e CryoTitan is equipped with a field emission gun (FEG) operating at 300 kV. Images were recorded using a 2k x 2k Gatan CCD camera equipped with a post column Gatan Energy Filter (GIF). The sample vitrification procedure was carried out using an automated vitrification robot (FEI Vitrobot™ Mark III). CryoTEM grids, R2/2 Quantifoil Jena grids, were purchased from Quantifoil Micro Tools GmbH. Prior to the vitrification procedure the grids were surface plasma treated using a Cressington 208 carbon coater operating at 5 mA for 40 s.

4.9.3 Dynamic Light Scattering

4.9.3.1 Generalities

We employed a Krypton Ion Laser with 413 nm wavelength and maximum intensity of 1W, made by Spectra Physics. The laser power was 200 mW. The measured polarized field autocorrelation functions $g_{VV}^{(1)}(q, t)$ is obtained for different the wave vectors (q). Where:

$$q = \frac{4 \pi n_0}{\lambda} \sin\left(\frac{\theta}{2}\right)$$

n_0 is the refractive index of the sample, λ is the wavelength of the laser, and θ is the angle at which the scattering is collected.

From the Contin analysis^{xiii} the distribution of relaxation times ($G(\tau)$) can be obtained, which contains the characteristic relaxation times (τ), that when are inverted give the decay constant ($\Gamma = \tau^{-1}$). In processes that are diffusive in nature, the decay constant is linear with the square of the wave vector and the slope is the diffusion constant (D_H):

$$\Gamma = D_H \cdot q^2$$

The hydrodynamic radius can be calculated by the Stokes Einstein equation, using the calculated diffusion constant, as follows:

$$R_H = \frac{k_B T}{6 \pi \eta D_H}$$

Where k_B is the Boltzmann constant, T is temperature and η the dynamic viscosity.

4.9.3.2 Electromagnet experiments

For the experiment involving the electromagnet, the following procedure was used: i) The sample (100 μ M solution in a 100 mM pH 6 citrate buffer) is immersed in a 25°C thermostated Toluene bath and allowed to thermally equilibrate for 40 min. ii) We then measured the angle dependent correlation function from 30 to 120 degree with a 15 deg increment. The integration time was 30 sec each. iii) 60 consecutive correlation functions are subsequently measured with a 30 sec integration time. iv) The sample is placed in a uniform magnetic field of 1 T or 2 T depending on the experiment for 1 hour.

^{xiii} Iari-Gabriel Marino (2007). rilt (<https://www.mathworks.com/matlabcentral/fileexchange/6523-rilt>), *MATLAB Central File Exchange*.

The electromagnet is from the DRUSCH company was powered by a 14 kW power supply with a distance between the two poles of 38 mm. Steps iii) and iv) are repeated until the scattering intensity collected reaches a plateau.

4.9.4 Fractal dimension

4.9.4.1 Fractal dimension from static light scattering

Mean scattering intensities (I_{sam}) have been measured for 6 angles from 30° to 120° in 15° increments at a laser wavelength of 413 nm and a laser power of 200 or 300 mW. Every measurement was repeated 4 times. In the measurements in a 1 T field, an ND filter was used for the angles 30° and 45°.

The Rayleigh-Ratio ($R(q)$) is obtained from the measured mean scattering intensity (I_{sam}) following the equation:

$$R(q) = \frac{I_{sam} - I_b}{I_{ref}} \cdot R_{ref} \cdot \left(\frac{n_0}{n_{ref}} \right)^2$$

Where

I_b	intensity of the background, measured	
I_{ref}	intensity of the reference (toluene), measured	
R_{ref}	Rayleigh ratio of the reference (toluene)	$1.35 \cdot 10^{-5} \text{ cm}^{-1}$.
n_0	refractive index of the sample solution, measured	1.338
n_{ref}	refractive index of the reference (toluene)	1.497

The angle is converted into scattering vector q according to the equation

$$q = \frac{4 \pi n_0 \cdot \sin\left(\frac{\theta}{2}\right)}{\lambda}$$

Where θ is the angle and λ the laser wavelength, here 413 nm.

The Rayleigh ratio is q -dependent, following a power law:

$$R(q) \sim q^{-d_F}$$

Where d_F is the fractal dimension of the process.

The logarithm of average Rayleigh ratio (over 5 measurements) is then plotted as a function of the logarithm of the scattering vector. Linear regression allows the determination of fractal dimension d_F , which is the slope.

4.9.4.2 Fractal dimension from cryo-TEM imaging: Box counting

The FracLac application in ImageJ was used to calculate the fractal dimension from the obtained cryo-transmission electron images (cryo-TEM). The program works as follows: a series of grids of decreasing caliber ϵ , referring to the number of pixels per box, is laid over a binary image of the structure to be analyzed, and the number of boxes N containing foreground pixels is recorded for every caliber. The fractal dimension d_f is obtained from the slope of the linear regression of logarithmic N versus the logarithm of ϵ .^{xiv}

$$d_f = \lim_{\epsilon \rightarrow 0} \frac{\ln N_\epsilon}{\ln \epsilon}$$

For example, Figure 4.5 was analyzed using three different methods. In method A (Figure 4.5–B), the original image is automatically converted by the software to produce a binary image, which is then analyzed. In method B (Figure 4.5–C), this conversion was done manually. Method C (Figure 4.5–D) is a grayscale option, in which the grid caliber is set in relation with the variation in average intensity of the I_ϵ instead of N_ϵ . where $\delta I_{j,j,\epsilon}$ is the difference between the maximum pixel intensity and the minimum pixel intensity.

Three basic types of d_f are reported, that differ in their way of accounting for the number of boxes or the intensity, respectively. For the determination of d_B , the sum of all intensities $I_{j,j,\epsilon}$ are considered, whereas for d_M it is the mean over all intensities $I_{j,j,\epsilon}$. For d_X , the average cover over all grids is calculated, and then processed as for d_B . The methods apply analogously for binary images, for which d_B and d_M are inherently equivalent.

4.9.5 SQUID (Superconducting Quantum Interference Device)

The SQUID measurements were done with a Quantum Design MPMS XL 5 SQUID magnetometer on the Gd(III)-DOTA-BTA and Y(III)-DOTA-BTA powders, Figure 4.3–A.

^{xiv} Box Counting <https://imagej.nih.gov/ij/plugins/fractalac/FLHelp/BoxCounting.htm> (2020).

The relaxation measurements, in Figure 4.3–B, were performed by placing a 100 μM (in a 100 mM pH 6 citrate buffer) solution of **Gd(III)-DOTA-BTA** (or **Y(III)-DOTA-BTA** as control) in the center of the coil of the SQUID magnetometer. A 5 T field is applied for the duration of the experiment and magnetization/susceptibility was measured *in situ*.

4.9.6 Magnetic dipole calculations

To ensure that, at room temperature, the local dipolar fields play no role in the arrangement of the magnetic moments, we calculate the magnetic ground state for a magnetic assembly of length N_m in an external magnetic field using a lattice sum approach:

1 – Impose an external field $\mathbf{B} = B_x \hat{x} + B_y \hat{y} + B_z \hat{z}$.

2 – Generate the positions of each rare earth atom in the BTA assemblies:

knowing that in a single monomer those positions are $(x, y, z) = (0, r, 0)$, $(\frac{\sqrt{3}r}{2}, \frac{r}{\sqrt{2}}, 0)$, and $(-\frac{\sqrt{3}r}{2}, \frac{r}{\sqrt{2}}, 0)$ where $r = 2.25$ nm, that the stacking distance between monomers is $d = 0.35$ nm, and that there is a helicity of 10° rotation per layer, which for the i^{th} atom of the j^{th} layer is:¹¹

$$\begin{bmatrix} x' \\ y' \\ z' \end{bmatrix}_{i,j} = \begin{bmatrix} \cos j\theta & -\sin j\theta & 1 \\ \sin j\theta & \cos j\theta & 1 \\ 0 & 0 & 1 \end{bmatrix} \begin{bmatrix} x \\ y \\ z + jd \end{bmatrix}_{i,j}$$

3 – Calculate each local dipole moment using either a Curie-Law or Brillouin function (at $T = 298$ K the difference is negligible) giving an array of

$$\mathbf{m} = m_x \hat{x} + m_y \hat{y} + m_z \hat{z}$$

4 – At each atomic site, calculate the dipolar field due to all other moments in the assembly using:

$$\mathbf{B}(\mathbf{r}) = \frac{\mu_0}{4\pi} \left[\frac{3\mathbf{m}(\mathbf{m} \cdot \hat{\mathbf{r}})}{r^5} - \frac{\mathbf{m}}{r^3} \right]$$

which is the magnetic field at a point in space due to a magnetic dipole, resulting in a matrix

$$\mathbf{B}_{\text{dip}} = B_{\text{dip},x} \hat{x} + B_{\text{dip},y} \hat{y} + B_{\text{dip},z} \hat{z}$$

5 – At each atomic site sum the external and dipole fields $\mathbf{B}_{\text{total}} = \mathbf{B}_{\text{ext}} + \mathbf{B}_{\text{dip}}$

6 – Calculate a new moment \mathbf{m}_{new} at each site using the local $\mathbf{B}_{\text{total}}$

7 – Calculate the mean L_2 norm for the difference between the updated and old moment vectors at each site:

$$\overline{\|m\|_2} = \frac{1}{N_{atoms}} \sum (m_{new} - m_{old})^2$$

Repeat 3–7 with updated total field and moments until $\overline{\|m\|_2} < \text{threshold}$

Other minimization approaches are possible, such as by fixing the magnitude of the magnetic moments and minimizing the energy cost function through a free rotation of each moment. A first, simpler cost function, takes a macro-spin approach, assigning one polar (θ) – azimuthal (ϕ) angle pair, with all atomic moments rotating coherently, which is minimised using the L-BFGS-B algorithm. The second allows the free rotation of each moment using basin hopping global optimization, with L-BFGS-B as the local optimizer. However, both approaches are slower than the L_2 norm method presented above, particularly the global optimization method.

Chapter 5. Magnetic Lanthanides to Control Supramolecular Polymers

Abstract: In this Chapter, we show the synthesis and characterization of a library of lanthanide-containing self-assembling perylene diimide derivatives. The supramolecular polymerization was analyzed by UV/Vis and CD spectroscopy, and a variable temperature isodesmic model could be fitted to the data. The morphology and size of the assemblies were probed by light scattering and microscopy techniques, showing that the molecule containing Holmium produces the largest assemblies among the studied library. This approach opens the door to new magnetic and/or luminescent materials whose structures and properties can be tuned by carefully choosing the rare earth metal ion that is included in the molecule.

5.1 Introduction

Molecular magnetic materials and compounds are of high importance for future technologies with molecular magnets and single chain magnets showing promise for data storage applications.^{221,222} Compounds containing paramagnetic lanthanides have been utilized to fabricate these magnetic materials because they possess large magnetic moment and anisotropy, and present significant magnetic hysteresis at low temperatures.²²³ Lanthanide complexes have also been extensively used as magnetic resonance imaging contrast agents because they optimally change the relaxation times of the protons in the water molecules surrounding them, with six clinically approved Gd-containing agents.²²⁴ Apart from their magnetic applications, lanthanides are also widely used for their luminescent²²⁵ and catalytic²²⁶ properties.

Lanthanides also have a property called single-ion anisotropy, where the charge density distribution of the 4*f* electrons deviate from spherical symmetry. This means that the spin-orbit interactions lead to the alignment of the magnetic moment of the materials within a specific direction in the crystal structure.¹¹

In Chapter 4 and in Section 1.4 of the first Chapter we have shown how self-assembled structures can be controlled using a magnetic field. In 2013 Polarz and colleagues presented a dysprosium-containing surfactant that self-assembles into macroscopic dumbbell-shaped assemblies, a phenomenon thought to be the result of the crystal-field interactions between the magnetic heads.¹⁶⁷ Inspired by this work, we now seek to understand how the interaction of paramagnetic lanthanides would influence supramolecular self-assembly, in absence of a magnetic field. By bringing paramagnetic lanthanide ions close to one another through self-assembly, magnetic dipole-dipole or crystal field interactions can possibly be induced, thus changing self-assembly. For that we synthesized a library of perylene diimide molecules coupled to DOTA (tetraazacyclododecane-tetraacetic acid) moieties chelating different lanthanides. The thermodynamic parameters of their self-assembly in water was investigated as well as the size and morphologies of the aggregates in solution.

5.2 Synthesis and Spectroscopic Characterization

To understand the influence rare earth ions have on supramolecular polymerization, we synthesized a library of bolaamphiphile perylene diimides functionalized with tetraazacyclododecane-tetraacetic acid (DOTA) moieties. This functionality is used to chelate different paramagnetic lanthanides: Ho(III), Er(III) and Gd(III); and a diamagnetic control, Y(III)^{xv} (Figure 5.1–A). **PDI-Ln** (where Ln is Ho, Er, Gd or Y) self-assembles in water by the π - π stacking of the perylene core, in addition to hydrophobic interactions. The close proximity between the magnetic heads, brought together by aggregation, would influence the final aggregate morphology or polymerization (Figure 5.1–B). From now on, each specific compound will be referred to **PDI-** followed by their specific rare earth (i.e. **PDI-Ho**, **PDI-Er**, **PDI-Gd** and **PDI-Y**). When referring to all the compounds simultaneously, the term **PDI-Ln** will be used.

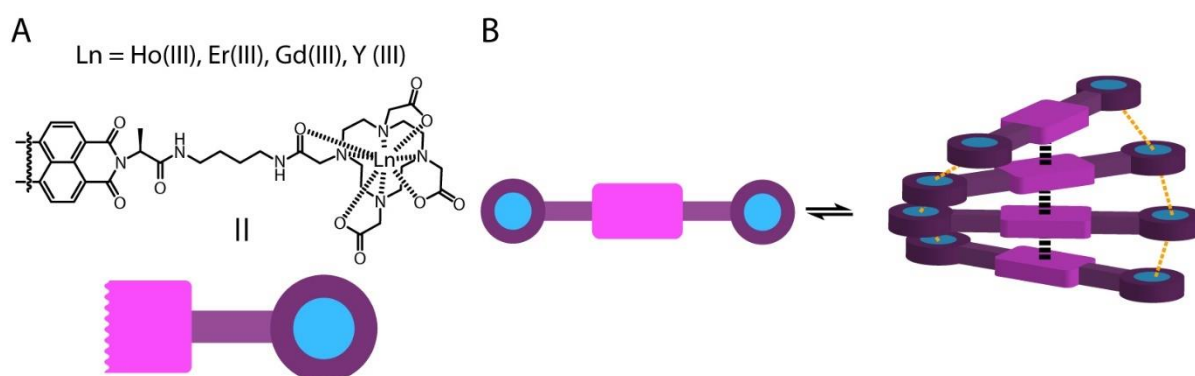


Figure 5.1 – A – Scheme of **PDI-Ln** and its cartoon representation. The perylene diimide is homodifunctionalized. B – Scheme of **PDI-Ln** self-assembly, through π - π stacking and the lanthanide-lanthanide interactions.

The synthetic scheme for the preparation of **PDI-Ln** is a four-step process (Figure 5.2):

- Imidization of perylenetetracarboxylic dianhydride (PTCDA) with L-alanine, catalyzed by imidazole, yielding **1**.¹¹⁵
- Coupling of the Perylene diimide di-alanine (**1**) with a butyl spacer through amide bond formation, producing **2**.²²⁷
- The DOTA moiety is attached to **2** by peptide coupling, giving **3**.

^{xv} Although Yttrium is not technically a lanthanide, it is often included in the studies because its size and coordination sphere are similar to lanthanides.

- Different lanthanides are chelated to **3** using a microwave reactor, forming **PDI-Ln** (Ln= Ho, Er, Gd, Y).²²⁸

The detailed procedure for the preparation of **PDI-Ln** is found in Sub-Section 5.8.1

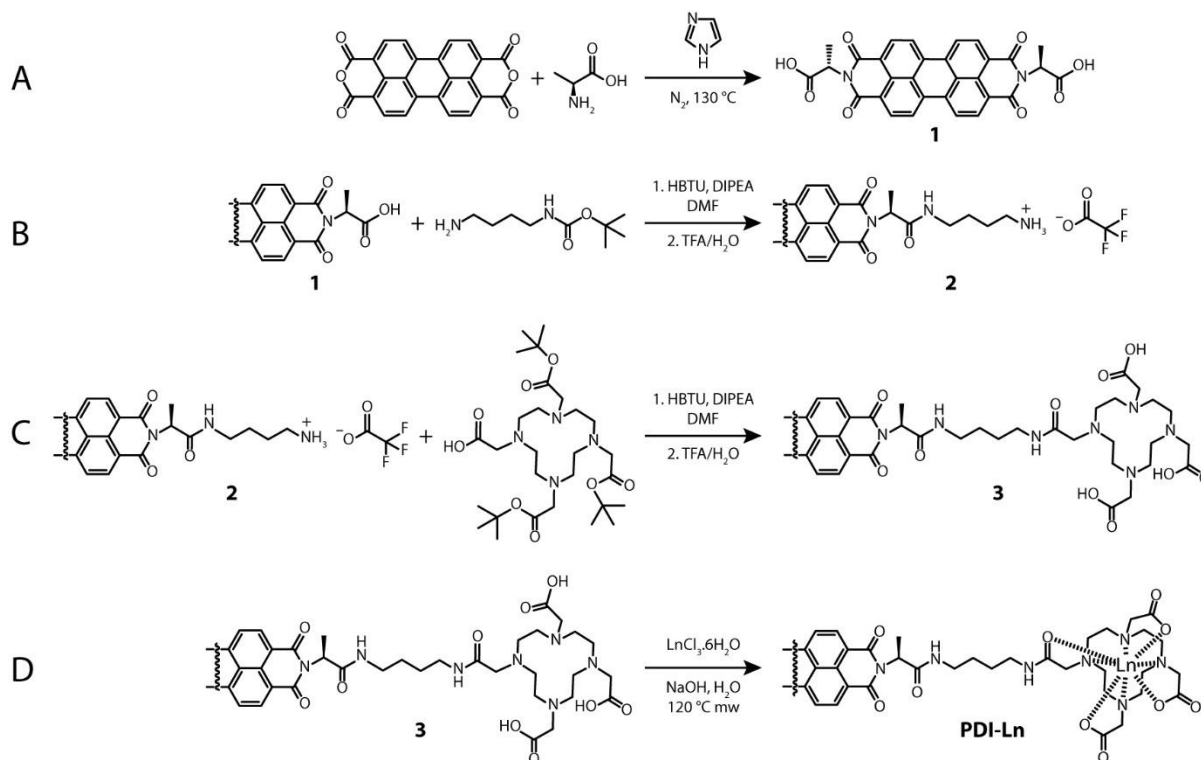


Figure 5.2 – Synthetic scheme of **PDI-Ln**. **A** – Imidazole for 30 minutes at 130 °C and under N₂ atmosphere. **B & C** – 1. HBTU, DIPEA in DMF for 14h. 2. TFA/H₂O (98:2) for 2h. **D** – 10 equivalents NaOH in H₂O at 120 °C in microwave reactor. Details in Sub-Section 5.8.1.

Perylene diimides are known to have a broad absorption band between 420 to 620 nm, due to S₀→S₁ transitions. In this region two maxima can be identified, one at ~500 nm, corresponding to the 0-1 transition and another at ~540 nm, relative to the 0-0 transition. PDI is a well-studied dye and supramolecular building block and a strong correlation has been found between self-assembly and the spectroscopic properties of the perylene diimide. For example, it is known that the ratio between the two maxima discussed above (I_{500}/I_{540}) is correlated to the degree of aggregation, with this fraction being equal to 0.65 when a PDI is monomeric. Furthermore, a red-shift is also observed in the Ultraviolet/Visible (UV/Vis) spectrum when PDI becomes more aggregated, accompanied by fluorescence quenching when the molecule self-assembles into H-aggregates.^{12,229}

To characterize spectroscopically **PDI-Ln** the samples were first dissolved in methanol, a solvent where they would be monomeric. The measured UV/Vis spectra at 4 μM (Figure 5.3–A for **PDI-Y** and Figure 5.14–A, C, E, G for all **PDI-Ln**) is typical for monomeric PDI, with three well resolved absorption maxima, and the ratio $I_{500}/I_{540} = 0.65$. Fluorometry in the same solvent yield emission (excitation at 522 nm) spectra that are mirror images of the absorbance. Normalized excitation spectra (measuring emission at 535 nm) are almost superimposed to the UV/Vis spectra, but a slightly higher intensity at the 0-1 transition. This indicates that **PDI-Ln** are molecularly dissolved in methanol at 4 μM concentration.

When the same measurements are performed in water, at the same concentration of 4 μM (Figure 5.3–B for **PDI-Y** and Figure 5.14–B, D, F, H for all **PDI-Ln**) a very different absorption spectrum is obtained, but typical for assembled PDI. Firstly, the three maxima are less resolved, with less prominent peaks. The spectra are all slightly red-shifted, and the ratio I_{500}/I_{540} doubled (~ 1.3). Moreover, the fluorescence spectra are also red-shifted and less intense. This strongly indicates that **PDI-Ln** are assembled into H-aggregates in water. Interestingly, the shape of the excitation and emission spectra is the same as in methanol, suggesting that the weak fluorescence is induced by the monomeric **PDI-Ln** that are in equilibrium with the assemblies.

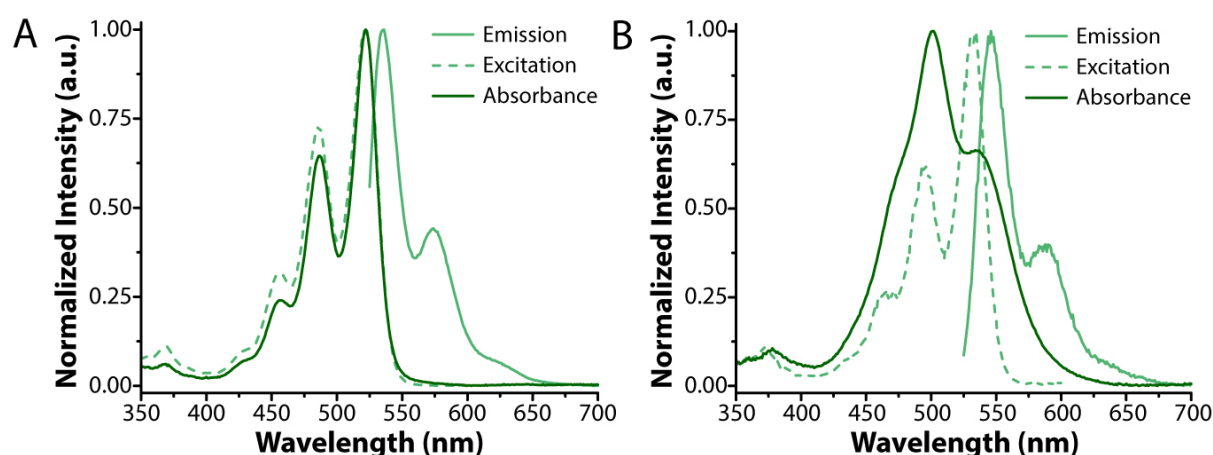


Figure 5.3 – Normalized fluorescence emission (522 nm) and excitation (535 nm) and UV/vis absorbance for **PDI-Y** in **A** – methanol and **B** – water. Concentration is 4 μM . For the spectra in the same conditions for all **PDI-Ln** see Figure 5.14 in Appendix.

Another indication for the assembly of **PDI-Ln** is the difference between the fluorescence intensities in the two solvents, Figure 5.4. In methanol all **PDI-Ln** present strong emission and

excitation intensities, that are more than ten times weaker in water. The quench in fluorescence is a further indication that all **PDI-Ln** are monomeric in methanol and strongly aggregated in water.

Curiously, fluorescence intensities were not the same for all the **PDI-Ln**. Consistently, at the same concentration of 4 μM , **PDI-Gd** and **PDI-Y** are more strongly fluorescent than **PDI-Ho** and **PDI-Er**, both in water and methanol. There are two possibilities: either **PDI-Ho** and **PDI-Er** are more susceptible to form dimers (or small oligomers) in methanol, which would slightly quench their fluorescence (without changing the UV/Vis spectrum); or the fact that erbium and holmium absorb around 400 to 500 nm ²³⁰ could interfere in the spectroscopic properties of **PDI-Ho** and **PDI-Er** (see Figure 5.15 in Appendix for the absorption spectra of the corresponding lanthanide chlorides).

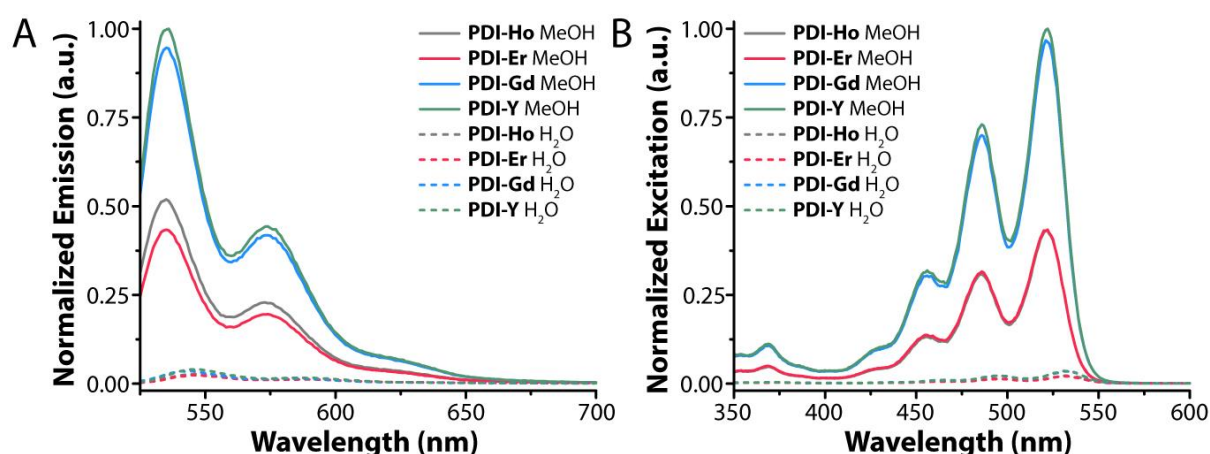


Figure 5.4 – Fluorescence emission (A, 522 nm) and excitation (B, 535 nm) for all **PDI-Ln** in water and methanol. The intensities were normalized to the highest measured intensity for both cases. All samples are at a 4 μM concentration.

The spectroscopic analysis show that all **PDI-Ln** are molecularly dissolved in methanol and aggregated in water, even at 4 μM . This indicates that the **PDI-Ln** are all strong assemblers in water, driven by the strong hydrophobicity of the perylene core.

5.3 Thermodynamics of Supramolecular Polymerization

To further investigate the self-assembly of **PDI-Ln** in water, UV/Vis spectra were collected at different concentrations, Figure 5.5–A for **PDI-Ho** and Figure 5.16–A, C, E, G for all **PDI-Ln**. UV/Vis absorbance is both dependent on the concentration of the sample and the

degree of aggregation. To remove the concentration as a variable, extinction coefficient (ϵ) (obtained by dividing the absorbance signal by the concentration and path length) was used as a comparison parameter. The extinction coefficient (ϵ) of all the samples decrease with increasing concentration, showing that increasing concentration increases aggregation, as expected.

Note that for **PDI-Er** and **PDI-Gd** the spectra at 800 μM have very diminished intensity, when compared to 160 μM for the same compounds and the same concentration for the others, and unresolved peaks. Also, the ratio I_{500}/I_{540} is lower than for 160 μM , which would indicate a lesser assembled state, which is not possible at a higher concentration. Even heating to 90°C and cooling the samples did not change the spectra. They are probably a result of a higher order of assembly occurring in **PDI-Er** and **PDI-Gd** for this concentration. For this reason, this concentration has been excluded for the following UV/Vis analysis for **PDI-Er** and **PDI-Gd**.

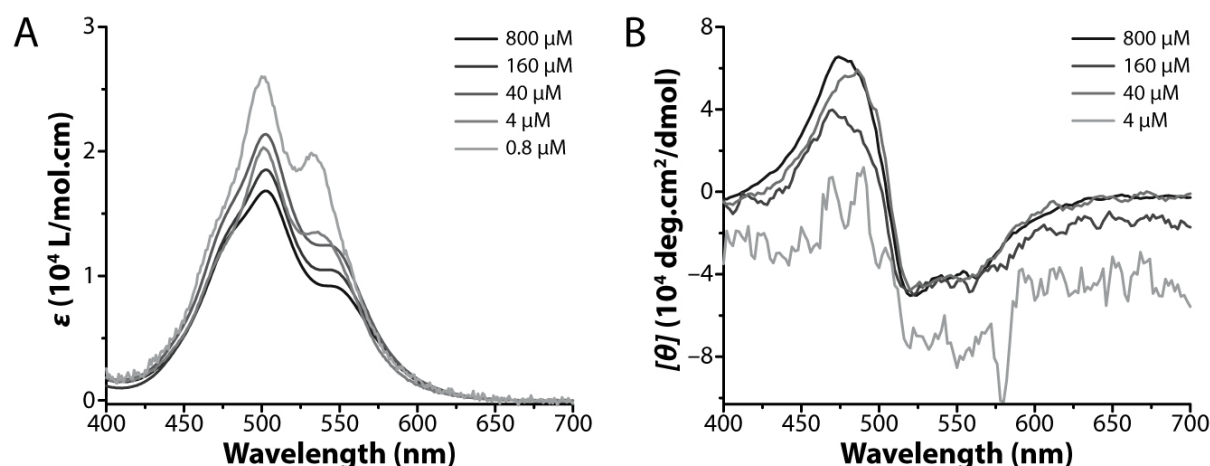


Figure 5.5 – Extinction coefficient (ϵ) in **A** (at 21°C) and molar ellipticity ($[\theta]$) (at 5 °C) in **B** of **PDI-Ho** as a function of wavelength at different concentrations. For extinction coefficient (ϵ) and molar ellipticity in ($[\theta]$) of all **PDI-Ln** see Figure 5.16 in Appendix.

The I_{500}/I_{540} ratio steadily increases with increasing concentration, further showing that higher concentration induces aggregation, Figure 5.6. Since there is a smooth transition in I_{500}/I_{540} with concentration, **PDI-Ln** are thought to polymerize by an isodesmic mechanism. Unfortunately, fitting of an equal K indefinite self-association model²³¹ was not possible and did not yield satisfying results. This happens most likely because the isodesmic model does not perfectly represent the mechanism of self-assembly of **PDI-Ln**, notably with its response to

concentration variation. Furthermore, within the working concentration, a plateau of the maximum I_{500}/I_{540} value is not reached, which hinders an optimal fit of a model.

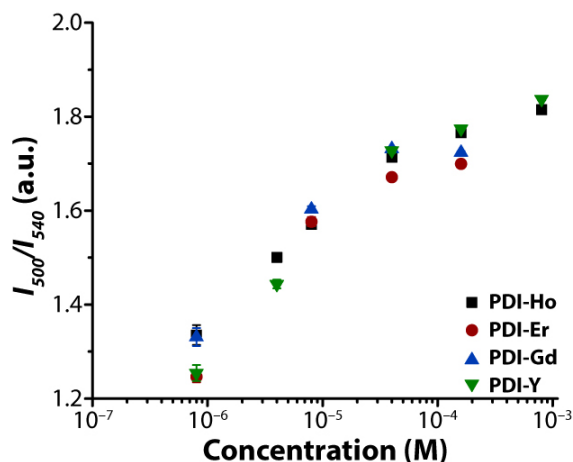


Figure 5.6 – Ratios of the two absorbance maxima at 500 nm and 540 nm (I_{500}/I_{540}) as a function of concentration for all **PDI-Ln**.

Since **PDI-Ln** present a chiral center, provided by the L-alanine, Circular Dichroism (CD) can be a good technique to study supramolecular polymerization. So, CD spectroscopy was measured at different concentrations, Figure 5.5–B for **PDI-Ho** and Figure 5.16–B, D, F, H for all **PDI-Ln**. Like for UV/Vis absorbance, circular dichroism is both dependent on the concentration of the sample and the degree of aggregation. So again, to remove the concentration as a variable, the molar ellipticity ($[\theta]$) (obtained by dividing the CD signal by the concentration and path length) was used as a comparison parameter. The CD spectrum of **PDI-Ln** present a strong negative Cotton effect, indicating that they form helical structures in water.²³² Differently from the UV/Vis experiments, the molar ellipticity did not change considerably when decreasing the concentration from 800 μM to 40 μM , with a strong dip observed at 8 μM . This is curious, since we know from UV/Vis experiments that aggregation is strongly influenced by concentration. This suggests that UV/Vis and CD spectroscopy probe different processes in the self-assembly of **PDI-Ln**. Indeed, when analyzing ‘infinite’ supramolecular polymers, the CD spectrum only probes the interactions between a chromophore and its nearest neighbors in the assembly. This means that for large supramolecular polymers, the observed CD signal corresponds to the sum of many small repeating units (sections of the aggregates containing a few molecules), and practically the

spectrum of an infinite assembly cannot be distinguishable from a mixture containing dimers and/or oligomers.²³³

Interestingly, useful information can be extracted from denaturation curves obtained by changing the volumetric ratio of methanol and water, while maintaining the concentration of **PDI-Y** constant, Figure 5.7–A. As expected, when increasing the amount of methanol (the denaturing solvent) the extinction coefficient becomes higher and the I_{500}/I_{540} ratio decreases. In contrast to the unsuccessful concentration series (see above), a denaturation isothermal isodesmic model could be fitted to the data, Figure 5.7–A (see Sub-Section 5.8.3.1).⁴³ The model yields a free energy of polymerization of $\Delta G = -31.4 \pm 0.8$ kJ/mol (at 298 K) with a denaturation potential of $m = 18.5 \pm 0.8$ kJ/mol of methanol. This means that in water **PDI-Y** is strongly assembled, and adding methanol depolymerizes it, increasing the free energy of polymerization by ~ 1.9 kJ/mol for each 10% of methanol that is added, reaching $\Delta G \sim -13$ kJ/mol with pure methanol. Those two values are smaller in magnitude than typical thermodynamic parameters of aggregation for perylene diimides in water and methanol,²³⁴ likely because the metal-containing moieties are very polar, increasing solubility of the molecule in polar solvents, and very big, partially hindering the stacking of the perylene core.

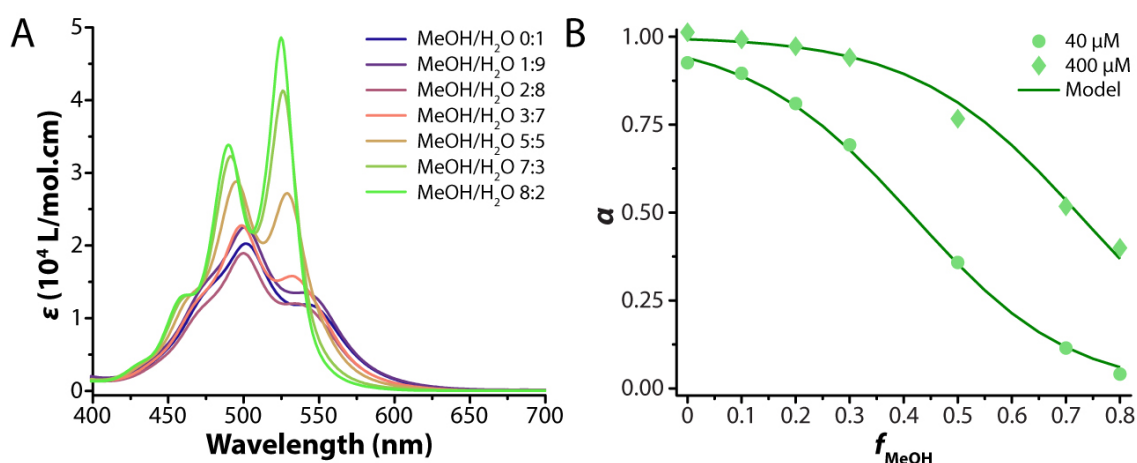


Figure 5.7 – **A** – UV/Vis spectra of **PDI-Y** in different solvent mixtures (methanol/water) at a concentration of 40 μM . **B** – Plot of the degree of aggregation (α) in function of the volume fraction of methanol (f_{MeOH}). The symbols are the data points and the solid line is the isodesmic model, containing solvent denaturation of the assemblies (see Sub-Section 5.8.3.1).

The next step of the thermodynamic characterization of **PDI-Ln** was performing variable temperature experiments. For that, UV/Vis spectra were measured from 0 to 90 $^{\circ}\text{C}$ at every 3

°C (or from 5 to 90 °C with measurements every 2 °C) with a 2-minute hold at each measurement temperature to assure equilibrium is reached for every stage (these temperature ramps were chosen so that no hysteresis between heating and cooling curves is observed). An example of these measurements can be found in Figure 5.8–A, for **PDI-Ho** at 4 μM. The absorption band increases in intensity when the sample is heated with a slight blue-shift. Furthermore, the I_{500}/I_{540} decreases with increasing temperature, Figure 5.8–B, meaning that **PDI-Ho** (and all **PDI-Ln**) becomes molecularly dissolved when it is heated in water.

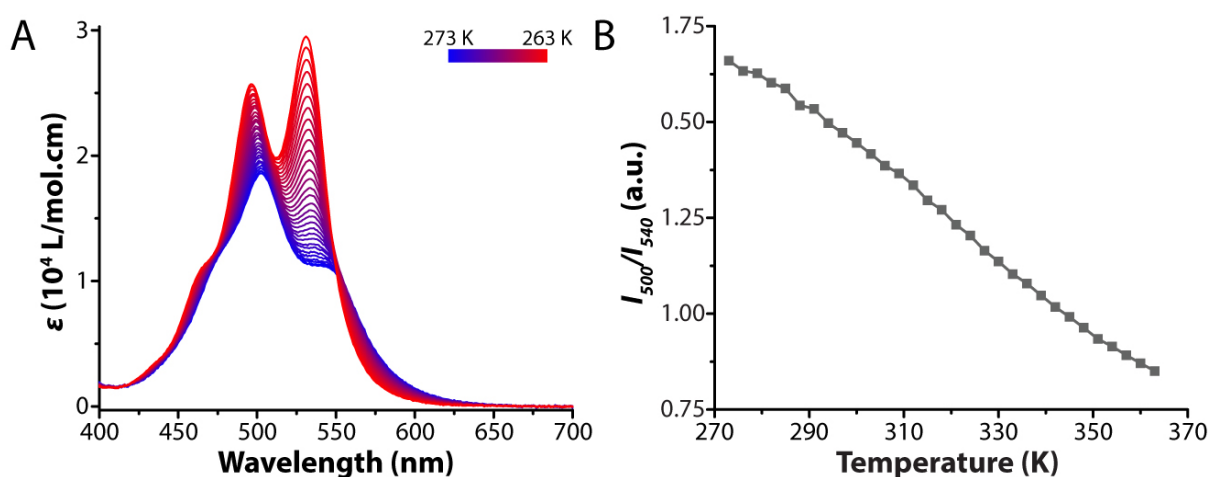


Figure 5.8 – **A** – UV/Vis spectra of **PDI-Ho** at 4 μM at different temperatures (from 0 to 90 °C). **B** – Ratios of the two absorbance maxima at 500 nm and 540 nm (I_{500}/I_{540}) as a function of temperature, data extracted from **A**.

The same experiment was repeated for different concentrations for all **PDI-Ln**. For each compound, a multi-fit of the isodesmic model to the variable temperature data for all concentrations was performed by relating the ratio of I_{500}/I_{540} to α . The model employed was the one described by Van der Schoot, for details see Sub-Section 5.8.3.2.^{13,37} With the model, the enthalpy of polymerization of each compound can be obtained, they are listed in Table 5.1 (a more detailed list is present in Table 5.2 in Appendix). With the obtained enthalpy (ΔH) and melting temperatures (T_m), the temperature data points can be converted to the reduced temperature ($T_R = \Delta H \frac{T - T_m}{RT_m^2}$) and all the concentrations can be collapsed in a single plot, Figure 5.9 for all **PDI-Ln**.

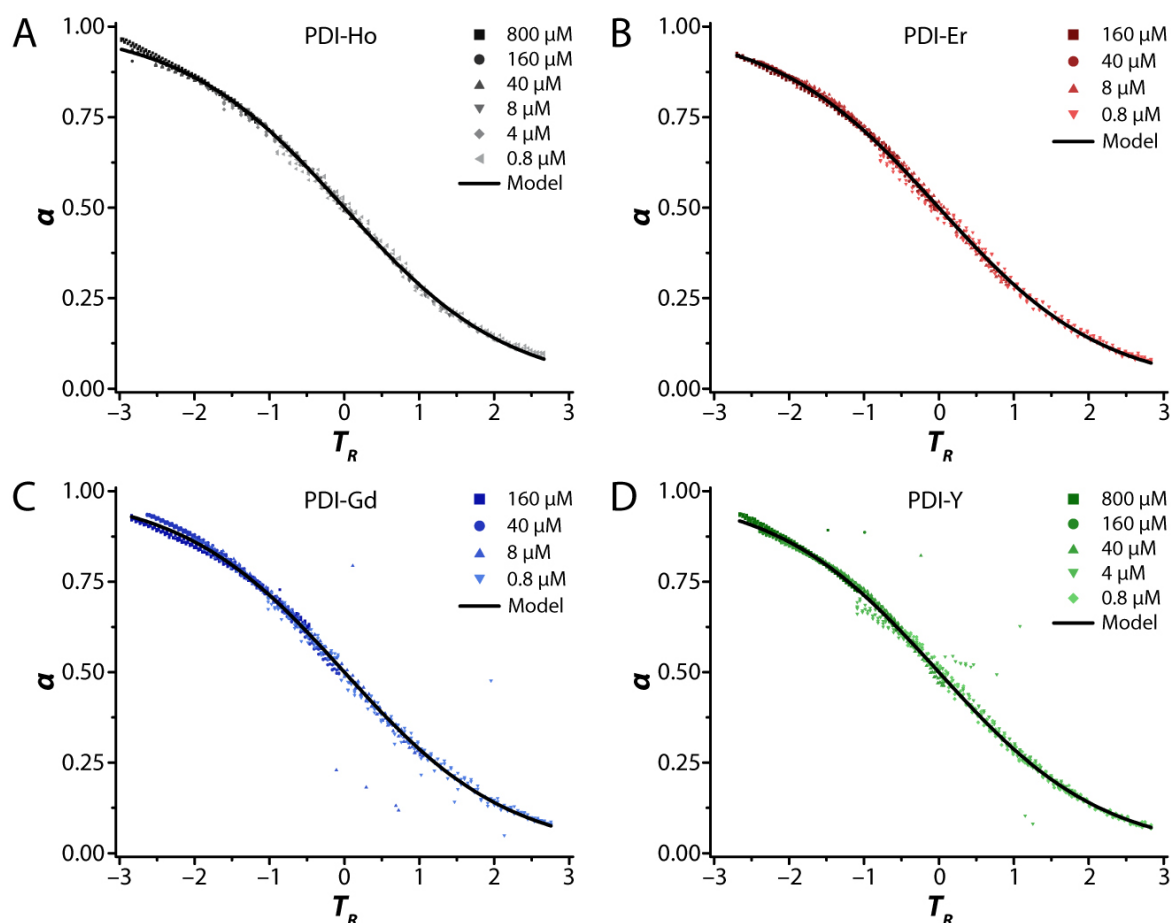


Figure 5.9 – Collapsed curves of the degree of aggregation (α) as a function of the reduced temperature (T_R) for different concentrations. **A** – PDI-Ho; **B** – PDI-Er; **C** – PDI-Gd; **D** – PDI-Y. The symbols are the treated data points and the solid lines are the isodesmic model for each compound. This data was obtained by UV/Vis spectroscopy.

The same can be done with CD spectroscopy, relating the molar ellipticity ($[\theta]$) with the degree of aggregation (α). The molar ellipticity (at 475 nm) was followed for every 1 °C between 5 and 90 °C with a 0.5 °C/min heating/cooling ramp. This heating/cooling rate is a little bit faster than for the UV/Vis experiments, but no hysteresis was observed in the CD variable temperature measurements. Similarly, the same isodesmic model was applied for the variable temperature data (see Sub-Section 5.8.3.2), with the results summed up in Table 5.1 (a more detailed list is present in Table 5.2 in Appendix). Again, the temperature was reduced into T_R and the curves of all the concentrations could be plotted in the same graph, Figure 5.10.

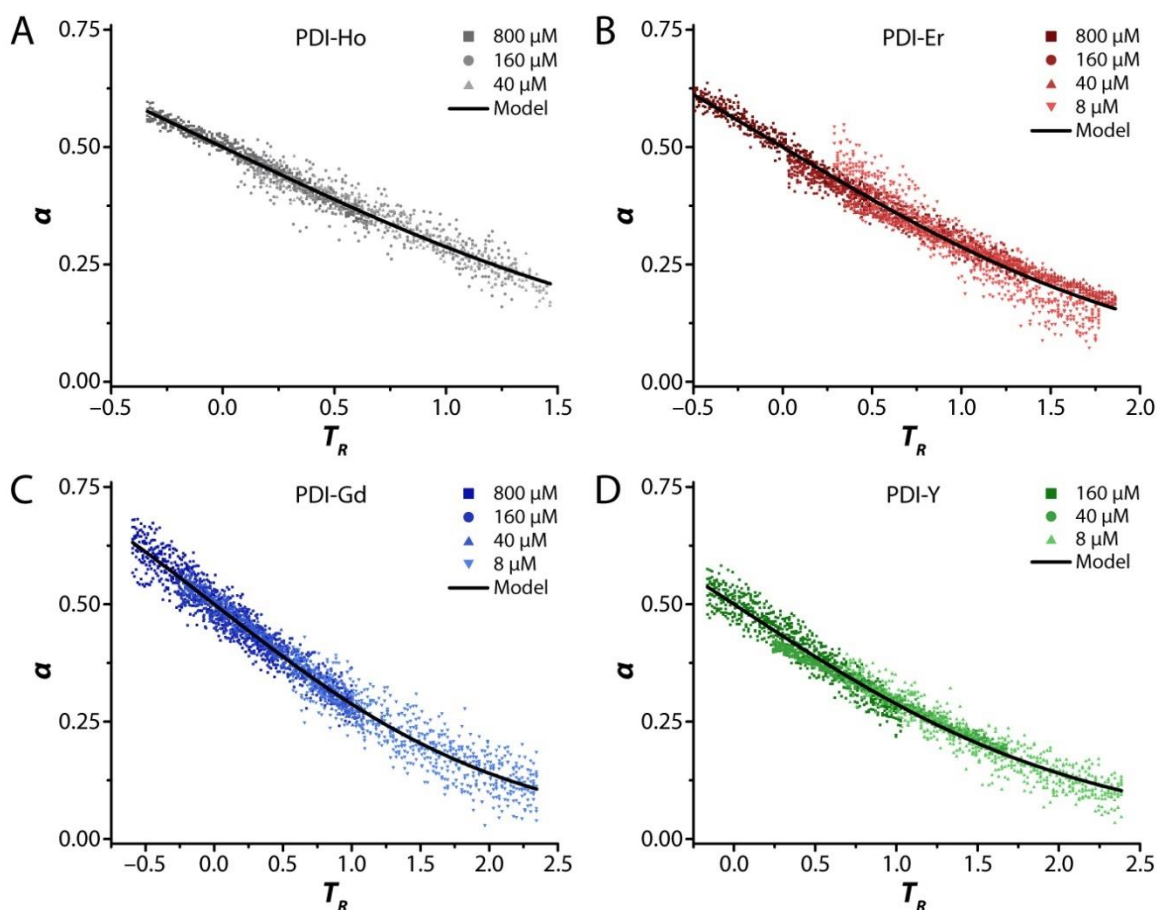


Figure 5.10 – Collapsed curves of the degree of aggregation (α) as a function of the reduced temperature (T_R) for different concentrations. **A** – **PDI-Ho**; **B** – **PDI-Er**; **C** – **PDI-Gd**; **D** – **PDI-Y**. The symbols are the treated data points and the solid lines are the isodesmic model for each compound. This data was obtained by CD spectroscopy.

When analyzing the obtained enthalpies of polymerization, Table 5.1 (full details in Table 5.2), the first impression is that the parameters obtained from UV/Vis and CD data are very different, with ΔH from UV/Vis being ~ 3 times larger than the one obtained from CD. This suggests that, as it has been discussed above, UV/Vis and CD spectroscopy probe different processes of supramolecular polymerization. The UV/Vis spectra give us an idea of the energetic transitions of PDI's that change when the perylene core is π - π stacking, so the overall spectrum is an average of both assembled and disassembled molecules in solution, linearly relating I_{500}/I_{540} to α ,^{12,229} while circular dichroism probes if chromophores are oriented in a chiral fashion with respect to each other.²³² For supramolecular building blocks like benzene-1,3,5-tricarboxamide (BTA), the CD spectrum is well related to the size of the supramolecular assemblies and the degree of aggregation, since these molecules usually self-assemble into one dimensional aggregates, that are well defined.³⁶ In our case, **PDI-Ln** self assembles into almost

spherical assemblies, with a less well-defined structure (see below), so it is possible that there is some interference in the CD spectra, or other interactions that yield unreliable results, even if the isodesmic model yielded good quality fits to the CD data. Also, the circular dichroism data is much noisier than the UV/Vis, which makes it difficult to identify subtle changes in the curve, such as the onset of a plateau. Finally, as discussed above, CD and UV/Vis probe different processes in the supramolecular self-assembly, with CD being mostly affected by the nearest neighbors in a stack,²³³ and does not probe overall aggregation in this type of assembly.

Table 5.1 – Results from the multi-fit of the isodesmic model to variable temperature UV/Vis and CD data. The errors are the 95% confidence interval of the fit.

Compound	ΔH from UV/Vis	ΔH from CD
PDI-Ho	-30.60 ± 0.23 kJ/mol	-9.07 ± 1.01 kJ/mol
PDI-Er	-31.01 ± 0.38 kJ/mol	-9.88 ± 0.78 kJ/mol
PDI-Gd	-33.44 ± 0.16 kJ/mol	-10.87 ± 0.87 kJ/mol
PDI-Y	-27.47 ± 0.13 kJ/mol	-9.76 ± 0.87 kJ/mol

The isodesmic model yielded good fits to the UV/Vis data, with $R^2 > 0.997$ for all **PDI-Ln** and the enthalpy of polymerization is around -30 kJ/mol for all compounds. They do not differ greatly among each other, with the biggest difference being between **PDI-Gd** and **PDI-Y** of ~ 6 kJ/mol. Even if this difference is greater than the error to the fits, it could arise by small interference in the data and bias of the fitting procedure. The values obtained for the enthalpy of polymerization are smaller in magnitude than values found in the literature for PDI self-assembly in water (or buffer),^{115,234} probably because the DOTA moiety increases the polarity and partially hinders the aggregation of **PDI-Ln**, as discussed above.

Overall, it can be said that **PDI-Ln** polymerizes following an isodesmic mechanism (where all steps have the same equilibrium constant) with an enthalpy of polymerization of -30 kJ/mol. The mechanism and energies associated are very similar for all the **PDI-Ln**, suggesting that the driving factor for supramolecular polymerization is the π - π stacking of the perylene core.

5.4 Size and Morphology of Assemblies

After analyzing the **PDI-Ln** aggregates and supramolecular polymerization spectroscopically, the size and morphology of the assemblies were studied by light scattering and microscopy techniques.

First, dynamic light scattering (DLS) measurements were performed in 800 and 160 μM solutions of all **PDI-Ln** (see details in Sub-Section 5.8.2.5). Multi-angle experiments were performed where the polarized field autocorrelation functions ($g_{VV}^{(1)}(q, t)$) were measured from 30° to 130° scattering angles, with 10° increments (Figure 5.17–A).

The polarized field autocorrelation function gives the distribution of relaxation times ($G(\tau)$ vs τ , Figure 5.17–A), by the Contin analysis.^{xvi} The inverse of the relaxation times (Γ , decay rate) is linear with the square of the wavevector (q^2) if the process is diffusive in nature, and the slope of the curve is the diffusion coefficient (D_H), Figure 5.17–B. From D_H the hydrodynamic radius (R_H) can be calculated using the Stokes-Einstein equation. This procedure was performed with the DLS data collected for all **PDI-Ln** at 800 and 160 μM , and the average R_H can be found in Figure 5.11

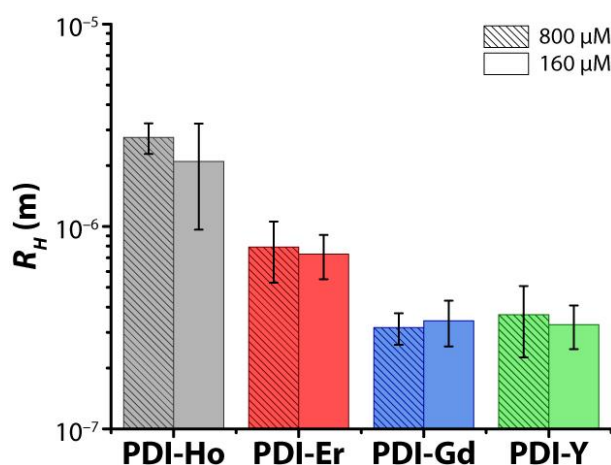


Figure 5.11 – Hydrodynamic radii obtained by DLS for all **PDI-Ln** at 160 and 800 μM . The error bars are either the propagation of the error to the fit or the standard deviation over two measurements, the biggest error was selected. Note that this error does not represent the polydispersity of the sample but the variation between each measurement.

^{xvi} Iari-Gabriel Marino (2007). rilt (<https://www.mathworks.com/matlabcentral/fileexchange/6523-rilt>), *MATLAB Central File Exchange*.

Interestingly, the hydrodynamic radii of the different **PDI-Ln** are very different from each other, even if the thermodynamics of supramolecular polymerization are very similar. **PDI-Gd** and **PDI-Y** present R_H between 320 and 370 nm, without much variation for the two studied concentrations. On the other hand, **PDI-Er** presents hydrodynamic radii of 790 and 720 nm, for 800 and 160 μM respectively. **PDI-Ho**, however, shows the largest assemblies with R_H of 2.1 and 2.8 μm for 160 and 800 μM respectively. These results are surprising because the thermodynamics of supramolecular polymerization were similar for each compound. This suggested that, as discussed before, the supramolecular polymerization of **PDI-Ln** is mainly driven by the π - π stacking of the perylene core, while the rare earths would influence the size of the assemblies.

To better understand the morphological properties of **PDI-Ln**, the aggregates were studied by Atomic Force Microscopy (AFM). Preliminary results, show that amorphous, almost spherical, aggregates are found in solution for all **PDI-Ln**. It can be seen in Figure 5.12–A that **PDI-Y** forms large spherulites, with diameter in the range of hundreds of nanometers. **PDI-Gd**, at lower concentration, forms fewer spherical aggregates, but with the same size, Figure 5.12–B. These types of aggregates were found in all samples of all **PDI-Ln**.

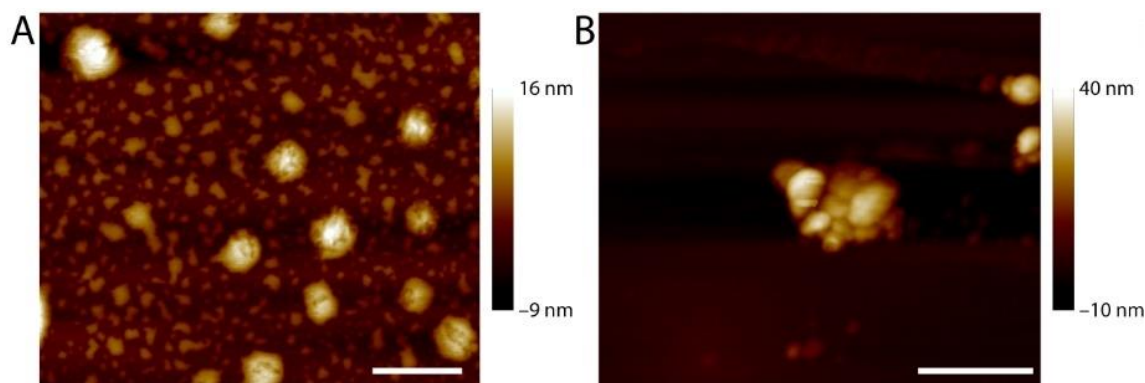


Figure 5.12 – AFM microscopy of the different assemblies found in **PDI-Ln**. **A** – Spherical assemblies found in **PDI-Y**, a 1.6 μM sample was drop casted on the substrate. Scale bar is 1 μm . **B** – Shapeless aggregate found in 0.08 nM **PDI-Gd** solution that was dip coated, followed by substrate washing. Scale bar is 500 nm. Scale bar is 1 μm . Samples were measured in Si/SiO₂ substrate.

Scanning electron microscopy (SEM) analysis of the **PDI-Ln** in powder form, lyophilized from 800 μM solutions (Figure 5.18 in Appendix), shows that in the solid phase these molecules form long fibers of hundreds of nm diameter and tens of μm in length. These fibers then bundle

and fuse forming mesh-like assemblies. These aggregates are very different than the ones found in solution, observed by AFM, probably due to drying effects during lyophilization.

Morphological characterization of the samples shows that even though thermodynamically all **PDI-Ln** are very similar to one another, structurally they are different. Light scattering shows that **PDI-Ho** forms the larger assemblies in the library, followed by **PDI-Er**, while **PDI-Y** and **PDI-Gd** show similar size. Structurally, **PDI-Ln** are similar, forming amorphous, close to spherical, aggregates in water, which was evidenced by AFM and long fibers in the solid phase.

5.5 Conclusions

We have shown the synthesis and characterization of a library of perylene diimides coupled to rare-earth-chelating DOTA moieties. These molecules self-assemble in water by an isodesmic mechanism with enthalpy of polymerization of around -30 kJ/mol. Although the thermodynamics and mechanism of polymerization is around the same for all **PDI-Ln**, the size of the aggregates is not, with **PDI-Ho** forming much larger aggregates than the other compounds. These results suggest that the polymerization of **PDI-Ln** is driven by the π - π stacking of the perylene core, but the choice of the lanthanide influences the final aggregates.

Since lanthanides present different magnetic properties, the magnetic interaction could be the source of the differences in morphology and size. However, lanthanides also differ in other properties, like electronic/spectroscopic and coordination/hydration sphere, that could also play a role in the self-assembly of **PDI-Ln**.²³⁰ Most likely a combination of all the factors are influencing, even if by a small degree, the final aggregate properties.

This work opens the door to new class of materials that can combine the different properties of lanthanides, such as luminescence or paramagnetism, with size control by choosing the right rare earth metal to be included in the structure. Furthermore, applications such as (supra)molecular magnetism can be developed and tuned by the choice of different paramagnetic lanthanide,²²³ or new classes of magnetic resonance imaging contrast agents can be synthesized and have a controlled morphology.^{224,235}

5.6 Appendix

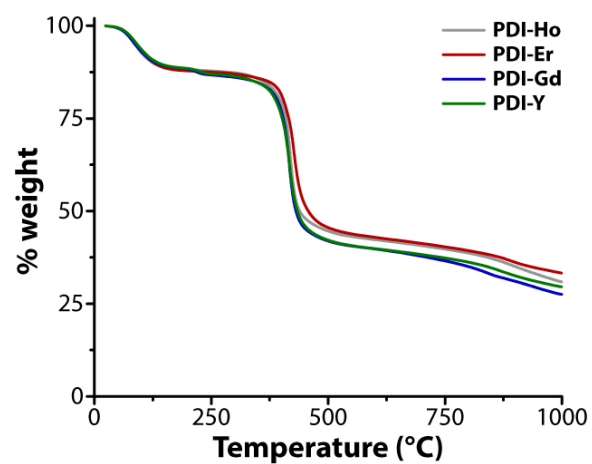


Figure 5.13 – Thermogravimetric analysis of all PDI-Ln. %weight loss as a function of temperature.

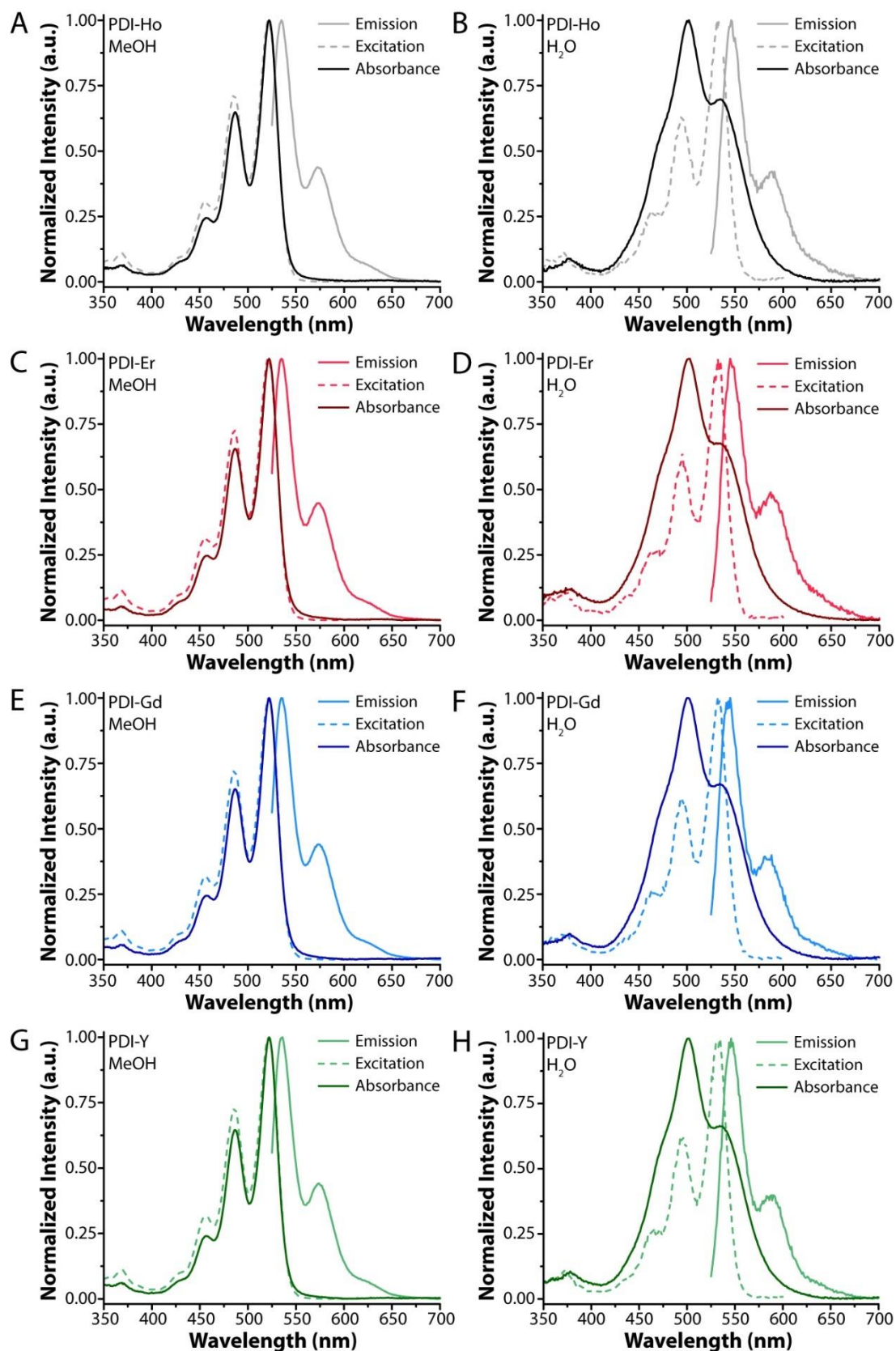


Figure 5.14 – Normalized fluorescence emission (522 nm) and excitation (535 nm) and UV/vis absorbance for: **PDI-Ho** in **A** – methanol and **B** – water; **PDI-Er** in **C** – methanol and **D** – water; **PDI-Gd** in **E** – methanol and **F** – water; **PDI-Y** in **G**– methanol and **H** – water. Concentration is 4 μM for all. Experiments performed at room temperature.

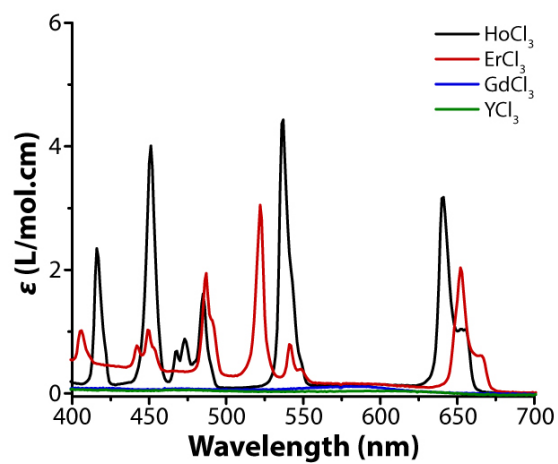


Figure 5.15 – Extinction coefficient (ϵ) of the lanthanide chlorides (corresponding to **PDI-Ln**) as a function of wavelength. Spectra collected at 21 °C and 25 mM in water for all of them.

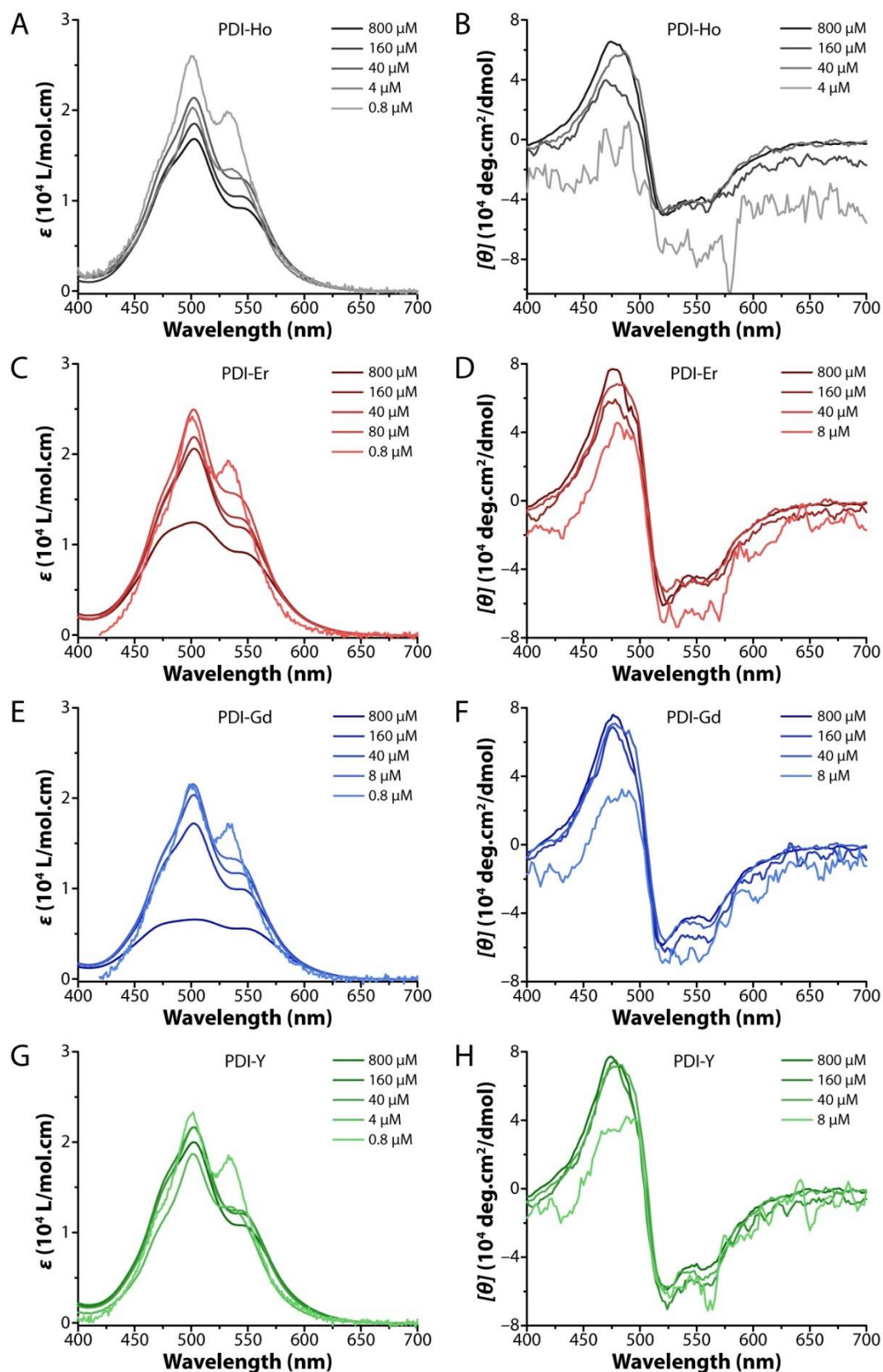


Figure 5.16 – Extinction coefficient (ϵ) in **A** and molar ellipticity in ($[\theta]$) in **B** of **PDI-Ln** as a function of wavelength at different concentrations. **A** – UV/Vis and **B** – CD for **PDI-Ho**. **C** – UV/Vis and **D** – CD for **PDI-Er**. **E** – UV/Vis and **F** – CD for **PDI-Gd**. **G** – UV/Vis and **H** – CD for **PDI-Y**. UV/Vis collected at 21 °C and CD at 5 °C.

Table 5.2 – List of the results from multi-fitting of the isodesmic model for UV/Vis and CD data. See Sub-Section 5.8.3.2 for details. The errors are the 95% confidence interval of the fit.

Parameter	PDI-Ho	PDI-Er	PDI-Gd	PDI-Y
UV/vis				
ΔH	–30.60 ± 0.23 kJ/mol	–31.01 ± 0.38 kJ/mol	–33.44 ± 0.16 kJ/mol	–27.47 ± 0.13 kJ/mol
$T_{m,800\mu\text{M}}$	413.7 \pm 1.0 K	–	–	420.1 \pm 0.6 K
$T_{m,160\mu\text{M}}$	384.0 \pm 0.6 K	385.2 \pm 0.8 K	379.9 \pm 0.3 K	385.7 \pm 0.4 K
$T_{m,40\mu\text{M}}$	359.2 \pm 0.4 K	364.1 \pm 0.5 K	365.4 \pm 0.2 K	360.4 \pm 0.3 K
$T_{m,8\mu\text{M}}$	323.0 \pm 0.3 K	335 \pm 0.4 K	333.9 \pm 0.2 K	–
$T_{m,4\mu\text{M}}$	314.9 \pm 0.3 K	–	–	309.6 \pm 0.2 K
$T_{m,0.8\mu\text{M}}$	298.8 \pm 0.3 K	296.3 \pm 0.4 K	300.9 \pm 0.2 K	290.6 \pm 0.2 K
adj-R ²	0.9986	0.9978	0.9996	0.9996
I_{500}/I_{540} max	1.919 \pm 0.004	1.842 \pm 0.005	1.866 \pm 0.002	1.966 \pm 0.002
Circular Dichroism				
ΔH	–9.07 ± 1.01 kJ/mol	–9.88 ± 0.78 kJ/mol	–10.87 ± 0.87 kJ/mol	–9.76 ± 0.87 kJ/mol
$T_{m,800\mu\text{M}}$	307.2 \pm 8.0 K	320.6 \pm 9.2 K	326.3 \pm 8.3 K	–
$T_{m,160\mu\text{M}}$	273.3 \pm 9.8 K	275.8 \pm 6.5 K	296.0 \pm 6.7 K	289.7 \pm 8.8 K
$T_{m,40\mu\text{M}}$	267.1 \pm 9.5 K	258.4 \pm 6.0 K	292.2 \pm 5.5 K	263.7 \pm 7.3 K
$T_{m,8\mu\text{M}}$	–	261.3 \pm 6.1 K	250.5 \pm 5.4 K	243 \pm 6.6 K
adj-R ²	0.9556	0.9471	0.9579	0.9603
$[\theta]$ max ($\frac{\text{deg}\cdot\text{L}}{\text{cm}\cdot\text{mol}}$)	1221 \pm 77	1301 \pm 62	1310 \pm 59	1273 \pm 73

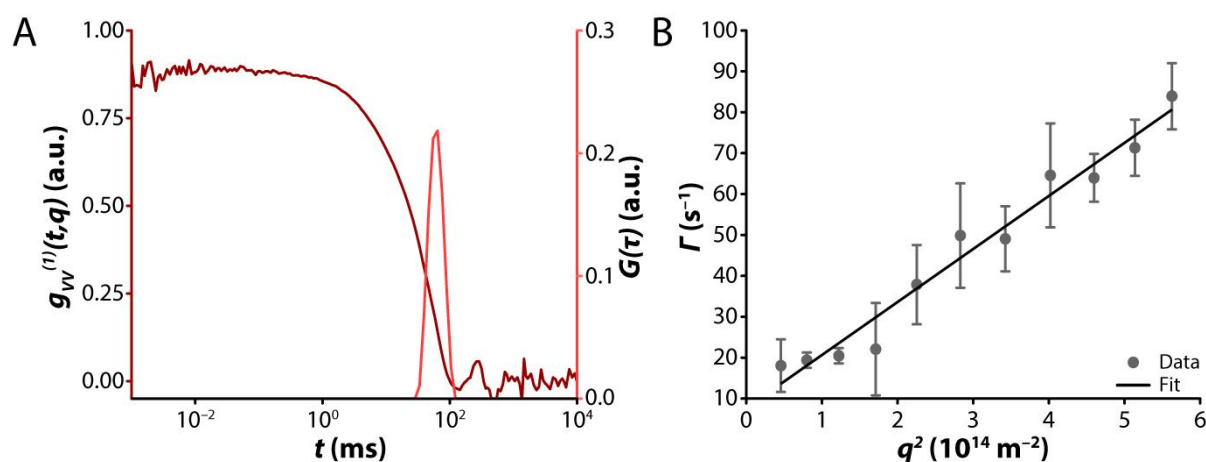


Figure 5.17 – Example of DLS data. **A** – Polarized field autocorrelation function $g_{VV}^{(1)}(q, t)$ (left axis) as a function of time and distribution of relaxation times $G(\tau)$ (right axis) as a function of the relaxation time τ for **PDI-Er** at 160 μM ($q = 0.00895 \text{ nm}^{-1}$). **B** – Decay constant (Γ) as a function of the square of the wavevector (q^2), the slope of the curve is the diffusion constant (D_H) of the particle. Symbols are the average over three consecutive measurements and the line is the linear fit. The error bars are the standard deviation of the three consecutive measurements. Data collected for **PDI-Ho** at 800 μM .

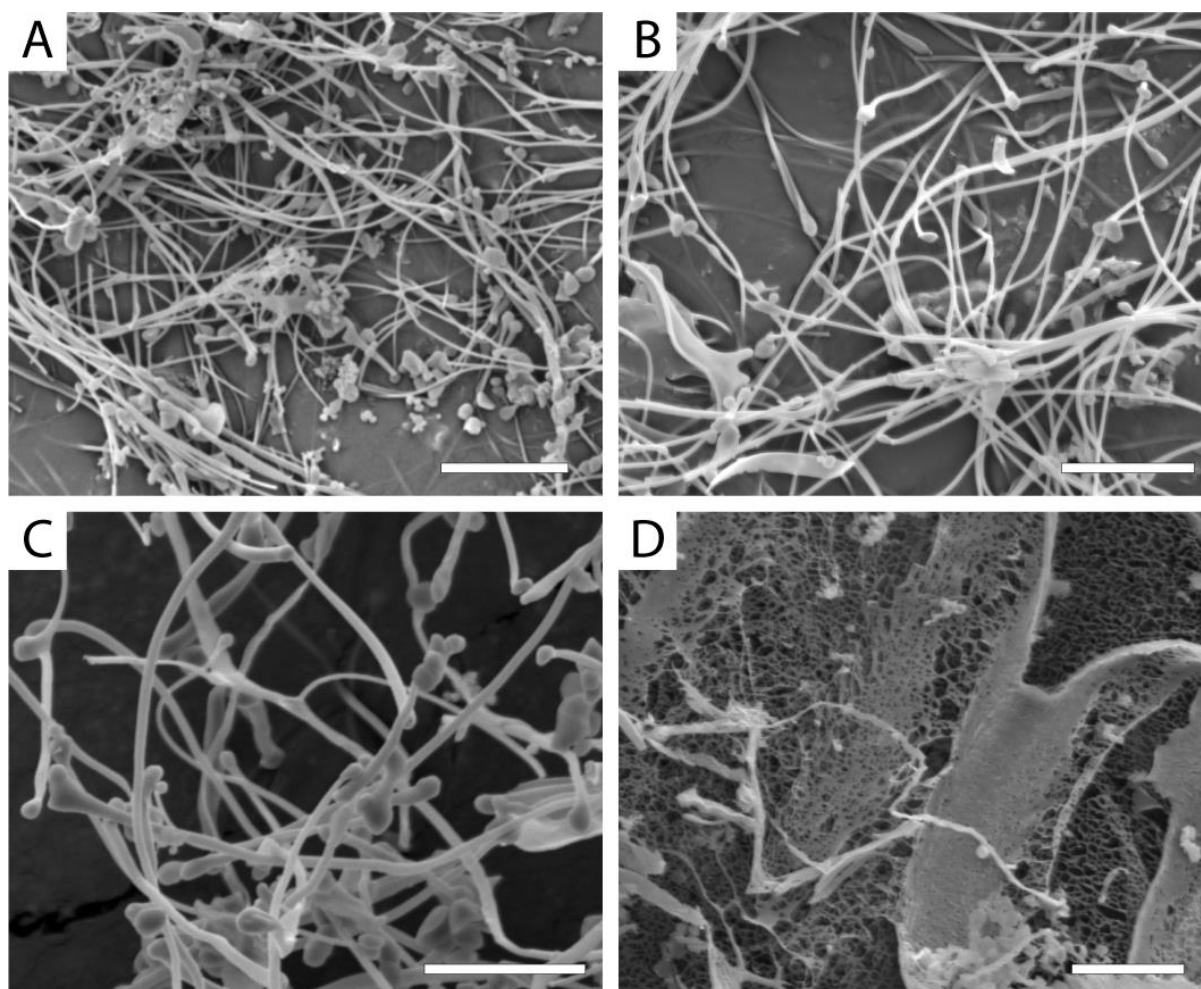


Figure 5.18 – SEM picture of PDI-Ln powder, lyophilized from a 800 μ M solution. For: A – PDI-Ho; B – PDI-Er; C – PDI-Gd; D – PDI-Y. Scale bars are 5 μ m.

5.7 Acknowledgements

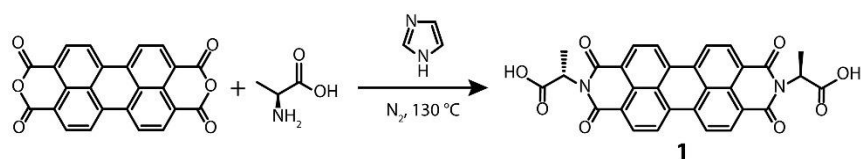
Georges Formon performed the synthesis and all the experiments apart from AFM, that was collected by Anastasiia Sharko. Alessandra Tassoni provided help with DLS measurements and data treatment. Prof. Thomas Hermans supervised the research.

5.8 Materials and Methods

5.8.1 Synthesis

All reagents were purchased from *TCI chemicals* and used without further purification.

5.8.1.1 Synthesis of **1**



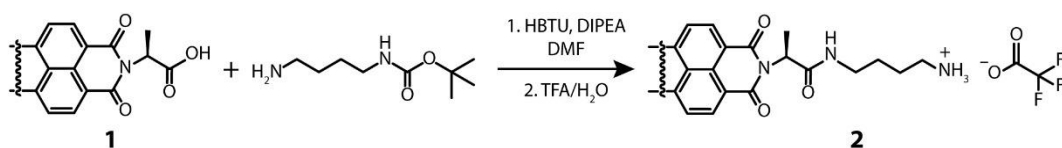
1 was synthesized following a published procedure.¹¹⁵ Perylene tetracarboxylic dianhydride (760 mg, 1.94 mmol), L-alanine (402 mg, 4.51 mmol) and imidazole (5756 mg, 84.6 mmol) were added to a round-bottom flask and purged with N₂. The mixture was heated to 130 °C for 35 minutes, under inert atmosphere. The reaction mixture was then cooled to 90 °C. Water (150 mL) was added and the resulting suspension was filtered. The filtrate was acidified with concentrated HCl to pH ~2. The precipitate was recovered by filtration and washed with water until the filtrate reached pH 7. The solid was dried overnight under vacuum at 55 °C yielding a dark purple solid (1032 mg, 99.5 %).

¹H NMR (500 MHz, 343 K, DMSO-*d*₆): δ 8.87 (dd, *J* = 8.2, 2.4 Hz, 4H), 8.57 (dd, *J* = 8.0, 1.3 Hz, 4H), 5.64 (q, *J* = 7.0 Hz, 2H), 1.64 (d, *J* = 7.0 Hz, 6H).

¹³C NMR (126 MHz, 343 K, DMSO-*d*₆): δ 170.70, 161.95, 134.04, 130.96, 128.34, 125.49, 122.25, 48.46, 14.20.

ESI-TOF (positive mode): *m/z* calculated for [C₃₀H₁₈N₂O₈+H]⁺: 535.1136; found: 535.1118.

5.8.1.2 Synthesis of **2**



1 (305 mg, 0.57 mmol) and HBTU (455 mg, 1.20 mmol) were purged with N₂ in a round bottom flask. DMF (40 mL) was added and the mixture was stirred for 15 min. After that, DIPEA (0.89 mL, 5.13 mmol) and N-(tert-butoxycarbonyl)-1,4-diaminobutane (0.23 mL, 1.20 mmol) were added and the solution was stirred for 12 h. Chloroform (100 mL) was added to the reaction mixture, and the organic phase was washed with saturated NaHCO₃ (3 x 100 mL) and brine (3 x 100 mL). The aqueous phases were combined and washed with chloroform (50 mL). The organic fractions were combined and dried over anhydrous MgSO₄, and the solvents were

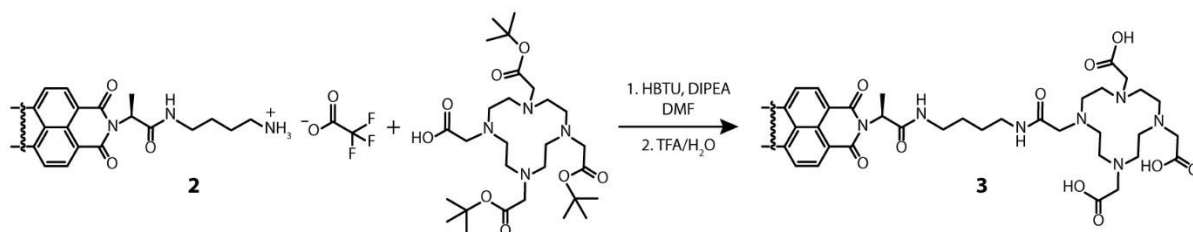
removed under reduced pressure. TFA/H₂O (9:1 – 4 mL) was added to the resulting solid and stirred for 12h. Diethyl ether (100mL) was added to the mixture and the precipitate was recovered via filtration and washed with more diethyl ether (100 mL). The product was dried overnight in a vacuum oven at 55 °C. The resulting product was a dark purple powder soluble in water (477 mg, 93 %).

¹H NMR (500 MHz, 343 K, DMSO-*d*₆): δ 8.74 (s, 4H), 8.38 (s, 4H), 7.55 (t, 2H), 5.30 (q, *J* = 6.9 Hz, 2H), 2.92 – 2.81 (m, 8H), 2.54 (d, *J* = 6.9 Hz, 6H), 2.54 – 2.47 (m, 4H), 1.42 – 1.32 (m, 8H).

¹³C NMR (126 MHz, 343 K, DMSO-*d*₆): δ 169.40, 163.02, 134.34, 131.35, 124.52, 123.61, 50.08, 49.07, 38.69, 26.52, 24.94, 14.83.

ESI-TOF (positive mode): *m/z* calculated for [C₃₈H₃₈N₆O₆+H]⁺: 675.2926; found: 675.2923.

5.8.1.3 Synthesis of **3**



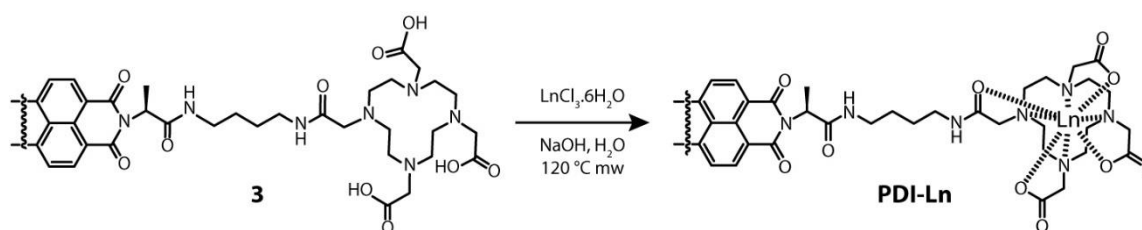
Tri-tert-butyl 1,4,7,10-tetraazacyclododecane-1,4,7,10-tetraacetate (635 mg, 1.11 mmol) and HBTU (460 mg, 1.21 mmol) were weighed in a round bottom flask and purged with N₂ for 15 minutes. DMF (40mL) and DIPEA (0.92 mL, 5.28 mol) were then added to the mixture, which was stirred for 15 minutes. **2** was added (477 mg, 0.53 mol) and the reaction mixture was stirred for 12h. Chloroform (80 mL) was added and the organic phase was washed with saturated NaHCO₃ (3 x 100 mL) and brine (3 x 100 mL). The aqueous phases were combined and washed with chloroform (50 mL). The combined organic phases were dried over MgSO₄ and evaporated under reduced pressure. The mixture was purified by normal phase flash chromatography CH₂Cl₂/MeOH (from 100:0 to 80:20). Solvent was removed under reduced pressure.

TFA/H₂O (9:1 – 4 mL) was added to the resulting solid and stirred for 12h. Diethyl ether (100mL) was added to the mixture and the precipitate was recovered via filtration and washed with more diethyl ether (100 mL). The product was further purified via reverse phase HPLC (High Performance Liquid Chromatography) with H₂O/CH₃CN (0.1 vol% TFA) as eluent. The resulting fractions were freeze-dried yielding a red/pink fluffy powder (350 mg, 46 %).

¹H NMR (500 MHz, 298 K, DMSO-*d*₆): δ 8.96 (s, 4H), 8.57 (s, 4H), 7.90 (s, 4H), 5.47 (s, 2H), 3.86 – 3.21 (m, 20H), 2.46 – 2.38 (m, 36H), 1.57 – 1.23 (m, 14H).

ESI-MS (positive mode): *m/z* calculated for [C₇₀H₉₀N₁₄O₂₀+H]⁺: 1447.6529; found: 1447.6515. *m/z* calculated for [C₇₀H₉₀N₁₄O₂₀+2H]²⁺: 724.3301; found: 724.3313.

5.8.1.4 Synthesis of **PDI-Ln**



The typical procedure for the synthesis of **PDI-Ln** was as follows. **3** (30 mg, 20.7 μmol), LnCl₃·6H₂O (207 μmol), NaOH 1 M (207 μL, 207 μmol) and water (5 mL) were placed in an appropriate Pyrex vial for microwave reaction. The vial was sealed and put inside a microwave reactor at 120 °C for 20 minutes. The reaction was considered complete when the peak of **3** could not be observed by LC-MS. The mixture was passed through a desalting column (Sephadex G-10, cut-off molecular weight of 700 Da) with water as eluent. The mixture was further purified via dialysis (SnakeSkin™ Dialysis Tubing, 3.5 k MWCO^{xvii}) against saturated NH₄Cl and distilled water. The resulting aqueous solutions were finally lyophilized resulting in red/pink fluffy powder.

Thermogravimetric analysis, Figure 5.13, show that around 20 % of water is present in the sample, that is lost between 100 at 200 °C for all samples. Further elemental analysis by Inductively Coupled Plasma Mass Spectrometry (ICP-MS) and Atomic Absorption

^{xvii} Since **PDI-Ln** forms large aggregates in water, no significant loss was observed even if the molecular weight cut-off is larger than the molecular weight of the molecule itself.

Spectroscopy (AAS) show consistently that ~80 % of the calculated metal is present in the sample, which was further confirmed by UV/Vis calibration. This happens because lanthanides are very hygroscopic and tend to retain water even when dried at high vacuum. To compensate for this error the concentrations have been corrected accordingly.

5.8.1.5 PDI-Y

^1H NMR (500 MHz, 343K, DMSO- d_6): δ 9.02 (m, 2H), 8.99 (d, $J = 7.9$ Hz, 4H), 8.61 (d, $J = 7.9$ Hz, 4H), 7.86 (t, $J = 5.7$ Hz, 2H), 5.51 (q, $J = 6.9$ Hz, 2H), 3.44 (m, 4H), 2.96 (m, 12H), 2.31 (m, 6H), 1.61 (d, $J = 6.9$ Hz, 6H), 1.50 – 1.41 (m, 8H).

^{13}C NMR (500 MHz, 343K, DMSO- d_6): δ 174.53, 169.34, 164.07, 163.21, 136.34, 134.45, 131.35, 124.83, 124.21, 50.20, 39.07, 26.92, 26.23, 14.89.

ESI-MS (positive mode): m/z calculated for $[\text{C}_{70}\text{H}_{84}\text{N}_{14}\text{O}_{20}\text{Y}_2+\text{H}]^+$: 1619.4176; found: 1619.4104. m/z calculated for $[\text{C}_{70}\text{H}_{84}\text{N}_{14}\text{O}_{20}\text{Y}_2+2\text{H}]^{2+}$: 810.2124; found: 810.2127.

5.8.1.6 PDI-Ho

ESI-MS (positive mode): m/z calculated for $[\text{C}_{70}\text{H}_{84}\text{N}_{14}\text{O}_{20}\text{Ho}_2+2\text{H}]^{2+}$: 886.2369; found: 886.2388.

ICP-MS (Ho^{III}): calculated 18.62 wt%, found 14.34 wt%

AAS (Ho^{III}): calculated 18.62 wt%, found 14.99 wt%

5.8.1.7 PDI-Gd

ESI-MS (positive mode): m/z calculated for $[\text{C}_{70}\text{H}_{84}\text{N}_{14}\text{O}_{20}\text{Gd}_2+2\text{H}]^{2+}$: 878.7315; found: 878.7321.

ICP-MS (Gd^{III}): calculated 17.91 wt%, found 14.94 wt%

5.8.1.8 PDI-Er

ESI-MS (positive mode): m/z calculated for $[\text{C}_{70}\text{H}_{84}\text{N}_{14}\text{O}_{20}\text{Er}_2+2\text{H}]^{2+}$: 888.7396; found: 888.7401.

ICP-MS (Er^{III}): calculated 18.84 wt%, found 15.3 wt%

5.8.2 Methods

5.8.2.1 Ultraviolet/Visible Spectroscopy

All Spectra were collected using a Cary 300 UV-Vis spectrophotometer manufactured by Agilent coupled with a Peltier temperature controller. For concentrations above 200 μM cuvettes with 1mm path length were used, for lower concentrations 1 cm.

Every spectrum was corrected with baseline and further corrected during treatment if an offset was still present.

For variable temperature experiments data was collected every 2 or 3 K, with a 2-minute equilibration at each temperature point.

5.8.2.2 Circular Dichroism Spectroscopy

CD spectra were recorded on JASCO J-1500 spectropolarimeter equipped with a Peltier temperature controller. For concentrations above 200 μM cuvettes with 1mm path length were used, for lower concentrations 1 cm.

Every spectrum was corrected with a recorded baseline during data treatment. For variable temperature experiments, data was collected every 1 $^{\circ}\text{C}$ with a temperature ramp of 0.5 $^{\circ}\text{C}/\text{min}$.

5.8.2.3 Fluorescence Spectroscopy

Steady-state fluorescence spectra were recorded using a Jobin-Yvon Fluorolog Spectrofluorometer.

5.8.2.4 Thermogravimetric Analysis

Thermogravimetric analyses were performed by using a TGA Q500 TA instrument 3 with a ramp of 10 $^{\circ}\text{C}/\text{min}$ under N_2 and a flow rate of 50 mL/min.

5.8.2.5 Dynamic Light Scattering

We employed a homebuilt light scattering setup using an Obis Laser with 629 nm wavelength and laser power of 25 mW. Mean scattering intensities (I_{sam}) and polarized field autocorrelation functions $g_{VV}^{(1)}(q, t)$ have been measured for 13 angles from 30 $^{\circ}$ to 130 $^{\circ}$.

The scattering angle can be transformed into the wavevector q by:

$$q = \frac{4 \pi n_0}{\lambda} \sin\left(\frac{\theta}{2}\right)$$

Where n_0 is the refractive index of the sample, λ is the wavelength of the laser (here 639 nm), and θ is the angle at which the scattering is collected.

From the Contin analysis^{xviii} the distribution of relaxation times ($G(\tau)$) can be obtained, Figure 5.17–A, which contains the characteristic relaxation times of the sample (τ), that when inverted give the decay constant ($\Gamma = \tau^{-1}$). In processes that are diffusive in nature, the decay constant is linear with the square of the wave vector and the slope is the diffusion constant (D_H), Figure 5.17–B:

$$\Gamma = D_H \cdot q^2$$

The hydrodynamic radius can be calculated by the Stokes Einstein equation, using the calculated diffusion constant, as follows:

$$R_H = \frac{k_B T}{6 \pi \eta D_H}$$

Where k_B is the Boltzmann constant, T is temperature and η the dynamic viscosity.

5.8.2.6 Scanning Electron Microscopy

SEM images were taken using a FEI Quanta FEG 450 microscope. Using a 5.0 kV High Voltage and dwell time of 50 μ s. The lyophilized samples were mounted on a silicon wafer and sputtered with 10 to 15 nm of gold.

5.8.2.7 Atomic Force Microscopy

AFM microscopy was performed with a Bruker Dimension Icon microscope under ambient conditions, operating in tapping mode using TESPA-V2 tips with spring constant $k = 42$ N/m. The samples were either dip or spin coated or drop casted on a Si/SiO₂ substrate.

5.8.2.8 Nuclear Magnetic Resonance

NMR spectra were recorded on a Bruker Ascend Spectroscopy Avance Neo-500 MHz (500 MHz for ¹H and 125 MHz for ¹³C). With deuterated DMSO-*d*₆ manufactured by Eurisotop.

^{xviii} Iari-Gabriel Marino (2007). rilt (<https://www.mathworks.com/matlabcentral/fileexchange/6523-rilt>), MATLAB Central File Exchange.

5.8.2.9 Preparative HPLC

Semi-preparative HPLC was performed with a LaPrep HPLC, manufactured by VWR, with a 250 x 30 mm Kromasil 100 C18 7 μm column.

5.8.3 Thermodynamic Model

5.8.3.1 Solvent Denaturation

The solvent denaturation model found in Figure 5.7 was built combining the solvent-dependent change in Gibbs free energy (ΔG), previously used by Korevaar, et al.:⁴³

$$\Delta G = \Delta G^0 + m \cdot f$$

Where ΔG^0 is the Gibbs free energy of supramolecular polymerization in the self-assembling solvent (in this case water), m is the denaturation energy and f is the volumetric fraction of the denaturizing solvent, in this case methanol.

The Gibbs free energy can be transformed to the equilibrium constant (K_{eq}) with the following equation:

$$K_{eq} = e^{-\frac{\Delta G}{RT}}$$

Where T is the temperature and R is the gas constant. The two previous equations we combined with the equal K indefinite self-association, or isodesmic, model, where all the polymerization steps are driven by the same equilibrium constant. As described by R. Bruce Martin:²³¹

$$\alpha = 1 - \frac{2K_{eq}C_{tot} + 1 - \sqrt{4K_{eq}C_{tot} + 1}}{2(K_{eq}C_{tot})^2}$$

Where α is the dimensionless degree of polymerization, *i.e.* the fraction of molecules in polymer form and C_{tot} is the total concentration of the sample.

By relating the ratio I_{500}/I_{540} with α , the denaturation data was fitted with a model containing the three previous equations with ΔG , m , and the I_{500}/I_{540}^{max} (I_{500}/I_{540} ratio when the molecule is fully polymerized) as free parameters. A custom algorithm using MATLAB® and its function fit was used (see Sub-Section 5.8.4.1).

5.8.3.2 Temperature Activated Polymerization

The temperature-dependent multi-concentration supramolecular polymerization data was fitted to the isodesmic model derived by Van der Schoot:^{13,37}

$$\alpha = \frac{1}{1 + \exp\left(-0.908\Delta H \frac{T - T_m}{RT_m^2}\right)}$$

Where ΔH is the enthalpy gain per mol of monomer getting polymerized, and T_m is the temperature at which $\alpha = 0.5$ (*i.e.* melting temperature).

By relating the UV/Vis ratio I_{500}/I_{540} , or molar ellipticity obtained with CD spectroscopy, with α , the temperature-dependent data was fitted with the isodesmic model with ΔH , T_m (different for each concentration), and the I_{500}/I_{540}^{max} (or $[\theta]^{max}$ for CD data) as free parameters. A custom algorithm using MATLAB® and its function fit were used to fit the model to the data (see Sub-Sections 5.8.4.2 and 5.8.4.3 for UV/Vis and CD data respectively).

The temperature was transformed to the reduced temperature (T_R) as follows:

$$T_R = \Delta H \frac{T - T_m}{RT_m^2}$$

That way all curves from different concentrations can be collapsed in the same plot of α versus T_R .

5.8.4 MATLAB® codes

5.8.4.1 Solvent Denaturation

```
function [Alpha]=isodesmic_equilibria_UV_equations_solvent(Sol,G,UVmax,T,c,m)
G_eff=G+m*Sol;
K=exp(-G_eff./(8.314*T));
MtK=c*K;
Alpha=(UVmax-0.65).*(1-((2.*MtK+1)-sqrt(4.*MtK+1))./(2.*MtK.^2))+0.65;
end
```

```
function isodesmic_equilibria_UV_Solvent
```

```

close all
load('GF03_Y_solvent_UV.mat')

c=40e-6;
T=298;
Sol=S_50uM;
UV=ratio_50uM;

fomm = fitoptions('Method', 'NonLinearLeastSquares', 'StartPoint', [-40000,1,2], ...
    'Lower', [-100000,0,1], 'Upper', [-10000,100000,4],...
    'TolFun',1e-16,'TolX',1e-16,'MaxIter',5000,'MaxFunEval',2500,'Display','off')

ftmm = fitype('isodesmic_equilibria_UV_equations_solvent(Sol,G,UVmax,T,c,m)',...
    'coefficients',{'G','m','UVmax'},...
    'independent', {'Sol'},...
    'problem',{'T','c'},...
    'options',fomm)

[f,gof,output] = fit (Sol, UV, ftmm,'problem',{T,c});

Alpha=(UV-0.65)/(f.UVmax-0.65);
Alpha_m=(isodesmic_equilibria_UV_equations_solvent(Sol,f.G,f.UVmax,f.T,f.c,f.m)-
0.65)/(f.UVmax-0.65);

%
% h=figure;
% plot(Sol,Alpha_m);
% hold on
% scatter(Sol,Alpha,'o','MarkerEdgeColor',[1 0 0]);
hold off
% plot(Tr,Alpha_model,'-','Linewidth',3,'Color',[0 0 0])
% hold off
% xlabel('Tr')
% ylabel(sprintf('%c',945));
% ylabel(ylabel);
% legend('1 mM','50 \muM','10 \muM','Model')

c=400e-6;
T=298;
Sol=S_500uM;
UV=ratio_500uM;

fomm = fitoptions('Method', 'NonLinearLeastSquares', 'StartPoint', [-40000,1,2], ...
    'Lower', [-100000,0,1], 'Upper', [-10000,100000,4],...
    'TolFun',1e-16,'TolX',1e-16,'MaxIter',5000,'MaxFunEval',2500,'Display','off')

ftmm = fitype('isodesmic_equilibria_UV_equations_solvent(Sol,G,UVmax,T,c,m)',...
    'coefficients',{'G','m','UVmax'},...
    'independent', {'Sol'},...
    'problem',{'T','c'},...
    'options',fomm)

[f,gof,output] = fit(Sol, UV, ftmm,'problem',{T,c});

Alpha=(UV-0.65)/(f.UVmax-0.65);
Alpha_m=(isodesmic_equilibria_UV_equations_solvent(Sol,f.G,f.UVmax,f.T,f.c,f.m)-
0.65)/(f.UVmax-0.65);

```

```

% h=figure;
% plot(Sol,Alpha_m);
% hold on
% scatter(Sol,Alpha,'o','MarkerEdgeColor',[1 0 0]);
% hold off

```

multifit

```

Sol(1:7,1)=S_500uM(:,1);
Sol(8:14,1)=S_50uM(:,1);

UV(1:7,1)=ratio_500uM(:,1);
UV(8:14,1)=ratio_50uM(:,1);

c500=400e-6;
c50=40e-6;
T=298;

fomm = fitoptions('Method', 'NonLinearLeastSquares', 'StartPoint', [-80000,1,1.84], ...
    'Lower', [-100000,0,1], 'Upper', [-10000,100000,4],...
    'TolFun',1e-16,'TolX',1e-16,'MaxIter',5000,'MaxFunEval',2500,'Display','off')

ftmm =
fitype('isodesmic_equilibria_UV_equations_solvent_multi(Sol,G,UVmax,T,c500,c50,m)',...
    'coefficients',{'G','m','UVmax'},...
    'independent',{'Sol'},...
    'problem',{'T','c500','c50'},...
    'options',fomm)

[f,gof,output] = fit (Sol, UV, ftmm,'problem',{T,c500,c50})

Alpha_500=(ratio_500uM-0.65)./(f.UVmax-0.65);
Alpha_50=(ratio_50uM-0.65)./(f.UVmax-0.65);

Solm=linspace(0, 0.8, 17);
Alpha_m_500=(isodesmic_equilibria_UV_equations_solvent(Solm,f.G,f.UVmax,f.T,f.c500,f.m)-
0.65)/(f.UVmax-0.65);
Alpha_m_50=(isodesmic_equilibria_UV_equations_solvent(Solm,f.G,f.UVmax,f.T,f.c50,f.m)-
0.65)/(f.UVmax-0.65);

h=figure;
plot(Solm,Alpha_m_500,'-', 'Linewidth',3, 'color',[0 128/250 0/255]);
hold on
plot(Solm,Alpha_m_50,'-', 'Linewidth',3, 'color',[0 128/250 0/255]);
hold on
scatter(S_500uM,Alpha_500,85,'d','MarkerEdgeColor',[120/255 220/255
120/255], 'MarkerFaceColor',[120/255 220/255 120/255]);
hold on
scatter(S_50uM,Alpha_50,85,'o','MarkerEdgeColor',[120/255 220/255
120/255], 'MarkerFaceColor',[120/255 220/255 120/255]);
hold off
    xlim([-0.02 0.82])
    ylim([-0.02 1.02])
xlabel('f_M_e_O_H','FontName','myriad pro','FontSize',16)
ylabel('\alpha','FontName','myriad pro','FontSize',16);

```

```

set(gca,'TickDir','out','FontName','myriad
pro','FontSize',14,'Linewidth',3,'box','off','xtick',[0:0.1:0.8],'ytick',[0:0.25:1],'TickLeng
th',[0.015 0])

title('PDI-Y','FontName','myriad pro','FontSize',16,'FontWeight','bold')
set(gcf,'color','w','Position',[0,0,1000,750]);
hold off

```

```

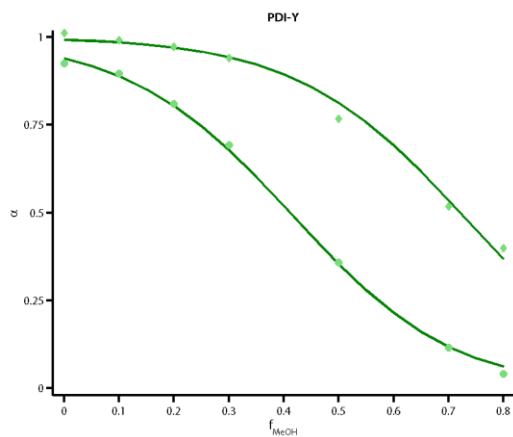
f =
General model:
f(Sol) = isodesmic_equilibria_UV_equations_solvent_multi(Sol,G,UVmax,T,c500,
c50,m)
Coefficients (with 95% confidence bounds):
G = -3.136e+04 (-3.216e+04, -3.056e+04)
m = 1.845e+04 (1.725e+04, 1.964e+04)
UVmax = 1.792 (1.764, 1.82)
Problem parameters:
T = 298
c500 = 0.0004
c50 = 4e-05

```

```

gof =
sse: 0.0062
rsquare: 0.9967
dfe: 11
adjrsquare: 0.9961
rmse: 0.0238

```



end

5.8.4.2 UV/Vis isodesmic model fitting

```

function
[Alpha]=isodesmic_multifit_UV_equations_Ho(T,Tm1000,Tm200,Tm50,Tm10,Tm5,Tm1,H,UVmax,s_cum)

nT=size(T);
Tu = unique(T);
nTu=size(Tu);
x_=1;

```

```

y=nT(1)/(nTu(1));

if nT(1)==nTu(1)
    Alpha(1:nT,1)=1;
else

    Alpha(1:s_cum(1,1),1)=(UVmax-0.65)/(1+exp(-0.908*...
        H*(T(1:s_cum(1,1),1)-Tm1000)/(8.314*Tm1000^2)))+0.65;
    Alpha(s_cum(1,1)+1:s_cum(2,1),1)=(UVmax-0.65)/(1+exp(-0.908*...
        H*(T(s_cum(1,1)+1:s_cum(2,1),1)-Tm200)/(8.314*Tm200^2)))+0.65;
    Alpha(s_cum(2,1)+1:s_cum(3,1),1)=(UVmax-0.65)/(1+exp(-0.908*...
        H*(T(s_cum(2,1)+1:s_cum(3,1),1)-Tm50)/(8.314*Tm50^2)))+0.65;
    Alpha(s_cum(3,1)+1:s_cum(4,1),1)=(UVmax-0.65)/(1+exp(-0.908*...
        H*(T(s_cum(3,1)+1:s_cum(4,1),1)-Tm10)/(8.314*Tm10^2)))+0.65;
    Alpha(s_cum(4,1)+1:s_cum(5,1),1)=(UVmax-0.65)/(1+exp(-0.908*...
        H*(T(s_cum(4,1)+1:s_cum(5,1),1)-Tm5)/(8.314*Tm5^2)))+0.65;
    Alpha(s_cum(5,1)+1:s_cum(6,1),1)=(UVmax-0.65)/(1+exp(-0.908*...
        H*(T(s_cum(5,1)+1:s_cum(6,1),1)-Tm1)/(8.314*Tm1^2)))+0.65;

end

```

end

```

function isodesmic_multifit_UV_Ho

clc
close all
load('PDI_Ho_UV_H2O.mat')

[s(1,1),s(1,2)]=size(ratio_1mM);
[s(2,1),s(2,2)]=size(ratio_200uM);
[s(3,1),s(3,2)]=size(ratio_50uM);
[s(4,1),s(4,2)]=size(ratio_10uM);
[s(5,1),s(5,2)]=size(ratio_5uM);
[s(6,1),s(6,2)]=size(ratio_1uM);

s_cum(1,1)=s(1,1);

for i=2:6
    s_cum(i,1)=s(i,1)+s_cum(i-1);
end

UV(1:s_cum(1,1),1)=ratio_1mM;
UV(s_cum(1,1)+1:s_cum(2,1),1)=ratio_200uM;
UV(s_cum(2,1)+1:s_cum(3,1),1)=ratio_50uM;
UV(s_cum(3,1)+1:s_cum(4,1),1)=ratio_10uM;
UV(s_cum(4,1)+1:s_cum(5,1),1)=ratio_5uM;
UV(s_cum(5,1)+1:s_cum(6,1),1)=ratio_1uM;

T(1:s_cum(1,1),1)=t_1mM;
T(s_cum(1,1)+1:s_cum(2,1),1)=t_200uM;
T(s_cum(2,1)+1:s_cum(3,1),1)=t_50uM;
T(s_cum(3,1)+1:s_cum(4,1),1)=t_10uM;
T(s_cum(4,1)+1:s_cum(5,1),1)=t_5uM;
T(s_cum(5,1)+1:s_cum(6,1),1)=t_1uM;

```

```

fomm = fitoptions('Method', 'NonLinearLeastSquares', 'StartPoint', [268,268,250,240,230,220,-
50e3,950], ...
    'Lower', [200,200,200,200,190,180,-100e3,1], 'Upper', [500,400,400,400,400,400,-10e3,3],...
    'TolFun',1e-14,'TolX',1e-
14,'MaxIter',5000,'MaxFunEval',2500,'Display','iter','Robust','LAR')

ftmm =
fittype('isodesmic_multifit_UV_equations_Ho(T,Tm1000,Tm200,Tm50,Tm10,Tm5,Tm1,H,UVmax,s_cum)',
...
    'coefficients',{'Tm1000','Tm200','Tm50','Tm10','Tm5','Tm1','H','UVmax'},...
    'independent',{'T'},...
    'problem',{'s_cum'},...
    'options',fomm)

[f,gof,output] = fit (T, UV, ftmm,'problem',{s_cum})

UV_model=isodesmic_multifit_UV_equations_Ho(T,f.Tm1000,f.Tm200,f.Tm50,f.Tm10,f.Tm5,f.Tm1,f.H,
f.UVmax,s_cum);

Alpha=(UV-0.65)/(f.UVmax-0.65);
Alpha_model=(UV_model-0.65)/(f.UVmax-0.65);

Tr1000=-f.H*(T(1:s_cum(1,1),1)-f.Tm1000)/(8.315*f.Tm1000^2);
Tr200=-f.H*(T(s_cum(1,1)+1:s_cum(2,1),1)-f.Tm200)/(8.315*f.Tm200^2);
Tr50=-f.H*(T(s_cum(2,1)+1:s_cum(3,1),1)-f.Tm50)/(8.315*f.Tm50^2);
Tr10=-f.H*(T(s_cum(3,1)+1:s_cum(4,1),1)-f.Tm10)/(8.315*f.Tm10^2);
Tr5=-f.H*(T(s_cum(4,1)+1:s_cum(5,1),1)-f.Tm5)/(8.315*f.Tm5^2);
Tr1=-f.H*(T(s_cum(5,1)+1:s_cum(6,1),1)-f.Tm1)/(8.315*f.Tm1^2);

Tr(1:s_cum(1,1),1)=Tr1000;
Tr(s_cum(1,1)+1:s_cum(2,1),1)=Tr200;
Tr(s_cum(2,1)+1:s_cum(3,1),1)=Tr50;
Tr(s_cum(3,1)+1:s_cum(4,1),1)=Tr10;
Tr(s_cum(4,1)+1:s_cum(5,1),1)=Tr5;
Tr(s_cum(5,1)+1:s_cum(6,1),1)=Tr1;

Tr=sort(Tr);
Alpha_model=sort(Alpha_model,'descend');

Alpha1000(:,1)=Alpha(1:s_cum(1,1),1);
Alpha200(:,1)=Alpha(s_cum(1,1)+1:s_cum(2,1),1);
Alpha50(:,1)=Alpha(s_cum(2,1)+1:s_cum(3,1),1);
Alpha10(:,1)=Alpha(s_cum(3,1)+1:s_cum(4,1),1);
Alpha5(:,1)=Alpha(s_cum(4,1)+1:s_cum(5,1),1);
Alpha1(:,1)=Alpha(s_cum(5,1)+1:s_cum(6,1),1);

Alpha_model1000(:,1)=Alpha_model(1:s_cum(1,1),1);
Alpha_model200(:,1)=Alpha_model(s_cum(1,1)+1:s_cum(2,1),1);
Alpha_model50(:,1)=Alpha_model(s_cum(2,1)+1:s_cum(3,1),1);
Alpha_model10(:,1)=Alpha_model(s_cum(3,1)+1:s_cum(4,1),1);
Alpha_model5(:,1)=Alpha_model(s_cum(4,1)+1:s_cum(5,1),1);
Alpha_model1(:,1)=Alpha_model(s_cum(5,1)+1:s_cum(6,1),1);

f1=scatter(Tr1000,Alpha1000,25,'o','MarkerEdgeColor','none',...
    'MarkerFaceColor',[75/255 75/255 75/255]);
hold on

```

```

f2=scatter(Tr200,Alpha200,25,'o','MarkerEdgeColor','none',...
'MarkerFaceColor',[95/255 95/255 95/255]);
hold on
f3=scatter(Tr50,Alpha50,25,'o','MarkerEdgeColor','none',...
'MarkerFaceColor',[115/255 115/255 115/255]);
hold on
f4=scatter(Tr10,Alpha10,25,'o','MarkerEdgeColor','none',...
'MarkerFaceColor',[136/255 136/255 136/255]);
hold on
f4=scatter(Tr5,Alpha5,25,'o','MarkerEdgeColor','none',...
'MarkerFaceColor',[158/255 158/255 158/255]);
hold on
f4=scatter(Tr1,Alpha1,25,'o','MarkerEdgeColor','none',...
'MarkerFaceColor',[180/255 180/255 180/255]);
hold on
plot(Tr,Alpha_model,'-','Linewidth',4,'Color',[0 0 0])
% ylbl=sprintf('%c',945);
ylabel('\alpha','FontName','myriad pro','FontSize',24);
xlabel('T_r','FontName','myriad pro','FontSize',24);
legend({'800 \muM', '160 \muM', '40 \muM', '8 \muM', '4 \muM', '0.8 \muM', 'Model'},...
'FontName','myriad pro','FontSize',16,'Fontweight','bold');
legend('boxoff')
set(gca,'TickDir','out','FontName','myriad pro','FontSize',16,...
'Linewidth',2,'box','off')
title('PDI-Ho','FontName','myriad pro','FontSize',24,'Fontweight','bold')
set(gcf,'color','w','Position',[0, 0, 1000, 750]);
hold off

end

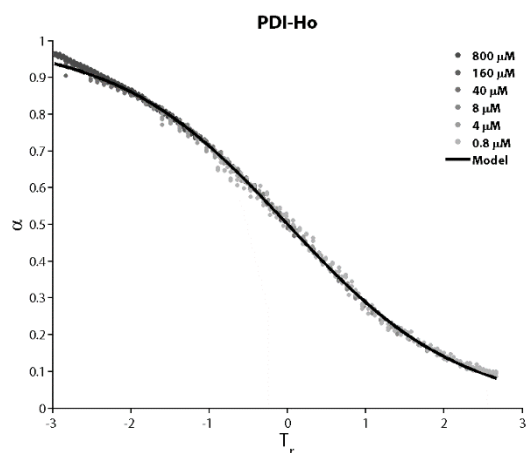
```

```

f =
General model:
f(T) = isodesmic_multifit_UV_equations_Ho(T,Tm1000,Tm200,Tm50,Tm10,Tm5,Tm1,
H,UVmax,s_cum)
Coefficients (with 95% confidence bounds):
Tm1000 = 414.2 (413.9, 414.4)
Tm200 = 384.8 (384.7, 385)
Tm50 = 360 (359.9, 360.1)
Tm10 = 323.7 (323.7, 323.8)
Tm5 = 315.7 (315.6, 315.7)
Tm1 = 299.3 (299.3, 299.4)
H = -3.117e+04 (-3.123e+04, -3.112e+04)
UVmax = 1.909 (1.909, 1.91)
Problem parameters:
s_cum = 6x1 double

gof =
sse: 0.0088
rsquare: 0.9999
dfe: 1198
adjrsquare: 0.9999
rmse: 0.0027

```

5.8.4.3 CD isodesmic model fitting

```
function [CD]=isodesmic_multifit_CD_equations_Gd(T,Tm1000,Tm200,Tm50,Tm10,H,CDmax,s_cum)
```

```
nT=size(T);
Tu = unique(T);
nTu=size(Tu);
x_=1;
y=nT(1)/(nTu(1));

if nT(1)==nTu(1)
    CD(1:nT,1)=1;
else

CD(1:s_cum(1,1),1)=CDmax./(1+exp(-0.908*H*...
    (T(1:s_cum(1,1),1)-Tm1000)/(8.314*Tm1000^2)));
CD(s_cum(1,1)+1:s_cum(2,1),1)=CDmax./(1+exp(-0.908*H*...
    (T(s_cum(1,1)+1:s_cum(2,1),1)-Tm200)/(8.314*Tm200^2)));
CD(s_cum(2,1)+1:s_cum(3,1),1)=CDmax./(1+exp(-0.908*H*...
    (T(s_cum(2,1)+1:s_cum(3,1),1)-Tm50)/(8.314*Tm50^2)));
CD(s_cum(3,1)+1:s_cum(4,1),1)=CDmax./(1+exp(-0.908*H*...
    (T(s_cum(3,1)+1:s_cum(4,1),1)-Tm10)/(8.314*Tm10^2)));

end

end
```

```
function isodesmic_multifit_CD_Gd

clc
close all
load('PDI_Gd_CD_H2O.mat')

[s(1,1),s(1,2)]=size(PDI_Gd_1mM_H2O_475nm_molar_ellipticity);
[s(2,1),s(2,2)]=size(PDI_Gd_200uM_H2O_475nm_molar_ellipticity);
[s(3,1),s(3,2)]=size(PDI_Gd_50uM_H2O_475nm_molar_ellipticity);
[s(4,1),s(4,2)]=size(PDI_Gd_10uM_H2O_475nm_molar_ellipticity);
```

```

s_cum(1,1)=s(1,1);

for i=2:4
s_cum(i,1)=s(i,1)+s_cum(i-1);
end

CD(1:s_cum(1,1),1)=PDI_Gd_1mM_H2O_475nm_molar_ellipticity(:,2);
CD(s_cum(1,1)+1:s_cum(2,1),1)=PDI_Gd_200uM_H2O_475nm_molar_ellipticity(:,2);
CD(s_cum(2,1)+1:s_cum(3,1),1)=PDI_Gd_50uM_H2O_475nm_molar_ellipticity(:,2);
CD(s_cum(3,1)+1:s_cum(4,1),1)=PDI_Gd_10uM_H2O_475nm_molar_ellipticity(:,2);

T(1:s_cum(1,1),1)=PDI_Gd_1mM_H2O_475nm_molar_ellipticity(:,1);
T(s_cum(1,1)+1:s_cum(2,1),1)=PDI_Gd_200uM_H2O_475nm_molar_ellipticity(:,1);
T(s_cum(2,1)+1:s_cum(3,1),1)=PDI_Gd_50uM_H2O_475nm_molar_ellipticity(:,1);
T(s_cum(3,1)+1:s_cum(4,1),1)=PDI_Gd_10uM_H2O_475nm_molar_ellipticity(:,1);

fomm = fitoptions('Method', 'NonLinearLeastSquares', 'StartPoint', [300,350,294,250,-
10e3,950], ...
'Lower', [200,250,200,200,-1000e3,200], 'Upper', [500,400,400,400,-1e3,20000],...
'TolFun',1e-14,'TolX',1e-14,'MaxIter',5000,'MaxFunEval',2500,'Display','iter')

ftmm =
fitype('isodesmic_multifit_CD_equations_Gd(T,Tm1000,Tm200,Tm50,Tm10,H,CDmax,s_cum)',...
'coefficients',{'Tm1000','Tm200','Tm50','Tm10','H','CDmax'},...
'independent',{'T'},...
'problem',{'s_cum'},...
'options',fomm)

[f,gof,output] = fit (T, CD, ftmm,'problem',{s_cum})

model=isodesmic_multifit_CD_equations_Gd(T,f.Tm1000,f.Tm200,f.Tm50,f.Tm10,f.H,f.CDmax,s_cum);

Alpha=CD/f.CDmax;
Alpha_model=model/f.CDmax;

Tr1000=-f.H*(T(1:s_cum(1,1),1)-f.Tm1000)/(8.315*f.Tm1000^2);
Tr200=-f.H*(T(s_cum(1,1)+1:s_cum(2,1),1)-f.Tm200)/(8.315*f.Tm200^2);
Tr50=-f.H*(T(s_cum(2,1)+1:s_cum(3,1),1)-f.Tm50)/(8.315*f.Tm50^2);
Tr10=-f.H*(T(s_cum(3,1)+1:s_cum(4,1),1)-f.Tm10)/(8.315*f.Tm10^2);

Alpha1000(:,1)=Alpha(1:s_cum(1,1),1);
Alpha200(:,1)=Alpha(s_cum(1,1)+1:s_cum(2,1),1);
Alpha50(:,1)=Alpha(s_cum(2,1)+1:s_cum(3,1),1);
Alpha10(:,1)=Alpha(s_cum(3,1)+1:s_cum(4,1),1);

Tr(1:s_cum(1,1),1)=Tr1000;
Tr(s_cum(1,1)+1:s_cum(2,1),1)=Tr200;
Tr(s_cum(2,1)+1:s_cum(3,1),1)=Tr50;
Tr(s_cum(3,1)+1:s_cum(4,1),1)=Tr10;

Tr=sort(Tr);
Alpha_model=sort(Alpha_model,'descend');

f1=scatter(Tr1000,Alpha1000,25,'o','MarkerEdgeColor','none','MarkerFaceColor',[0/255 0/255
160/255]);

```

```

hold on
f2=scatter(Tr200,Alpha200,25,'o','MarkerEdgeColor','none','MarkerFaceColor',[21/255 62/250
191/255]);
hold on
f3=scatter(Tr50,Alpha50,25,'o','MarkerEdgeColor','none','MarkerFaceColor',[58/255 106/255
217/255]);
hold on
f4=scatter(Tr10,Alpha10,25,'o','MarkerEdgeColor','none','MarkerFaceColor',[100/255 149/255
237/255]);
hold on
% plot(Tr1000,Alpha_model1000,'-','Linewidth',3,'Color',[0 0 0])
% hold on
% % plot(Tr200,Alpha_model200,'-','Linewidth',3,'Color',[0 0 0])
% % hold on
% plot(Tr50,Alpha_model50,'-','Linewidth',3,'Color',[0 0 0])
% hold on
% plot(Tr10,Alpha_model10,'-','Linewidth',3,'Color',[0 0 0])
% hold off
plot(Tr,Alpha_model,'-','Linewidth',5,'Color',[0 0 0])
hold off
ylabel('\alpha','FontName','myriad pro','FontSize',24);
xlabel('T_r','FontName','myriad pro','FontSize',24);
legend({'800 \muM','160 \muM','40 \muM','8 \muM','Model'],'FontName','myriad
pro','FontSize',16,'FontWeight','bold');
legend('boxoff')
set(gca,'TickDir','out','FontName','myriad pro','FontSize',16,'Linewidth',2,'box','off')
title('PDI-Gd','FontName','myriad pro','FontSize',24,'FontWeight','bold')
set(gcf,'color','w','Position',[0,0,1000,750]);
hold off

end

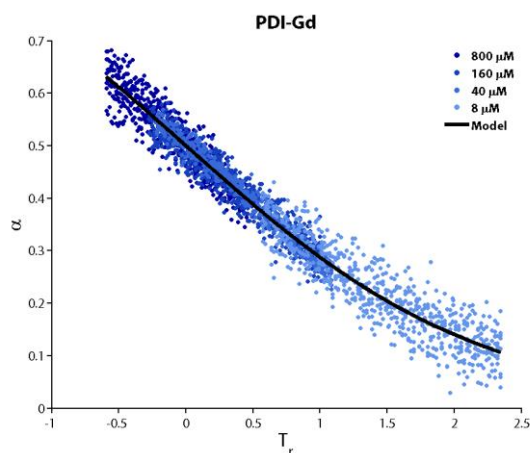
```

```

f =
General model:
f(T) = isodesmic_multifit_CD_equations_Gd(T,Tm1000,Tm200,Tm50,Tm10,H,CDmax,
s_cum)
Coefficients (with 95% confidence bounds):
Tm1000 = 326.3 (318.1, 334.6)
Tm200 = 296 (289.4, 302.7)
Tm50 = 292.2 (285.7, 298.7)
Tm10 = 250.5 (245.1, 255.9)
H = -1.087e+04 (-1.174e+04, -9998)
CDmax = 1310 (1252, 1369)
Problem parameters:
s_cum = 4x1 double

gof =
sse: 3.3864e+06
rsquare: 0.9579
dfe: 2455
adjrsquare: 0.9578
rmse: 37.1400

```



5.8.4.4 DLS data treatment

```
function fit_dls_data_Ho20190625_1mM
```

```
close all
clc
load('GF03_Ho_1mM_2019_06_24_25mW.mat')

[n,m]=size(g);
red=[1 0 0];
blue=[0 0 1];
green=[0 1 0];
colors1=[linspace(red(1),blue(1),(m+1)/2)',linspace(red(2),blue(2),(m+1)/2)',linspace(red(3),
blue(3),(m+1)/2)'];
colors2=[linspace(blue(1),green(1),(m-1)/2)',linspace(blue(2),green(2),(m-
1)/2)',linspace(blue(3),green(3),(m-1)/2)'];
colors=[colors1;colors2];
[mc,nc]=size(colors);
if mc<m
colors(m,:)= [0 0 0];
end
jk=0;
for i=1:1:m
if i==21
m=m;
end
[pks,loc]= findpeaks(g(:,i),'MinPeakHeight',0.005,'MinPeakDistance',1);
locs=s(loc);
plot(s,g(:,i),'color',colors(i,:),'Linewidth',2)
l=size(locs);
if l(1,1)>1
for j=1:l
if i>10
if locs(j)>0 && locs(j)<100
L(i)=locs(j)*1e-3;
J=j;
jk=1;
else
if jk ~1
L(i)=0;
J=1;
end
end
end
end
```

```

        locs(J)=NaN;
        pks(J)=NaN;
    end
end
else
    if i>9
        if locs(j)>0 && locs(j)<100
            L(i)=locs(j)*1e-3;
            J=j;
            J=j;
            jk=1;
        else
            if jk ~=1
                L(i)=0;
                J=1;
                locs(J)=NaN;
                pks(J)=NaN;
            end
        end
    else
        if locs(j)>0 && locs(j)<100
            L(i)=locs(j)*1e-3;
            J=j;
            jk=1;
        else
            if jk ~=1
                L(i)=0;
                J=1;
                locs(J)=NaN;
                pks(J)=NaN;
            end
        end
        %         end
        %         end
        %         end
    end
end
end
end

else

    if l(1,1)<1
        L(i)=0;
        J=1;
        locs(J)=NaN;
        pks(J)=NaN;
    else
        if locs>0 && locs<1000
            L(i)=locs*1e-3;
        else
            L(i)=0;
            locs(J)=NaN;
            pks(J)=NaN;
        end
        J=1;
    end
    % end
end
end

```

```

hold on
scatter(locs(J),pks(J),'o','MarkerEdgeColor',[1 0 0])
set(gca, 'xScale', 'log')
hold on
% pause
pks=0;
locs=0;
jk=0;
end
Legend('30','30','30','30','30','30','40','40','40','40','40','40',...
'50','50','50','50','50','50','60','60','60','60','60','60',...
'70','70','70','70','70','70','80','80','80','80','80','80',...
'90','90','90','90','90','90','100','100','100','100','100','100',...
'110','110','110','110','110','110','120','120','120','120','120','120',...
'130','130','130','130','130','130','Location','west')
ylabel('G(\tau)','FontName','myriad pro','FontSize',24);
xlabel('\tau (ms)','FontName','myriad pro','FontSize',24);
set(gca,'TickDir','out','FontName','myriad pro','FontSize',16,'Linewidth',2,'box','off')
title('PDI-Ho','FontName','myriad pro','FontSize',24,'FontWeight','bold')
set(gcf,'color','w','Position',[0,0,1000,750]);
hold off

% theta=[30;30;30;40;40;40;50;50;50;60;60;60;70;70;70;80;80;80]*pi()/180;
% theta=[30;30;40;40;50;50;60;60;70;70;80;80;90;90;100;100;110;110;120;120;130;130]*pi()/180;
% theta=[30;40;50;60;70;80;90;100;110;120;130]*pi()/180;
theta=[30;30;30;40;40;40;50;50;50;60;60;60;70;70;70;80;80;80;90;90;90;100;100;100;110;110;110;
;120;120;120;130;130;130]*pi()/180;
%
theta=[30;30;30;40;40;40;50;50;50;60;60;60;70;70;70;80;80;80;90;90;90;100;100;100;110;110;110;
;120;120;120;130;130]*pi()/180;
% theta=[30;40;50;60;70;80]*pi()/180;
e1=0;
tau_inv=L([1:m-e1]).^-1;

kB=1.38064852e-23;
T=293;
mu=0.563e-3;
n0=1.331;
lambda=639e-9;

p=2;
h=figure;
[AX,H1,H2]=plotyy(s,g(:,p),t,AxB(:,p));
% xlim([10 1000])
set(AX, 'xScale', 'log', 'XLim', [1e-3 1e4], 'TickDir', 'out', 'FontName', 'myriad
pro', 'FontSize', 16, 'Linewidth', 3, 'box', 'off');
% ylabel('G(\tau)', 'FontName', 'myriad pro', 'FontSize', 24);
set(get(AX(1), 'YLabel'), 'String', 'G(\tau)', 'FontName', 'myriad pro', 'FontSize', 24);
set(get(AX(2), 'YLabel'), 'String', 'g_v_v^\Lambda(q,t)', 'FontName', 'myriad pro', 'FontSize', 24);
set(AX(1), 'YColor', [0 0 0], 'YTick', [0 0.05 0.1 0.15 0.2]);
set(AX(2), 'YLim', [-0.05 1], 'YColor', [0.5 0.5 0.5], 'YTick', [0 0.25 0.5 0.75
1], 'Linewidth', 3, 'TickDir', 'out', 'FontName', 'myriad pro', 'FontSize', 16);
set(H1, 'color', [0 0 0], 'Linewidth', 3);
set(H2, 'color', [0.5 0.5 0.5], 'Linewidth', 3);
xlabel('t (ms)', 'FontName', 'myriad pro', 'FontSize', 24);
title('PDI-Ho', 'FontName', 'myriad pro', 'FontSize', 24, 'FontWeight', 'bold');
set(gcf, 'color', 'w', 'Position', [0, 0, 1200, 750]);

```

```

hold off

q_plot=(4*pi*n0/lambda)*sin(theta(p)/2)
q_sqr_d_plot=q_plot.^2;

D_int=((s/1e3).^-1) ./q_sqr_d_plot;
Rh_plot=((kB.*T./(6.*3.14.*mu.*(D_int)))) .*1e9;

h=figure;
plot (Rh_plot,g(:,p), 'color',[0 0 0], 'Linewidth',3)
xlim([100 10000])
set(gca, 'xScale', 'log')
ylabel('G(\tau)', 'FontName', 'myriad pro', 'FontSize',24);
xlabel('R_H (nm)', 'FontName', 'myriad pro', 'FontSize',24);
set(gca, 'TickDir', 'out', 'FontName', 'myriad pro', 'FontSize',16, 'Linewidth',2, 'box', 'off')
title('PDI-Ho', 'FontName', 'myriad pro', 'FontSize',24, 'FontWeight', 'bold')
set(gcf, 'color', 'w', 'Position', [0, 0, 1000, 750]);
hold off

n=m-1;
k=0;
for i=1:n-1
    if L(i)==0 ||tau_inv(i-k)>700
%     if L(i)==0
        tau_inv(i-k)=[];
        theta(i-k)=[];
        k=k+1;
    end
end
% tau_inv(12)=[];
% theta(12)=[];
% tau_inv(11)=[];
% theta(11)=[];
% tau_inv(6)=[];
% theta(6)=[];
% tau_inv(13)=[];
% theta(13)=[];
% tau_inv(8)=[];
% theta(8)=[];
% tau_inv(7)=[];
% theta(7)=[];

q=(4*pi*n0/lambda)*sin(theta/2);
q_sqr_d=q.^2;
tau_inv_1000000=tau_inv.*1e9;

fomm = fitoptions('Method', 'NonLinearLeastSquares', 'StartPoint', [1e-6,1e9], ...
    'Lower', [1e-9,-1e11], 'Upper', [1e-1,1e11],...
    'TolFun',1e-14,'TolX',1e-14,'MaxIter',5000,'MaxFunEval',2500)

ftmm = fitype('D*q_sqr_d+b',...
    'coefficients',{ 'D','b'},...
    'independent', {'q_sqr_d'},...
    'options',fomm)

```

```

[f,gof,output] = fit (q_sqr, tau_inv_1000000, ftmm)
figure
D_lin=f.D/1e9;
b_lin=f.b/1e9;
tau_inv_mod=q_sqr*D_lin+b_lin;
hold on

f1=scatter(q_sqr, tau_inv,120,'o','MarkerEdgeColor','none','MarkerFaceColor',[180/255 0/255
0]);
hold on
plot(q_sqr, tau_inv_mod,'-','Linewidth',3,'Color','k')
ylabel('\Gamma (s^-1)','FontName','myriad pro','FontSize',24);
xlabel('q^2 (m^-2)','FontName','myriad pro','FontSize',24);
legend({'Data','Fit'],'FontName','myriad
pro','FontSize',16,'FontWeight','bold','Location','NorthWest');
legend('boxoff')
set(gca,'TickDir','out','FontName','myriad pro','FontSize',16,'Linewidth',2,'box','off')
title('PDI-Ho','FontName','myriad pro','FontSize',24,'FontWeight','bold')
set(gcf,'color','w','Position', [0, 0, 1000, 750]);
hold off

hold off
Rh_lin=(kB*T/(6*3.14*mu*(f.D/1e9)));

D_lin_int= confint(f)
Conf_D_lin=abs(D_lin_int(:,1)-f.D)/1e9
Conf_D_lin_avg=mean(Conf_D_lin)
Conf_Rh_lin=Rh_lin*sqrt((Conf_D_lin_avg/D_lin)^2)
D=[D_lin]
Rh=[Rh_lin]

```

```

q_plot =
    6.7746e+06

```

```

fomm =
    Normalize: 'off'
    Exclude: []
    weights: []
    Method: 'NonlinearLeastSquares'
    Robust: 'off'
    StartPoint: [1.0000e-06 1.0000e+09]
    Lower: [1.0000e-09 -1.0000e+11]
    Upper: [0.1000 1.0000e+11]
    Algorithm: 'Trust-Region'
    DiffMinChange: 1.0000e-08
    DiffMaxChange: 0.1000
    Display: 'Notify'
    MaxFunEvals: 2500
    MaxIter: 5000
    TolFun: 1.0000e-14
    TolX: 1.0000e-14

```

```

ftmm =
    General model:
    ftmm(D,b,q_sqr) = D*q_sqr+b

```



```
f =
  General model:
  f(q_sqrD) = D*q_sqrD+b
  Coefficients (with 95% confidence bounds):
  D = 0.0001297 (0.0001123, 0.0001472)
  b = 7.652e+09 (1.765e+09, 1.354e+10)
```

```
gof =
  sse: 2.1647e+21
  rsquare: 0.8814
  dfe: 31
  adjrsquare: 0.8776
  rmse: 8.3563e+09
```

```
output =
  numobs: 33
  numparam: 2
  residuals: [33x1 double]
  Jacobian: [33x2 double]
  exitflag: 3
  firstorderopt: 4.3151e+08
  iterations: 47
  funcCount: 144
  cgiterations: 0
  algorithm: 'trust-region-reflective'
  message: [1x86 char]
```

```
D_lin_int =
  1.0e+10 *
  0.0000 0.1765
  0.0000 1.3540
```

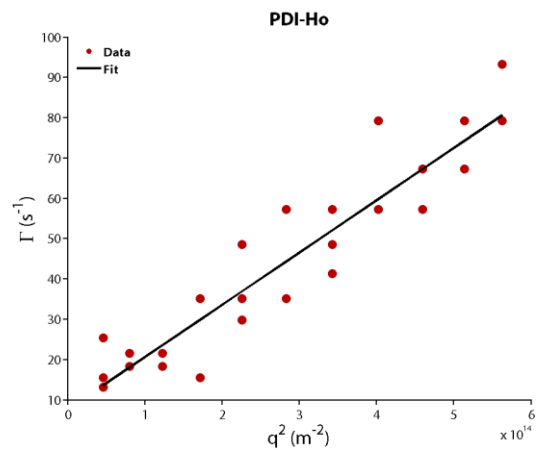
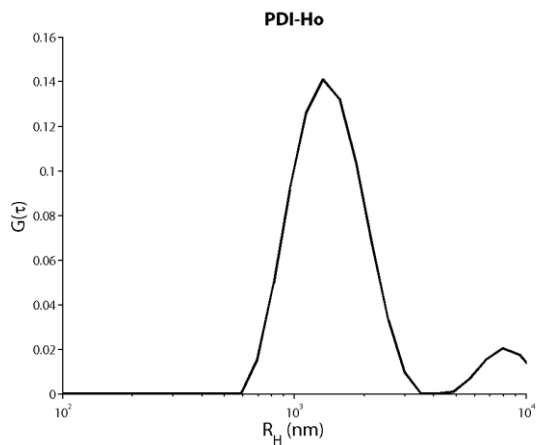
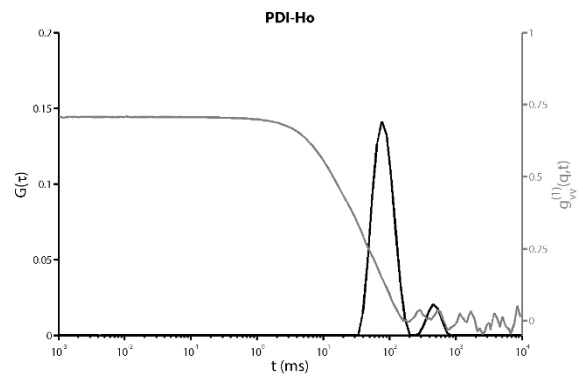
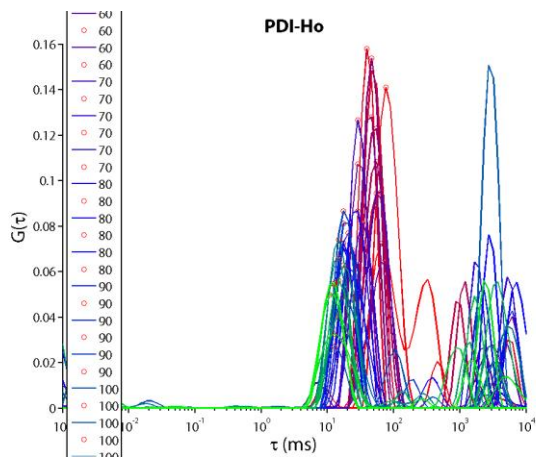
```
Conf_D_lin =
  1.0e-13 *
  0.1743
  0.1743
```

```
Conf_D_lin_avg =
  1.7431e-14
```

```
Conf_Rh_lin =
  3.9499e-07
```

```
D =
  1.2973e-13
```

```
Rh =
  2.9398e-06
```



avg

```

theta_u=unique(theta);
[nu,m]=size(theta_u);

for i=1:nu
    tau_inv_med(i)=mean(tau_inv(theta==theta_u(i)));
    tau_inv_std(i)=std(tau_inv(theta==theta_u(i)));
end

q_u=(4*pi*n0/lambda)*sin(theta_u/2);
q_u_sqrd=q_u.^2;
tau_inv_1000000_med=tau_inv_med'*1e9;

fomm = fitoptions('Method', 'NonLinearLeastSquares', 'StartPoint', [1e-6,1e9], ...
    'Lower', [1e-9,-1e11], 'Upper', [1e-1,1e11],...
    'TolFun',1e-14,'TolX',1e-14,'MaxIter',5000,'MaxFunEval',2500)

ftmm = fitype('D*q_sqrd+b',...
    'coefficients',{'D','b'},...
    'independent',{'q_sqrd'},...
    'options',fomm)

[f,gof,output] = fit (q_u_sqrd, tau_inv_1000000_med, ftmm)
figure
D_lin=f.D/1e9;
b_lin=f.b/1e9;
tau_u_inv_mod=q_u_sqrd*D_lin+b_lin;

```

```

hold on

f1=errorbar(q_u_sqrD,tau_inv_med,tau_inv_std,'o','MarkerSize',10,'Linewidth',3,'Color',[150/250 150/255 150/255],'MarkerEdgeColor','none','MarkerFaceColor',[150/250 150/255 150/255]);
hold on
plot(q_u_sqrD, tau_u_inv_mod,'-','Linewidth',3,'Color','k')
ylabel('\Gamma (s^-1)','FontName','myriad pro','FontSize',24);
xlabel('q^2 (m^-2)','FontName','myriad pro','FontSize',24);
legend({'Data','Fit'],'FontName','myriad pro','FontSize',16,'FontWeight','bold','Location','NorthWest');
legend('boxoff')
set(gca,'TickDir','out','FontName','myriad pro','FontSize',16,'Linewidth',2,'box','off')
title('PDI-Ho','FontName','myriad pro','FontSize',24,'FontWeight','bold')
set(gcf,'color','w','Position',[0,0,1000,750]);
saveas(gca,'C:\Users\Owner\Google Drive\Doctorat\OneDrive\Thesis\Chapter V\Figures\Data\PDI-Ho-DLS-Linear-1mM_2.eps')

hold off
Rh_lin=(kB*T/(6*3.14*mu*(f.D/1e9)));

D_lin_int= confint(f)
Conf_D_lin=abs(D_lin_int(:,1)-f.D)/1e9
Conf_D_lin_avg=mean(Conf_D_lin)
Conf_Rh_lin=Rh_lin*sqrt((Conf_D_lin_avg/D_lin)^2)
D=[D_lin]
Rh=[Rh_lin]

```

```

fmm =
  Normalize: 'off'
  Exclude: []
  weights: []
  Method: 'NonlinearLeastSquares'
  Robust: 'Off'
  StartPoint: [1.0000e-06 1.0000e+09]
  Lower: [1.0000e-09 -1.0000e+11]
  Upper: [0.1000 1.0000e+11]
  Algorithm: 'Trust-Region'
  DiffMinChange: 1.0000e-08
  DiffMaxChange: 0.1000
  Display: 'Notify'
  MaxFunEvals: 2500
  MaxIter: 5000
  TolFun: 1.0000e-14
  TolX: 1.0000e-14

ftmm =
  General model:
  ftmm(D,b,q_sqrD) = D*q_sqrD+b

f =
  General model:
  f(q_sqrD) = D*q_sqrD+b
Coefficients (with 95% confidence bounds):
  D = 0.0001297 (0.0001116, 0.0001479)
  b = 7.652e+09 (1.514e+09, 1.379e+10)

```

```

gof =
  sse: 1.8510e+20
  rsquare: 0.9666
  dfe: 9
  adjrsquare: 0.9629
  rmse: 4.5351e+09

output =
  numobs: 11
  numparam: 2
  residuals: [11x1 double]
  Jacobian: [11x2 double]
  exitflag: 0
  firstorderopt: 2.0391e+15
  iterations: 833
  funcCount: 2502
  cgiterations: 0
  algorithm: 'trust-region-reflective'
  message: [1x104 char]

```

```

D_lin_int =
  1.0e+10 *
  0.0000  0.1514
  0.0000  1.3791

```

```

Conf_D_lin =
  1.0e-13 *
  0.1817
  0.1817

```

```

Conf_D_lin_avg =
  1.8175e-14

```

```

Conf_Rh_lin =
  4.1184e-07

```

```

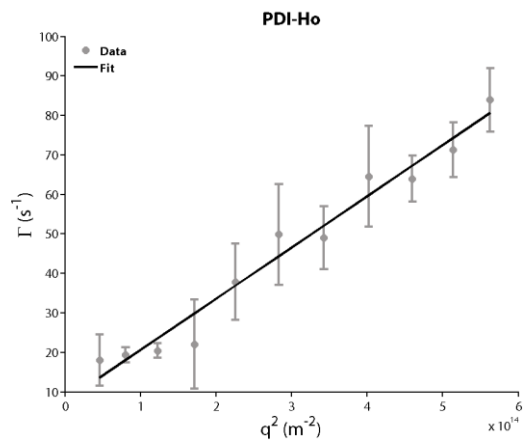
D =
  1.2973e-13

```

```

Rh =
  2.9398e-06

```



end

Chapter 6. Overall conclusions and outlook

There are still a multitude of unanswered fundamental questions in supramolecular polymers and polymerization, such as the dynamic behavior within and between self-assembled structures or controlling supramolecular copolymerization, showing that there is a long road to master supramolecular polymerization in the same way as we understand 'traditional' covalent polymers.²³⁶ But there is plenty of room for innovation beyond the fundamental questions, with the advent of Systems Chemistry, methods to temporally control self-assembly have led to the creation of life-like materials and systems that present autonomous formation and destruction of building blocks and feed-back loops.⁸³ There are important challenges, such as the development of reaction cycles where waste products can easily be removed or do not interfere with the different chemical processes,⁹⁰ and the creation of biocompatible or biorthogonal systems that could potentially lead to biomedical applications.²³⁷ Spatial control, in the same way that is achieved by biological structures, is still a great challenge, with chemists needing to better understand the mechanisms involved and develop new methodologies to achieve three dimensional control over supramolecular materials.²³⁸ Overall, the future of supramolecular polymerization, besides understanding the fundamentals mechanisms, will involve the programmed creation or adaptation of materials according to their surroundings, tailoring the materials' response to the environmental needs, working in collaboration with living systems.²³⁹ By dominating the challenges listed above and combining these different approaches, I believe that creating a true living material will be possible in the not-so-distant future.

In this thesis, we have shown how to gain better control over supramolecular polymers and polymerization. In Chapter 1, the state of the art of the techniques to control supramolecular polymers in and out-of-equilibrium have been shown. Three gaps in the field have been identified, in a more practical way that has been discussed above:

- Simple, efficient, and universal spatiotemporal control over supramolecular polymerization.
- A wider diversity in the reactions utilized for non-equilibrium reaction cycles.⁹⁰
- The use of easily achievable magnetic field (or lack thereof) to control molecular self-assembly.

In this thesis we tried to respond to each of these challenges.

To tackle the first problem, in Chapter 2 we developed a simple methodology where supramolecular polymer layers can be grown from polymeric surfaces through diffusion of protons. We used a PDMS cube to absorb HCl and release it in a solution containing a pH-responsive hydrogelator. A gel layer, in the mm range, could be grown from the surface of the polymer, and mathematical modeling showed that the diffusion of the protons from the material has to be slower than the nucleation rate of the supramolecular polymer, otherwise only precipitation is observed. This approach is very versatile, since a plethora of commercial porous materials can be used to absorb any reactant, and subsequently release it into the environment, allowing spatiotemporal control over many chemically triggered supramolecular materials.

The next challenge was confronted by the development, in Chapter 3, of a new aldehyde-targeting reaction cycle, that exclusively uses commercially available chemical fuels to gain the temporal control of a hydrogelator. This cycle utilizes the catalytic hydrolysis of a formaldehyde releasing agent (HMTA) to gain the delay needed for an autonomous reaction cycle. Surprisingly, the amount of catalyst influences the kinetics of the reaction cycle, which impacts the morphology of the final aggregates and the mechanical properties of the hydrogel.^{59,200} With this method not only we achieved temporal control over hydrogelation, but also control over the final properties of the material. Aldehyde being a biologically relevant²⁴⁰ and widely utilized chemical group, this reaction cycle opens the door for the controlled assembly of a wide variety of (bio)molecular building blocks.

Finally, the last problem was undertaken in Chapter 4 and Chapter 5 by achieving the control over supramolecular networks with easily accessible magnetic field by self-assembly of many lanthanides together. In Chapter 4 the densification and increase in branching of a Gd-

containing paramagnetic supramolecular rod network could be achieved by applying relatively weak magnetic fields (< 2 T). The same was not observed when using a diamagnetic control or in the absence of magnetic field. Mathematical calculations showed that these assemblies are large enough so that the magnetic energies involved surpass the thermal noise, but the mechanism responsible for the change in topology is still unknown. In Chapter 5, a library of lanthanide-containing perylene diimides was synthesized, and the size of their aggregates formed in water could be controlled depending on the lanthanide chosen. Since the thermodynamics of polymerization are virtually the same for all the compounds, pointing to the perylene core being the main driving factor for aggregation, with the lanthanide interactions possibly responsible for their size differences. Although there are still some constraints for the wide application of magnetically controlled supramolecular polymers, these examples are paving the way to facilitate the development of the field, by eliminating the need of (costly) strong electromagnets, such as bitter or superconducting magnets.¹¹ Furthermore, since magnetic fields are extensively used for biomedical applications, mainly in imaging, and it is virtually a biorthogonal stimulus, these lanthanide-containing magneto-responsive assemblies could open the door for the creation of new materials for theranostics applications.²⁴¹

The work presented in this thesis provides simple (but not simplistic) solutions to currently open problems in supramolecular polymerization. Each chapter showing new methods to control supramolecular polymerization and aggregate properties. These advances in the fundamental science of supramolecular chemistry can pave the way for smart materials that can be both autonomous and directed.

Personally, I believe that the future of supramolecular polymerization lies on the combination of non-equilibrium reaction cycles and stimuli-responsiveness to achieve orthogonal control over the properties of a single material. The use of biocompatible and biorthogonal chemistries and stimuli will be an important steppingstone for smart biomaterials working inside and in collaboration with biological systems. Of course, we are far from achieving such complex (and complicated) feat because we first need to fully understand each specific phenomenon. Because of this, I believe that the work presented in this thesis will help

to further understand supramolecular polymerization and develop new methodologies for the control over supramolecular polymerization, possibly leading to new applications.

References

- (1) Lehn, J. M. Toward Self-Organization and Complex Matter. *Science* **2002**, 295 (5564), 2400–2403. <https://doi.org/10.1126/science.1071063>.
- (2) Lehn, J. M. Toward Complex Matter: Supramolecular Chemistry and Self-Organization. *Proc. Natl. Acad. Sci. U. S. A.* **2002**, 99 (8), 4763–4768. <https://doi.org/10.1073/pnas.072065599>.
- (3) Steed, J. W.; Atwood, J. L. *Supramolecular Chemistry: Second Edition*, 2nd ed.; John Wiley & Sons, Ltd: Chichester, UK, 2009; Vol. 6. <https://doi.org/10.1002/9780470740880>.
- (4) Aida, T.; Meijer, E. W.; Stupp, S. I. Functional Supramolecular Polymers. *Science* **2012**, 335 (6070), 813–817. <https://doi.org/10.1126/science.1205962>.
- (5) Savyasachi, A. J.; Kotova, O.; Shanmugaraju, S.; Bradberry, S. J.; Ó'Máille, G. M.; Gunnlaugsson, T. Supramolecular Chemistry: A Toolkit for Soft Functional Materials and Organic Particles. *Chem* **2017**, 3 (5), 764–811. <https://doi.org/10.1016/j.chempr.2017.10.006>.
- (6) Meisl, G.; Kirkegaard, J. B.; Arosio, P.; Michaels, T. C. T.; Vendruscolo, M.; Dobson, C. M.; Linse, S.; Knowles, T. P. J. Molecular Mechanisms of Protein Aggregation from Global Fitting of Kinetic Models. *Nat. Protoc.* **2016**, 11 (2), 252–272. <https://doi.org/10.1038/nprot.2016.010>.
- (7) Spitzer, D.; Marichez, V.; Formon, G. J. M.; Besenius, P.; Hermans, T. M. Surface-Assisted Self-Assembly of a Hydrogel by Proton Diffusion. *Angew. Chemie - Int. Ed.* **2018**, 57 (35), 11349–11353. <https://doi.org/10.1002/anie.201806668>.
- (8) Chen, Q.; Lv, Y.; Zhang, D.; Zhang, G.; Liu, C.; Zhu, D. Cysteine and PH-Responsive Hydrogel Based on a Saccharide Derivative with an Aldehyde Group. *Langmuir* **2010**, 26 (5), 3165–3168. <https://doi.org/10.1021/la903102z>.
- (9) Besenius, P.; Portale, G.; Bomans, P. H. H.; Janssen, H. M.; Palmans, A. R. A.; Meijer, E. W. Controlling the Growth and Shape of Chiral Supramolecular Polymers in Water. *Proc. Natl. Acad. Sci. U. S. A.* **2010**, 107 (42), 17888–17893. <https://doi.org/10.1073/pnas.1009592107>.
- (10) Besenius, P.; Goedegebure, Y.; Driessé, M.; Koay, M.; Bomans, P. H. H.; Palmans, A. R. A.; Dankers, P. Y. W.; Meijer, E. W. Peptide Functionalised Discotic Amphiphiles and Their Self-Assembly into Supramolecular Nanofibres. *Soft Matter* **2011**, 7 (18), 7980–7983. <https://doi.org/10.1039/c1sm05896g>.
- (11) Coey, J. M. D. *Magnetism and Magnetic Materials*; Cambridge University Press: Cambridge, UK, 2010. <https://doi.org/10.1017/CBO9780511845000>.
- (12) Würthner, F.; Saha-Möller, C. R.; Fimmel, B.; Ogi, S.; Leowanawat, P.; Schmidt, D. Perylene Bisimide Dye Assemblies as Archetype Functional Supramolecular Materials. *Chem. Rev.* **2016**, 116 (3), 962–1052. <https://doi.org/10.1021/acs.chemrev.5b00188>.

- (13) Ciferri, A. *Supramolecular Polymers*, 2nd ed.; CRC Press: Boca Raton, FL, USA, 2005. <https://doi.org/10.1201/9781420027921>.
- (14) Boyle, J.; Nelson, D. L.; Cox, M. M. *Lehninger Principles of Biochemistry*, 4th ed.; W.H. Freeman and Company: New York, 2005. <https://doi.org/10.1002/bmb.2005.494033010419>.
- (15) Liu, Z.; Qiao, J.; Niu, Z.; Wang, Q. Natural Supramolecular Building Blocks: From Virus Coat Proteins to Viral Nanoparticles. *Chem. Soc. Rev.* **2012**, *41* (18), 6178–6194. <https://doi.org/10.1039/c2cs35108k>.
- (16) Pieters, B. J. G. E.; Van Eldijk, M. B.; Nolte, R. J. M.; Mecinović, J. Natural Supramolecular Protein Assemblies. *Chem. Soc. Rev.* **2016**, *45* (1), 24–39. <https://doi.org/10.1039/c5cs00157a>.
- (17) Boyer, P. D. The Atp Synthase—a Splendid Molecular Machine. *Annu. Rev. Biochem.* **1997**, *66* (1), 717–749. <https://doi.org/10.1146/annurev.biochem.66.1.717>.
- (18) Stock, D.; Leslie, A. G. W.; Walker, J. E. Molecular Architecture of the Rotary Motor in ATP Synthase. *Science* **1999**, *286* (5445), 1700–1705. <https://doi.org/10.1126/science.286.5445.1700>.
- (19) Fujita, D.; Ueda, Y.; Sato, S.; Mizuno, N.; Kumasaka, T.; Fujita, M. Self-Assembly of Tetravalent Goldberg Polyhedra from 144 Small Components. *Nature* **2016**, *540* (7634), 563–566. <https://doi.org/10.1038/nature20771>.
- (20) Giri, N.; Del Pópolo, M. G.; Melaugh, G.; Greenaway, R. L.; Rätzke, K.; Koschine, T.; Pison, L.; Gomes, M. F. C.; Cooper, A. I.; James, S. L. Liquids with Permanent Porosity. *Nature* **2015**, *527* (7577), 216–220. <https://doi.org/10.1038/nature16072>.
- (21) Ma, L.; Haynes, C. J. E.; Grommet, A. B.; Walczak, A.; Parkins, C. C.; Doherty, C. M.; Longley, L.; Tron, A.; Stefankiewicz, A. R.; Bennett, T. D.; Nitschke, J. R. Coordination Cages as Permanently Porous Ionic Liquids. *Nat. Chem.* **2020**, *12* (3), 270–275. <https://doi.org/10.1038/s41557-020-0419-2>.
- (22) Yamashina, M.; Tanaka, Y.; Lavendomme, R.; Ronson, T. K.; Pittelkow, M.; Nitschke, J. R. An Antiaromatic-Walled Nanospace. *Nature* **2019**, *574* (7779), 511–515. <https://doi.org/10.1038/s41586-019-1661-x>.
- (23) Fielden, S. D. P.; Leigh, D. A.; Woltering, S. L. Molecular Knots. *Angew. Chemie - Int. Ed.* **2017**, *56* (37), 11166–11194. <https://doi.org/10.1002/anie.201702531>.
- (24) Lewandowski, B.; De Bo, G.; Ward, J. W.; Papmeyer, M.; Kuschel, S.; Aldegunde, M. J.; Gramlich, P. M. E.; Heckmann, D.; Goldup, S. M.; D'Souza, D. M.; Fernandes, A. E.; Leigh, D. A. Sequence-Specific Peptide Synthesis by an Artificial Small-Molecule Machine. *Science* **2013**, *339* (6116), 189–193. <https://doi.org/10.1126/science.1229753>.
- (25) De Bo, G.; Gall, M. A. Y.; Kuschel, S.; De Winter, J.; Gerbaux, P.; Leigh, D. A. An Artificial Molecular Machine That Builds an Asymmetric Catalyst. *Nat. Nanotechnol.* **2018**, *13* (5), 381–385. <https://doi.org/10.1038/s41565-018-0105-3>.
- (26) Rothmund, P. W. K. Folding DNA to Create Nanoscale Shapes and Patterns. *Nature* **2006**, *440* (7082),

- 297–302. <https://doi.org/10.1038/nature04586>.
- (27) Marras, A. E.; Zhou, L.; Su, H. J.; Castro, C. E. Programmable Motion of DNA Origami Mechanisms. *Proc. Natl. Acad. Sci. U. S. A.* **2015**, *112* (3), 713–718. <https://doi.org/10.1073/pnas.1408869112>.
- (28) Tikhomirov, G.; Petersen, P.; Qian, L. Fractal Assembly of Micrometre-Scale DNA Origami Arrays with Arbitrary Patterns. *Nature* **2017**, *552* (7683), 67–71. <https://doi.org/10.1038/nature24655>.
- (29) Brunsveld, L.; Folmer, B. J. B.; Meijer, E. W.; Sijbesma, R. P. Supramolecular Polymers. *Chem. Rev.* **2001**, *101* (12), 4071–4097. <https://doi.org/10.1021/cr990125q>.
- (30) Desai, A.; Mitchison, T. J. Microtubule Polymerization Dynamics. *Annu. Rev. Cell Dev. Biol.* **1997**, *13* (1), 83–117. <https://doi.org/10.1146/annurev.cellbio.13.1.83>.
- (31) Cheeseman, I. M.; Desai, A. Molecular Architecture of the Kinetochores-Microtubule Interface. *Nat. Rev. Mol. Cell Biol.* **2008**, *9* (1), 33–46. <https://doi.org/10.1038/nrm2310>.
- (32) Knowles, T. P. J.; Vendruscolo, M.; Dobson, C. M. The Amyloid State and Its Association with Protein Misfolding Diseases. *Nat. Rev. Mol. Cell Biol.* **2014**, *15* (6), 384–396. <https://doi.org/10.1038/nrm3810>.
- (33) De Greef, T. F. A.; Smulders, M. M. J.; Wolffs, M.; Schenning, A. P. H. J.; Sijbesma, R. P.; Meijer, E. W. Supramolecular Polymerization. *Chem. Rev.* **2009**, *109* (11), 5687–5754. <https://doi.org/10.1021/cr900181u>.
- (34) Sijbesma, R. P.; Beijer, F. H.; Brunsveld, L.; Folmer, B. J. B.; Hirschberg, J. H. K. K.; Lange, R. F. M.; Lowe, J. K. L.; Meijer, E. W. Reversible Polymers Formed from Self-Complementary Monomers Using Quadruple Hydrogen Bonding. *Science* **1997**, *278* (5343), 1601–1604. <https://doi.org/10.1126/science.278.5343.1601>.
- (35) Sorrenti, A.; Leira-Iglesias, J.; Markvoort, A. J.; De Greef, T. F. A.; Hermans, T. M. Non-Equilibrium Supramolecular Polymerization. *Chem. Soc. Rev.* **2017**, *46* (18), 5476–5490. <https://doi.org/10.1039/c7cs00121e>.
- (36) Cantekin, S.; de Greef, T. F. A.; Palmans, A. R. A. Benzene-1,3,5-Tricarboxamide: A Versatile Ordering Moiety for Supramolecular Chemistry. *Chem. Soc. Rev.* **2012**, *41* (18), 6125–6137. <https://doi.org/10.1039/c2cs35156k>.
- (37) Smulders, M. M. J.; Nieuwenhuizen, M. M. L.; De Greef, T. F. A.; Van Der Schoot, P.; Schenning, A. P. H. J.; Meijer, E. W. How to Distinguish Isodesmic from Cooperative Supramolecular Polymerisation. *Chem. - A Eur. J.* **2010**, *16* (1), 362–367. <https://doi.org/10.1002/chem.200902415>.
- (38) Görl, D.; Würthner, F. Entropically Driven Self-Assembly of Bolaamphiphilic Perylene Dyes in Water. *Angew. Chemie - Int. Ed.* **2016**, *55* (39), 12094–12098. <https://doi.org/10.1002/anie.201606917>.
- (39) Syamala, P. P. N.; Soberats, B.; Görl, D.; Gekle, S.; Würthner, F. Thermodynamic Insights into the Entropically Driven Self-Assembly of Amphiphilic Dyes in Water. *Chem. Sci.* **2019**, *10* (40), 9358–9366. <https://doi.org/10.1039/c9sc03103k>.

- (40) Rao, K. V.; Miyajima, D.; Nihonyanagi, A.; Aida, T. Thermally Bisignate Supramolecular Polymerization. *Nat. Chem.* **2017**, *9* (11), 1133–1139. <https://doi.org/10.1038/NCHEM.2812>.
- (41) Li, X. Q.; Zhang, X.; Ghosh, S.; Würthner, F. Highly Fluorescent Lyotropic Mesophases and Organogels Based on J-Aggregates of Core-Twisted Perylene Bisimide Dyes. *Chem. - A Eur. J.* **2008**, *14* (27), 8074–8078. <https://doi.org/10.1002/chem.200800915>.
- (42) Fennel, F.; Wolter, S.; Xie, Z.; Plötz, P. A.; Kühn, O.; Würthner, F.; Lochbrunner, S. Biphasic Self-Assembly Pathways and Size-Dependent Photophysical Properties of Perylene Bisimide Dye Aggregates. *J. Am. Chem. Soc.* **2013**, *135* (50), 18722–18725. <https://doi.org/10.1021/ja409597x>.
- (43) Korevaar, P. A.; Schaefer, C.; De Greef, T. F. A.; Meijer, E. W. Controlling Chemical Self-Assembly by Solvent-Dependent Dynamics. *J. Am. Chem. Soc.* **2012**, *134* (32), 13482–13491. <https://doi.org/10.1021/ja305512g>.
- (44) Mabesoone, M. F. J.; Markvoort, A. J.; Banno, M.; Yamaguchi, T.; Helmich, F.; Naito, Y.; Yashima, E.; Palmans, A. R. A.; Meijer, E. W. Competing Interactions in Hierarchical Porphyrin Self-Assembly Introduce Robustness in Pathway Complexity. *J. Am. Chem. Soc.* **2018**, *140* (25), 7810–7819. <https://doi.org/10.1021/jacs.8b02388>.
- (45) Yagai, S.; Kitamura, A. Recent Advances in Photoresponsive Supramolecular Self-Assemblies. *Chem. Soc. Rev.* **2008**, *37* (8), 1520–1529. <https://doi.org/10.1039/b703092b>.
- (46) Koumura, N.; Kudo, M.; Tamaoki, N. Photocontrolled Gel-to-Sol-to-Gel Phase Transitioning of Meta-Substituted Azobenzene Bisurethanes through the Breaking and Reforming of Hydrogen Bonds. *Langmuir* **2004**, *20* (23), 9897–9900. <https://doi.org/10.1021/la048334f>.
- (47) Eastoe, J.; Sánchez-Dominguez, M.; Wyatt, P.; Heenan, R. K. A Photo-Responsive Organogel. *Chem. Commun.* **2004**, No. 22, 2608–2609. <https://doi.org/10.1039/b410158h>.
- (48) Zhan, T. G.; Lin, M. Di; Wei, J.; Liu, L. J.; Yun, M. Y.; Wu, L.; Zheng, S. T.; Yin, H. H.; Kong, L. C.; Zhang, K. Da. Visible-Light Responsive Hydrogen-Bonded Supramolecular Polymers Based on: Ortho-Tetrafluorinated Azobenzene. *Polym. Chem.* **2017**, *8* (47), 7384–7389. <https://doi.org/10.1039/c7py01612c>.
- (49) Vollmer, M. S.; Clark, T. D.; Steinem, C.; Ghadiri, M. R. Photoswitchable Hydrogen-Bonding in Self-Organized Cylindrical Peptide Systems. *Angew. Chemie - Int. Ed.* **1999**, *38* (11), 1598–1601. [https://doi.org/10.1002/\(SICI\)1521-3773\(19990601\)38:11<1598::AID-ANIE1598>3.0.CO;2-J](https://doi.org/10.1002/(SICI)1521-3773(19990601)38:11<1598::AID-ANIE1598>3.0.CO;2-J).
- (50) Lucas, L. N.; Van Esch, J.; Kellogg, R. M.; Feringa, B. L. Photocontrolled Self-Assembly of Molecular Switches. *Chem. Commun.* **2001**, No. 8, 759–760. <https://doi.org/10.1039/b101231m>.
- (51) Yagai, S.; Iwai, K.; Yamauchi, M.; Karatsu, T.; Kitamura, A.; Uemura, S.; Morimoto, M.; Wang, H.; Würthner, F. Photocontrol over Self-Assembled Nanostructures of π - π Stacked Dyes Supported by the Parallel Conformer of Diarylethene. *Angew. Chemie - Int. Ed.* **2014**, *53* (10), 2602–2606.

- <https://doi.org/10.1002/anie.201310773>.
- (52) Li, L. S.; Jiang, H.; Messmore, B. W.; Bull, S. R.; Stupp, S. I. A Torsional Strain Mechanism to Tune Pitch in Supramolecular Helices. *Angew. Chemie - Int. Ed.* **2007**, *46* (31), 5873–5876. <https://doi.org/10.1002/anie.200701328>.
- (53) Fredy, J. W.; Méndez-Ardoy, A.; Kwangmettata, S.; Bochicchio, D.; Matt, B.; Stuart, M. C. A.; Huskens, J.; Katsonis, N.; Pavan, G. M.; Kudernac, T. Molecular Photoswitches Mediating the Strain-Driven Disassembly of Supramolecular Tubules. *Proc. Natl. Acad. Sci.* **2017**, 201711184. <https://doi.org/10.1073/pnas.1711184114>.
- (54) Weyandt, E.; Ter Huurne, G. M.; Vantomme, G.; Markvoort, A. J.; Palmans, A. R. A.; Meijer, E. W. Photodynamic Control of the Chain Length in Supramolecular Polymers: Switching an Intercalator into a Chain Capper. *J. Am. Chem. Soc.* **2020**, *142* (13), 6295–6303. <https://doi.org/10.1021/jacs.0c00858>.
- (55) Segarra-Maset, M. D.; Nebot, V. J.; Miravet, J. F.; Escuder, B. Control of Molecular Gelation by Chemical Stimuli. *Chem. Soc. Rev.* **2013**, *42* (17), 7086–7098. <https://doi.org/10.1039/c2cs35436e>.
- (56) Méndez-Ardoy, A.; Granja, J. R.; Montenegro, J. PH-Triggered Self-Assembly and Hydrogelation of Cyclic Peptide Nanotubes Confined in Water Micro-Droplets. *Nanoscale Horizons* **2018**. <https://doi.org/10.1039/C8NH00009C>.
- (57) Morris, K. L.; Chen, L.; Raeburn, J.; Sellick, O. R.; Cotanda, P.; Paul, A.; Griffiths, P. C.; King, S. M.; O'Reilly, R. K.; Serpell, L. C.; Adams, D. J. Chemically Programmed Self-Sorting of Gelator Networks. *Nat. Commun.* **2013**, *4* (1), 1480. <https://doi.org/10.1038/ncomms2499>.
- (58) Draper, E. R.; Eden, E. G. B.; McDonald, T. O.; Adams, D. J. Spatially Resolved Multicomponent Gels. *Nat. Chem.* **2015**, *7* (10), 848–852. <https://doi.org/10.1038/nchem.2347>.
- (59) Boekhoven, J.; Poolman, J. M.; Maity, C.; Li, F.; Van Der Mee, L.; Minkenberg, C. B.; Mendes, E.; Van Esch, J. H.; Eelkema, R. Catalytic Control over Supramolecular Gel Formation. *Nat. Chem.* **2013**, *5* (5), 433–437. <https://doi.org/10.1038/nchem.1617>.
- (60) Chen, J.; Wu, W.; McNeil, A. J. Detecting a Peroxide-Based Explosive via Molecular Gelation. *Chem. Commun.* **2012**, *48* (58), 7310–7312. <https://doi.org/10.1039/c2cc33486k>.
- (61) Krieg, E.; Shirman, E.; Weissman, H.; Shimoni, E.; Wolf, S. G.; Pinkas, I.; Rybtchinski, B. Supramolecular Gel Based on a Perylene Diimide Dye: Multiple Stimuli Responsiveness, Robustness, and Photofunction. *J. Am. Chem. Soc.* **2009**, *131* (40), 14365–14373. <https://doi.org/10.1021/ja903938g>.
- (62) Foster, J. A.; Piepenbrock, M. O. M.; Lloyd, G. O.; Clarke, N.; Howard, J. A. K.; Steed, J. W. Anion-Switchable Supramolecular Gels for Controlling Pharmaceutical Crystal Growth. *Nat. Chem.* **2010**, *2* (12), 1037–1043. <https://doi.org/10.1038/nchem.859>.
- (63) Rodríguez-Llansola, F.; Miravet, J. F.; Escuder, B. A Supramolecular Hydrogel as a Reusable Heterogeneous Catalyst for the Direct Aldol Reaction. *Chem. Commun.* **2009**, No. 47, 7303–7305.

- <https://doi.org/10.1039/b916250j>.
- (64) Rodríguez-Llansola, F.; Miravet, J. F.; Escuder, B. Aldehyde Responsive Supramolecular Hydrogels: Towards Biomarker-Specific Delivery Systems. *Chem. Commun.* **2011**, 47 (16), 4706–4708. <https://doi.org/10.1039/c1cc10640f>.
- (65) Korevaar, P. A.; George, S. J.; Markvoort, A. J.; Smulders, M. M. J.; Hilbers, P. A. J.; Schenning, A. P. H. J.; De Greef, T. F. A.; Meijer, E. W. Pathway Complexity in Supramolecular Polymerization. *Nature* **2012**, 481 (7382), 492–496. <https://doi.org/10.1038/nature10720>.
- (66) Aliprandi, A.; Mauro, M.; De Cola, L. Controlling and Imaging Biomimetic Self-Assembly. *Nat. Chem.* **2016**, 8 (1), 10–15. <https://doi.org/10.1038/nchem.2383>.
- (67) Ogi, S.; Sugiyasu, K.; Manna, S.; Samitsu, S.; Takeuchi, M. Living Supramolecular Polymerization Realized through a Biomimetic Approach. *Nat. Chem.* **2014**, 6 (3), 188–195. <https://doi.org/10.1038/nchem.1849>.
- (68) Fukui, T.; Kawai, S.; Fujinuma, S.; Matsushita, Y.; Yasuda, T.; Sakurai, T.; Seki, S.; Takeuchi, M.; Sugiyasu, K. Control over Differentiation of a Metastable Supramolecular Assembly in One and Two Dimensions. *Nat. Chem.* **2017**, 9 (5), 493–499. <https://doi.org/10.1038/nchem.2684>.
- (69) Kang, J.; Miyajima, D.; Mori, T.; Inoue, Y.; Itoh, Y.; Aida, T. A Rational Strategy for the Realization of Chain-Growth Supramolecular Polymerization. *Science* **2015**, 347 (6222), 646–651. <https://doi.org/10.1126/science.aaa4249>.
- (70) Haedler, A. T.; Meskers, S. C. J.; Zha, R. H.; Kivala, M.; Schmidt, H. W.; Meijer, E. W. Pathway Complexity in the Enantioselective Self-Assembly of Functional Carbonyl-Bridged Triarylamine Trisamides. *J. Am. Chem. Soc.* **2016**, 138 (33), 10539–10545. <https://doi.org/10.1021/jacs.6b05184>.
- (71) Tidhar, Y.; Weissman, H.; Wolf, S. G.; Gulino, A.; Rybtchinski, B. Pathway-Dependent Self-Assembly of Perylene Diimide/Peptide Conjugates in Aqueous Medium. *Chem. - A Eur. J.* **2011**, 17 (22), 6068–6075. <https://doi.org/10.1002/chem.201003419>.
- (72) Amabilino, D. B.; Smith, D. K.; Steed, J. W. Supramolecular Materials. *Chem. Soc. Rev.* **2017**, 46 (9), 2404–2420. <https://doi.org/10.1039/c7cs00163k>.
- (73) Vigier-Carrière, C.; Boulmedais, F.; Schaaf, P.; Jierry, L. Surface-Assisted Self-Assembly Strategies Leading to Supramolecular Hydrogels. *Angew. Chemie - Int. Ed.* **2018**, 57 (6), 1448–1456. <https://doi.org/10.1002/anie.201708629>.
- (74) Ziemecka, I.; Koper, G. J. M.; Olive, A. G. L.; Van Esch, J. H. Chemical-Gradient Directed Self-Assembly of Hydrogel Fibers. *Soft Matter* **2013**, 9 (5), 1556–1561. <https://doi.org/10.1039/c2sm27095a>.
- (75) Olive, A. G. L.; Abdullah, N. H.; Ziemecka, I.; Mendes, E.; Eelkema, R.; Van Esch, J. H. Spatial and Directional Control over Self-Assembly Using Catalytic Micropatterned Surfaces. *Angew. Chemie - Int. Ed.* **2014**, 53 (16), 4132–4136. <https://doi.org/10.1002/anie.201310776>.
- (76) Maity, C.; Hendriksen, W. E.; Van Esch, J. H.; Eelkema, R. Spatial Structuring of a Supramolecular

- Hydrogel by Using a Visible-Light Triggered Catalyst. *Angew. Chemie - Int. Ed.* **2015**, *54* (3), 998–1001. <https://doi.org/10.1002/anie.201409198>.
- (77) Johnson, E. K.; Adams, D. J.; Cameron, P. J. Directed Self-Assembly of Dipeptides to Form Ultrathin Hydrogel Membranes. *J. Am. Chem. Soc.* **2010**, *132* (14), 5130–5136. <https://doi.org/10.1021/ja909579p>.
- (78) Johnson, E. K.; Chen, L.; Kubiak, P. S.; McDonald, S. F.; Adams, D. J.; Cameron, P. J. Surface Nucleated Growth of Dipeptide Fibres. *Chem. Commun.* **2013**, *49* (77), 8698–8700. <https://doi.org/10.1039/c3cc44738c>.
- (79) Raeburn, J.; Alston, B.; Kroeger, J.; McDonald, T. O.; Howse, J. R.; Cameron, P. J.; Adams, D. J. Electrochemically-Triggered Spatially and Temporally Resolved Multi-Component Gels. *Mater. Horizons* **2014**, *1* (2), 241–246. <https://doi.org/10.1039/c3mh00150d>.
- (80) Williams, R. J.; Smith, A. M.; Collins, R.; Hodson, N.; Das, A. K.; Ulijn, R. V. Enzyme-Assisted Self-Assembly under Thermodynamic Control. *Nat. Nanotechnol.* **2009**, *4* (1), 19–24. <https://doi.org/10.1038/nnano.2008.378>.
- (81) Conte, M. P.; Lau, K. H. A.; Ulijn, R. V. Biocatalytic Self-Assembly Using Reversible and Irreversible Enzyme Immobilization. *ACS Appl. Mater. Interfaces* **2017**, *9* (4), 3266–3271. <https://doi.org/10.1021/acsami.6b13162>.
- (82) Méndez-Ardoy, A.; Bayón-Fernández, A.; Yu, Z.; Abell, C.; Granja, J. R.; Montenegro, J. Spatially Controlled Supramolecular Polymerization of Peptide Nanotubes by Microfluidics. *Angew. Chemie - Int. Ed.* **2020**, *59* (17), 6902–6908. <https://doi.org/10.1002/anie.202000103>.
- (83) Ashkenasy, G.; Hermans, T. M.; Otto, S.; Taylor, A. F. Systems Chemistry. *Chem. Soc. Rev.* **2017**, *46* (9), 2543–2554. <https://doi.org/10.1039/C7CS00117G>.
- (84) van Rossum, S. A. P.; Tena-Solsona, M.; van Esch, J. H.; Eelkema, R.; Boekhoven, J. Dissipative Out-of-Equilibrium Assembly of Man-Made Supramolecular Materials. *Chem. Soc. Rev.* **2017**, *46*, 5519–5535. <https://doi.org/10.1039/C7CS00246G>.
- (85) Merindol, R.; Walther, A. Materials Learning from Life: Concepts for Active, Adaptive and Autonomous Molecular Systems. *Chem. Soc. Rev.* **2017**, *46*, 5588–5619. <https://doi.org/10.1039/C6CS00738D>.
- (86) Leira-Iglesias, J.; Tassoni, A.; Adachi, T.; Stich, M.; Hermans, T. M. Oscillations, Travelling Fronts and Patterns in a Supramolecular System. *Nat. Nanotechnol.* **2018**, *13* (November), 1021–1028. <https://doi.org/10.1038/s41565-018-0270-4>.
- (87) Green, L. N.; Subramanian, H. K. K.; Mardanlou, V.; Kim, J.; Hariadi, R. F.; Franco, E. Autonomous Dynamic Control of DNA Nanostructure Self-Assembly. *Nat. Chem.* **2019**. <https://doi.org/10.1038/s41557-019-0251-8>.
- (88) Agarwal, S.; Franco, E. Enzyme-Driven Assembly and Disassembly of Hybrid DNA-RNA Nanotubes. *J. Am. Chem. Soc.* **2019**, *141* (19), 7831–7841. <https://doi.org/10.1021/jacs.9b01550>.

- (89) te Brinke, E.; Groen, J.; Herrmann, A.; Heus, H. A.; Rivas, G.; Spruijt, E.; Huck, W. T. S. Dissipative Adaptation in Driven Self-Assembly Leading to Self-Dividing Fibrils. *Nat. Nanotechnol.* **2018**, *13* (9), 849–855. <https://doi.org/10.1038/s41565-018-0192-1>.
- (90) Singh, N.; Formon, G. J. M.; De Piccoli, S.; Hermans, T. M. Devising Synthetic Reaction Cycles for Dissipative Nonequilibrium Self-Assembly. *Adv. Mater.* **2020**, *32* (20), 1906834. <https://doi.org/10.1002/adma.201906834>.
- (91) Boekhoven, J.; Brizard, A. M.; Kowligi, K. N. K.; Koper, G. J. M.; Eelkema, R.; Van Esch, J. H. Dissipative Self-Assembly of a Molecular Gelator by Using a Chemical Fuel. *Angew. Chemie - Int. Ed.* **2010**, *49* (28), 4825–4828. <https://doi.org/10.1002/anie.201001511>.
- (92) Boekhoven, J.; Hendriksen, W. E.; Koper, G. J. M.; Eelkema, R.; Van Esch, J. H. Transient Assembly of Active Materials Fueled by a Chemical Reaction. *Science* **2015**, *349* (6252), 1075–1079. <https://doi.org/10.1126/science.aac6103>.
- (93) Van Ravensteijn, B. G. P.; Hendriksen, W. E.; Eelkema, R.; Van Esch, J. H.; Kegel, W. K. Fuel-Mediated Transient Clustering of Colloidal Building Blocks. *J. Am. Chem. Soc.* **2017**, *139* (29), 9763–9766. <https://doi.org/10.1021/jacs.7b03263>.
- (94) Dambeniaks, A. K.; Vu, P. H. Q.; Fyles, T. M. Dissipative Assembly of a Membrane Transport System. *Chem. Sci.* **2014**, *5* (9), 3396–3403. <https://doi.org/10.1039/c4sc01258e>.
- (95) Wood, C. S.; Browne, C.; Wood, D. M.; Nitschke, J. R. Fuel-Controlled Reassembly of Metal-Organic Architectures. *ACS Cent. Sci.* **2015**, *1* (9), 504–509. <https://doi.org/10.1021/acscentsci.5b00279>.
- (96) Tena-Solsona, M.; Rieß, B.; Grötsch, R. K.; Löhrer, F. C.; Wanzke, C.; Käs Dorf, B.; Bausch, A. R.; Müller-Buschbaum, P.; Lieleg, O.; Boekhoven, J. Non-Equilibrium Dissipative Supramolecular Materials with a Tunable Lifetime. *Nat. Commun.* **2017**, *8* (May), 15895. <https://doi.org/10.1038/ncomms15895>.
- (97) Tena-Solsona, M.; Wanzke, C.; Riess, B.; Bausch, A. R.; Boekhoven, J. Self-Selection of Dissipative Assemblies Driven by Primitive Chemical Reaction Networks. *Nat. Commun.* **2018**, *9* (1), 1–8. <https://doi.org/10.1038/s41467-018-04488-y>.
- (98) Rieß, B.; Wanzke, C.; Tena-Solsona, M.; Grötsch, R. K.; Maity, C.; Boekhoven, J. Dissipative Assemblies That Inhibit Their Deactivation. *Soft Matter* **2018**, *14* (23), 4852–4859. <https://doi.org/10.1039/c8sm00822a>.
- (99) Grötsch, R. K.; Wanzke, C.; Speckbacher, M.; Angl, A.; Rieger, B.; Boekhoven, J. Pathway Dependence in the Fuel-Driven Dissipative Self-Assembly of Nanoparticles. *J. Am. Chem. Soc.* **2019**. <https://doi.org/10.1021/jacs.9b02004>.
- (100) Kariyawasam, L. S.; Hartley, C. S. Dissipative Assembly of Aqueous Carboxylic Acid Anhydrides Fueled by Carbodiimides. *J. Am. Chem. Soc.* **2017**, *139* (34), 11949–11955. <https://doi.org/10.1021/jacs.7b06099>.
- (101) Grötsch, R. K.; Angl, A.; Mideksa, Y. G.; Wanzke, C.; Tena-Solsona, M.; Feige, M. J.; Rieger, B.; Boekhoven,

- J. Dissipative Self-Assembly of Photoluminescent Silicon Nanocrystals. *Angew. Chemie - Int. Ed.* **2018**, *57* (44), 14608–14612. <https://doi.org/10.1002/anie.201807937>.
- (102) Zhang, B.; Jayalath, I. M.; Ke, J.; Sparks, J. L.; Hartley, C. S.; Konkolewicz, D. Chemically Fueled Covalent Crosslinking of Polymer Materials. *Chem. Commun.* **2019**, *55* (14), 2086–2089. <https://doi.org/10.1039/c8cc09823a>.
- (103) Wanzke, C.; Jussupow, A.; Kohler, F.; Dietz, H.; Kaila, V. R. I.; Boekhoven, J. Dynamic Vesicles Formed By Dissipative Self-Assembly. *ChemSystemsChem* **2020**, *2* (1). <https://doi.org/10.1002/syst.201900044>.
- (104) Panja, S.; Dietrich, B.; Adams, D. J. Chemically Fuelled Self-Regulating Gel-to-Gel Transition. *ChemSystemsChem* **2020**, *2* (1). <https://doi.org/10.1002/syst.201900038>.
- (105) Wanzke, C.; Tena-Solsona, M.; Rieß, B.; Tebcharani, L.; Boekhoven, J. Active Droplets in a Hydrogel Release Drugs with a Constant and Tunable Rate. *Mater. Horizons* **2020**, *7* (5), 1397–1403. <https://doi.org/10.1039/c9mh01822k>.
- (106) Donau, C.; Späth, F.; Sosson, M.; Kriebisch, B.; Schnitter, F.; Tena-Solsona, M.; Kang, H.-S.; Salibi, E.; Sattler, M.; Mutschler, H.; Boekhoven, J. Active Coacervate Droplets as a Model for Membraneless Organelles and a Platform Towards Synthetic Life. *ChemRxiv* **2020**. <https://doi.org/10.26434/CHEMRXIV.11648598.V1>.
- (107) Hossain, M. M.; Atkinson, J. L.; Hartley, C. S. Dissipative Assembly of Macrocycles Comprising Multiple Transient Bonds. *Angew. Chemie - Int. Ed.* **2020**, anie.202001523. <https://doi.org/10.1002/anie.202001523>.
- (108) Colomer, I.; Morrow, S. M.; Fletcher, S. P. A Transient Self-Assembling Self-Replicator. *Nat. Commun.* **2018**, *9* (1), 1–6. <https://doi.org/10.1038/s41467-018-04670-2>.
- (109) Bal, S.; Das, K.; Ahmed, S.; Das, D. Chemically Fueled Dissipative Self-Assembly That Exploits Cooperative Catalysis. *Angew. Chemie - Int. Ed.* **2019**, *58* (1), 244–247. <https://doi.org/10.1002/anie.201811749>.
- (110) Jain, A.; Dhiman, S.; Dhayani, A.; Vemula, P. K.; George, S. J. Chemical Fuel-Driven Living and Transient Supramolecular Polymerization. *Nat. Commun.* **2019**, *10* (1), 1–9. <https://doi.org/10.1038/s41467-019-08308-9>.
- (111) Morrow, S. M.; Colomer, I.; Fletcher, S. P. A Chemically Fuelled Self-Replicator. *Nat. Commun.* **2019**, *10* (1), 1–9. <https://doi.org/10.1038/s41467-019-08885-9>.
- (112) Maiti, S.; Fortunati, I.; Ferrante, C.; Scrimin, P.; Prins, L. J. Dissipative Self-Assembly of Vesicular Nanoreactors. *Nat. Chem.* **2016**, *8* (7), 725–731. <https://doi.org/10.1038/nchem.2511>.
- (113) Debnath, S.; Roy, S.; Ulijn, R. V. Peptide Nanofibers with Dynamic Instability through Nonequilibrium Biocatalytic Assembly. *J. Am. Chem. Soc.* **2013**, *135* (45), 16789–16792. <https://doi.org/10.1021/ja4086353>.
- (114) Pappas, C. G.; Sasselli, I. R.; Ulijn, R. V. Biocatalytic Pathway Selection in Transient Tripeptide Nanostructures. *Angew. Chemie - Int. Ed.* **2015**, *54* (28), 8119–8123. <https://doi.org/10.1002/anie.201500867>.

- (115) Sorrenti, A.; Leira-Iglesias, J.; Sato, A.; Hermans, T. M. Non-Equilibrium Steady States in Supramolecular Polymerization. *Nat. Commun.* **2017**, *8* (May), 15899. <https://doi.org/10.1038/ncomms15899>.
- (116) Heuser, T.; Steppert, A. K.; Molano Lopez, C.; Zhu, B.; Walther, A. Generic Concept to Program the Time Domain of Self-Assemblies with a Self-Regulation Mechanism. *Nano Lett.* **2015**, *15* (4), 2213–2219. <https://doi.org/10.1021/nl5039506>.
- (117) Heinen, L.; Heuser, T.; Steinschulte, A.; Walther, A. Antagonistic Enzymes in a Biocatalytic PH Feedback System Program Autonomous DNA Hydrogel Life Cycles. *Nano Lett.* **2017**, *17* (8), 4989–4995. <https://doi.org/10.1021/acs.nanolett.7b02165>.
- (118) Leira-Iglesias, J.; Sorrenti, A.; Sato, A.; Dunne, P. A.; Hermans, T. M. Supramolecular Pathway Selection of Perylenediimides Mediated by Chemical Fuels. *Chem. Commun.* **2016**, *52* (58), 9009–9012. <https://doi.org/10.1039/C6CC01192F>.
- (119) Wojciechowski, J. P.; Martin, A. D.; Thordarson, P. Kinetically Controlled Lifetimes in Redox-Responsive Transient Supramolecular Hydrogels. *J. Am. Chem. Soc.* **2018**, *140* (8), 2869–2874. <https://doi.org/10.1021/jacs.7b12198>.
- (120) Rikken, R. S. M.; Nolte, R. J. M.; Maan, J. C.; van Hest, J. C. M.; Wilson, D. A.; Christianen, P. C. M. Manipulation of Micro- and Nanostructure Motion with Magnetic Fields. *Soft Matter* **2014**, *10* (9), 1295–1308. <https://doi.org/10.1039/C3SM52294F>.
- (121) Coey, J. M. D.; Rhen, F. M. F.; Dunne, P.; McMurry, S. The Magnetic Concentration Gradient Force-Is It Real? *J. Solid State Electrochem.* **2007**, *11* (6), 711–717. <https://doi.org/10.1007/s10008-006-0254-4>.
- (122) Shevkoplyas, S. S.; Siegel, A. C.; Westervelt, R. M.; Prentiss, M. G.; Whitesides, G. M. The Force Acting on a Superparamagnetic Bead Due to an Applied Magnetic Field. *Lab Chip* **2007**, *7* (10), 1294–1302. <https://doi.org/10.1039/b705045c>.
- (123) Dunne, P.; Adachi, T.; Dev, A. A.; Sorrenti, A.; Giacchetti, L.; Bonnin, A.; Bourdon, C.; Mangin, P. H.; Coey, J. M. D.; Doudin, B.; Hermans, T. M. Liquid Flow and Control without Solid Walls. *Nature* **2020**, *581* (7806), 58–62. <https://doi.org/10.1038/s41586-020-2254-4>.
- (124) Lim, J.; Lanni, C.; Everts, E. R.; Lanni, F.; Tilton, R. D.; Majetich, S. A. Magnetophoresis of Nanoparticles. *ACS Nano* **2011**, *5* (1), 217–226. <https://doi.org/10.1021/nn102383s>.
- (125) Dill, K. A.; Bromberg, S. *Molecular Driving Forces: Statistical Thermodynamics in Biology, Chemistry, Physics, and Nanoscience*, 2nd ed.; Garland Science: London ; New York, 2011.
- (126) Berg-Sørensen, K.; Flyvbjerg, H. The Colour of Thermal Noise in Classical Brownian Motion: A Feasibility Study of Direct Experimental Observation. *New J. Phys.* **2005**, *7*, 38–38. <https://doi.org/10.1088/1367-2630/7/1/038>.
- (127) Kubo, R.; Toda, M.; Hashitsume, N. *Statistical Physics II*; Springer Series in Solid-State Sciences; Springer Berlin Heidelberg: Berlin, Heidelberg, 1991; Vol. 31. <https://doi.org/10.1007/978-3-642-58244-8>.

- (128) Hejazian, M.; Li, W.; Nguyen, N. T. Lab on a Chip for Continuous-Flow Magnetic Cell Separation. *Lab Chip* **2015**, *15* (4), 959–970. <https://doi.org/10.1039/c4lc01422g>.
- (129) Shannon, R. D. Revised Effective Ionic Radii and Systematic Studies of Interatomic Distances in Halides and Chalcogenides. *Acta Crystallogr. Sect. A* **1976**, *32* (5), 751–767. <https://doi.org/10.1107/S0567739476001551>.
- (130) Kittel, C. *Introduction to Solid State Physics*, 8th ed.; Wiley: Hoboken, NJ, 2005.
- (131) Atkins, P. W.; Paula, J. de. *Physical Chemistry*; Oxford University Press: Oxford; New York, 2006.
- (132) Shklyarevskiy, I. O.; Jonkheijm, P.; Christianen, P. C. M.; Schenning, A. P. H. J.; Meijer, E. W.; Henze, O.; Kilbinger, A. F. M.; Feast, W. J.; Del Guerzo, A.; Desvergne, J. P.; Maan, J. C. Magnetic Deformation of Self-Assembled Sexithiophene Spherical Nanocapsules. *J. Am. Chem. Soc.* **2005**, *127* (4), 1112–1113. <https://doi.org/10.1021/ja0431096>.
- (133) Glucksman, M. J.; Hay, R. D.; Makowski, L. X-Ray Diffraction from Magnetically Oriented Solutions of Macromolecular Assemblies. *Science* **1986**, *231* (4743), 1273–1276. <https://doi.org/10.1126/science.3945822>.
- (134) Kimura, T. Study of the Effect of Magnetic Fields on Polymeric Materials and Its Application. *Polym. J.* **2003**, *35* (11), 823–843. <https://doi.org/10.1295/polymj.35.823>.
- (135) Shklyarevskiy, I. O.; Jonkheijm, P.; Christianen, P. C. M.; Schenning, A. P. H. J.; Del Guerzo, A.; Desvergne, J. P.; Meijer, E. W.; Maan, J. C. Magnetic Alignment of Self-Assembled Anthracene Organogel Fibers. *Langmuir* **2005**, *21* (6), 2108–2112. <https://doi.org/10.1021/la047166o>.
- (136) Löwik, D. W. P. M.; Shklyarevskiy, I. O.; Ruizendaal, L.; Christianen, P. C. M.; Maan, J. C.; Van Hest, J. C. M. A Highly Ordered Material from Magnetically Aligned Peptide Amphiphile Nanofiber Assemblies. *Adv. Mater.* **2007**, *19* (9), 1191–1195. <https://doi.org/10.1002/adma.200602295>.
- (137) Draper, E. R.; Wallace, M.; Honecker, D.; Adams, D. J. Aligning Self-Assembled Perylene Bisimides in a Magnetic Field. *Chem. Commun.* **2018**, *54* (78), 10977–10980. <https://doi.org/10.1039/c8cc05968c>.
- (138) Beck, P.; Liebi, M.; Kohlbrecher, J.; Ishikawa, T.; Riiegger, H.; Zepik, H.; Fischer, P.; Walde, P.; Windhab, E. Magnetic Field Alignable Domains in Phospholipid Vesicle Membranes Containing Lanthanides. *J. Phys. Chem. B* **2010**, *114* (1), 174–186. <https://doi.org/10.1021/jp907442e>.
- (139) Boulon, M. E.; Cucinotta, G.; Luzon, J.; Degl'Innocenti, C.; Perfetti, M.; Bernot, K.; Calvez, G.; Caneschi, A.; Sessoli, R. Magnetic Anisotropy and Spin-Parity Effect along the Series of Lanthanide Complexes with DOTA. *Angew. Chemie - Int. Ed.* **2013**, *52* (1), 350–354. <https://doi.org/10.1002/anie.201205938>.
- (140) Brown, P.; Butts, C. P.; Eastoe, J. Stimuli-Responsive Surfactants. *Soft Matter* **2013**, *9* (8), 2365–2374. <https://doi.org/10.1039/c3sm27716j>.
- (141) Brown, P.; Alan Hatton, T.; Eastoe, J. Magnetic Surfactants. *Curr. Opin. Colloid Interface Sci.* **2015**, *20* (3), 140–150. <https://doi.org/10.1016/j.cocis.2015.08.002>.

- (142) Brown, P.; Bushmelev, A.; Butts, C. P.; Cheng, J.; Eastoe, J.; Grillo, I.; Heenan, R. K.; Schmidt, A. M. Magnetic Control over Liquid Surface Properties with Responsive Surfactants. *Angew. Chemie - Int. Ed.* **2012**, *51* (10), 2414–2416. <https://doi.org/10.1002/anie.201108010>.
- (143) Brown, P.; Bushmelev, A.; Butts, C. P.; Eloi, J. C.; Grillo, I.; Baker, P. J.; Schmidt, A. M.; Eastoe, J. Properties of New Magnetic Surfactants. *Langmuir* **2013**, *29* (10), 3246–3251. <https://doi.org/10.1021/la400113r>.
- (144) Brown, P.; Butts, C. P.; Cheng, J.; Eastoe, J.; Russell, C. A.; Smith, G. N. Magnetic Emulsions with Responsive Surfactants. *Soft Matter* **2012**, *8* (29), 7545. <https://doi.org/10.1039/c2sm26077h>.
- (145) Brown, P.; Khan, A. M.; Armstrong, J. P. K.; Perriman, A. W.; Butts, C. P.; Eastoe, J. Magnetizing DNA and Proteins Using Responsive Surfactants. *Adv. Mater.* **2012**, *24* (46), 6244–6247. <https://doi.org/10.1002/adma.201202685>.
- (146) Singh, G.; Chan, H.; Baskin, A.; Gelman, E.; Reprin, N.; Král, P.; Klajn, R. Self-Assembly of Magnetite Nanocubes into Helical Superstructures. *Science* **2014**, *345* (6201), 1149–1153. <https://doi.org/10.1126/science.1254132>.
- (147) Mehdizadeh Taheri, S.; Michaelis, M.; Friedrich, T.; Förster, B.; Drechsler, M.; Römer, F. M.; Bösecke, P.; Narayanan, T.; Weber, B.; Rehberg, I.; Rosenfeldt, S.; Förster, S. Self-Assembly of Smallest Magnetic Particles. *Proc. Natl. Acad. Sci.* **2015**, *112* (47), 14484–14489. <https://doi.org/10.1073/pnas.1511443112>.
- (148) Santos, P. J.; Macfarlane, R. J. Reinforcing Supramolecular Bonding with Magnetic Dipole Interactions to Assemble Dynamic Nanoparticle Superlattices. *J. Am. Chem. Soc.* **2020**, *142* (3), 1170–1174. <https://doi.org/10.1021/jacs.9b11476>.
- (149) Hoffmann, C.; Mazari, E.; Lallet, S.; Le Borgne, R.; Marchi, V.; Gosse, C.; Gueroui, Z. Spatiotemporal Control of Microtubule Nucleation and Assembly Using Magnetic Nanoparticles. *Nat. Nanotechnol.* **2013**, *8* (3), 199–205. <https://doi.org/10.1038/nnano.2012.246>.
- (150) Li, T. L.; Wang, Z.; You, H.; Ong, Q.; Varanasi, V. J.; Dong, M.; Lu, B.; Paşca, S. P.; Cui, B. Engineering a Genetically Encoded Magnetic Protein Crystal. *Nano Lett.* **2019**, *19* (10), 6955–6963. <https://doi.org/10.1021/acs.nanolett.9b02266>.
- (151) Yang, X.; Tschulik, K.; Uhlemann, M.; Odenbach, S.; Eckert, K. Enrichment of Paramagnetic Ions from Homogeneous Solutions in Inhomogeneous Magnetic Fields. *J. Phys. Chem. Lett.* **2012**, *3* (23), 3559–3564. <https://doi.org/10.1021/jz301561q>.
- (152) Pulko, B.; Yang, X.; Lei, Z.; Odenbach, S.; Eckert, K. Magnetic Separation of Dy(III) Ions from Homogeneous Aqueous Solutions. *Appl. Phys. Lett.* **2014**, *105* (23), 232407. <https://doi.org/10.1063/1.4903794>.
- (153) Franczak, A.; Binnemans, K.; Jan Fransaer, J. F. Magnetomigration of Rare-Earth Ions in Inhomogeneous Magnetic Fields. *Phys. Chem. Chem. Phys.* **2016**, *18* (39), 27342–27350. <https://doi.org/10.1039/C6CP02575G>.

- (154) Fujiwara, M.; Kodoi, D.; Duan, W.; Tanimoto, Y. Separation of Transition Metal Ions in an Inhomogeneous Magnetic Field. *J. Phys. Chem. B* **2001**, *105* (17), 3344–3345. <https://doi.org/10.1021/jp003562d>.
- (155) Fujiwara, M.; Chie, K.; Sawai, J.; Shimizu, D.; Tanimoto, Y. On the Movement of Paramagnetic Ions in an Inhomogeneous Magnetic Field. *J. Phys. Chem. B* **2004**, *108* (11), 3531–3534. <https://doi.org/10.1021/jp0303523>.
- (156) Fujiwara, M.; Mitsuda, K.; Tanimoto, Y. Movement and Diffusion of Paramagnetic Ions in a Magnetic Field. *J. Phys. Chem. B* **2006**, *110* (28), 13965–13969. <https://doi.org/10.1021/jp061482p>.
- (157) Gorobets, O. Y.; Gorobets, Y. I.; Bondar, I. A.; Legenkiy, Y. A. Quasi-Stationary Heterogeneous States of Electrolyte at Electrodeposition and Etching Process in a Gradient Magnetic Field of a Magnetized Ferromagnetic Ball. *J. Magn. Magn. Mater.* **2013**, *330*, 76–80. <https://doi.org/10.1016/j.jmmm.2012.10.015>.
- (158) Gorobets, O. Y.; Gorobets, Y. I.; Rospotniuk, V. P.; Legenkiy, Y. A. Electric Cell Voltage at Etching and Deposition of Metals under an Inhomogeneous Constant Magnetic Field. *Condens. Matter Phys.* **2014**, *17* (4), 43401. <https://doi.org/10.5488/CMP.17.43401>.
- (159) Gorobets, O. Y.; Gorobets, Y. I.; Rospotniuk, V. P. Magnetophoretic Potential at the Movement of Cluster Products of Electrochemical Reactions in an Inhomogeneous Magnetic Field. *J. Appl. Phys.* **2015**, *118* (7), 073902. <https://doi.org/10.1063/1.4928671>.
- (160) Rodrigues, I. R.; Lukina, L.; Dehaeck, S.; Colinet, P.; Binnemans, K.; Fransaer, J. Magnetomigration of Rare-Earth Ions Triggered by Concentration Gradients. *J. Phys. Chem. Lett.* **2017**, *8* (21), 5301–5305. <https://doi.org/10.1021/acs.jpcllett.7b02226>.
- (161) Butcher, T. A.; Formon, G. J. M.; Dunne, P.; Hermans, T. M.; Ott, F.; Noirez, L.; Coey, J. M. D. Neutron Imaging of Liquid-Liquid Systems Containing Paramagnetic Salt Solutions. *Appl. Phys. Lett.* **2020**, *116* (2), 022405. <https://doi.org/10.1063/1.5135390>.
- (162) Rodrigues, I. R.; Lukina, L.; Dehaeck, S.; Colinet, P.; Binnemans, K.; Fransaer, J. Effect of Magnetic Susceptibility Gradient on the Magnetomigration of Rare-Earth Ions. *J. Phys. Chem. C* **2019**, *123* (37), 23131–23139. <https://doi.org/10.1021/acs.jpcc.9b06706>.
- (163) Lei, Z.; Fritzsche, B.; Eckert, K. Evaporation-Assisted Magnetic Separation of Rare-Earth Ions in Aqueous Solutions. *J. Phys. Chem. C* **2017**, *121* (39), 24576–24587. <https://doi.org/10.1021/acs.jpcc.7b07344>.
- (164) Higgins, R. F.; Cheisson, T.; Cole, B. E.; Manor, B. C.; Carroll, P. J.; Schelter, E. J. Magnetic Field Directed Rare-Earth Separations. *Angew. Chemie - Int. Ed.* **2020**, *59* (5), 1851–1856. <https://doi.org/10.1002/anie.201911606>.
- (165) Schefer, L.; Bulant, A.; Zeder, C.; Saha, A.; Mezzenga, R. Magnetic Control of Macromolecular Conformations in Supramolecular Anionic Polysaccharide-Iron Complexes. *Angew. Chemie - Int. Ed.*

- 2015, 54 (45), 13289–13292. <https://doi.org/10.1002/anie.201506898>.
- (166) Yue, B.; Jin, X.; Zhao, P.; Zhu, M.; Zhu, L. Directed Self-Assembly of Templatable Block Copolymers by Easily Accessible Magnetic Control. *Small* **2019**, 15 (7), 1–7. <https://doi.org/10.1002/smll.201804572>.
- (167) Polarz, S.; Bährle, C.; Landsmann, S.; Klaiber, A. Panoscopic Structures by Hierarchical Cascade Self-Assembly of Inorganic Surfactants with Magnetic Heads Containing Dysprosium Ions. *Angew. Chemie - Int. Ed.* **2013**, 52 (51), 13665–13670. <https://doi.org/10.1002/anie.201303565>.
- (168) Langereis, S.; De Lussanet, Q. G.; Van Genderen, M. H. P.; Backes, W. H.; Meijer, E. W. Multivalent Contrast Agents Based on Gadolinium- Diethylenetriaminepentaacetic Acid-Terminated Poly(Propylene Imine) Dendrimers for Magnetic Resonance Imaging. *Macromolecules* **2004**, 37 (9), 3084–3091. <https://doi.org/10.1021/ma035983+>.
- (169) Yu, X.; Yuan, X.; Zhao, Y.; Ren, L. From Paramagnetic to Superparamagnetic Ionic Liquid/Poly(Ionic Liquid): The Effect of π - π Stacking Interaction. *ACS Macro Lett.* **2019**, 8 (11), 1504–1510. <https://doi.org/10.1021/acsmacrolett.9b00714>.
- (170) Karsenti, E. Self-Organization in Cell Biology: A Brief History. *Nat. Rev. Mol. Cell Biol.* **2008**, 9 (3), 255–262. <https://doi.org/10.1038/nrm2357>.
- (171) Good, M. C.; Zalatan, J. G.; Lim, W. A. Scaffold Proteins: Hubs for Controlling the Flow of Cellular Information. *Science* **2011**, 332 (6030), 680–686. <https://doi.org/10.1126/science.1198701>.
- (172) Agapakis, C. M.; Boyle, P. M.; Silver, P. A. Natural Strategies for the Spatial Optimization of Metabolism in Synthetic Biology. *Nat. Chem. Biol.* **2012**, 8 (6), 527–535. <https://doi.org/10.1038/nchembio.975>.
- (173) Güttinger, S.; Laurell, E.; Kutay, U. Orchestrating Nuclear Envelope Disassembly and Reassembly during Mitosis. *Nat. Rev. Mol. Cell Biol.* **2009**, 10 (3), 178–191. <https://doi.org/10.1038/nrm2641>.
- (174) Tiller, J. C. Increasing the Local Concentration of Drugs by Hydrogel Formation. *Angew. Chemie Int. Ed.* **2003**, 42 (27), 3072–3075. <https://doi.org/10.1002/anie.200301647>.
- (175) Angelerou, M. G. F.; Sabri, A.; Creasey, R.; Angelerou, P.; Marlow, M.; Zelzer, M. Surface-Directed Modulation of Supramolecular Gel Properties. *Chem. Commun.* **2016**, 52 (23), 4298–4300. <https://doi.org/10.1039/c6cc00292g>.
- (176) Liu, Y.; Xu, X.-D.; Chen, J.-X.; Cheng, H.; Zhang, X.-Z.; Zhuo, R.-X. Surface Self-Assembly of N-Fluorenyl-9-Methoxycarbonyl Diphenylalanine on Silica Wafer. *Colloids Surf. B. Biointerfaces* **2011**, 87 (1), 192–197. <https://doi.org/10.1016/j.colsurfb.2011.04.032>.
- (177) Von Gröning, M.; de Feijter, I.; Stuart, M. C. A. A.; Voets, I. K.; Besenius, P. Tuning the Aqueous Self-Assembly of Multistimuli-Responsive Polyanionic Peptide Nanorods. *J. Mater. Chem. B* **2013**, 1 (15), 2008–2012. <https://doi.org/10.1039/c3tb00051f>.
- (178) Spitzer, D.; Rodrigues, L. L.; Straßburger, D.; Mezger, M.; Besenius, P. Tuneable Transient Thermogels Mediated by a PH- and Redox-Regulated Supramolecular Polymerization. *Angew. Chemie - Int. Ed.* **2017**,

- 56 (48), 15461–15465. <https://doi.org/10.1002/anie.201708857>.
- (179) Joon Cho, T.; Zangmeister, R. A.; MacCuspie, R. I.; Patri, A. K.; Hackley, V. A. Newkome-Type Dendron-Stabilized Gold Nanoparticles: Synthesis, Reactivity, and Stability. *Chem. Mater.* **2011**, *23* (10), 2665–2676. <https://doi.org/10.1021/cm200591h>.
- (180) Knowles, T. P. J.; Waudby, C. A.; Devlin, G. L.; Cohen, S. I. A.; Aguzzi, A.; Vendruscolo, M.; Terentjev, E. M.; Welland, M. E.; Dobson, C. M. An Analytical Solution to the Kinetics of Breakable Filament Assembly. *Science* **2009**, *326* (5959), 1533–1537. <https://doi.org/10.1126/science.1178250>.
- (181) Cohen, S. I. A.; Vendruscolo, M.; Welland, M. E.; Dobson, C. M.; Terentjev, E. M.; Knowles, T. P. J. Nucleated Polymerization with Secondary Pathways. I. Time Evolution of the Principal Moments. *J. Chem. Phys.* **2011**, *135* (6). <https://doi.org/10.1063/1.3608916>.
- (182) Cohen, S. I. A.; Vendruscolo, M.; Dobson, C. M.; Knowles, T. P. J. Nucleated Polymerization with Secondary Pathways. II. Determination of Self-Consistent Solutions to Growth Processes Described by Non-Linear Master Equations. *J. Chem. Phys.* **2011**, *135* (6). <https://doi.org/10.1063/1.3608917>.
- (183) Cohen, S. I. A.; Vendruscolo, M.; Dobson, C. M.; Knowles, T. P. J. Nucleated Polymerization with Secondary Pathways. III. Equilibrium Behavior and Oligomer Populations. *J. Chem. Phys.* **2011**, *135* (6). <https://doi.org/10.1063/1.3608918>.
- (184) Cohen, S. I. A.; Cukalevski, R.; Michaels, T. C. T.; Šarić, A.; Törnquist, M.; Vendruscolo, M.; Dobson, C. M.; Buell, A. K.; Knowles, T. P. J.; Linse, S. Distinct Thermodynamic Signatures of Oligomer Generation in the Aggregation of the Amyloid- β Peptide. *Nat. Chem.* **2018**, *10*, 523–532. <https://doi.org/10.1038/s41557-018-0023-x>.
- (185) Baram, J.; Weissman, H.; Rybtchinski, B. Supramolecular Polymer Transformation: A Kinetic Study. *J. Phys. Chem. B* **2014**, *118* (41), 12068–12073. <https://doi.org/10.1021/jp507945t>.
- (186) Krieg, E.; Bastings, M. M. C.; Besenius, P.; Rybtchinski, B. Supramolecular Polymers in Aqueous Media. *Chem. Rev.* **2016**, *116* (4), 2414–2477. <https://doi.org/10.1021/acs.chemrev.5b00369>.
- (187) Atkin, P.; Paula, J. *Physical Chemistry*; 2006. <https://doi.org/10.1039/C1CS15191F>.
- (188) Novák, B.; Tyson, J. J. Design Principles of Biochemical Oscillators. *Nat. Rev. Mol. Cell Biol.* **2008**, *9* (12), 981–991. <https://doi.org/10.1038/nrm2530>.
- (189) Semenov, S. N.; Wong, A. S. Y.; Van Der Made, R. M.; Postma, S. G. J.; Groen, J.; Van Roekel, H. W. H.; De Greef, T. F. A.; Huck, W. T. S. Rational Design of Functional and Tunable Oscillating Enzymatic Networks. *Nat. Chem.* **2015**, *7* (2), 160–165. <https://doi.org/10.1038/nchem.2142>.
- (190) Semenov, S. N.; Kraft, L. J.; Ainla, A.; Zhao, M.; Baghbanzadeh, M.; Campbell, V. E.; Kang, K.; Fox, J. M.; Whitesides, G. M. Autocatalytic, Bistable, Oscillatory Networks of Biologically Relevant Organic Reactions. *Nature* **2016**, *537* (7622), 656–660. <https://doi.org/10.1038/nature19776>.
- (191) Montagne, K.; Plasson, R.; Sakai, Y.; Fujii, T.; Rondelez, Y. Programming an in Vitro DNA Oscillator Using

- a Molecular Networking Strategy. *Mol. Syst. Biol.* **2011**, *7* (1), 466. <https://doi.org/10.1038/msb.2010.120>.
- (192) Fujii, T.; Rondelez, Y. Predator - Prey Molecular Ecosystems. *ACS Nano* **2013**, *7* (1), 27–34. <https://doi.org/10.1021/nn3043572>.
- (193) Van Roekel, H. W. H.; Meijer, L. H. H.; Masroor, S.; Félix Garza, Z. C.; Estévez-Torres, A.; Rondelez, Y.; Zagaris, A.; Peletier, M. A.; Hilbers, P. A. J.; De Greef, T. F. A. Automated Design of Programmable Enzyme-Driven DNA Circuits. *ACS Synth. Biol.* **2015**, *4* (6), 735–745. <https://doi.org/10.1021/sb500300d>.
- (194) Gines, G.; Zadorin, A. S.; Galas, J.-C.; Fujii, T.; Estevez-Torres, A.; Rondelez, Y. Microscopic Agents Programmed by DNA Circuits. *Nat. Nanotechnol.* **2017**, *12* (4), 351–359. <https://doi.org/10.1038/nnano.2016.299>.
- (195) Joesaar, A.; Yang, S.; Bögels, B.; van der Linden, A.; Pieters, P.; Kumar, B. V. V. S. P. V. S. P.; Dalchau, N.; Phillips, A.; Mann, S.; de Greef, T. F. A.; Linden, A. Van Der; Pieters, P.; Kumar, B. V. V. S. P. V. S. P.; Dalchau, N.; Phillips, A.; Mann, S.; Greef, T. F. A. De. DNA-Based Communication in Populations of Synthetic Protocells. *Nat. Nanotechnol.* **2019**. <https://doi.org/10.1038/s41565-019-0399-9>.
- (196) Zadorin, A.; Rondelez, Y.; Gines, G.; Dilhas, V.; Zambrano, A.; Galas, J.-C.; Estevez-Torres, A. Synthesis and Materialization of a Reaction-Diffusion French Flag Pattern. *Nat. Chem.* **2017**, No. May, 1–7. <https://doi.org/10.1038/nchem.2770>.
- (197) de Vries, J. G.; Kellogg, R. M. Reduction of Aldehydes and Ketones by Sodium Dithionite. *J. Org. Chem.* **1980**, *45* (21), 4126–4129. <https://doi.org/10.1021/jo01309a011>.
- (198) Kulkarni, C.; Meijer, E. W.; Palmans, A. R. A. Cooperativity Scale: A Structure-Mechanism Correlation in the Self-Assembly of Benzene-1,3,5-Tricarboxamides. *Acc. Chem. Res.* **2017**, *50* (8), 1928–1936. <https://doi.org/10.1021/acs.accounts.7b00176>.
- (199) Cohen, S. I. A.; Linse, S.; Luheshi, L. M.; Hellstrand, E.; White, D. A.; Rajah, L.; Otzen, D. E.; Vendruscolo, M.; Dobson, C. M.; Knowles, T. P. J. Proliferation of Amyloid-42 Aggregates Occurs through a Secondary Nucleation Mechanism. *Proc. Natl. Acad. Sci.* **2013**, *110* (24), 9758–9763. <https://doi.org/10.1073/pnas.1218402110>.
- (200) Hirst, A. R.; Roy, S.; Arora, M.; Das, A. K.; Hodson, N.; Murray, P.; Marshall, S.; Javid, N.; Sefcik, J.; Boekhoven, J.; Van Esch, J. H.; Santabarbara, S.; Hunt, N. T.; Ulijn, R. V. Biocatalytic Induction of Supramolecular Order. *Nat. Chem.* **2010**, *2* (12), 1089–1094. <https://doi.org/10.1038/nchem.861>.
- (201) Conte, M. P.; Singh, N.; Sasselli, I. R.; Escuder, B.; Ulijn, R. V. Metastable Hydrogels from Aromatic Dipeptides. *Chem. Commun.* **2016**, *52* (96), 13889–13892. <https://doi.org/10.1039/C6CC05821C>.
- (202) Klug, A. From Macromolecules to Biological Assemblies (Nobel Lecture). *Angew. Chemie Int. Ed. English* **1983**, *22* (8), 565–582. <https://doi.org/10.1002/anie.198305653>.
- (203) Wang, S. Q.; Gelbart, W. M.; Ben-Shaul, A. Flow Effects on Micellar Size Distribution. *J. Phys. Chem.* **1990**, *94* (6), 2219–2221. <https://doi.org/10.1021/j100369a001>.

- (204) Sun, J.; Li, Y.; Yan, F.; Liu, C.; Sang, Y.; Tian, F.; Feng, Q.; Duan, P.; Zhang, L.; Shi, X.; Ding, B.; Liu, M. Control over the Emerging Chirality in Supramolecular Gels and Solutions by Chiral Microvortices in Milliseconds. *Nat. Commun.* **2018**, *9* (1), 2599. <https://doi.org/10.1038/s41467-018-05017-7>.
- (205) Bejagam, K. K.; Kulkarni, C.; George, S. J.; Balasubramanian, S. External Electric Field Reverses Helical Handedness of a Supramolecular Columnar Stack. *Chem. Commun.* **2015**, *51* (89), 16049–16052. <https://doi.org/10.1039/c5cc05569e>.
- (206) Ellis, T. K.; Galerne, M.; Armao, J. J.; Osypenko, A.; Martel, D.; Maaloum, M.; Fuks, G.; Gavat, O.; Moulin, E.; Giuseppone, N. Supramolecular Electropolymerization. *Angew. Chemie* **2018**, *130* (48), 15975–15979. <https://doi.org/10.1002/ange.201809756>.
- (207) Sardone, L.; Palermo, V.; Devaux, E.; Credgington, D.; de Loos, M.; Marletta, G.; Cacialli, F.; van Esch, J.; Samorì, P. Electric-Field-Assisted Alignment of Supramolecular Fibers. *Adv. Mater.* **2006**, *18* (10), 1276–1280. <https://doi.org/10.1002/adma.200600269>.
- (208) Prosser, R. S.; Hwang, J. S.; Vold, R. R. Magnetically Aligned Phospholipid Bilayers with Positive Ordering: A New Model Membrane System. *Biophys. J.* **1998**, *74* (5), 2405–2418. [https://doi.org/10.1016/S0006-3495\(98\)77949-4](https://doi.org/10.1016/S0006-3495(98)77949-4).
- (209) Polarz, S.; Bährle, C.; Landsmann, S.; Klaiber, A. Panoramic Structures by Hierarchical Cascade Self-Assembly of Inorganic Surfactants with Magnetic Heads Containing Dysprosium Ions. *Angew. Chemie - Int. Ed.* **2013**, *52* (51), 13665–13670. <https://doi.org/10.1002/anie.201303565>.
- (210) Feijter, I. De; Besenius, P.; Albertazzi, L.; Meijer, E. W.; Palmans, A. R. A.; Voets, I. Mechanistic Control over Morphology: Self-Assembly of a Discotic Amphiphile in Water. *Soft Matter* **2013**, *9*, 10025–10030. <https://doi.org/10.1039/c3sm52104d>.
- (211) Tirado, M. M.; Martínez, C. L.; García de la Torre, J. Comparison of Theories for the Translational and Rotational Diffusion Coefficients of Rod-like Macromolecules. Application to Short DNA Fragments. *J. Chem. Phys.* **1984**, *81*, 2047–2052. <https://doi.org/10.1063/1.447827>.
- (212) Hermans, T. M.; Broeren, M. a C.; Gomopoulos, N.; van der Schoot, P.; van Genderen, M. H. P.; Sommerdijk, N. a J. M.; Fytas, G.; Meijer, E. W. Self-Assembly of Soft Nanoparticles with Tunable Patchiness. *Nat. Nanotechnol.* **2009**, *4* (11), 721–726. <https://doi.org/10.1038/nnano.2009.232>.
- (213) Raper, J. A.; Amal, R. Measurement of Aggregate Fractal Dimensions Using Static Light Scattering. *Part. Part. Syst. Charact.* **1993**, *10* (5), 239–245. <https://doi.org/10.1002/ppsc.19930100505>.
- (214) Mohraz, A.; Moler, D. B.; Ziff, R. M.; Solomon, M. J. Effect of Monomer Geometry on the Fractal Structure of Colloidal Rod Aggregates. *Phys. Rev. Lett.* **2004**, *92* (15), 1555031–1555034. <https://doi.org/10.1103/PhysRevLett.92.155503>.
- (215) Hough, L. A.; Islam, M. F.; Hammouda, B.; Yodh, A. G.; Heiney, P. A. Structure of Semidilute Single-Wall Carbon Nanotube Suspensions and Gels. *Nano Lett.* **2006**, *6* (2), 313–317.

- (216) Lehner, D.; Lindner, H.; Glatter, O. Determination of the Translational and Rotational Diffusion Coefficients of Rodlike Particles Using Depolarized Dynamic Light Scattering. *Langmuir* **2000**, *16* (4), 1689–1695. <https://doi.org/10.1021/la9910273>.
- (217) Schaefer, D. W. Polymers, Fractals, and Ceramic Materials. *Science* **1989**, *243*, 1023–1027.
- (218) Schaefer, D. W.; Brown, J. M.; Anderson, D. P.; Zhao, J.; Chokalingam, K.; Tomlin, D.; Ilavsky, J. Structure and Dispersion of Carbon Nanotubes. In *Journal of Applied Crystallography*; 2003; Vol. 36, pp 553–557. <https://doi.org/10.1107/S0021889803005028>.
- (219) Bauer, B. J.; Hobbie, E. K.; Becker, M. L. Small-Angle Neutron Scattering from Labeled Single-Wall Carbon Nanotubes. *Macromolecules* **2006**, *39*, 2637–2642.
- (220) Virtanen, P.; Gommers, R.; Oliphant, T. E.; Haberland, M.; Reddy, T.; Cournapeau, D.; Burovski, E.; Peterson, P.; Weckesser, W.; Bright, J.; van der Walt, S. J.; Brett, M.; Wilson, J.; Millman, K. J.; Mayorov, N.; Nelson, A. R. J.; Jones, E.; Kern, R.; Larson, E.; Carey, C. J.; Polat, İ.; Feng, Y.; Moore, E. W.; VanderPlas, J.; Laxalde, D.; Perktold, J.; Cimrman, R.; Henriksen, I.; Quintero, E. A.; Harris, C. R.; Archibald, A. M.; Ribeiro, A. H.; Pedregosa, F.; van Mulbregt, P.; Vijaykumar, A.; Bardelli, A. Pietro; Rothberg, A.; Hilboll, A.; Kloeckner, A.; Scopatz, A.; Lee, A.; Rokem, A.; Woods, C. N.; Fulton, C.; Masson, C.; Häggström, C.; Fitzgerald, C.; Nicholson, D. A.; Hagen, D. R.; Pasechnik, D. V.; Olivetti, E.; Martin, E.; Wieser, E.; Silva, F.; Lenders, F.; Wilhelm, F.; Young, G.; Price, G. A.; Ingold, G. L.; Allen, G. E.; Lee, G. R.; Audren, H.; Probst, I.; Dietrich, J. P.; Silterra, J.; Webber, J. T.; Slavič, J.; Nothman, J.; Buchner, J.; Kulick, J.; Schönberger, J. L.; de Miranda Cardoso, J. V.; Reimer, J.; Harrington, J.; Rodríguez, J. L. C.; Nunez-Iglesias, J.; Kuczynski, J.; Tritz, K.; Thoma, M.; Newville, M.; Kümmerer, M.; Bolingbroke, M.; Tartre, M.; Pak, M.; Smith, N. J.; Nowaczyk, N.; Shebanov, N.; Pavlyk, O.; Brodtkorb, P. A.; Lee, P.; McGibbon, R. T.; Feldbauer, R.; Lewis, S.; Tygier, S.; Sievert, S.; Vigna, S.; Peterson, S.; More, S.; Pudlik, T.; Oshima, T.; Pingel, T. J.; Robitaille, T. P.; Spura, T.; Jones, T. R.; Cera, T.; Leslie, T.; Zito, T.; Krauss, T.; Upadhyay, U.; Halchenko, Y. O.; Vázquez-Baeza, Y. SciPy 1.0: Fundamental Algorithms for Scientific Computing in Python. *Nat. Methods* **2020**, *17* (3), 261–272. <https://doi.org/10.1038/s41592-019-0686-2>.
- (221) Sun, H. L.; Wang, Z. M.; Gao, S. Strategies towards Single-Chain Magnets. *Coord. Chem. Rev.* **2010**, *254* (9–10), 1081–1100. <https://doi.org/10.1016/j.ccr.2010.02.010>.
- (222) Gatteschi, D.; Sessoli, R. Molecular Nanomagnets: The First 10 Years. *J. Magn. Magn. Mater.* **2004**, *272–276*, 1030–1036. <https://doi.org/10.1016/j.jmmm.2003.12.004>.
- (223) Luzon, J.; Sessoli, R. Lanthanides in Molecular Magnetism: So Fascinating, so Challenging. *Dalt. Trans.* **2012**, *41* (44), 13556–13567. <https://doi.org/10.1039/c2dt31388j>.
- (224) Bottrill, M.; Kwok, L.; Long, N. J. Lanthanides in Magnetic Resonance Imaging. *Chem. Soc. Rev.* **2006**, *35* (6), 557–571. <https://doi.org/10.1039/b516376p>.
- (225) Armelao, L.; Quici, S.; Barigelletti, F.; Accorsi, G.; Bottaro, G.; Cavazzini, M.; Tondello, E. Design of

- Luminescent Lanthanide Complexes: From Molecules to Highly Efficient Photo-Emitting Materials. *Coord. Chem. Rev.* **2010**, *254* (5–6), 487–505. <https://doi.org/10.1016/j.ccr.2009.07.025>.
- (226) Shibasaki, M.; Yoshikawa, N. Lanthanide Complexes in Multifunctional Asymmetric Catalysis. *Chem. Rev.* **2002**, *102* (6), 2187–2209. <https://doi.org/10.1021/cr010297z>.
- (227) El-Faham, A.; Albericio, F. Peptide Coupling Reagents, More than a Letter Soup. *Chem. Rev.* **2011**, *111* (11), 6557–6602. <https://doi.org/10.1021/cr100048w>.
- (228) Velikyan, I.; Lendvai, G.; Vällilä, M.; Roivainen, A.; Yngve, U.; Bergström, M.; Långström, B. Microwave Accelerated ⁶⁸Ga-Labeling of Oligonucleotides. *J. Label. Compd. Radiopharm.* **2004**, *47* (1), 79–89. <https://doi.org/10.1002/jlcr.799>.
- (229) Würthner, F. Perylene Bisimide Dyes as Versatile Building Blocks for Functional Supramolecular Architectures. *Chem. Commun.* **2004**, *4* (14), 1564–1579. <https://doi.org/10.1039/b401630k>.
- (230) *Systematics and the Properties of the Lanthanides*; Sinha, S. P., Ed.; Springer Netherlands: Dordrecht, 1983. <https://doi.org/10.1007/978-94-009-7175-2>.
- (231) Martin, R. B. Comparisons of Indefinite Self-Association Models. *Chem. Rev.* **1996**, *96* (8), 3043–3064. <https://doi.org/10.1021/cr960037v>.
- (232) Gottarelli, G.; Lena, S.; Masiero, S.; Pieraccini, S.; Spada, G. P. The Use of Circular Dichroism Spectroscopy for Studying the Chiral Molecular Self-Assembly: An Overview. *Chirality* **2008**, *20* (3–4), 471–485. <https://doi.org/10.1002/chir.20459>.
- (233) Pescitelli, G.; Di Bari, L.; Berova, N. Application of Electronic Circular Dichroism in the Study of Supramolecular Systems. *Chem. Soc. Rev.* **2014**, *43* (15), 5211–5233. <https://doi.org/10.1039/c4cs00104d>.
- (234) Görl, D.; Zhang, X.; Würthner, F. Molecular Assemblies of Perylene Bisimide Dyes in Water. *Angew. Chemie - Int. Ed.* **2012**, *51* (26), 6328–6348. <https://doi.org/10.1002/anie.201108690>.
- (235) Caravan, P.; Ellison, J. J.; McMurry, T. J.; Lauffer, R. B. Gadolinium(III) Chelates as MRI Contrast Agents: Structure, Dynamics, and Applications. *Chem. Rev.* **1999**, *99* (9), 2293–2352. <https://doi.org/10.1021/cr980440x>.
- (236) Aida, T.; Meijer, E. W. Supramolecular Polymers – We’ve Come Full Circle. *Isr. J. Chem.* **2020**, *60* (1–2), 33–47. <https://doi.org/10.1002/ijch.201900165>.
- (237) Devaraj, N. K. The Future of Bioorthogonal Chemistry. *ACS Cent. Sci.* **2018**, *4* (8), 952–959. <https://doi.org/10.1021/acscentsci.8b00251>.
- (238) Vigier-Carrière, C.; Boulmedais, F.; Schaaf, P.; Jierry, L. Surface-Assisted Self-Assembly Strategies Leading to Supramolecular Hydrogels. *Angew. Chemie - Int. Ed.* **2018**, *57* (6), 1448–1456. <https://doi.org/10.1002/anie.201708629>.
- (239) Nguyen, P. Q.; Courchesne, N. M. D.; Duraj-Thatte, A.; Praveschotinunt, P.; Joshi, N. S. Engineered Living Materials: Prospects and Challenges for Using Biological Systems to Direct the Assembly of Smart

- Materials. *Adv. Mater.* **2018**, *30* (19), 1704847. <https://doi.org/10.1002/adma.201704847>.
- (240) Uchida, K. Role of Reactive Aldehyde in Cardiovascular Diseases. *Free Radic. Biol. Med.* **2000**, *28* (12), 1685–1696. [https://doi.org/10.1016/S0891-5849\(00\)00226-4](https://doi.org/10.1016/S0891-5849(00)00226-4).
- (241) Kelkar, S. S.; Reineke, T. M. Theranostics: Combining Imaging and Therapy. *Bioconjug. Chem.* **2011**, *22* (10), 1879–1903. <https://doi.org/10.1021/bc200151q>.

Keyword Index

A

Arrhenius 63, 64, 66, 86, 88

B

Benzene-1,3,5-tricarboxamide 7, 10, 57, 58, 59, 60, 137, 168

C

Cooperative 5, 7, 9, 13, 16, 17, 20, 30, 34, 62, 84, 87, 100, 102, 104, 137

D

Dynamic light scattering 137, 138, 139, 140, 170, 177, 178

E

Elongation 5, 14, 20, 58, 62, 63, 66, 67, 69, 84, 85, 88, 103, 104, 105, 107, 108, 111, 120, 121, 122

Enthalpy 7, 88, 166, 169, 172, 186

F

Fractal dimension 139, 140, 146, 153, 154

G

Gel 10, 11, 12, 14, 21, 23, 24, 28, 30, 32, 56, 66, 101, 107, 108, 110, 111, 112, 115, 117, 206

Gelation 11, 13, 21, 23, 28, 34, 59, 104, 107, 108, 109, 111, 114, 117, 122, 139

H

Half-times of polymerization 15, 62, 63, 103, 104, 121

Hydrogel 11, 12, 13, 21, 22, 23, 24, 32, 33, 35, 56, 58, 66, 67, 69, 99, 101, 102, 105, 107, 108, 109, 110, 112, 118, 206

I

Isodesmic 5, 7, 9, 16, 17, 157, 163, 165, 166, 167, 168, 169, 172, 177, 185, 186

L

Lanthanide 43, 157, 158, 159, 162, 172, 207

M

Magnetic energy 36, 38, 39, 41, 43, 52, 135, 136, 140, 143, 144, 145, 150

Magnetic field 35, 36, 38, 39, 40, 41, 42, 43, 44, 46, 48, 49, 50, 51, 52, 53, 54, 57, 135, 136, 139, 140, 141, 142, 145, 146, 152, 155, 158, 206

Model fitting 62, 63, 65, 86, 87, 88, 105, 113, 122, 163, 166, 169, 170, 177, 185, 186

N

Network structures 139, 140, 144, 145, 207

Nucleation 5, 14, 23, 24, 48, 56, 58, 59, 62, 63, 66, 69, 84, 85, 88, 103, 104, 105, 107, 108, 112, 120, 121, 206

P

Perylene diimide 8, 12, 20, 32, 34, 57, 157, 158, 159, 160, 161, 162, 163, 164, 165, 167, 168, 169, 170, 171, 172, 177

Proton diffusion 56, 58, 66, 67, 68, 69

R

Reaction cycle 27, 28, 29, 30, 31, 32, 34, 56, 99, 100, 101, 102, 105, 107, 108, 109, 110, 111, 112, 115, 117, 206

S

Scattering intensity 139, 140, 153

Secondary nucleation 103, 104, 105, 108, 120, 121

Résumé

L'objectif de cette thèse était de développer de nouvelles techniques pour mieux contrôler des polymères supramoléculaires, trois différentes stratégies ont été présentées. Premièrement, le contrôle spatiotemporel d'un hydrogel a été réalisé par la diffusion d'un acide à partir d'un matériau poreux, ce qui active une molécule sensible au pH. La deuxième stratégie s'appuie sur un cycle réactionnel hors équilibre à fin d'obtenir le contrôle temporel et des propriétés mécaniques d'un hydrogel. La dernière méthode repose sur l'utilisation de stimuli magnétiques de deux façons : en utilisant des champs magnétiques (< 2 T) pour influencer la topologie de réseaux de fibres supramoléculaires contenant des ions paramagnétique ; et contrôler la taille d'agrégats supramoléculaires, sans champ magnétique, juste en incluant des différents lanthanides paramagnétiques dans leur structure moléculaire. Ces nouvelles méthodes sont un avancement vers un meilleur contrôle des polymères supramoléculaires.

Mots-clés : polymères supramoléculaires, autoassemblage, contrôle magnétique, cycle réactionnel hors équilibre, terres rares.

Résumé en anglais

The aim of this thesis was to develop new techniques to better control supramolecular polymers, three different strategies were presented. First, spatiotemporal control of a hydrogel was achieved by diffusion of protons from a porous material, which activates a pH-responsive hydrogelator. The second strategy relies on an out-of-equilibrium reaction cycle to obtain temporal and mechanical control of a hydrogel. The last method relies on the magnetic control of supramolecular assemblies in two ways: using magnetic fields (< 2 T) to influence the topology of supramolecular rod networks containing a paramagnetic lanthanide; and controlling the size of supramolecular aggregates, without a magnetic field, by including different paramagnetic lanthanides in the molecular structure and inducing their interaction through supramolecular self-assembly. These new methods are an advancement towards better kinetic and thermodynamic control of supramolecular polymers in and out-of-equilibrium.

Keywords: supramolecular polymers, self-assembly, magnetic control, out-of-equilibrium reaction cycle, rare earths.